

**Some pages of this thesis may have been removed for copyright restrictions.**

If you have discovered material in Aston Research Explorer which is unlawful e.g. breaches copyright, (either yours or that of a third party) or any other law, including but not limited to those relating to patent, trademark, confidentiality, data protection, obscenity, defamation, libel, then please read our [Takedown policy](#) and contact the service immediately (openaccess@aston.ac.uk)

# **Advanced Digital Signal Processing for Coherent Optical OFDM Transmissions**

Son Thai Le

Doctor of Philosophy

ASTON UNIVERSITY

January 2016

©Son Thai Le, 2016

Son Thai Le asserts his moral right to be identified as the author of this thesis

This copy of the thesis has been supplied on condition that anyone who consults it is understood to recognise that its copyright rests with its author and that no quotation from the thesis and no information derived from it may be published without appropriate permission or acknowledgement.

**Aston University**

# **Advanced Digital Signal Processing for Coherent Optical OFDM Transmissions**

**Son Thai Le**

Doctor of Philosophy

January 2016

Coherent optical orthogonal frequency division multiplexing (CO-OFDM) has been actively considered as a potential candidate for long-haul transmission and 400 Gb/s to 1 Tb/s Ethernet transport because of its high spectral efficiency, efficient implementation, flexibility and robustness against linear impairments such as chromatic dispersion and polarization mode dispersion. However, due to the long symbol duration and narrow subcarrier spacing, CO-OFDM systems are sensitive to laser phase noise and fibre nonlinearity induced penalties. As a result, the development of CO-OFDM transmission technology crucially relies on efficient techniques to compensate for the laser phase noise and fibre nonlinearity impairments.

In this thesis, high performance and low complexity digital signal processing techniques for laser phase noise and fibre nonlinearity compensation in CO-OFDM transmissions are demonstrated. For laser phase noise compensation, three novel techniques, namely quasi-pilot-aided, decision-directed-free blind and multiplier-free blind are introduced. For fibre nonlinear compensation, two novel techniques which are referred to as phase conjugated pilots and phase conjugated subcarrier coding, are proposed. All these abovementioned digital signal processing techniques offer high performances and flexibilities while requiring relatively low complexities in comparison with other existing phase noise and nonlinear compensation techniques. As a result of the developments of these digital signal processing techniques, CO-OFDM technology is expected to play a significant role in future ultra-high capacity optical network. In addition, this thesis also presents preliminary study on nonlinear Fourier transform based transmission schemes in which OFDM is a highly suitable modulation format. The obtained result paves the way towards a truly flexible nonlinear wave-division multiplexing system that allows the current nonlinear transmission limitations to be exceeded.

**Additional keywords and phrases:** Optical communications, OFDM, phase noise compensation, fibre nonlinearity compensation, nonlinear Fourier transform.

# Dedication

*To my mother - Nguyen Thi Thu, who dedicated the whole life for a better future of her children and to my sister - Le Thi Hong Nhung, whom I love more than anything in the world.*

# Acknowledgements

First of all, I would like to thank my supervisor Prof. Sergei Turitsyn for providing me the opportunity to pursue my PhD at Aston University. I am deeply grateful for the excellent guidance and support I have received throughout my PhD. Without his continued motivation, patience, support and advice the completion of this thesis would not be possible.

I would like to thank Prof. Andrew Ellis for countless lessons on optical communications and enormous supports on both research related and general academic issues. I have learnt a lot from his deep knowledge, exceptional technical skills and wisdom.

I would like to thank Prof. Keith Blow for teaching me countless fundamental lessons on optical communications and numerical modelling. His expertise has helped me tremendously in solving a lot of research problems.

I would like to thank Dr. Yaroslav Prylepkiy for a close, fruitful collaboration and for teaching me the basic of nonlinear Fourier transforms. It is a great pleasure to collaborate with him because of his deep understanding and inspiring ideas.

I would like to thank Dr. Paul Harper, Dr. Mary McCarthy, Dr. Ian Phillips, Dr Naoise MacSuibhne and Dr. Thavamaran Kanesan for number of experimental lessons in the labs. I would like to thank my colleagues, Dr. Paul Haigh, Mr. Mingming Tam, Dr. Srikanth Sugavanam, Dr. Nikita Tarasov, Mr. Morteza Kamalian Kopae for countless discussions, fruitful collaborations and for being such wonderful friends.

I also would like to thank to all other colleagues from Aston University, UCL, Oxford University, Northumbria University and Novosibirsk University whom I had chance to meet and collaborate with.

Finally, I would like to thank all members of my family for always being beside and supporting me in my PhD journey.

# Contents

|          |  |           |
|----------|--|-----------|
| <b>1</b> | <b>Introduction</b>  | <b>26</b> |
| 1.1      | Overview . . . . .   | 26        |
| 1.2      | Motivation . . . . .   | 29        |
| 1.3      | Organization of the thesis . . . . .   | 31        |
| 1.4      | Contributions of the thesis . . . . .  | 32        |
| 1.5      | Patent . . . . .   | 36        |
| 1.6      | Publications . . . . .   | 36        |
| <b>2</b> | <b>Statistical Properties and Indirect Bit Error Rate Estimation Methods for CO-OFDM</b> | <b>44</b> |
| 2.1      | Introduction . . . . .   | 44        |
| 2.2      | BER estimation methods for QPSK transmissions . . . . .                                  | 46        |
| 2.2.1    | Direct error-counting . . . . .  | 46        |
| 2.2.2    | Data-aided EVM . . . . .   | 46        |
| 2.2.3    | Nodata-aided EVM (Q factor 1, Q1) . . . . .  | 47        |
| 2.2.4    | Q factor 2, (Q2) . . . . .   | 48        |
| 2.2.5    | Q factor 3, (Q3) . . . . .   | 48        |
| 2.3      | Simulation setup of 112 Gb/s QPSK CO-OFDM transmissions . . . . .                        | 49        |
| 2.4      | Statistical properties of QPSK signals in CO-OFDM transmissions . . . . .                | 51        |
| 2.5      | Novel indirect BER estimation methods for QPSK CO-OFDM . . . . .                         | 54        |
| 2.6      | Comparison of BER estimation methods for QPSK CO-OFDM . . . . .                          | 56        |
| 2.6.1    | Impact of the laser phase noise . . . . .  | 59        |
| 2.6.2    | Impact of frequency offset . . . . .   | 61        |

|          |   |            |
|----------|---|------------|
| 2.7      | Experimental verification . . . . .   | 63         |
| 2.7.1    | Experimental setup . . . . .  | 63         |
| 2.7.2    | Experimental results and discussions . . . . .  | 64         |
| 2.8      | Conclusion . . . . .  | 69         |
| <b>3</b> | <b>Low-Complexity Phase Noise Estimation Methods for CO-OFDM</b>                                  | <b>70</b>  |
| 3.1      | System model . . . . .  | 70         |
| 3.1.1    | Phase noise model . . . . .   | 71         |
| 3.1.2    | Fibre channel model . . . . .   | 71         |
| 3.1.3    | CO-OFDM system model . . . . .  | 72         |
| 3.2      | Quasi-pilot aided phase noise estimation for CO-OFDM . . . . .                                    | 74         |
| 3.2.1    | Introduction . . . . .  | 74         |
| 3.2.2    | QPA concept . . . . .   | 75         |
| 3.2.3    | Experimental results and discussions . . . . .  | 78         |
| 3.3      | Blind phase noise estimation for CO-OFDM . . . . .  | 79         |
| 3.3.1    | Blind phase noise tracking . . . . .  | 81         |
| 3.3.2    | Decision directed free PNC . . . . .  | 85         |
| 3.3.3    | Performance comparison . . . . .  | 89         |
| 3.3.4    | Complexity comparison . . . . .   | 93         |
| 3.4      | Multiplier-free blind PNE for CO-OFDM . . . . .   | 94         |
| 3.4.1    | Experimental results and discussions . . . . .  | 97         |
| 3.5      | Conclusion . . . . .  | 98         |
| <b>4</b> | <b>Low-Complexity Fiber Nonlinearity Compensation Methods for CO-OFDM</b>                         | <b>100</b> |
| 4.1      | Introduction . . . . .  | 100        |
| 4.2      | Phase conjugated pilots for for fibre nonlinearity compensation in CO-OFDM transmission . . . . . | 103        |
| 4.2.1    | Concept of PCP . . . . .  | 103        |
| 4.2.2    | Simulation . . . . .  | 105        |
| 4.2.3    | Experimental setup and results . . . . .  | 112        |

|          |   |            |
|----------|---|------------|
| 4.3      | Phase conjugated subcarrier coding for fibre nonlinear mitigation in CO-OFDM Transmission . . . . . | 116        |
| 4.3.1    | Concept of PCSC . . . . .   | 116        |
| 4.3.2    | Simulation . . . . .  | 118        |
| 4.3.3    | Experimental setup and results . . . . .  | 123        |
| 4.4      | Conclusion . . . . .  | 126        |
| <b>5</b> | <b>Nonlinear Fourier Transform Based Optical Communication Systems</b>                              | <b>128</b> |
| 5.1      | Introduction . . . . .  | 128        |
| 5.2      | NLSE model of optical fibre communication channel . . . . .   | 131        |
| 5.3      | Basic of NFT operations . . . . .   | 132        |
| 5.3.1    | Direct NFT . . . . .  | 132        |
| 5.3.2    | INFT operation (for the left set of scattering data) . . . . .                                      | 135        |
| 5.4      | Basic designs of NFT-based communication systems . . . . .  | 136        |
| 5.5      | Numerical methods for NFT operations . . . . .  | 137        |
| 5.5.1    | Numerical methods for NFT . . . . .   | 138        |
| 5.5.2    | Numerical methods for INFT . . . . .  | 142        |
| 5.6      | NIS transmission methods for lossless fibre links . . . . .   | 147        |
| 5.6.1    | Basis of NIS-based transmissions . . . . .  | 147        |
| 5.6.2    | Computational complexities of NIS method . . . . .  | 148        |
| 5.6.3    | Simulation results and discussions . . . . .  | 150        |
| 5.7      | NIS for optical links with lumped amplification . . . . .   | 159        |
| 5.7.1    | LPA model for optical links with EDFAs . . . . .  | 159        |
| 5.7.2    | Simulation results and discussions . . . . .  | 163        |
| 5.8      | Modified NIS for optical links with distributed raman amplification . . . . .                       | 167        |
| 5.8.1    | Random DFB raman amplification . . . . .  | 167        |
| 5.8.2    | NIS for non-ideal distributed Raman amplification . . . . .   | 169        |
| 5.8.3    | Simulation results and discussions . . . . .  | 174        |
| 5.9      | Experimental demonstration of NIS transmission over transoceanic distances                          | 178        |
| 5.9.1    | Experimental setup of 10 Gbaud NIS-based OFDM transmission .  | 178        |

|          |  |            |
|----------|--|------------|
| 5.9.2    | Simulation results . . . . .                   | 180        |
| 5.9.3    | Experimental results and discussions . . . . . | 184        |
| 5.10     | Conclusion . . . . .                           | 187        |
| <b>6</b> | <b>Conclusion</b>                              | <b>189</b> |
| 6.1      | General conclusion . . . . .                   | 189        |
| 6.2      | Future research . . . . .                      | 190        |

# List of Figures

|     |   |    |
|-----|---|----|
| 2.1 | Constellation diagram and error vector for a QPSK signal. Vector $\mathbf{E}_{t,i}$ is the transmitted signal, vector $\mathbf{E}_{r,i}$ is the received signal and $\mathbf{E}_{err,i} = \mathbf{E}_{r,i} - \mathbf{E}_{t,i}$ is the error vector . . . . .                      | 47 |
| 2.2 | Block diagrama of 112 Gb/s PDM CO-OFDM transmissions. S/P: serial/parallel conversion, P/S: parallel/serial conversion, SM: symbol mappings, TS: training symbol, DAC: digital-to-analog converter, I/Q: I/Q modulator, OLO: optical local oscilator . . . . .                    | 49 |
| 2.3 | Histogram of in-phase and quadrature components of the received QPSK symbols in x and y-polarization. Propagation over 800 km in nonlinear limited regime (3 dBm). Gaussian fitting is superimposed to each histogram, KSSTAT values are also included in each histogram. . . . . | 52 |
| 2.4 | Histogram of in-phase and quadrature components of the received QPSK symbols in x-polarization. Propagation over 800 km in nonlinear limited regime with the launch power of 6 dBm. . . . .   | 53 |
| 2.5 | Histogram of the received QPSK symbols phases (x-polarization) in four quadrants of the constellation diagram. Propagation over 800 km in nonlinear limited regime with the launch power of 3 dBm. . . . .  | 54 |
| 2.6 | Histogram of the received QPSK symbols phases (x-polarization) in four quadrants of the constellation diagram. Propagation over 800 km in nonlinear limited regime with the launch power of 6 dBm. . . . .  | 55 |
| 2.7 | Q-factor values (average over x-and y-polarization) as a function of the launch power in 112 Gb/s QPSK PDM CO-OFDM after 2400 km of transmission. Q(EVM), Q1, Q2, Q3 all follow the lower curve. . . . .  | 57 |

|      |  |    |
|------|--|----|
| 2.8  | Q-factor values (average over x-and y-polarization) as a function of the launch power in 112 Gb/s QPSK PDM RGI-CO-OFDM after 4000 km of transmission. . . . .  | 57 |
| 2.9  | Q-factor values for the center channel (average over x-and y-polarization) as a function of the launch power in $7 \times 112$ Gb/s QPSK PDM WDM RGI-CO-OFDM after 3200 km of transmission. . . . .  | 58 |
| 2.10 | Q-factor values (average over x-and y-polarization) as a function of the launch power in 112 Gb/s 8-PSK PDM CO-OFDM after 800 km of transmission. . . . .  | 58 |
| 2.11 | Q-factor values (average over x-and y-polarization) as a function of the combined laser linewidth in 112 Gb/s PDM CO-OFDM after 2000 km of transmission; the launch power was 1 dBm. . . . .   | 59 |
| 2.12 | Q-factor values (average over x-and y-polarization) as a function of the combined laser linewidth in 112 Gb/s PDM RGI-CO-OFDM after 4000 km of transmission; the launch power was 1 dBm. . . . .   | 60 |
| 2.13 | Q-factor values (average over x-and y-polarization) as a function of the frequency offset in 112 Gb/s PDM CO-OFDM after 2000 km of transmission; the launch power was 1dBm. . . . .  | 62 |
| 2.14 | Q-factor values (average over x-and y-polarization) as a function of the frequency offset in 112 Gb/s PDM RGI-CO-OFDM after 4000 km of transmission; the launch power was 1dBm. . . . .  | 62 |
| 2.15 | Schematic of experimental setup of WDM CO-OFDM transmission. ECL: external cavity laser, PMM: polarization maintaining multiplexer, WSS: wavelength selective switch, DFB: distributed feedback laser, BPF: band-pass filter (optical), AOM: acousto-optic modulator, GFF: gain flattening filter, OSA: optical spectrum analyser, LO: local oscillator (optical), EDFA: Erbium-doped fibre amplifier. . . . . | 64 |
| 2.16 | Histograms of in-phase and quadrature components of the received QPSK symbols in the first quadrant. Gaussian fitting is superimposed to each histogram; KSSTAT values are also included in each histogram. . . . .  | 65 |

|      |  |    |
|------|--|----|
| 2.17 | Histogram of the received QPSK symbols phase of the center channel in four quadrants of the constellation diagram. . . . .   | 65 |
| 2.18 | (a) - Q-factor values for the center channel as a function of the launch power at 2400km, (b) received optical spectrum at 3200km. . . . .   | 66 |
| 2.19 | Q-factor values for the second channel as a function of the launch power at 2400km. . . . .  | 67 |
| 2.20 | Performance comparison of BER estimation methods in the back-to-back case (simulation results), without (a) and with (b) the laser phase noise, the combined laser linewidth is 200 kHz. . . . . | 68 |
| 2.21 | STD of the Q-factor obtained using different BER estimation methods as a function of the number of processed symbols. . . . .  | 68 |
| 3.1  | Block diagram of the CO-OFDM system with laser phase noise and non-linear phase noise acquired during optical fibre transmission. . . . .  | 71 |
| 3.2  | BER versus OSNR with 200 kHz combined linewidth in 40 Gb/s 16QAM OFDM transmission. . . . .  | 79 |
| 3.3  | BER versus number of PSs at 26 dB OSNR in 40 Gb/s 16QAM OFDM transmission. . . . .   | 79 |
| 3.4  | BER versus combined laser linewidth also at 26 dB OSNR in 40 Gb/s 16QAM OFDM transmission. . . . .   | 80 |
| 3.5  | Block diagram of blind PNE with a feedback loop for phase tracking. . .  | 82 |
| 3.6  | (a) block diagrams of (a) blind PNE schemes without feedback loop, (b) phase unwrapping block. . . . .   | 82 |
| 3.7  | Phase cycle-slip probability as a function of symbol-duration-linewidth product in CO-OFDM systems with blind PNE. . . . .   | 84 |
| 3.8  | Maximum allowable laser linewidth as a function of symbol duration for implementing blind PNE in CO-OFDM systems. . . . .  | 84 |
| 3.9  | Calculated cost function $J_1(\varphi - \Phi_m)$ and its estimations using three test phases as function of phase offsets for 16QAM with $N = 200$ subcarriers and 6 dB. . . . .                 | 87 |

|      |   |    |
|------|---|----|
| 3.10 | Calculated cost functions $J_2(\varphi - \Phi_m)$ , $J_3(\varphi - \Phi_m)$ and its estimations using three test phases as function of phase offsets for 16QAM with $N = 200$ subcarriers and $SNR = 6$ dB. . . . .   | 89 |
| 3.11 | Root-mean-square-error (RMSE) of CPE as a function of SNR for DDF PNE techniques employing $J_1(\varphi)$ , $J_2(\varphi)$ and $J_3(\varphi)$ for 16QAM CO-OFDM transmission with $N = 100$ subcarriers. . . . .  | 90 |
| 3.12 | Required SNRs for a RMSE of 0.1 rad as a function of number of subcarriers ( $N$ ) for DDF PNE techniques employing $J_1(\varphi)$ , $J_2(\varphi)$ and $J_3(\varphi)$ for 16QAM CO-OFDM transmission. . . . .  | 91 |
| 3.13 | a) BER performances of PNE techniques, including PA-aided with 16 pilots (blue), BPS with 16 test phases (brown) and DDF blind PNE with different cost functions (red- $J_1(\varphi)$ , green- $J_2(\varphi)$ , pink- $J_3(\varphi)$ ) with feedback loop (solid) and digital phase tracking (open) for 16QAM, the symbol duration linewidth product is $5 \times 10^{-3}$ ; (b) BER performance of the same PNE (only showing digital phase tracking) for 64QAM, the symbol duration linewidth product is $2 \times 10^{-3}$ . . . . . | 92 |
| 3.14 | Constellation diagrams for 16QAM at a SNR of 23 dB, before PNE (a), after PNE using PA-aided technique with 16 pilots (b), after PNE with DDF blind PNE technique with digital phase tracking and $J_1(\varphi)$ (c), after PNE using BPS with 16 test phases (d), after PNE DDF blind PNE technique with digital phase tracking and $J_2(\varphi)$ and $J_3(\varphi)$ (e, f). . . . .  | 92 |
| 3.15 | The SNR penalty at a BER of $10^{-3}$ as a function of $\nu T_S$ for PA-aided, BPS and DDF blind PNE with different cost functions for 16QAM transmission with 200 subcarriers; (b) similar result for 16QAM and 100 subcarriers; (c) similar result for 64QAM at a BER of $10^{-2}$ and 200 subcarriers; (d) SNR penalty as a function of $N$ at a BER of $10^{-2}$ for 64QAM and TS of $10^{-3}$ . . . . .  | 93 |
| 3.16 | Estimating the MPB with a bin width of using the scanning algorithm with overlapping bins and small scanning step. The histogram with small bin width is also shown. . . . .  | 95 |

|      |  |     |
|------|--|-----|
| 3.17 | Block diagram of the proposed PNC technique for 16QAM CO-OFDM systems. For QPSK the amplitude partitioning block is not needed. . . . .  | 96  |
| 3.18 | Impact of $\alpha$ and $\Delta\alpha$ on the performance of MF bind PNC technique in 16QAM CO-OFDM transmissions in back-to-back case. The dash lines show the BER performance when the CPE is perfectly compensated. . . . .  | 97  |
| 3.19 | BER versus OSNR in back-to-back case for 40 Gb/s 16QAM CO-OFDM transmission. . . . .   | 97  |
| 3.20 | (a) BER versus power for 20 Gb/s QPSK transmission over 4000 km, (b) BER versus combined laser linewidth for 40 Gb/s 16QAM transmission in back-to-back case. . . . .  | 98  |
| 4.1  | Inserting phase-conjugated pilots for fibre nonlinearity compensation. . . . .   | 103 |
| 4.2  | Block diagram of 112 Gb/s PDM CO-OFDM transmissions. S/P: serial/parallel conversion, P/S: parallel/serial conversion, SM: symbol mappings, TS: training symbol, DAC: digital-to-analog converter, ADC: analog-to-digital converter, I/Q: I/Q modulator, PBS: polarization beam splitter, OLO: optical local oscillator. . . . . | 106 |
| 4.3  | Nonlinear noise cancellation based on the coherent superposition of PCP pairs. The transmission distance is 1200 km, launch power is 5 dBm, ASE noise is not considered and 50 % pre-EDC is adopted. . . . .   | 107 |
| 4.4  | Measured reduction of signal variance from both nonlinear distortion ( $\sigma_{NL}^2$ ) and linear noise ( $\sigma_L^2$ ) as a function of the launch power, in systems with and without 50 % pre-EDC. The transmission distance is 1200 km, ASE noise is included. . . . .   | 107 |
| 4.5  | Measured reduction of signal variance as a function of the frequency spacing. The transmission distance is 1200 km, the launch power is 5 dB, ASE noise is included and the number of subcarriers is varied, keeping the same data rate (112 Gb/s). . . . .  | 108 |

|      |   |     |
|------|---|-----|
| 4.6  | Nonlinear cancellation using coherent superposition of PCP pairs in long-haul 56 Gb/s (net data rate) CO-OFDM transmission. The transmission distances are 3200 km (open symbols) and 6400 km (closed symbols) . . .  | 109 |
| 4.7  | Received constellation diagrams in 112 Gb/s PDM CO-OFDM systems without (with the same bandwidth, before CS) (a) and with PCPs for fibre nonlinearity compensation (b - 12.5 %, c - 25 %, d - 50 % overhead). The Transmission distance is 1200 km, the launch power is 5 dBm. . . . .  | 110 |
| 4.8  | Signal enhancement of a 3200 km PDM NGI CO-OFDM system at the optimum launch power as a function of the fraction of subcarriers allocated as phase conjugate pilots, showing measured reduction in signal variance (red symbols), net gain after subtraction of overhead (purple) and predicted signal to noise ratio gain (blue symbols). . . . .  | 110 |
| 4.9  | Schematic of experimental setup of WDM CO-OFDM transmission with PCPs for fibre nonlinearity compensation. ECL: external cavity laser, PMM: polarization maintaining multiplexer, WSS: Wavelength Selective Switch, DFB: distributed feedback laser, BPF: band-pass filter (optical), AOM: acousto-optic modulator, GFF: gain flatten filter, OSA: optical spectrum analyser, LO: local oscillator. . . . . | 113 |
| 4.10 | Cancellation of the nonlinear distortions by CS of subcarriers with its counterpart PCPs in WDM CO-OFDM transmission, 800 km of distance, the launch power (per/ch) was 0 dBm. . . . .  | 114 |
| 4.11 | Q-factor of the center channel as a function of the launch power in system with and without PCPs for fibre nonlinearity compensation. . . . .   | 114 |
| 4.12 | Constellation diagrams for the center channel at $P_{in} = -1.5$ dBm for the cases of without PCPs (a) and with 2.5%, 50 % of PCPs (b and c) respectively. The transmission distance is 3200 km . . . . .   | 114 |
| 4.13 | Performance gain as a function of the additional overhead due to PCPs for the center channel, after 3200 km of distance. Without PCPs, an overhead of $\sim 8$ % was required for CPE compensation. . . . .   | 115 |
| 4.14 | Phase-conjugated subcarrier coding scheme for CO-OFDM transmission.   | 117 |

|      |   |     |
|------|---|-----|
| 4.15 | PCSC symbol mapping for BPSK and QPSK. the numbers (in red) are the probabilities of symbols in the constellation set. . . . .  | 117 |
| 4.16 | Sensitivities of OFDM systems with and without PCSC in the linear channel with white Gaussian noise. . . . .  | 118 |
| 4.17 | Dispersion map of an optical link with 50 % pre-EDC. L is the link distance and D is the dispersion coefficient. . . . .  | 118 |
| 4.18 | Block diagram of PDM CO-OFDM transmissions with PCSC. S/P: serial/parallel conversion, P/S: parallel/serial conversion, SM: symbol mappings, TS: training symbol, DAC: digital-to-analog converter, ADC: analog-to-digital converter, I/Q: I/Q modulator, PBS: polarization beam splitter, OLO: optical local oscillator. . . . .                                     | 119 |
| 4.19 | Q-factor as a function of the launch power in 150 Gb/s PDM CO-OFDM system with and without PCSC, the transmission distance is 8000 km. . .  | 120 |
| 4.20 | Constellation diagrams on x-polarization in 150 Gb/s PDM CO-OFDM system over 8000 km, 8 dBm of the launch power, a) without PCSC, b, c) with PCSC, before and after decoding. . . . .   | 120 |
| 4.21 | PDF of real and imaginary components for the 1 symbol in systems with and without the PCSC, the launch power was 7 dBm. . . . .   | 121 |
| 4.22 | Q-factor as a function of the launch power in 300 Gb/s PDM CO-OFDM system with and without PCSC and constellation diagrams (before (a) and after (b) decoding) at 4 dBm, after 3200 km of transmission distance. . . .  | 122 |
| 4.23 | Performance gain in systems with PCSC as a function of the frequency spacing for different modulation formats. . . . .  | 122 |
| 4.24 | Schematic of experimental setup of WDM CO-OFDM transmission with PCPs for fibre nonlinearity compensation. ECL: external cavity laser, PMM: polarization maintaining multiplexer, WSS: Wavelength Selective Switch, DFB: distributed feedback laser, BPF: band-pass filter (optical), GFF: gain flatten filter, OSA: optical spectrum analyser, LO: local oscillator. | 124 |
| 4.25 | (a)-Optical spectrum after the transmitter. (c) optical spectrum after 2400 km of transmission distance. . . . .  | 124 |

|      |  |     |
|------|--|-----|
| 4.26 | Back-to-back performance of OFDM systems with and without PCSC with BPSK and QPSK modulation formats. . . . .  | 125 |
| 4.27 | Received constellation diagrams of the center channel at 4000 km of transmission distance, the launch power/channel was -3 dBm, a) without PCSC, b, c) with PCSC, before and after decoding. . . . . | 125 |
| 4.28 | Q-factor as a function of the launch power/channel for the center channel in BPSK WDM CO-OFDM systems with and without PCSC, the transmission distance is 6000 km. . . . .                           | 126 |
| 4.29 | Q-factor as a function of the launch power/channel for the center channel in QPSK WDM CO-OFDM systems with and without PCSC, the transmission distance is 4000 km. . . . .                           | 127 |
| 5.1  | Basic designs of NFT-based transmission systems (a); transmission in the nonlinear Fourier domain (NFD) (b); nonlinear Fourier domain based BDP (NFD-DBP) (c). . . . .                               | 137 |
| 5.2  | (a) Continuous spectrum of rectangular pulse for $A = 1, T_2 - T_1 = 1$ (b) Continuous spectrum of rectangular pulse for $A = 6, T_2 - T_1 = 1$ . . . . .  | 141 |
| 5.3  | Mean square error as a function of the simulation time resolution ( $dt$ ) . . . . .   | 141 |
| 5.4  | Comparison between the numerical and analytical results. (a) numerical and analytical solution for $q(t)$ , $dt = 0.01$ . (b) error of numerical method as a function of $t$ . . . . .               | 146 |
| 5.5  | RMSE as a function of the time resolution $dt$ . . . . .   | 146 |
| 5.6  | Block diagram of NIS-based optical communication systems . . . . .   | 147 |
| 5.7  | Illustration of a burst mode transmission, in which neighbouring packets are separated by a guard time . . . . .   | 150 |
| 5.8  | Linear spectra of OFDM signals before and after BNFT, the launch power is 0 dBm. . . . .   | 154 |
| 5.9  | Q-factor as a function of the launch power for the (a) OFDM and (b) Nyquist-shaped NIS-based systems without the ASE noise. . . . .  | 154 |

|      |  |     |
|------|--|-----|
| 5.10 | Performance comparison of the 100 Gb/s QPSK OFDM systems with the NIS vs. the DBP methods for fibre nonlinearity compensation. The receiver filter bandwidth used was 40 GHz, the distance is 2000 km. . . . .   | 155 |
| 5.11 | Constellation diagrams at the optimum launch powers of the 100 Gb/s QPSK OFDM systems with and without the NIS and DBP methods for fibre compensation; (a) without NIS and DBP, (b) with the NIS method, (c) DBP with 10 steps/span, (d) DBP with 20 steps/span. . . . .   | 155 |
| 5.12 | Performance comparison of the 100 Gb/s QPSK Nyquist-shaped systems with the NIS and DBP methods for fibre nonlinearity compensation. The receiver filter bandwidth is 40 GHz, the distance is 2000 km. . . . .   | 156 |
| 5.13 | Constellation diagrams at the optimum launch powers of the 100 Gb/s QPSK OFDM systems with and without the NIS and DBP methods for fibre compensation; (a) without NIS and DBP, (b) with the NIS method, (c) DBP with 10 steps/span, (d) DBP with 20 steps/span. . . . .   | 157 |
| 5.14 | Performance comparison of the 300 Gb/s 64QAM OFDM systems with the NIS and DBP methods for fibre nonlinearity compensation. The receiver filter bandwidth was 40 GHz, the distance is 800 km. . . . .  | 158 |
| 5.15 | A comparison of output fields obtained by using the standard NLSE and the LPA NLSE, the amplifier spacing is 80 km. (b) NMSE as a function of the transmission distance. (c) NMSE as a function of the signals bandwidth for a given input power and a given input power density. (d) NMSE as a function of the input power. . . . . | 161 |
| 5.16 | Level curves of NMSE (in dB) indicating the error of using LPA NLSE (5.50), plotted as a function of the signals bandwidth (in GHz) and the input power (in dBm) for the propagation distance 2000 km. . . . .   | 162 |
| 5.17 | Q-factor as a function of the launch power for 100 Gb/s QPSK OFDM NIS-based system in the back-to-back case and in a 2000 km optical link, the ASE is ignored . . . . .  | 164 |

|      |   |     |
|------|---|-----|
| 5.18 | Performance comparison of the 100 Gb/s QPSK OFDM systems with the NIS vs. the DBP methods for fibre nonlinearity compensation, and constellation diagrams at the optimum launch powers for the cases: (b) without NIS and DBP, (c) DBP with 10 steps/span (d) with the NIS method, (e) DBP with 20 steps/span. The propagation distance is 2000 km. . . . . | 165 |
| 5.19 | Performance comparison of the 200 Gb/s 16QAM OFDM systems with the NIS vs. the DBP methods for fibre nonlinearity compensation and constellation diagrams at the optimum launch powers for (b) Without NIS and DBP, (b) with the NIS method. The transmission distance is 2000 km. . . . .  | 165 |
| 5.20 | Performance comparison of the 300 Gb/s 64QAM OFDM systems with the NIS vs. the DBP methods for fibre nonlinearity compensation and constellation diagrams at the optimum launch powers for (b) Without NIS and DBP, (b) with the NIS method. The transmission distance is 640 km. . . . .   | 166 |
| 5.21 | Schematic of the random DFB laser Raman amplifier. . . . .  | 167 |
| 5.22 | Raman gain (a) and noise (b) profiles along 80 km SMF span for different value of the forward pump power (FPP). . . . .   | 168 |
| 5.23 | AGV and NLCC as a function of the forward pump power; the span length was 80 km. . . . .  | 168 |
| 5.24 | A comparison of output fields obtained by using the standard NLSE and the LPA NLSE for 50 Raman spans (4000 km) and a burst power of 0 dBm. . . . .   | 171 |
| 5.25 | NMSEs as functions of the transmission distance for different values of the FPP. The burst power is fixed at 0 dBm. . . . .   | 171 |
| 5.26 | NMSEs as functions of the burst power for different values of the FPP. The transmission distance is fixed at 4000 km. . . . .   | 172 |
| 5.27 | NMSEs as functions of the FPP for different values of the transmission distances. The normalized power is fixed at -4 dBm. . . . .  | 172 |
| 5.28 | (a) Block diagram of NIS-based transmission systems, (b) Illustration of a burst mode transmission. . . . .   | 173 |

|      |   |     |
|------|---|-----|
| 5.29 | (a)-Performance comparison of OFDM systems with and without NIS, and the modified NIS scheme for $FPP = 0$ W (backward pumping only case), (b)-(d) constellations at the optimum launch powers for system without NIS (b), with NIS (c) and with the modified NIS (d) schemes at $FPP = 0$ W, respectively. . . . .   | 175 |
| 5.30 | Performance comparison of OFDM systems with and without NIS, and the modified NIS scheme for $FPP = 2.7$ W. The transmission distance is 4000 km. . . . .   | 176 |
| 5.31 | Optimum Q-factor as a function of FPP for OFDM systems with and without NIS, and the modified NIS scheme. The transmission distance was 4000 km. . . . .  | 176 |
| 5.32 | (a): Schematic of the experimental setup of 10 Gbaud NIS-based transmission in fibre link with EDFA-only amplification; (b) block diagram of the Tx DSP; (c) block diagram of the Rx DSP; (d) illustration of a transmitted burst with a duration of 30 ns carrying 120 bits (60 QPSK symbols) and illustration of synchronization error, (e) - structure of the transmitted signal, including one synchronization symbol, two training symbols for channel estimation and 100 OFDM NIS-based bursts. . . . . | 179 |
| 5.33 | Comparison of output signals of the INFT block given the same input 10 Gbaud OFDM waveform with different power levels. . . . .   | 181 |
| 5.34 | Simulated back-to-back performance of NIS-based 10 Gbaud OFDM system at 25 Gs/s with and without NFT receiver. The DAC resolutions are 5 and 10 bits, no noise was added. . . . .   | 182 |
| 5.35 | Received constellations of NIS-based 10 Gbaud OFDM system at 25 Gs/s with and without NFT receiver, $P_{burst} = -3$ dBm. . . . .   | 182 |
| 5.36 | Simulated back-to-back performance of NIS-based 10 Gbaud OFDM system sampling at 25 Gs/s with different values of the burst power the Tx DAC resolutions. . . . .   | 183 |

|      |   |     |
|------|---|-----|
| 5.37 | Back-to-back performances of 10 Gbaud OFDM and NIS-based OFDM systems for different burst power values. Closed symbols are experimental data. The solid lines with open symbols are simulation results, the DAC resolution was set to 5 bits. . . . .           | 184 |
| 5.38 | Constellation diagrams at the burst power of -5 dBm after 4080 km of transmission distance, (a) before dispersion removal, (b) before channel estimation, (c) before phase noise compensation, (d) final constellation after phase noise compensations. . . . . | 185 |
| 5.39 | Q-factor as a function of the burst power after 4080 km. The numbers are power correction values for each burst power value. . . . .  | 186 |
| 5.40 | Optimum Q-factor as functions of the transmission distance. The numbers are power correction values for each distance value at the optimum burst power. . . . .   | 186 |

# List of Tables

|     |  |    |
|-----|--|----|
| 3.1 | Complexities of DDF and BPS Blind PNE Techniques . . . . . | 94 |
|-----|--|----|

# List of Acronyms

**ADC** analog to digital converter.

**AGV** average gain variation.

**ASE** amplified spontaneous emission.

**ASK** amplitude-shift-keying.

**AWGN** additive white Gaussian noise.

**BPSK** binary-phase-shift-keying.

**CMOS** complementary metal-oxide-semiconductor.

**CP** cyclic prefix.

**CPE** common phase error.

**DA** data-aided.

**DAC** Digital to analog converter.

**DBP** digital back propagation.

**DD** decision directed.

**DDF** decision-directed-free.

**DQPSK** differential quadrature phase-shift-keyed.

**DSP** digital signal processing.

**ECL** external cavity laser.

**EDFA** erbium-doped fibre amplifier.

**EENP** equalization-enhanced phase noise.

**EVM** error vector magnitude.

**FBG** fiber Bragg grating.

**FEC** forward error correction.

**FPP** forward pump power.

**GFF** gain flattening filter.

**ICI** inter-carrier interference.

**IDFT** inverse discrete Fourier transform.

**ISI** inter-symbol interference.

**ITU** international telecommunication union.

**LO** local oscillator.

**MF** multiplier-free.

**ML** maximum-likelihood.

**MPB** most populated bin.

**NFD** nonlinear Fourier domain.

**NFT** nonlinear Fourier transform.

**NIS** nonlinear inverse synthesis.

**NLCC** nonlinear correction coefficient.

**NLIN** nonlinear interference noise.

**NLPN** nonlinear phase noise.

**NLSE** nonlinear Schrödinger equation.

**OFDE** overlapped frequency-domain equalizers.

**OOK** on-off-keyed.

**OPC** optical phase conjugation.

**OSNR** optical signal to noise ratio.

**OTDM** orthogonal time division multiplexing.

**PA** pilot-aided.

**PCP** phase conjugated pilot.

**PCSC** phase conjugated subcarrier coding.

**PCTW** phase conjugated twin wave.

**PDM** polarization division multiplexed.

**PMD** polarization mode dispersion.

**PNC** phase noise compensation.

**PS** pilot subcarrier.

**QAM** quadrature amplitude modulation.

**QPA** quasi-pilot-aided.

**RGI** reduced-guard-interval.

**RMSE** root-mean-square-error.

**SDM** space division multiplexing.

**SE** spectral efficiency.

**SNR** signal to noise ratio.

**SSFM** split-Step Fourier method.

**SSMF** standard single mode fiber.

**STD** standard deviation.

**TSI** two-stage-iterative.

**WDM** wavelength-division multiplexing.

**WSS** wavelength selective switch.

# Chapter 1

## Introduction

### 1.1 Overview

Fibre-optic communications became feasible in the early 1970s after the developments of low loss (below 20 dB/km), high bandwidth silica fibres [1] and compact GaAs semiconductor lasers [2]. These achievements enabled the first commercial fibre-optic communication system (first generation) operating at wavelength of around  $0.8 \mu\text{m}$  with a data rate of 45 Mb/s and repeater spacing of 7 km over multi-mode fibre [3].

The second generation fibre-optic communication systems were developed in early 1980s, which operated at wavelength of  $1.3 \mu\text{m}$  over single mode fibre to minimize chromatic dispersion and eliminate modal dispersion. However, the fibre loss at  $1.3 \mu\text{m}$  was still high, which was around 0.5 dB/km. As a result, typical repeater spacing of less than 50 km was required [4].

Third generation systems were developed at  $1.5 \mu\text{m}$  as the fibre losses could be reduced to 0.2 dB/km at this wavelength. In addition, dispersion-shifted fibre was developed, leading to the development of dispersion management to deal with the high chromatic dispersion at  $1.5 \mu\text{m}$ . As a result, a data rate of 2.5 Gb/s was commercially available in 1990 [4].

However, in third generation systems, the typical repeater spacing was limited at 60 – 70 km. To address this problem, coherent detection was considered as a potential solution to increase the repeater spacing due to its improved sensitivity compared to direct-detection. Coherent optical systems are similar to microwave systems, in which the re-

ceived signal is mixed with a local oscillator (LO) at the receiver. Such detection scheme provides sensitivity which approaches the shot noise limit with the increasing of LO power. However, the complexity of coherent receiver was high as polarization-matching between the received signal and LO laser and carrier phase locking were required [4].

However, coherent detection was superseded with the invention of erbium-doped fibre amplifier (EDFA) [5] as EDFA provided a much cheaper and simpler way to increase the repeater spacing. In addition, as EDFA could provide THz of bandwidth, enabling amplification of several wavelength channels simultaneously, wavelength-division multiplexing (WDM) was proposed to increase dramatically the total information throughput of single mode fibre in the fourth generation fibre-optic systems. By 2001, commercial systems could provide a bit rate of 2.4 Tb/s over a single mode fibre [4]. The use of WDM technology had improved the throughput of undersea fibre-optic systems by a factor of 10,000 by 2001 [4].

Although the increase in achievable information throughput per fibre enabled by EDFAs and WDM has scaled well in the past, a hard limit on throughput exists while on-off-keyed (OOK) modulation is used, given that the maximum achievable spectral efficiency (SE) is 1 b/s/Hz. As a result, while maintaining the compatibility with the international telecommunication union (ITU) frequency grid of 50 GHz for WDM systems, the maximum data rate per channel with OOK is 50 Gb/s. In fact, the data rate per channel of WDM systems with OOK format was limited to 10 Gb/s due to number of limiting factors such as dispersive and nonlinear effects, the bandwidth limitation of electronic components and interchannel crosstalk [4].

On the other hand, over the last two decades, the amount of traffic carried on backbone networks has been growing exponentially, from 30 % – 60 % (i. e. 1.1 dB to 2 dB) per year depending on available services offered by various network operators in different geographic regions [6]. In addition, as forecasted by CISCO [7], the data traffic will continuously to growth exponentially in the next decade due to the increasing demand from the growing number of bandwidth-hungry applications and on-line services such as cloud computing, HD video streams, on-line content sharing and many others. This exponential traffic growth is exerting great pressure on the networks infrastructure at every scale and

tremendous research activities have been carried out on maximizing the total throughput per fibre. To increase the total throughput of single mode fibre, it is crucial to increase the SE by encoding more than 1 bit per symbol using high order modulation formats and exploring other physical dimensions supported by optical fibre such as quadrature, polarization and space.

The quest for higher SE lead to the rebirth of coherent detection systems in early 2000s. Unlike direct detection, coherent detection can provide full information of the transmitted signal, including two polarization stages, amplitude and phase. In addition, with the advances in high-speed analog to digital converter (ADC) and Digital to analog converter (DAC) built in 40-nm complementary metal-oxide-semiconductor (CMOS) technology, digital signal processing (DSP) can be effectively applied in fibre-optic communication systems to compensate impairments acquired during propagation. Together with coherent detection, DSP have made it possible to use all available physical dimensions supported by optical fibre for data transmission. As a result, coherent detector and powerful digital signal processors have formed the basic building blocks of modern fibre-optic communication systems.

In 2010, single carrier 100 Gb/s transponders using polarization division multiplexed (PDM) differential quadrature phase-shift-keyed (DQPSK) was commercially available [8]. Using high order quadrature amplitude modulation (QAM) and high SE multiplexing techniques such as orthogonal time division multiplexing (OTDM) (also known as Nyquist-WDM) and OFDM, a data rate above 100 Tb/s over single mode fibre have been experimentally demonstrated [9, 10]. To further increase the throughput of optical fibre systems, space division multiplexing (SDM) with the use of spatial modes or multiple fibre cores have also been actively investigated [11]. Using multimode and multicore fibres, the total throughput above 2 Pb/s have been demonstrated recently [12, 13]. However, SDM technology is still in its infancy and SDM approach also requires enormous upgrade in the systems infrastructure. As a result, a lot of technological advances are required to make SDM technology appropriate for practical implementations [11].

As mentioned above, using high order modulation formats is an effective method to increase the bit-rate per channel and the total throughput of fibre-optics systems. However,

high order modulation formats are sensitive to amplified spontaneous emission (ASE) noise generated from optical amplifiers [14, 15] and thus, requiring high optical signal to noise ratio (OSNR) at the receiver. In linear systems, such as wireless communication systems, this problem can be solved by increasing the transmitted signal power. However, such approach is not always effective for optical fibre channel due to the fibre's nonlinearity effects (Kerr effect). At a high signal launch power value, the nonlinear distortion due to the Kerr effect, including signal  $\times$  signal nonlinear distortion and signal  $\times$  noise nonlinear interaction, become the dominant source of distortion. As a result, the distance reaches of fibre-optic systems significantly reduce with the increasing of modulation level (or number of bits per symbol). With a fixed distance reach, the highest achievable SE in fibre-optic communication systems is usually referred to as nonlinear Shannon limit [14]. Combating the nonlinear impairments to maximize the throughput and distance reach of fibre-optic communication systems in practical and flexible ways is an intense ongoing research area.

## 1.2 Motivation

To satisfy the ever-increasing capacity demands in an economically attractive manner, the data rate per WDM channel has also been increasing exponentially over the last two decades. Recently, the concept of superchannel has been proposed, aiming to increase per-channel interface rate as well as total throughput of WDM systems in a cost-effective manner [16]. Superchannel evades electronic bottleneck via optical parallelism and provide high data rate per WDM channel (on the order of Tb/s) and better spectral utilization, especially in transparent optical mesh networks [8].

The term of superchannels was first proposed in [16] to refer to multiple single-carrier-modulated signals modulated under optical OFDM condition. Lately, superchannel concept has been generalized to any collections of optical signals that are [8]:

- Modulated and multiplexed together with high SE at a common originating site.

- Transmitted and routed together over a common optical link.
- Received at a common destination side.

The usage of superchannel concept in WDM systems can provide a lot of advantages [8], such as the ability to meet the demand for high-speed serial interface rates, which increase faster than the speed of DACs and ADCs. It also provides higher SE in WDM transmission by reducing the wasted optical spectrum between neighbouring channels. In addition, superchannel effectively increases efficiency in DSP and lower implementation cost per bit and is compatible to software-defined optical transmission enable by flexible DSP at the transmitter and receiver

However, the next generation optical transponders based on superchannel concept also need to satisfy several critical and challenging criteria as follows:

- High reliability and performance.
- Low implementation transceivers complexity.
- Capabilities to flexibly trade the throughput for distance reach.

In order to meet these criteria, next generation optical transponders should operate with high SE multiplexing techniques, low complexity and high performance DSP algorithms and multiple modulation formats or coding overheads. A wide range of research activities are being carried out in finding optimum combination of DSP, modulation formats and coding techniques for next generation optical transponders.

Due to the high SE multiplexing, Nyquist-WDM and multiband OFDM have been considered as the most promising technologies for realizing Tb/s superchannels. The potential of Nyquist-WDM and multiband OFDM multiplexing techniques for superchannel transmission have been demonstrated through number of hero experiments [17, 18]. In comparison to Nyquist-WDM, OFDM can provide a more efficient DSP implementation as no extra filtering is required for pulse shaping. In addition, due to the long symbol duration OFDM is also more resilient to linear impairments such as chromatic dispersion and polarization mode dispersion. Furthermore, hybrid QAM can also be applied more

effectively with OFDM than Nyquist-WDM. Hybrid QAM can be considered as a much simpler technique to maximize the SE in comparison to rate-adaptive [19] forward error correction (FEC).

However, CO-OFDM technology also has several serious challenges. First of all, due to the long symbol duration, CO-OFDM systems are very sensitive to laser phase noise impairments. Secondly, due to the narrow frequency spacing OFDM is also sensitive to the fibre nonlinearity impairments. Therefore, in order to realize OFDM-based high SE, flexible next generation Tb/s optical transponders, this thesis is focused on efficient DSP techniques for CO-OFDM as follows:

1. Low-complexity, low-overhead laser phase noise compensation techniques.
2. Low-complexity, flexible and high performance fibre nonlinearity compensation techniques.
3. Novel nonlinear tolerant transmission techniques.

## **1.3 Organization of the thesis**

The thesis is organized as follows:

### **Chapter 1. Introduction**

This chapter presents an overview about optical communication and the motivation behind this research in the area of DSP for CO-OFDM transmissions.

### **Chapter 2. Statistical Properties and Indirect Bit Error Rate Estimation Methods for CO-OFDM**

In this chapter, the statistical properties of OFDM signal in fibre-optic communication systems are investigated. Based on these statistical properties, a novel indirect BER estimation method was proposed and compared with other well-known BER estimation methods such as data-aided and non-data-aided error vector magnitude (EVM). The impact of various system's imperfections such as laser phase noise and frequency offset are also presented.

### **Chapter 3. Low Complexity Phase Noise Compensation Techniques for CO-OFDM**

In this chapter, three novel PNC techniques for CO-OFDM, namely quasi-pilot-aided (QPA), decision-directed-free (DDF) blind and multiplier-free (MF) blind, are presented. The performances of these techniques are compared with existing techniques both numerically and experimentally.

#### **Chapter 4: Low Complexity Fibre Nonlinear Compensation Techniques for CO-OFDM**

In this chapter, two novel fibre nonlinear compensation techniques for CO-OFDM are presented, namely phase conjugated pilot (PCP) and phase conjugated subcarrier coding (PCSC). The performances of PCP and PCSC techniques are demonstrated experimentally.

#### **Chapter 5: Nonlinear Fourier Transform Based Optical Communications**

In this chapter, the basic principle and designs of nonlinear Fourier transform (NFT)-based transmission systems are discussed. The nonlinear inverse synthesis (NIS) scheme, where the transmitted information is encoded directly onto the continuous part of the nonlinear signal spectrum, is investigated in details. In addition, modified NIS schemes for optical links with EDFAs and Raman amplifiers are discussed. Furthermore, the first experimental demonstration of NIS-based OFDM transmission over transoceanic distance is also presented.

#### **Chapter 6: Conclusion and Future Works**

This chapter summarizes the outcomes of this thesis and discusses related future research directions.

## **1.4 Contributions of the thesis**

This thesis has made number of contributions to the field of fibre-optic communications as listed below:

### **Chapter 2**

- This thesis presents a detailed investigation on the statistical properties of OFDM signals in long-haul optical fibre transmissions. The obtained results give an insight on the impact of fibre nonlinearity on the statistical properties of OFDM signal,

which are important in designing the next generation FEC codes for optical fibre transmission systems.

- An accurate bit error rate estimation method for QSK CO-OFDM transmission is proposed based on the probability density function of the received QPSK symbols. By comparing with other known approaches, including data-aided and nondata-aided EVM, this thesis shows that the proposed method offers the most accurate estimate of the system performance for both single channel and wavelength division multiplexing QPSK CO-OFDM transmission systems.

### **Chapter 3**

- A novel phase noise estimation scheme - the QPA method is proposed. In this method, the phases of transmitted pilot subcarriers are deliberately correlated to the phases of data subcarriers. Accounting for this correlation in the receiver allows the required number of pilots needed for a sufficient estimation and compensation of phase noise to be reduced by a factor of 2 in comparison with traditional pilot-aided phase noise estimation method.
- The performance of different blind phase noise estimation schemes for coherent optical orthogonal frequency division multiplexing transmissions is discussed in details. A general model of CO-OFDM systems with phase noise is derived. Based on this model, the phase cycle slip probability in blind phase noise estimation is calculated. For blind phase tracking, the implementation and performance of feedback loop and digital phase tracking are presented.
- The author proposes and analyses the performance of a novel blind PNC scheme – DDF blind scheme, in which only three test phases are required for phase noise compensation. It is shown that the DDF blind scheme is transparent to QAM formats and can provide a similar performance to the conventional blind phase search employing 16 test phases.
- The author proposes an effective blind phase noise estimation technique for QPSK and 16QAM CO-OFDM transmissions based on statistical properties of the received

symbols phases – the MF blind technique. MF blind technique operates in polar coordinates, providing very low implementation complexity as no multipliers are required.

#### **Chapter 4**

- A novel fibre nonlinearity compensation technique for CO-OFDM systems based on the transmission of phase-conjugated pilots (PCPs) is demonstrated. In this scheme, a portion of OFDM subcarriers (up to 50%) is transmitted with its phase-conjugates, which are used at the receiver to estimate the nonlinear distortions in the respective subcarriers and other subcarriers, which are not accompanied by PCPs. Simulation and experimental results show that, by varying the PCP overhead a performance improvement up to 4 dB can be achieved. In addition, the proposed technique can be effectively applied in both single polarization and polarization mode dispersion (PMD) systems, in both single channel and WDM systems, thus, offering highest flexibility in implementations.
- A novel subcarrier coding scheme for fibre nonlinearity mitigation in CO-OFDM systems – the PCSC technique is demonstrated. Simulation and experimental results show that this simple technique combined with 50% pre-EDC can effectively offer up to 1.5 dB and 0.8 dB performance gains in CO-OFDM systems with BPSK and QPSK modulation formats, respectively. This clearly confirms that nonlinearity mitigation can be achieved by encoding and processing neighbouring OFDM subcarriers simultaneously. In addition, the PCSC technique can also be effectively applied in PDM and WDM transmissions.

#### **Chapter 5**

- Various designs for NFT-based fibre-optic communications systems are presented and its potentials in next generation networks are discussed.
- The performance of the NIS method, in which the information is encoded directly onto the continuous part of the nonlinear signal spectrum, is investigated. This transmission technique, combined with appropriate distributed Raman amplification, can

provide an effective eigenvalue division multiplexing with high spectral efficiency, thanks to highly suppressed channel cross talk. The feasibility of merging the NIS technique in a burst mode with high spectral efficiency multiplexing methods, such as orthogonal frequency division multiplexing and Nyquist pulse shaping with advanced modulation formats (e.g., QPSK, 16QAM, and 64QAM) is demonstrated, showing a performance improvement up to 4.5 dB, which is comparable to results achievable with multi-step per span digital back propagation.

- This thesis proposes and assesses a modified scheme of the NIS method, which can be used effectively in standard optical links with lumped a fibre loss to obtain an integrable model (lossless path-averaged (LPA) model) to which the NIS technique is applicable. It is found that the error between lossless path-averaged and lossy models increases linearly with transmission distance and input power (measured in dB). The feasibility of the proposed NIS scheme in a burst mode with OFDM transmission scheme with advanced modulation formats (e.g., QPSK, 16QAM, and 64QAM) is demonstrated, showing a performance improvement up to 3.5 dB. These results are comparable to those achievable with multi-step per span digital back-propagation.
- The author investigates in details the impact of a non-ideal Raman gain profile on the performance of the NIS scheme. The LPA model for fibre links with non-ideal Raman gain profile by taking into account the average effect of the Raman gain is proposed. It is shown that the NIS scheme employing the LPA model can offer a performance gain of 3 dB regardless of the Raman gain profiles.
- This thesis demonstrates the generation, detection and transmission performance over transoceanic distances of 10 Gbaud NIS-based signal. By applying effective digital signal processing techniques, a reach of 7344 km was achieved with a bit-error-rate (BER) ( $2.1 \times 10^{-2}$ ) below the 20% FEC threshold. This represents an improvement by a factor of 12 in data throughput x distance product compared with other previously demonstrated NFT-based systems, showing a significant advance in the active research area of NFT-based communication systems.

## Chapter 6

- The author briefly discusses future research directions in the area of DSP for CO-OFDM and NFT-based communication systems.

## 1.5 Patent

1. **Son T. Le** and Andrew D. Ellis “Method of Non-Linearity Compensation in Optical Fibre Communications” EU Patent, pending.

## 1.6 Publications

1. **Son T. Le**, Ian D. Philips, Jaroslaw E. Prilepsky, Paul Harper, Andrew D. Ellis and Sergei K. Turitsyn, “Demonstration of Nonlinear Inverse Synthesis Transmission over Transoceanic Distances,” accepted to Journal of Lightwave Technology, Feb. 2016.
2. **Son T. Le**, Jaroslaw E. Prilepsky, P. Rosa, Juan D. Ania-Castanon and Sergei K. Turitsyn, “Nonlinear Inverse Synthesis for Optical Links with Distributed Raman Amplification,” Journal of Lightwave Technology, vol. 34, no. 5, pp. 1-9, Mar. 2016 (**invited**).
3. M. Tan, P. Rosa, **Son T. Le**, Md. A. Iqbal, I. D. Phillips, and P. Harper, “Transmission performance improvement using random DFB laser based Raman amplification and bidirectional second-order pumping,” Opt. Express 24, 2215-2221 (2016).
4. **Son T. Le**, Paul A. Haigh, Andrew D. Ellis and Sergei K. Turitsyn, “Blind Phase Noise Compensation for CO-OFDM Transmission,” Journal of Lightwave Technology, vol. PP, no. 99, Aug, 2015 (**invited**).
5. **Son T. Le**, Mary E. McCarthy, Naoise Mac Suibhne, Andrew D. Ellis and Sergei K. Turitsyn, “Phase-conjugated Pilots for Fibre Nonlinearity Compensation in CO-

- OFDM Transmission,” Journal of Lightwave Technology, vol.33, no.5, pp.1-7, Mar, 2015 (**invited**).
6. **Son T. Le**, Mary E. McCarthy, Naoise Mac Suibhne, Mohammad A. Z. Al-Khateeb, Elias Giacomidis, Nick Doran, Andrew D. Ellis and Sergei K. Turitsyn, “Demonstration of Phase-conjugated Subcarrier Coding for Fiber Nonlinearity Compensation in CO-OFDM Transmission,” Journal of Lightwave Technology, vol.33, no.11, pp.2206-2212, June, 2015.
  7. **Son T. Le**, Jaroslaw E. Prilepsky, and Sergei K. Turitsyn, “Nonlinear inverse synthesis technique for optical links with lumped amplification,” Opt. Express Vol. 23, Issue 7, pp. 8317-8328 (2015).
  8. Pawel Rosa, **Son Thai Le**, Giuseppe Rizzelli, Mingming Tan, and Juan Diego Ania-Castan, “Signal power asymmetry optimisation for optical phase conjugation using Raman amplification,” Opt. Express 23, 31772-31778 (2015).
  9. Elias Giacomidis, **Son T. Le**, Mohammad Ghanbarisabagh, Mary Mccarthy, Ivan Aldaya, Sofien Mhatli, Mutsam A. Jarajreh, Paul A. Haigh, Nick J. Doran, Andrew D. Ellis and Benjamin J. Eggleton, “Fiber nonlinearity-induced penalty reduction in coherent optical OFDM by ANN-based nonlinear equalization,” Optics Letters, Oct. 2015.
  10. Pawel Rosa, Mingming Tan, **Son T. Le**, Ian D. Philips, Juan Diego Ania-Castanon, Stylianos Sygletos and Paul Harper, “Unrepeated DP-QPSK transmission over 350 km standard fibre using URFL amplification,” PTL, vol.27, no.11, pp.1189-1192, June1, 1 2015.
  11. Mingming Tan, Pawe Rosa, **Son T. Le**, Ian. D. Phillips, and Paul Harper, “Evaluation of 100G DP-QPSK long-haul transmission performance using second order co-pumped Raman laser based amplification,” Opt. Express 23, 22181-22189 (2015).
  12. M Jarajreh, Elias Giacomidis, Ivan Aldaya, **Son T. Le**, Athanasios Tsokanos, Zabih Ghassemlooy, Nick J Doran, “Artificial Neural Network Nonlinear Equalizer for Co-

herent Optical OFDM,” in IEEE Photonics Technology Letters, vol. 27, no. 4, pp. 387-390, Feb.15, 15 2015.

13. Paul A. Haigh, **Son T. Le**, Stanislav Zvanovec, Zabih Ghassemlooy, Pengfei Luo, Tongyang Xu, Petr Chvojka, Thavamaran Kanesan, Elias Giacoumidis, Pep Canyelles-Pericas, Hoa Le Minh, Wasiu Popoola, Sujan Rajbhandari, Ioannis Papakonstantinou and Izzat Darwazeh, “Multi-band Carrier-less Amplitude and Phase Modulation for Band limited Visible Light Communications Systems,” Wireless Communications, IEEE , vol.22, no.2, pp.46,53, April 2015.
14. **Son. T. Le**, J. E. Prilepsky, and S. K. Turitsyn, “Nonlinear inverse synthesis for high spectral efficiency transmission in optical fibres,” Opt. Express Vol. 22, Iss. 22, pp. 2672026741 (2014).
15. **Son T. Le**, Blow, K. J., Mezentsev, V.K., Turitsyn, S.K., “Bit Error Rate Estimation Methods for QPSK CO-OFDM Transmission,” Journal of Lightwave Technology, vol.32, no.17, pp.2951-2959, Sept.1, 2014.
16. **Son T. Le**, K. Blow, and S. Turitsyn, “Power pre-emphasis for suppression of FWM in coherent optical OFDM transmission,” Opt. Express 22, 7238-7248 (2014).
17. **Son T. Le**, Kanesan, T., Giacoumidis, E., Doran, N.J., Ellis, A.D., “Quasi-Pilot Aided Phase Noise Estimation for Coherent Optical OFDM Systems,” Photonics Technology Letters, IEEE , vol.26, no.5, pp.504-507, March, 2014.
18. **Son T. Le**, McCarthy, M.E., Suibhne, N.M., Giacoumidis, E., Doran, N.J., Ellis, A.D., Blow, K.J., “Comparison of Bit Error Rate Estimation Methods for QPSK CO-OFDM Transmission,” Photonics Technology Letters, IEEE , vol.26, no.22, pp.2244-2247, Nov.15, 15 2014.
19. **Son T. Le**, T. Kanesan, F. Bausi, P. Haigh, S. Rajbhandari, Z. Ghassemlooy, I. Papakonstantinou, W. Popoola, A. Burton, H. Le Minh, F. Cacialli, and A. Ellis, “A 10Mb/s visible light transmission system using a polymer light-emitting diode with

- orthogonal frequency division multiplexing,” *Opt. Lett.* Vol. 39, pp. 3876-3879 (2014).
20. T. Kanesan, **Son T. Le**, D. Roque, and A. Ellis, “Non-rectangular perfect reconstruction pulse shaping based ICI reduction in CO-OFDM,” *Opt. Express* 22, 1749-1759 (2014).
  21. Haigh, P.A., Bausi, F.; Kanesan, T., **Son T. Le**, Rajbhandari, S., Ghassemlooy, Z., Papakonstantinou, I., Popoola, W., Burton, A., Hoa Le Minh, Ellis, A.D.; Cacialli, F., “A 20-Mb/s VLC Link With a Polymer LED and a Multilayer Perceptron Equalizer,” *Photonics Technology Letters, IEEE* , vol.26, no.19, pp.1975-1978, Oct.1, 1 2014.
  22. E. Giacomidis, M. Jarajreh, S. Sygletos, **Son T. Le**, F. Farjady, A. Tsokanos, A. Hami, E. Pincemin, Y. Jaoun, A. Ellis, and N. Doran, “Dual-polarization multi-band optical OFDM transmission and transceiver limitations for up to 500 Gb/s uncompensated long-haul links,” *Opt. Express* 22, 10975-10986 (2014).
  23. Giacomidis, E., Aldaya, I., Jarajreh, M.A., Tsokanos, A., **Son T. Le**, Farjady, F., Jaouen, Y., Ellis, A.D., Doran, N.J., “Volterra-Based Reconfigurable Nonlinear Equalizer for Coherent OFDM,” *Photonics Technology Letters, IEEE* , vol.26, no.14, pp.1383,1386, July15, 2014
  24. **Son T. Le** and Sergei. Turitsyn, “Techniques for Noise and Nonlinear Impairments Compensation in CO-OFDM Transmission,” *ICTON 2015*, paper Tu.A1.5 (**invited**).
  25. A.D. Ellis, **Son T. Le**, M.A.Z. Al-Khateeb, S.K. Turitsyn, G. Liga, D. Lavery, T.Xu, P. Bayvel, “The Impact of Phase Conjugation on the Nonlinear-Shannon Limit, The Difference between Optical and Electrical Phase Conjugation,” *IEEE Summer Topical*, 2015 (**invited**).
  26. AD Ellis, **Son T Le**, ME McCarthy, SK Turitsyn, “The impact of parametric noise amplification on long haul transmission throughput,” *ICTON 2015* (**invited**).

27. N. Mac Suibhne, M. E. McCarthy, **Son T. Le**, S. Sygletos, F. M. Ferreira and A. D. Ellis, "Optical Fibre Limits: An approach Using ASE Channel Estimation," Progress In Electromagnetics Research Symposium (PIERS), Prague, 2015 (**invited**).
28. **Son T. Le**, M.E. McCarthy, S. K. Turitsyn, I. Phillips, D. Lavery, T.Xu, P. Bayvel, A.D. Ellis, "Optical and Digital Phase Conjugation Techniques for Fiber Nonlinearity Compensation," OECC, Shanghai, China 2015 (**invited**).
29. Sander Walhs, **Son T. Le**, J. E. Prilepsky, H. Vincent Poor and S. K. Turitsyn, "Digital Back Propagation in the Nonlinear Fourier Domain", SPAWC2015 (**invited**).
30. P. A. Haigh, F. Bausi, T. Kanesan, **Son T. Le**, S. Rajbhandari, Z. Ghassemlooy, I. Papakonstantinou, W. O.Popoola, A. Burton, H. Le Minh, A. D. Ellis and F. Caccioli, "A 10 Mb/s Visible Light Communication System using a Low Bandwidth PolymerLight-Emitting Diode," International Symposium on communications systems Networks and Digital Signal Processing (CSNDSP), Manchester, pp999-1004, 2014 (**invited**).
31. E. Giacomidis, **Son T. Le**, I. D. Phillips and N. J. Doran, "Dual-Polarization Multi-Band OFDM Signals for Next-Generation Core Networks," International Symposium on communications systems Networks and Digital Signal Processing (CSNDSP), Manchester, pp34-39, 2014 (**invited**).
32. **Son T. Le**, N. Mac Suibhne, M. E. McCarthy A. D. Ellis and S. K. Turitsyn, "Multiplier-free Blind Phase Noise Estimation for CO-OFDM Transmission," ECOC 2015, Valencia, Spain, paper Mo.4.3.6
33. **Son T. Le**, J. E. Prilepsky, M. Kamalian, P. Rosa, M. Tan, J. D. Ania-Castan, P. Harper and S. K. Turitsyn, "Modified Nonlinear Inverse Synthesis for Optical Links with Distributed Raman Amplification," ECOC 2015, Valencia, Spain, paper, Tu.1.1.3 (**Highly scored**)
34. **Son T. Le**, S. Wahl, D. Lavery, J. E. Prilepsky and S. K. Turitsyn, "Reduced Complexity Nonlinear Inverse Synthesis for Nonlinearity Compensation in Optical Fiber

Links,” CLEO, Germany 2015

35. **Son T. Le**, Ian Philips, Yaroslav Prilepsky, Paul Harper, Nick Doran, Andrew Ellis, Sergei Turitsyn, “First Experimental Demonstration of Nonlinear Inverse Synthesis Transmission over Transoceanic Distances,” to be presented at OFC 2016, Anaheim, paper Tu2A.1, Mar. 2016.
36. Elias Giacomidis, **Son T. Le**, Ivan Aldaya, Jinlong Wei, Mary McCarthy, Nick Doran, Benjamin Eggleton, “Experimental Comparison of Artificial Neural Network and Volterra based Nonlinear Equalization for CO-OFDM,” to be presented at OFC 2016, paper W3A.4, Anaheim, Mar. 2016.
37. Elias Giacomidis, Sofien Mhatli, Tu Nguyen, **Son T. Le**, Ivan Aldaya, Mary McCarthy, Benjamin Eggleton, “Kerr-Induced Nonlinearity Reduction in Coherent Optical OFDM by Low Complexity Support Vector Machine Regression-based Equalization,” to be presented at OFC 2016, paper Th2A.49, Anaheim, Mar. 2016.
38. Elias Giacomidis, **Son T. Le**, Mary McCarthy, Andrew Ellis, Benjamin Eggleton, “Record Intrachannel Nonlinearity Reduction in 40-Gb/s 16QAM Coherent Optical OFDM using Support Vector Machine based Equalization,” 40th Australian Conference on Optical Fibre Technology, Dec. 2015 (**Postdeadline paper**)
39. **Son T. Le**, M. E. McCarthy, Naoise Mac Suibhne, Paul A. Haigh, A. D. Ellis and S. K. Turitsyn, “Decision-Directed-Free Blind Phase Noise Estimation for CO-OFDM,” OFC 2015, paper W1E.5 (**Top scored**)
40. Elias Giacomidis, Giuseppe Talli, N. Mac Suibhne, **Son T. Le**, Nick J. Doran and David B. Payne, “100 Gb/s Point-to-point Solutions for Long-reach Passive Optical Networks in Sparse Rural and Urban Areas,” accepted to Progress In Electromagnetics Research Symposium (PIERS), Prague, 2015.
41. Elias Giacomidis, Jinlong Wei, Mutsam A. Jarajreh, **Son T. Le**, Paul A. Haigh, Andreas Perentos, Naoise Mac Suibhne, Sofien Mhatli, Mohammad Ghanbarisabagh, Stanislav Zvanovec, Ivan Aldaya and Nick J. Doran, “Numerical Analysis

of Artificial Neural Network and Volterra-based Nonlinear Equalizers for Coherent Optical OFDM,” Progress In Electromagnetics Research Symposium (PIERS), Prague, 2015.

42. **Son T. Le**, Andrew D. Ellis and Sergei Turitsyn, “Communication above the Nonlinear-Shannon Limit,” Royal Society meeting on “Communication networks beyond the capacity crunch further discussion,” 13-14 May, 2015.
43. Paul A. Haigh, Petr Chvojka, Stanislav Zvanovec, Zabih Ghassemlooy, **Son T. Le**, Thavamaran Kanesan, Elias Giacomidis, Nick J. Doran, Ioannis Papakonstantinou and Izzat Darwazeh, “Visible Light Communications based on Multi-band Carrierless Amplitude and Phase Modulation with 5 b/s/Hz Spectral Efficiency,” OFC 2015, paper Tu2G.2.
44. Pawel Rosa, Mingming Tan, Ian D Phillips, **Son T. Le**, Juan Diego Ania-Castanon, Stylianos Sygletos and Paul Harper “Unrepeated DP-QPSK transmission over 350 km standard fibre using URFL based amplification,” Asia Communications and Photonics Conference 2014, paper ATH4E.
45. **Son T. Le**, E. Giacomidis, N. Doran, A. D. Ellis, and S. K. Turitsyn, “Phase-conjugated Subcarrier Coding for Fibre Nonlinearity Mitigation in CO-OFDM Transmission,” presented at the ECOC, Cannes, France, paper We.3.3.2, 2014 (**Highly scored**)
46. **Son T. Le**, M. E. McCarthy, N. M. Suibhne, A. D. Ellis, and S. K. Turitsyn, “Phase-conjugated Pilots for Fibre Nonlinearity Compensation in CO-OFDM Transmission,” presented at the ECOC, Cannes, France, paper We.2.3.1, 2014 (**Highly scored**)
47. **Son T. Le**, T. Kanesan, M. McCarthy, E. Giacomidis, I. Phillips, M. F. Stephens, et al., “Experimental Demonstration of Data-dependent Pilot-aided Phase Noise Estimation for CO-OFDM,” in Optical Fiber Communication Conference, San Francisco, California, 2014, p. Tu3G.4 (**Best scored**)

48. **Son T. Le**, K. J. Blow, V. K. Menzentssev, and S. K. Turitsyn, "Comparison of numerical bit error rate estimation methods in 112Gbs QPSK CO-OFDM transmission," in Optical Communication (ECOC 2013), 39th European Conference and Exhibition on, 2013, pp. 1-3
49. M. E. McCarthy, N. M. Suibhne, **Son T. Le**, P. Harper, and A. D. Ellis, "High Spectral Efficiency Transmission Emulation for Non-Linear Transmission Performance Estimation for High Order Modulation Formats," presented at the ECOC, Cannes, France, paper P.5.7, 2014.
50. **Son T. Le**, M. E. McCarthy and S. K. Turitsyn, "Optimized Hybrid QPSK/8QAM for CO-OFDM Transmissions," International Symposium on communications systems Networks and Digital Signal Processing (CSNDSP), Manchester, pp763-766, 2014.
51. **Son T. Le**, M. E. McCarthy, E. Giacomidis and N. J. Doran, "Adaptive Time Synchronization and Frequency Offset Estimation for CO-OFDM," International Symposium on communications systems Networks and Digital Signal Processing , Manchester, pp767-770, 2014.
52. Phillips, M. Tan, M. Stephens, M. McCarthy, E. Giacomidis, S. Sygletos, P. Rosa, S. Fabbri, **Son T Le**,. Kanesan, S. Turitsyn, N. Doran, P. Harper, and A. Ellis, "Exceeding the Nonlinear-Shannon Limit using Raman Laser Based Amplification and Optical Phase Conjugation," in Optical Fiber Communication Conference, OSA Technical Digest (online) (Optical Society of America, 2014), paper M3C.1

## Chapter 2

# Statistical Properties and Indirect Bit Error Rate Estimation Methods for CO-OFDM

**Son T. Le**, Blow, K. J., Mezentsev, V.K., Turitsyn, S.K., “Bit Error Rate Estimation Methods for QPSK CO-OFDM Transmission,” *Journal of Lightwave Technology*, vol.32, no.17, pp.2951-2959, Sept.1, 2014.

**Son T. Le**, McCarthy, M.E., Suibhne, N.M., Giacomidis, E., Doran, N.J., Ellis, A.D., Blow, K.J., “Comparison of Bit Error Rate Estimation Methods for QPSK CO-OFDM Transmission,” *Photonics Technology Letters, IEEE* , vol.26, no.22, pp.2244-2247, Nov.15, 15 2014.

### 2.1 Introduction

In digital communication systems, un-coded BER is considered as the most popular performance indicator [20]. The BER in CO-OFDM systems can be estimated in numerical investigations using Monte Carlo simulation and in experiments (typically with off-line signal processing) by directly counting the number of errors at the receiver. The corresponding Q-factor can be calculated using the inverse complementary error function [20]. However, this method relies on a large number of statistical samples and, in general, is

time-consuming, especially if the signal quality is high and massive optimization modelling is required. As a result, it is highly desirable and practically important to develop efficient indirect numerical and statistical methods for evaluating CO-OFDM system performance.

For coherent communication systems with multi-level signals both in amplitude and in phase, the EVM is commonly used as a fast measure of the received digital signals quality [21, 22]. The EVM describes the effective distance of the received complex symbol from its ideal position in the constellation diagram. In an additive white Gaussian noise (AWGN) transmission channel the connection of EVM to BER can be determined theoretically [22]. The standard EVM is a data-aided estimation technique, where for measurement purposes the transmitted data are known [21]. On the other hand, it is more common for real-world receivers that the sent data (e.g. training sequences) are unknown. In this case, nondata-aided reception can be applied as shown in [23]. Several other relevant methods of evaluating the signal quality have recently been proposed, experimentally verified and compared for single carrier QPSK systems [24, 25]. However, the exact relationship between the BER and the EVM in CO-OFDM still remains an open problem. In addition, the relative performances of different BER estimation methods for coherent QPSK systems have to be examined carefully when being applied for CO-OFDM transmission.

In this chapter, the author discusses a novel statistical BER estimation method for CO-OFDM transmissions [26–28] based on the probability density function of the received QPSK symbols. The statistical properties of QPSK signals are studied and the effectiveness of the proposed BER estimation method is demonstrated in reduced-guard-interval (RGI) and WDM CO-OFDM transmissions. In addition, the robustness of the proposed BER estimation method to laser phase noise and frequency offset is also discussed.

## 2.2 BER estimation methods for QPSK transmissions

### 2.2.1 Direct error-counting

The BER can be directly measured by counting the number of errors at the receiver subject to sufficient symbols being recorded. The measured (or estimated) BER is usually converted to an equivalent Gaussian noise Q-factor in dB using the expression:

$$Q_{BER} = 20 \cdot \log_{10}(\sqrt{2} \operatorname{erfc}^{-1}(2BER)), \quad (2.1)$$

where  $\operatorname{erfc}^{-1}$  is the inverse complementary error function. This sets the reference Q-factor used in the following evaluation of different indirect methods.

### 2.2.2 Data-aided EVM

In an optical communication system with QPSK modulation format, the complex amplitude of this field can be described by 4 points in a complex constellation plane. At the receiver, the received signal vector  $\mathbf{E}_r$  deviates by an error vector  $\mathbf{E}_{err}$  from the ideal transmitted vector  $\mathbf{E}_t$  as shown in Fig. 2.1. The data-aided EVM is defined by a root mean square of  $\mathbf{E}_{err}$  and embraces all (linear and nonlinear) impairments [21]:

$$EVM_m = \frac{\sigma_{err}}{|\mathbf{E}_{t,m}|}, \sigma_{err}^2 = \langle |\mathbf{E}_{err,i}|^2 \rangle, \mathbf{E}_{err,i} = \mathbf{E}_{r,i} - \mathbf{E}_{t,i}, \quad (2.2)$$

where  $\langle \cdot \rangle$  stands for the averaging operation,  $\mathbf{E}_{t,m}$  is the longest ideal constellation vector, serving for normalization.

By applying the definition 2.2, the EVM in QPSK CO-OFDM transmissions can be calculated as:

$$EVM = \frac{\sqrt{\langle |c_k - c_{k,ideal}|^2 \rangle}}{|c_{ideal}|}, \quad (2.3)$$

where  $c_k$  is the kth received symbol and  $c_{k,ideal}$  is the corresponding ideal constellation point. For a QPSK system with AGWN channel the BER can be estimated from the EVM

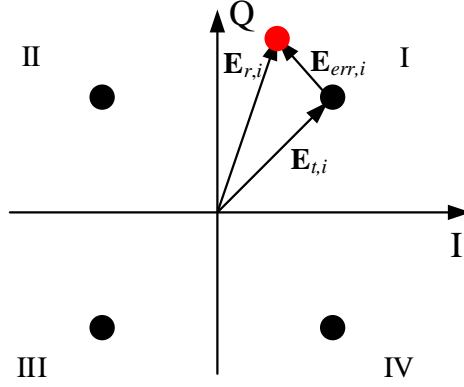


**Figure 2.1:** Constellation diagram and error vector for a QPSK signal. Vector  $\mathbf{E}_{t,i}$  is the transmitted signal, vector  $\mathbf{E}_{r,i}$  is the received signal and  $\mathbf{E}_{err,i} = \mathbf{E}_{r,i} - \mathbf{E}_{t,i}$  is the error vector

as [22]:

$$BER = 0.5 \cdot \operatorname{erfc} \left( \frac{EVM^{-1}}{\sqrt{2}} \right) \quad (2.4)$$

By substituting 2.4 into 2.1, the equivalent Q-factor in dB can be defined knowing the EVM as:

$$Q_{EVM} = -20 \log_{10} (EVM) \quad (2.5)$$

### 2.2.3 Nodata-aided EVM (Q factor 1, Q1)

The EVM can also be calculated without knowing the transmitted data. The most common approach for calculating nodata-aided EVM is to perform hard decision on the received symbols and then apply the expression 2.2 [22]. In this case, the error vector of a received symbol is calculated according to the nearest ideal constellation point. As a consequence, nodata-aided EVM tends to under-estimate the EVM if the received signal is strongly noisy. In addition, the EVM is also calculated by replacing the four ideal QPSK constellation points with the mean values of the received symbols in the four quadrants of the constellation diagram [23]:

$$EVM1 = \sqrt{\left\langle \frac{|c_{k,i} - c_{arg,i}|^2}{|c_{arg,i}|^2} \right\rangle}, \quad (2.6)$$

where  $c_{avg,i}, i = 1, 2, 3, 4$  are the means of the received symbols  $c_{k,i}$  that fall into the  $i$ th quadrant of the constellation diagram. For comparison purpose this nodata-aided EVM

is also converted into an equivalent Q-factor in dB by the expression 2.5.

#### 2.2.4 Q factor 2, (Q2)

It has been shown [29] that for single carrier QPSK systems without optical dispersion compensation, the four components of a QPSK signal (in-phase x-polarization, in-phase y- polarization, quadrature x-polarization, quadrature y- polarization) are Gaussian distributed (or at least nearly Gaussian distributed) and statistically independent both before and after the digital signal processing (DSP) in the receiver [29]. Therefore, a QPSK constellation can be decomposed into two binary-phase-shift-keying (BPSK) constellations (0 and  $\pi$ ), or equivalently two amplitude-shift-keying (ASK) constellations (1 and -1), for the in-phase and quadrature components [30]. As a result, following the same well known approach for calculating the conventional Q-factor for OOK signals, we can define the Q-factors of the in-phase and quadrature components of the received QPSK signals by [24]:

$$Q_{Re} = \frac{\langle c_{k,Re} (c_{k,Re} > 0) \rangle - \langle c_{k,Re} (c_{k,Re} < 0) \rangle}{\sigma_{k,Re} (c_{k,Re} > 0) + \sigma_{k,Re} (c_{k,Re} < 0)} \quad (2.7)$$

$$Q_{Im} = \frac{\langle c_{k,Im} (c_{k,Im} > 0) \rangle - \langle c_{k,Im} (c_{k,Im} < 0) \rangle}{\sigma_{k,Im} (c_{k,Im} > 0) + \sigma_{k,Im} (c_{k,Im} < 0)} \quad (2.8)$$

where  $\sigma(\cdot)$  denotes the standard deviation (STD) of the statistical samples. In 2.7 and 2.8  $Q_{Re}$  ( $Q_{Im}$ ) are calculated as the ratio between the difference of the means and the sum of the STDs of in-phase (quadrature) components with opposite signs. The BER then can be obtained by using the estimations from both in-phase and quadrature components:

$$BER = \left\langle \frac{1}{2} \operatorname{erfc} \left( \frac{Q_{Re}}{\sqrt{2}} \right), \frac{1}{2} \operatorname{erfc} \left( \frac{Q_{Im}}{\sqrt{2}} \right) \right\rangle \quad (2.9)$$

#### 2.2.5 Q factor 3, (Q3)

Another definition of Q-factor was introduced in [31] as the ratio between the mean and the STD value of each constellation point. For the symbol in the first quadrant, the Q-factors

are:

$$Q_{1,Re} = \frac{|\langle c_{k,Re} (c_{k,Re} > 0, c_{k,Im} > 0) \rangle|}{\sigma_{k,Re} (c_{k,Re} > 0, \sigma_{k,Im} > 0)} \quad (2.10)$$

$$Q_{1,Im} = \frac{|\langle c_{k,Im} (c_{k,Re} > 0, c_{k,Im} > 0) \rangle|}{\sigma_{k,Im} (c_{k,Re} > 0, \sigma_{k,Im} > 0)} \quad (2.11)$$

The overall BER can be obtained by using  $Q_{i,Re}$  and  $Q_{i,Im}$ ,  $i = 1, 2, 3, 4$  of all the constellation symbols [25, 31, 31]:

$$BER = \left\langle \frac{1}{2} \operatorname{erfc} \left( \frac{Q_{i,Re}}{\sqrt{2}} \right), \frac{1}{2} \operatorname{erfc} \left( \frac{Q_{i,Im}}{\sqrt{2}} \right) \right\rangle \quad (2.12)$$

## 2.3 Simulation setup of 112 Gb/s QPSK CO-OFDM transmissions

For investigating the statistical properties of QPSK signals and comparing the performances of different BER estimation methods, a 112 Gb/s PDM CO-OFDM transmission system is considered, the block diagram of which is shown in Fig. 2.2.

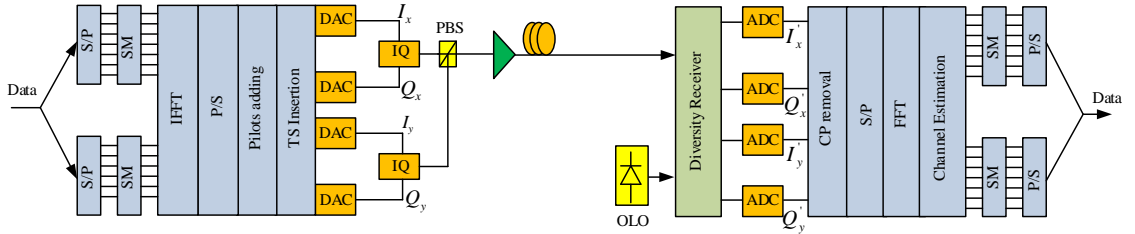


**Figure 2.2:** Block diagram of 112 Gb/s PDM CO-OFDM transmissions. S/P: serial/parallel conversion, P/S: parallel/serial conversion, SM: symbol mappings, TS: training symbol, DAC: digital-to-analog converter, I/Q: I/Q modulator, OLO: optical local oscillator

The data stream is first divided into x- and y-polarizations, each of which is then mapped onto 2048 subcarriers using QPSK modulation format with Gray code and subsequently transferred to the time domain by an IFFT of size 4096 while zeros occupy the remainder for oversampling purpose. The OFDM useful duration is 60 ns. A cyclic prefix (CP) of length 12 ns is used to accommodate dispersion. The long-haul fibre link is assumed to consist of 80-km spans of standard single mode fiber (SSMF) with the loss parameter of 0.2 dB/km, nonlinearity coefficient of 1.22 /W/km, dispersion of 16 ps/nm/km

and PMD coefficient of  $0.1 \text{ ps}/\sqrt{\text{km}}$ . The fibre span loss is compensated by EDFA with 16 dB of gain and a noise figure of 6 dB. In the simulation ASE noise is added inline. The transmitter and receiver lasers have the same linewidth of 100 kHz. The laser phase noise is modeled as a Wiener-Levy process with a variance  $\sigma^2 = 2\nu t$  where  $\nu$  is the combined laser linewidth and  $t$  is the time difference between two samples [32]. The simulated time window contains 100 OFDM symbols (409600 bits). The channel estimation and equalization (including polarization demultiplexing and channel response equalization) is done with the assistance of an initial training sequence (2 OFDM symbols in each polarization) using the zero forcing estimation method with MIMO processing [33]. The common phase error (CPE) due to laser phase noises is estimated and compensated using the pilot-aided technique by inserting 16 pilot subcarriers in each OFDM symbol. In the simulation the timing synchronization is assumed to be perfect.

Another CO-OFDM configuration known as reduced-guard-interval CO-OFDM [34] is also considered here. In RGI CO-OFDM transmissions a short CP is added to each OFDM symbol to accommodate the inter-symbol interference (ISI) with short memory, such as fibre PMD or residual chromatic dispersion. The accumulated dispersion of the optical link is compensated at the receiver using overlapped frequency-domain equalizers (OFDE) [35] or time domain finite impulse response filters [36]. In this work the OFDE with overlap-save method was applied [35]. As the chromatic dispersion can be effectively compensated at the receiver, a shorter symbol duration can be used in RGI CO-OFDM. As a result, in RGI CO-OFDM transmissions a smaller number of subcarriers can be used [34]. A 112 Gb/s RGI CO-OFDM transmission system with 112 subcarriers is considered. The useful OFDM symbol duration is 3.8 ns and the CP length is 0.2 ns. In applying OFDE with overlap-save method, a block size of 10 OFDM symbols (40 ns) was used.

## 2.4 Statistical properties of QPSK signals in CO-OFDM transmissions

In this section, the statistical properties of QPSK signal in PDM CO-OFDM transmissions is discussed in details. Both the in-phase and quadrature components and the phase of the QPSK signal are taken into account.

The histograms of in-phase and quadrature components of QPSK signal in 112 Gb/s PDM CO-OFDM transmissions are shown in Fig. 3 and Fig. 4 (only for x-polarization, a similar result for y-polarization is observed) for different values of the launch power (3 dBm and 6 dBm). The Gaussian fitting is obtained by calculating the mean and STD of the received statistical samples. In this simulation the amplified spontaneous emission (ASE) noise added by EDFAs is not considered in order to analyze the distribution of signal components alone. In addition, the transmitter and receiver lasers are considered as noiseless. The only source of noise is the fibre nonlinearity. It is found that the distributions of in-phase and quadrature components of QPSK signals are Gaussian-like only for small values of the launch power. Herein, the well-known Kolmogorov-Smirnov test (K-S test) was applied to define if a statistical signal has a Gaussian-like distribution. The Kolmogorov-Smirnov statistic (KSSTAT) for a given cumulative distribution function  $F(x)$  is defined as:

$$D = \sup |F_n(x) - F(x)|, \quad (2.13)$$

where  $F_n(x)$  is the empirical distribution function for  $n$  observations of the statistical signal. The typical value of the KSSTAT for a Gaussian-like signal is below 0.05.

If the launch power is set to 3 dBm (no errors were detected at the receiver, 409600 bits were sent) a small mismatch between the actual distribution and its Gaussian fitting can be observed (Fig. 2.3). If the launch power is increased to 6 dBm (BER=0.0002) the mismatch becomes obvious (Fig. 2.4) and the Gaussian distribution shows a poor approximation of the distribution of in-phase and quadrature components of the received QPSK symbols.

This result is different from what has been observed for single carrier QPSK transmis-

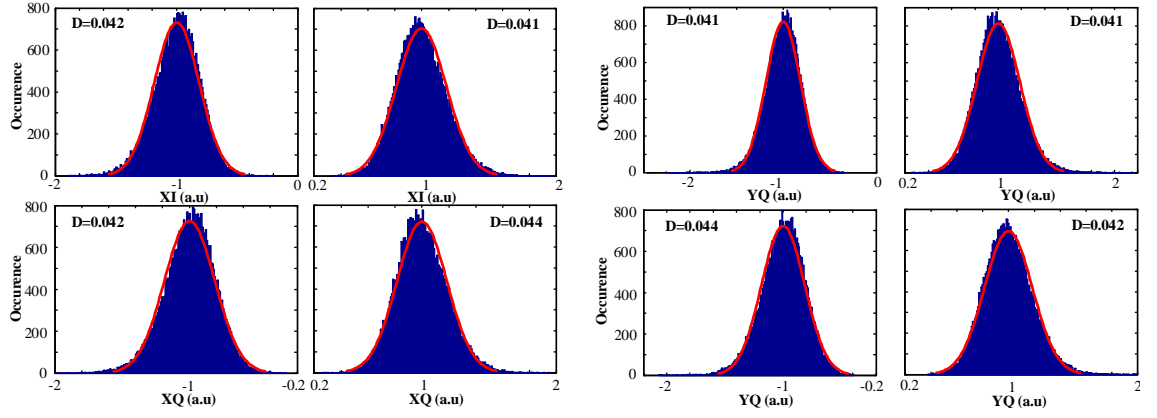


**Figure 2.3:** Histogram of in-phase and quadrature components of the received QPSK symbols in x and y-polarization. Propagation over 800 km in nonlinear limited regime (3 dBm). Gaussian fitting is superimposed to each histogram, KSSTAT values are also included in each histogram.

sions in [29], showing that at high values of the launch power the nonlinear interference noise (NLIN) in CO-OFDM transmission deviates from Gaussian distribution. The obtained result herein agrees well with a recent study on the statistical property of NLIN in CO-OFDM transmission [37], indicating that the Gaussian assumption of NLIN, which is the key in the derivation of closed-form expression for the nonlinear performance of CO-OFDM in [38] is, in general, not satisfied.

In addition, the statistical properties of in-phase and quadrature components of the received QPSK symbols in CO-OFDM transmissions are also sensitive to the specific DSP technique used, especially the CPE estimation and compensation. The CPE due to laser phase noise and fibre nonlinearity rotates the constellation diagram and thus changes the statistical properties of the in-phase and quadrature components significantly. In the presence of CPE offset due to the estimation inaccuracy, which usually occurs in the nonlinear limited regime, the PDF of in-phase and quadrature components cannot be approximated accurately by a Gaussian distribution (Fig. 2.4). As a consequence, the two aforementioned Gaussian assumption based BER estimation methods (Q2 and Q3) may not be effective for QPSK CO-OFDM transmissions.

Herein, the statistical properties of the phases of the received QPSK symbols are studied. The histograms of the received QPSK symbols phases (x-polarization) in four quadrants of the constellation diagram are shown in Fig. 2.5 and Fig. 2.6 for different values of the launch power (3 dBm and 6 dBm). It is found that the distribution of the received

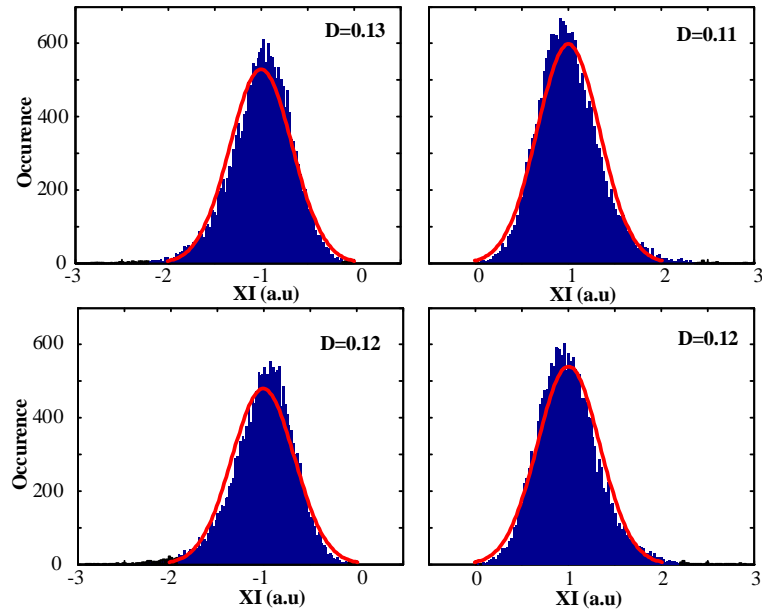


**Figure 2.4:** Histogram of in-phase and quadrature components of the received QPSK symbols in x-polarization. Propagation over 800 km in nonlinear limited regime with the launch power of 6 dBm.

QPSK symbols phases in each quadrant of the constellation diagram is essentially Gaussian ( $D < 0.05$ ), independent of the launch power and the transmission distance. For the investigated system our analysis is carried out by changing the launch power from -9 dBm to 9 dBm (in 3 dB steps) and the transmission distance from 400 to 2400 km (in 400 km steps). This phenomenon can be explained by the fact that the nonlinear phase noise in CO-OFDM transmission is dominated by FWM and its interaction with ASE noise. As a result, when independent data is carried on a large number of subcarriers, the central limit theorem can be applied for the nonlinear phase noise. In addition, the distribution of the received QPSK symbols phases in each quadrant is nearly insensitive to the CPE offset, especially when the number of subcarriers is large, as the CPE offset affects only the mean value but not the STD of the received QPSK symbols phases. As a result, a more reliable statistical BER estimation method for QPSK CO-OFDM transmissions can be developed based on the statistical properties of the QPSK symbols phases.

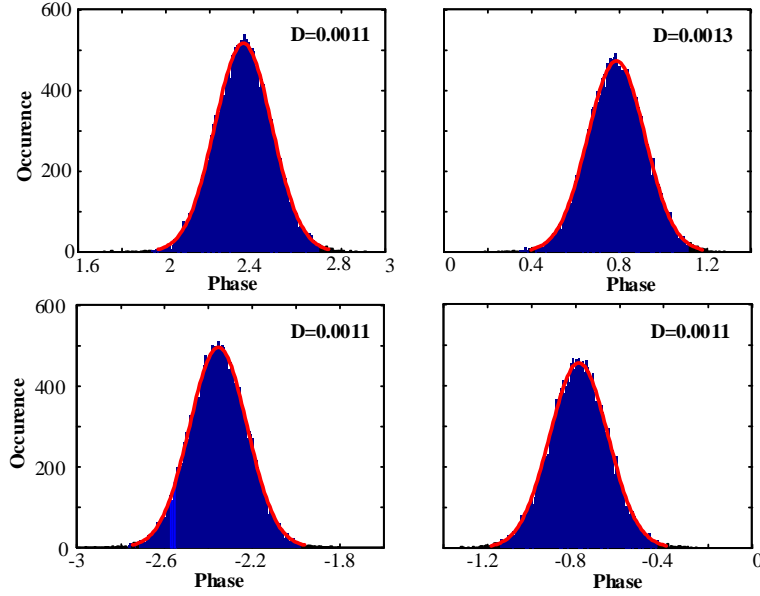


**Figure 2.5:** Histogram of the received QPSK symbols phases (x-polarization) in four quadrants of the constellation diagram. Propagation over 800 km in nonlinear limited regime with the launch power of 3 dBm.

## 2.5 Novel indirect BER estimation methods for QPSK CO-OFDM

It has been shown in the previous section that the distribution of the received QPSK symbols phases in each quadrant of the constellation diagram is in good agreement with a Gaussian distribution. Using a Gaussian approximation, the probability density function (PDF) of the received QPSK symbols phases in four constellation quadrants can be expressed as:

$$f_k(\phi) = \frac{1}{\sigma_k \sqrt{2\pi}} \exp\left(-\frac{(\phi - \bar{\phi}_k)^2}{2\sigma_k^2}\right), \quad (2.14)$$

where  $f_k(\phi)$ ,  $\bar{\phi}_k$  and  $\sigma_k$  denote the PDF, mean and standard deviation of the received phases in the  $k$ th quadrant ( $k = 1, 2, 3, 4$ ). In QPSK (Gray coded) CO-OFDM systems, information symbols can have one of the four following values:  $X_1 = \sqrt{2}\exp(j\pi/4)$ ,  $X_2 = \sqrt{2}\exp(j3\pi/4)$ ,  $X_3 = \sqrt{2}\exp(-j3\pi/4)$ ,  $X_4 = \sqrt{2}\exp(-j\pi/4)$ . The error proba-

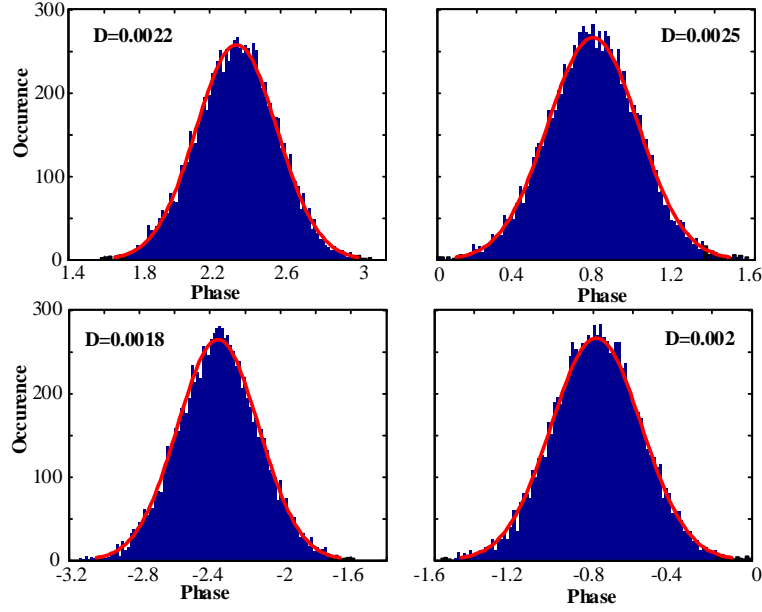


**Figure 2.6:** Histogram of the received QPSK symbols phases (x-polarization) in four quadrants of the constellation diagram. Propagation over 800 km in nonlinear limited regime with the launch power of 6 dBm.

bility when  $X_1$  is transmitted can be calculated as follows:

$$\begin{aligned}
 P_E(X_1) &= \int_{-\infty}^0 f_1(\phi) d\phi + \int_{\pi/2}^{+\infty} f_1(\phi) d\phi \\
 &= \frac{1}{2} \left( \operatorname{erfc} \left( \frac{\bar{\phi}_1}{\sigma_1 \sqrt{2}} \right) + \operatorname{erfc} \left( \frac{\pi/2 - \bar{\phi}_1}{\sigma_1 \sqrt{2}} \right) \right)
 \end{aligned} \tag{2.15}$$

Similarly, we can obtain expressions for  $P_E(X_2)$ ,  $P_E(X_3)$ ,  $P_E(X_4)$ , then the systems BER is given by:

$$\text{BER} = \frac{1}{8} \sum_{k=1}^4 \left[ \operatorname{erfc} \left( \frac{\bar{\phi}_k - \theta_k + \pi/4}{\sigma_k \sqrt{2}} \right) + \operatorname{erfc} \left( \frac{\theta_k + \pi/4 - \bar{\phi}_k}{\sigma_k \sqrt{2}} \right) \right] \tag{2.16}$$

where  $\theta_k = \arg(X_k)$ ,  $k = 1, 2, 3, 4$ . This expression offers a relatively simple way to estimate the performance of a CO-OFDM system by calculating the means and STDs of the received phases in each quadrant of the constellation diagram. This BER estimation method is nondata-aided.

The proposed BER estimation method can also be extended for m-PSK CO-OFDM

transmission as:

$$BER = \frac{1}{2m} \sum_{k=1}^m \left[ \operatorname{erfc} \left( \frac{\bar{\phi}_k - \theta_k + \pi/m}{\sigma_k \sqrt{2}} \right) + \operatorname{erfc} \left( \frac{\theta_k + \pi/m - \bar{\phi}_k}{\sigma_k \sqrt{2}} \right) \right] \quad (2.17)$$

where  $\theta_k = (2k + 1)\pi/m$ ,  $k = 0, 1 \dots m - 1$  are the phases of m-PSK information symbols.

## 2.6 Comparison of BER estimation methods for QPSK CO-OFDM

In this section, the performances of different BER estimation methods, namely data-aided EVM, nondata-aided EVM (Q-factor 1), Q-factor 2, Q-factor 3 and the proposed method (expression (2.16)), are compared for QPSK PDM CO-OFDM and 8-PSK PDM CO-OFDM transmissions. For comparison purposes the estimated BERs for x- and y-polarization are averaged and then converted to a Q-factor using the expression (2.1).

The investigated BER estimation methods for 112 Gb/s QPSK PDM CO-OFDM are compared in Fig. 2.7. The blue line with circle markers (Q(BER)) is the reference result of the direct error counting from Monte Carlo simulations (10 runs). The red line with square markers (Q-proposed) shows the result obtained using the estimation method proposed here based on a Gaussian approximation of the phase noise statistics (expression 2.16). In Fig. 2.7 almost no mismatch between Q(BER) and Q-proposed is observed. This result indicates that the proposed BER estimation method is highly accurate. On the other hand, all the other BER estimation methods, namely EVM (data-aided, nondata-aided), Q-factor 2 and Q-factor 3, underestimate the system performance by approximately 1 dB, even in the ASE-dominated transmission regime. This is due to the fact that the noise distribution diverges from Gaussian distribution under the influence of large laser phase noise. Interestingly, all these BER estimation methods show almost the same performance for CO-OFDM transmission.

The performance of the BER estimation methods for 112 Gb/s QPSK PDM RGI-CO-OFDM is shown in Fig. 2.8. In 112 Gb/s QPSK RGI-CO-OFDM transmissions with OFDE at the receiver, the proposed BER estimation method also shows excellent agree-

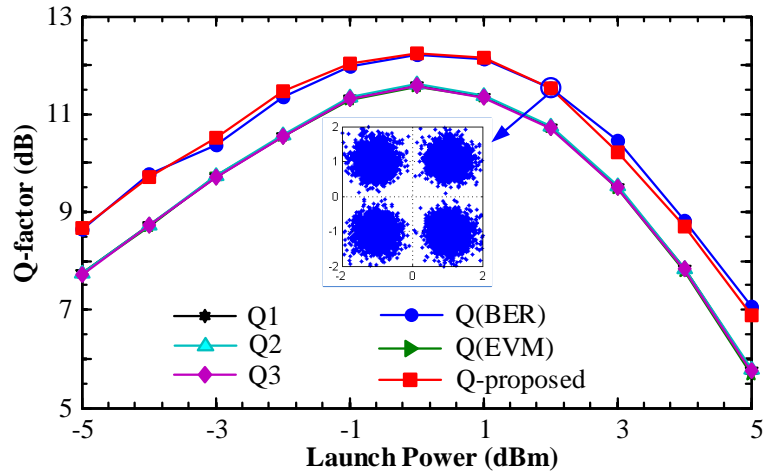


**Figure 2.7:** Q-factor values (average over x- and y-polarization) as a function of the launch power in 112 Gb/s QPSK PDM CO-OFDM after 2400 km of transmission. Q(EVM), Q1, Q2, Q3 all follow the lower curve.

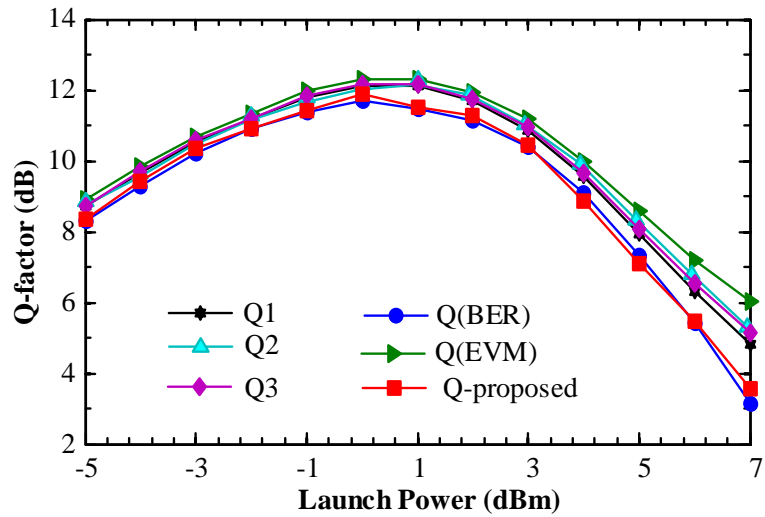


**Figure 2.8:** Q-factor values (average over x- and y-polarization) as a function of the launch power in 112 Gb/s QPSK PDM RGI-CO-OFDM after 4000 km of transmission.

ment with the direct error counting result. Other BER estimation methods, unlike the case of the conventional CO-OFDM transmission, overestimate the system performance. These BER estimation methods all show similar performance and the estimation inaccuracy increases with the launch power. When the launch power is low (ASE limited regime) EVM (data-aided and nondata-aided), Q-factor 2, Q-factor 3 show good agreement with the direct error counting technique. However, at a high level of the launch power (the nonlinear limited regime) the inaccuracy in estimation is significant and increases proportionally with the launch power.

The BER estimation methods applied in WDM CO-OFDM transmissions transmis-

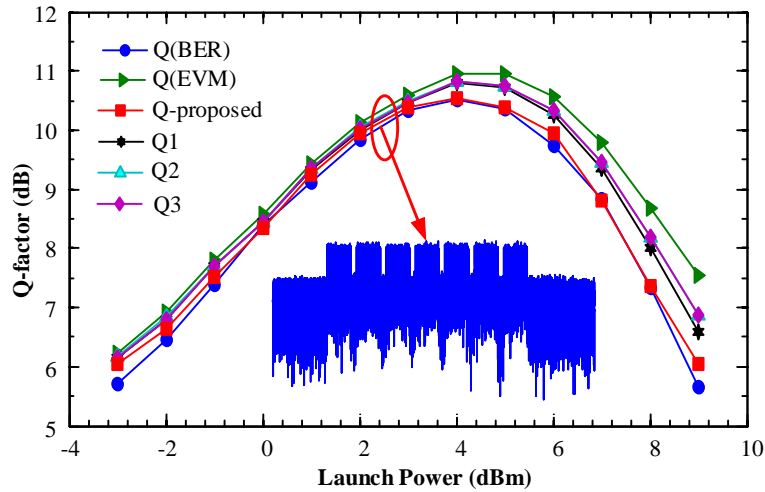


**Figure 2.9:** Q-factor values for the center channel (average over x-and y-polarization) as a function of the launch power in  $7 \times 112$  Gb/s QPSK PDM WDM RGI-CO-OFDM after 3200 km of transmission.

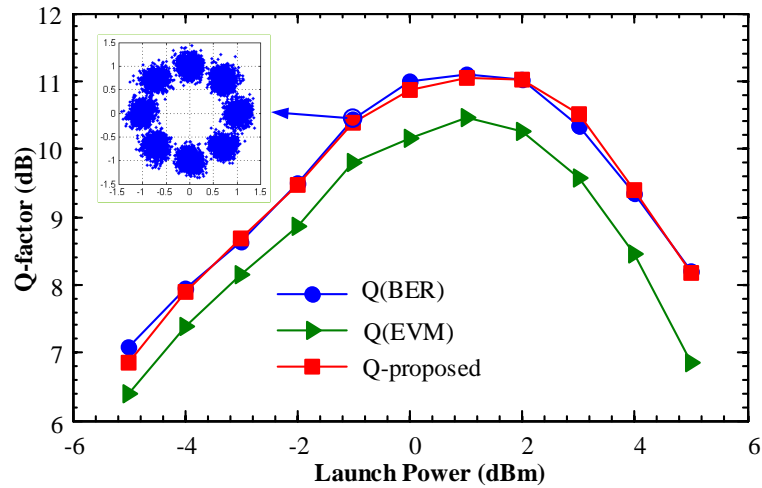


**Figure 2.10:** Q-factor values (average over x-and y-polarization) as a function of the launch power in 112 Gb/s 8-PSK PDM CO-OFDM after 800 km of transmission.

sion are now investigated.  $7 \times 112$  Gb/s PDM WDM RGI-CO-OFDM transmissions with 50 GHz frequency spacing are simulated. In Fig. 2.9 the Q-factors obtained by using different BER estimation methods for the center channel are compared. The proposed BER estimation method also shows an excellent performance despite the nonlinear impairments from neighboring WDM channels. Similar to single channel PDM RGI-CO-OFDM transmission, all other BER estimation methods overestimate the system performance. The data-aided EVM also shows the worst performance and nondata-aided, Q-factor 2 and Q-factor 3 have a similar performance.

Figure. 2.10 shows the performance of the proposed BER estimation method for 112 Gb/s

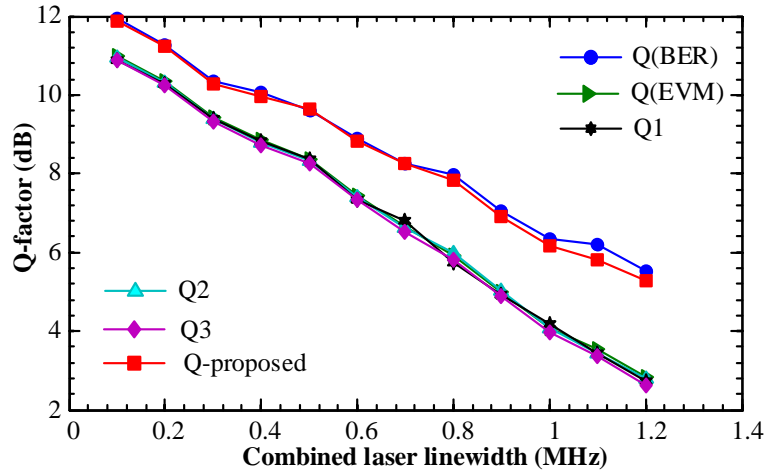


**Figure 2.11:** Q-factor values (average over x-and y-polarization) as a function of the combined laser linewidth in 112 Gb/s PDM CO-OFDM after 2000 km of transmission; the launch power was 1 dBm.

8-PSK PDM CO-OFDM transmission. The estimation of the BER from data-aided EVM for 8-PSK systems can be found in [22]. As long as the received phases of each transmitted symbol has a Gaussian distribution, the proposed method also offers very accurate estimation of the system performance if m-PSK modulation format is adopted. However, the obtained results cannot be extended directly to high-order QAM modulation formats such as 8 QAM or 16 QAM, in which the decision is made by taking into account both the phases and amplitudes of the received symbols. For high-order QAM modulation formats, a 3D PDF would be required for estimating the systems BER. In this case, a larger number of statistical samples would be required for an accurate estimation which significantly increases the complexity of the estimator. This problem is beyond the scope of this thesis. However, further investigation on this subject is of great interest.

### 2.6.1 Impact of the laser phase noise

In this section, the robustness of the proposed BER estimation method to laser phase noise is studied. The laser phase noise can change the statistical properties of the received QPSK symbols, and thus affects the performance of all statistical BER estimation methods. For all results presented in this section the CPE is estimated and compensated using the pilot-aided technique. For the conventional 112 Gb/s CO-OFDM transmission 16 pilot subcarriers are inserted in each OFDM symbol, while for RGI-CO-OFDM the number of

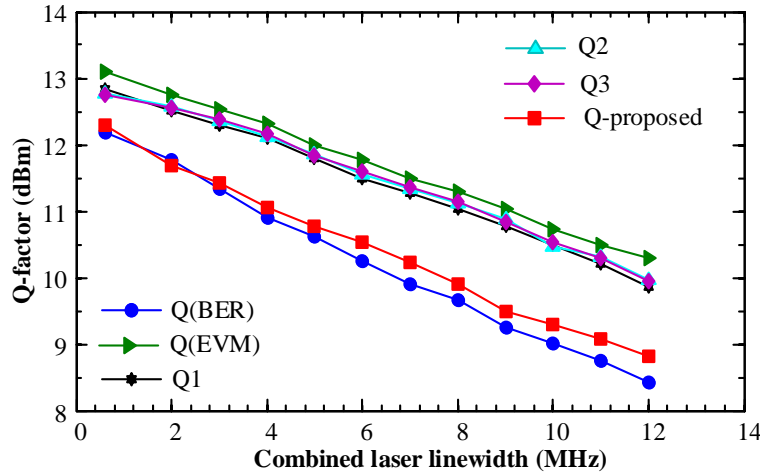


**Figure 2.12:** Q-factor values (average over x-and y-polarization) as a function of the combined laser linewidth in 112 Gb/s PDM RGI-CO-OFDM after 4000 km of transmission; the launch power was 1 dBm.

pilot subcarriers used is 6 [39]. Note that a smaller number of pilot subcarriers can be used in RGI-CO-OFDM due to the shorter symbol duration.

The impact of laser phase noise on the performances of the BER estimation methods is shown in Fig. 2.11 and Fig. 2.12 for CO-OFDM and RGI-CO-OFDM transmissions. The combined laser linewidth is the sum of the linewidths of the transmitter and receiver lasers. It is assumed here that the transmitter and receiver lasers have the same linewidth, which is equal to half of the combined linewidth. It has been shown [40] that the impact of receiver laser phase noise is more significant than transmitter phase noise due to equalization enhanced phase noise phenomenon. Equalization enhanced phase noise occurs in RGI CO-OFDM systems and does not effect the CO-OFDM systems employing CP. For simplicity only the case that the transmitter and receiver lasers have the same linewidth is considered in this thesis. All the obtained results are presented in term of combined laser linewidth.

For 112 Gb/s PDM CO-OFDM transmission almost no mismatch between the BERs estimated by the proposed method and the direct error counting was observed when the combined laser linewidth is increased up to 1.2 MHz. This result indicates that the proposed BER estimation method is extremely tolerant to laser phase noise. Note that commercial external-cavity lasers have a linewidth of around 100 kHz. Other BER estimation methods, on the other hand, are much less tolerant to laser phase noise as their accuracy

decreases when the combined laser linewidth is increased. At the combined laser linewidth of 200 kHz, all the aforementioned methods underestimate the system performance by approximately 1 dB. However, if the combined laser linewidth is increased to 1.2 MHz the difference in Q-factor increases to over 2.5 dB.

For 112 Gb/s PDM RGI-CO-OFDM the combined laser linewidth is increased to 12 MHz for investigating its impact on the performance of BER estimation methods. It can be seen that RGI-CO-OFDM is much more tolerant to laser phase noise in comparison with the conventional CO-OFDM because of the shorter symbol duration. In the investigated systems the symbol duration of RGI-CO-OFDM is 4 ns, which is 18 times shorter than the symbol duration of the CO-OFDM system (72 ns). For the CO-OFDM system a 3 dB penalty due to laser phase noise is observed at 0.5 MHz of combined laser linewidth while for RGI-CO-OFDM it occurs at 9 MHz (also 18 times difference). As shown in Fig. 2.12, the proposed BER estimation method also shows an excellent tolerance towards the combined laser linewidth. Even though at high level of the combined laser linewidth this method also overestimates the system performance but the inaccuracy is relatively small, below 0.5 dB for 12 MHz of the combined laser linewidth. On the other hand, for the same value of the combined laser linewidth, other BER estimation methods overestimate the system performance by around 3 dB. Note that for RGI-CO-OFDM data aided EVM offers the worst performance while the combined laser linewidth is varied.

The results obtained in this section indicate that the proposed BER estimation method is highly tolerant to laser phase noise, both in CO-OFDM and RGI-CO-OFDM transmissions.

## **2.6.2 Impact of frequency offset**

Similar to laser phase noise, the frequency offset between the transmitter and receiver lasers also changes the statistical properties of the received QPSK symbols. In CO-OFDM transmissions, this frequency offset can be effectively estimated and compensated using DSP techniques [41]. However, a residual uncompensated carrier frequency offset is always present in the system and thus the performance of statistical BER estimation methods

may be affected. In this section, the impact of carrier frequency offset on the effectiveness of the proposed BER estimation method is investigated.

For this investigation the frequency offset in CO-OFDM and RGI-CO-OFDM systems is varied up to 4 MHz and 36 MHz respectively. As the frequency spacing in RGI-CO-OFDM system can be much larger than that of the traditional CO-OFDM system, RGI-CO-OFDM is also more tolerant to the frequency offset. This is another major advantage of RGI-CO-OFDM as compared to traditional CO-OFDM systems.

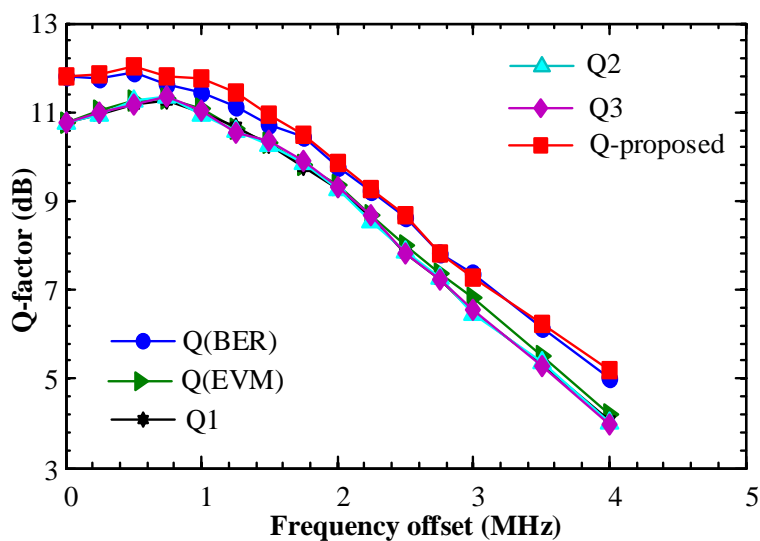


**Figure 2.13:** Q-factor values (average over x-and y-polarization) as a function of the frequency offset in 112 Gb/s PDM CO-OFDM after 2000 km of transmission; the launch power was 1dBm.

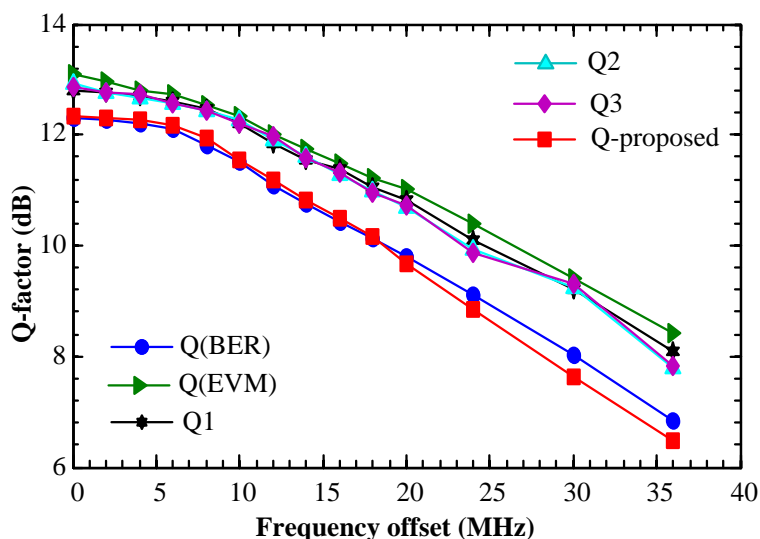


**Figure 2.14:** Q-factor values (average over x-and y-polarization) as a function of the frequency offset in 112 Gb/s PDM RGI-CO-OFDM after 4000 km of transmission; the launch power was 1dBm.

The simulation results are shown in Fig. 2.13 and Fig. 2.14. Remarkably, for both the conventional CO-OFDM and RGI-CO-OFDM systems the proposed BER estimation method also offers the most accurate estimation of the system performance in the presence of carrier frequency offset. However, some differences were observed for CO-OFDM and RGI-CO-OFDM transmissions. For RGI-CO-OFDM, the performances of all the BER estimation methods become worse if the frequency offset is increased. If the frequency offset is set to 36 MHz, the data-aided EVM overestimates the system performance by over 2 dB in comparison with 1 dB when no frequency offset is included. The proposed BER estimation method also underestimates the system performance in the presence of high frequency offset. For CO-OFDM system, the proposed BER estimation method shows an excellent performance even in the presence of large frequency offset. Other BER estimation methods also offer good performances and their inaccuracies do not seem to increase with the frequency offset (up to 4 MHz). However, in general, the proposed BER estimation method shows a much better performance than other considered here techniques.

## **2.7 Experimental verification**

### **2.7.1 Experimental setup**

For studying the statistical properties of a QPSK modulated OFDM signal and comparison of different BER estimation methods, a WDM CO-OFDM transmission system is set up as shown in Fig. 2.15. This comprised a laser grid of five standard DFB lasers on a 100 GHz grid which were substituted in turn by a 100 kHz linewidth external cavity laser. The DFBs were located between 193.5 to 193.9 THz. Twenty additional loading channels (10 GHz bandwidth) were generated using an ASE source which was spectrally shaped using a WaveShaper wavelength selective switch (WSS). These loading channels were spread symmetrically around the test wavelengths so that the total bandwidth of the transmission signal was 2.5 THz. A wideband filter was used to filter out of band ASE noise at the transmitter. The transmission path is an acousto-optic modulator based recirculating loop consisting of  $4 \times 100$  km spans of Sterlite OH-LITE (E) fibre, having 18.9

to 19.5 dB insertion loss (per 100 km span) and dual stage amplifiers (EDFA, 5dB-6 dB of noise figure). The loop switch was located in the mid-stage of the first EDFA and a gain flattening filter was placed in the mid stage of the third EDFA. After fibre propagation the signal was filtered using a 4.2 nm flat topped filter and coherently detected. The received electrical signals were then sampled by a real-time oscilloscope at 80 GS/s and processed offline in MATLAB.

The OFDM signals (400 symbols each of 20.48 ns length, 2% cyclic prefix) encoded with QPSK modulation format were generated offline in MATLAB using an IFFT size of 512, where 210 subcarriers were filled with data and the remainder zeros giving a potential line rate of 20 Gb/s per channel. The DSP at the receiver included combining x- and y-polarizations using the maximum-ratio combining method [42], frequency offset compensation, chromatic dispersion compensation using a frequency domain equalizer (overlap-and-save method), channel estimation and equalization with the assistance of initial training sequence (2 training symbols every 100 symbols), CPE compensation by distributing 8 pilots uniformly across the OFDM band, giving a net data rate of 17.4 Gbit/s.

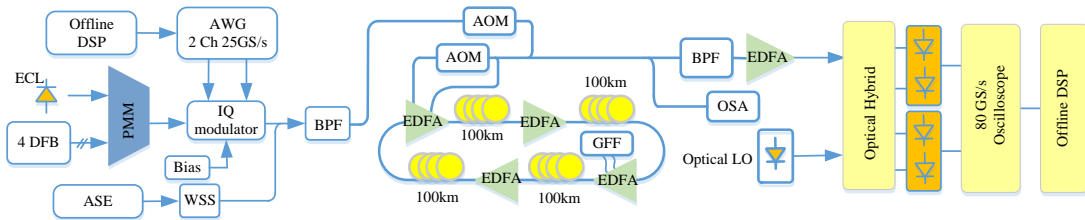


**Figure 2.15:** Schematic of experimental setup of WDM CO-OFDM transmission. ECL: external cavity laser, PMM: polarization maintaining multiplexer, WSS: wavelength selective switch, DFB: distributed feedback laser, BPF: band-pass filter (optical), AOM: acousto-optic modulator, GFF: gain flattening filter, OSA: optical spectrum analyser, LO: local oscillator (optical), EDFA: Erbium-doped fibre amplifier.

## 2.7.2 Experimental results and discussions

Figure 2.16 shows the histograms of in-phase and quadrature components of the received QPSK signal for the center channel. The Gaussian fitting is obtained by calculating the mean and STD of the received statistical samples ( $8 \times 10^5$  in total). The Gaussian fitting

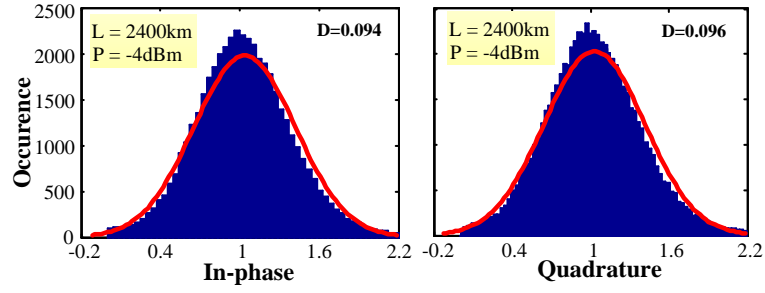


**Figure 2.16:** Histograms of in-phase and quadrature components of the received QPSK symbols in the first quadrant. Gaussian fitting is superimposed to each histogram; KSSTAT values are also included in each histogram.

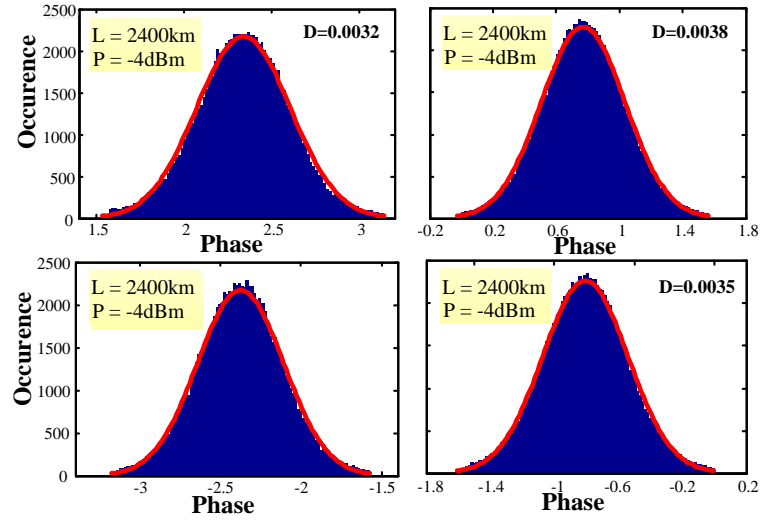


**Figure 2.17:** Histogram of the received QPSK symbols phase of the center channel in four quadrants of the constellation diagram.

and KSSTAT values shown in Fig.2.16 indicate that at this power level the nonlinear interference noise (NLIN) in CO-OFDM transmission deviates from Gaussian distribution. The obtained result herein agrees well with simulation results presented in previous section (Fig. 2.3), indicating that the Gaussian assumption of NLIN, which is the key in the derivation of closed-form expression for the nonlinear performance of CO-OFDM [38] is, in general, not satisfied exactly. On the other hand, as shown in Fig. 2.17, the distribution of the received QPSK symbols phase in each quadrant of the constellation diagram is essentially Gaussian. This result agrees well with numerical results presented in the previous section, indicating that the nonlinear interaction of the ASE noise and signal induces the distribution of QPSK phases in OFDM systems (rather than the in-phase/quadrature components) to be Gaussian.

Bit-error-rate estimation methods for WDM CO-OFDM transmission are compared in

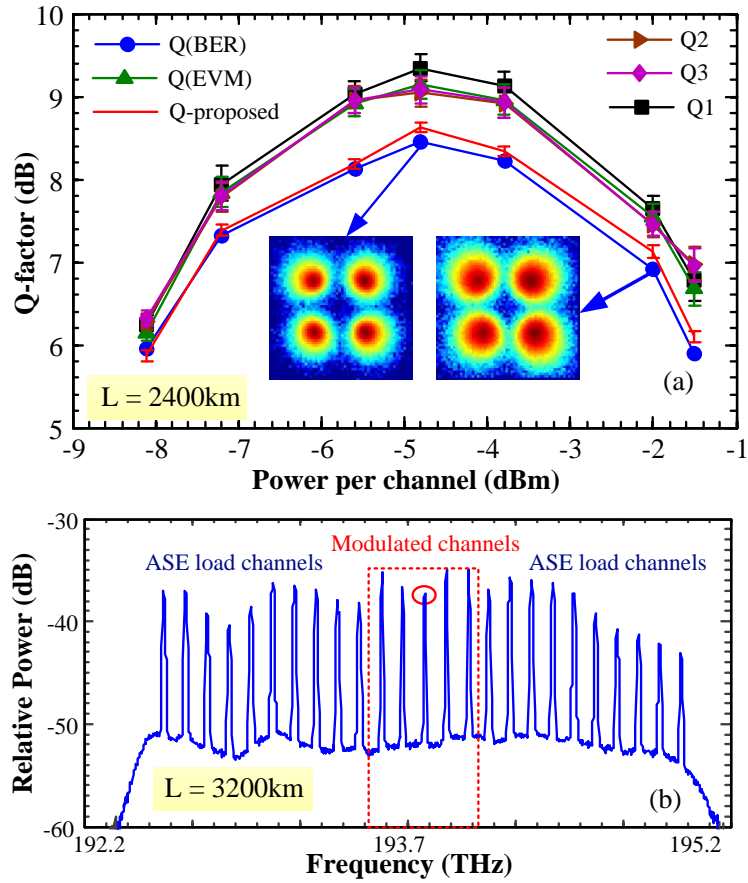


**Figure 2.18:** (a) - Q-factor values for the center channel as a function of the launch power at 2400km, (b) received optical spectrum at 3200km.

Fig. 2.18 (a) for the centre channel and in Fig. 2.19 for the second channel. Similar results, which were obtained for other modulated channels, are not shown here. In Fig. 2.18 only a small mismatch ( $<0.2$  dB) between Q(BER) and Q-proposed is observed, indicating that this BER estimation method is highly accurate. In addition, as Q-proposed is based on the assumption that the received symbols phases are Gaussian distributed, this method is tolerant to residual CPE as the residual CPE, which is common to all subcarriers, affects only the mean but not the variance of the symbols phases. This phenomenon is confirmed by the simulated results for the back-to-back case (AWGN channel) shown in the Fig. 2.20. Without the laser phase noise, Q-proposed offers slightly worse performance in comparison to other methods because in the AWGN channel the symbols phases do not follow a Gaussian distribution [14]. However, in the presence of the laser phase noise Q3 offers the best performance (Fig. 2.20(b)), because the random phase noise makes the distribution of the QPSK phases conforms more closely to a Gaussian distribution as a result of the

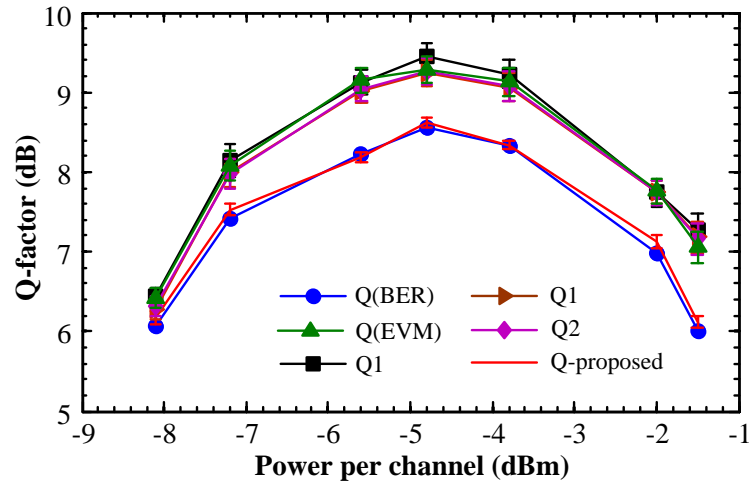


**Figure 2.19:** Q-factor values for the second channel as a function of the launch power at 2400km.

central limit theorem. As a result, Q-proposed still offers an excellent performance even in the ASE limited regime. This result also suggests that the proposed BER estimation method can be effectively applied for single carrier transmission scheme. However, a detailed comparison of this BER comparison method with other well-know BER estimation methods is open for future research.

On the other hand, all the other BER estimation methods, namely EVM Q1 and Q2, Q3 overestimate the system performance by approximately 0.7 to 1 dB. Moreover, unlike Q3-proposed method, Q(EVM), Q1, Q2, Q3 methods are sensitive to residual CPE because the residual CPE strongly affects the distributions of the in-phase and quadrature components of the QPSK signal.

Figure 2.21 shows the STDs obtained using different BER estimation methods as a function of the number of processed statistical symbols in each trace (N) when processing 20 recorded traces. When  $N > 10^3$  the STD of Q3, which is only around 0.1 dB, is the smallest among those obtained with BER estimation methods studied here. This result indicates that the proposed statistical BER estimation method can be applied effectively with a relatively small number of received symbols ( $\sim 10^3$ ) in comparison with other methods, offering a fast and accurate BER estimation method for QPSK CO-OFDM transmission.

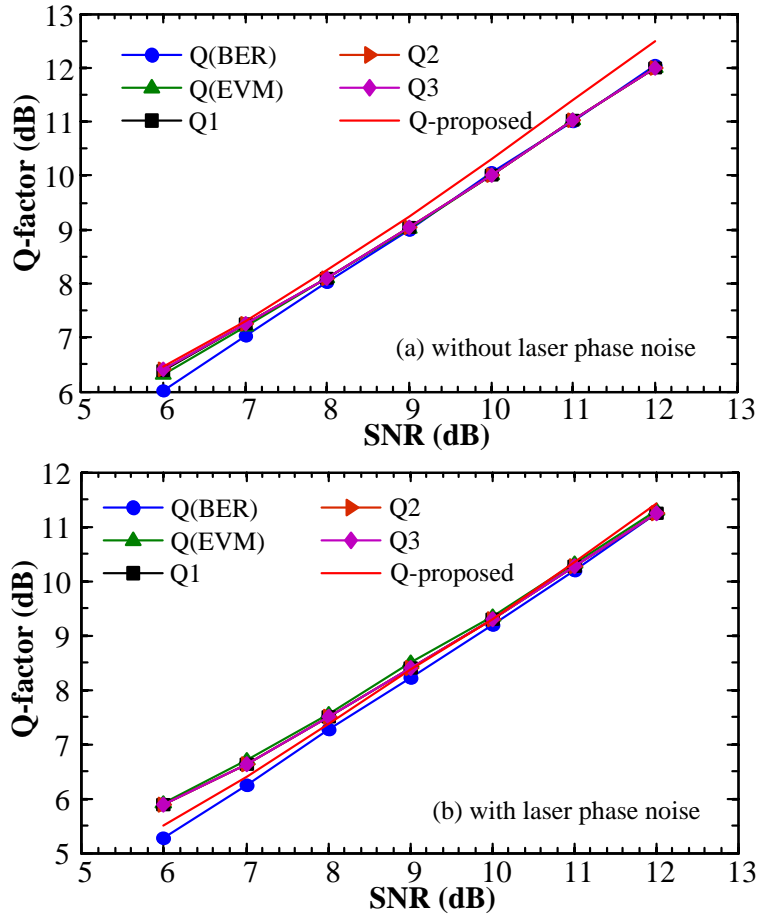


**Figure 2.20:** Performance comparison of BER estimation methods in the back-to-back case (simulation results), without (a) and with (b) the laser phase noise, the combined laser linewidth is 200 kHz.

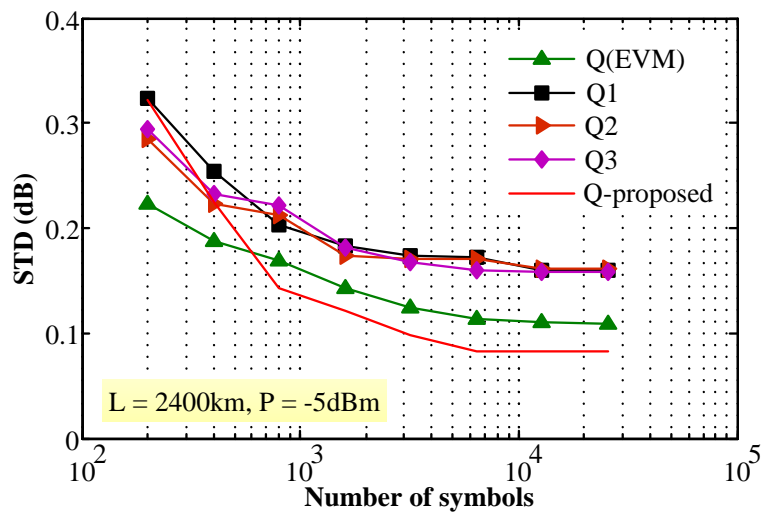


**Figure 2.21:** STD of the Q-factor obtained using different BER estimation methods as a function of the number of processed symbols.

## 2.8 Conclusion

The statistical properties of CO-OFDM transmission are rather different from intensity modulation direct detection and single carrier coherent fibre-optic systems. Therefore, new rules for BER estimates from numerical modelling have to be developed and verified. In this chapter, the performance of a novel BER estimation method, which is based on the statistical properties of the received QPSK symbols, for CO-OFDM transmissions has been investigated. Through numerical modeling and experimental demonstration it has been shown that this method is more accurate compared to commonly used BER estimators. In addition, it has been also shown that the proposed BER estimation method is extremely tolerant to the laser phase noise and the frequency offset between transmitter and receiver lasers.

# Chapter 3

## Low-Complexity Phase Noise

### Estimation Methods for CO-OFDM

**Son T. Le**, Kanesan, T., Giacomidis, E., Doran, N.J., Ellis, A.D., “Quasi-Pilot Aided Phase Noise Estimation for Coherent Optical OFDM Systems,” *Photonics Technology Letters, IEEE* , vol.26, no.5, pp.504-507, March, 2014.

**Son T. Le**, Paul A. Haigh, Andrew D. Ellis and Sergei K. Turitsyn, “Blind Phase Noise Compensation for CO-OFDM Transmission,” *Journal of Lightwave Technology*, vol. PP, no. 99, Aug, 2015 (**invited**).

**Son T. Le**, N. Mac Suibhne, M. E. McCarthy A. D. Ellis and S. K. Turitsyn, “Multiplier-free Blind Phase Noise Estimation for CO-OFDM Transmission,” *ECOC 2015, Valencia, Spain*, paper Mo.4.3.6

#### 3.1 System model

Compared to single carrier system, CO-OFDM has longer symbol duration [43], and therefore is more sensitive to laser phase noise. Laser phase noise introduces both CPE and inter-carrier interference (ICI) [44], which significantly degrades the system performance. Therefore, it is crucial that the laser phase is rigorously tracked, estimated and effectively compensated.

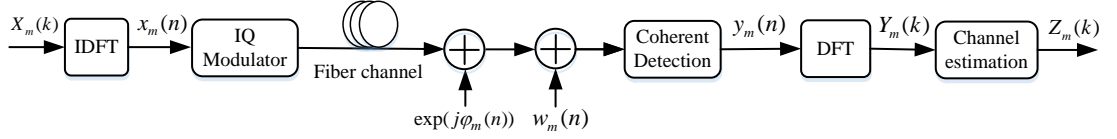


**Figure 3.1:** Block diagram of the CO-OFDM system with laser phase noise and nonlinear phase noise acquired during optical fibre transmission.

In this section, the author introduces the models of laser phase noise, fibre channel, and a general CO-OFDM system with phase noise (Fig. 3.1). For simplicity, the impact of fibre nonlinearity is not considered. In addition, it is assumed that perfect FFT window synchronization and frequency offset compensation are achieved. Furthermore, a baseband system with single polarization signals is considered noting that the analysis can be readily extended to passband systems with dual polarized signals without any difficulties.

### 3.1.1 Phase noise model

The laser phase noise  $\phi(t)$ , generated at both transmitter and receiver, can be modeled as a continuous Brownian motion or a Wiener process with zero mean and variance  $\sigma^2 = 2\pi\beta t$ , where  $\beta$  denotes the combined laser linewidth, i.e., frequency spacing between 3 dB points of the Lorentzian power spectral density function [45]. The discrete-time model of the laser phase noise on the  $n$ th sample of the  $m$ th OFDM symbol can be expressed as:

$$\phi_m(n) = \phi_{m-1}(N-1) + \sum_{i=-N_{cp}}^n u(m(N+N_{cp}+i)), \quad (3.1)$$

where  $u(i)$  represents the independently incremental movement of phase noise at time instant  $i$  and is Gaussian distributed with zero mean and variance  $\sigma^2 = 2\pi\beta dt$ , where  $dt$  is the sampling time,  $N$  and  $N_{cp}$  are the DFT length and cyclic prefix length, respectively.

### 3.1.2 Fibre channel model

Herein, only dispersion-compensation-free fibre transmission links (highly dispersed channels) is considered. In addition, it is assumed here that the fibre loss is perfectly compensated using optical amplifiers such as erbium doped fibre amplifiers or Raman-based amplifiers. As a result, the fibre channel model can be simply expressed in the frequency

domain as:

$$H(z, \omega) = \exp\left(-j\frac{D\lambda^2 z}{4\pi c}\omega^2\right), \quad (3.2)$$

where  $\omega$  is the angular frequency,  $z$  is the transmission distance,  $D$  is the fibre chromatic dispersion parameter,  $c$  is the speed of light and  $\lambda$  is the carrier wavelength.

### 3.1.3 CO-OFDM system model

In OFDM systems, the  $m$ th symbol in the time domain is generated from the modulated data in the frequency domain using the inverse discrete Fourier transform (IDFT) operation as follows:

$$x_m(n) = \frac{1}{\sqrt{N}} \sum_{k=0}^{N-1} X_m(k) \exp\left(\frac{j2\pi nk}{N}\right), \quad (3.3)$$

where the samples  $n$  range from  $-N_{cp}$  to  $N-1$ . Due to the ASE noise, chromatic dispersion and phase noise the received OFDM signal can be written as:

$$y_m(n) = \exp(j\phi_m(n)) [x_m(n) \otimes F^{-1}(H_m(k))] + w_m(n), \quad (3.4)$$

where  $\otimes$  and  $F^{-1}(H_m(k))$  denote the circular convolution and IDFT, respectively, while  $w_m(n)$  indicates the total ASE noise generated from inline optical amplifiers,  $H_m(k)$  is the channel gain in the frequency domain of the  $k$ th subcarrier defined as (3.2). It is assumed here that the intersymbol interference is absent, after taking the DFT operation we obtain

$$Y_m(k) = X_m(k)H_m(k)I_m(0) + ICI_m(k) + W_m(k), \quad (3.5)$$

where the intercarrier interference  $ICI_m(k)$  is defined as:

$$ICI_m(k) = \sum_{l=0, l \neq k}^{N-1} X_m(l)H_m(l)I_m(l-k), \quad (3.6)$$

where  $I_m(k)$  is given by

$$I_m(k) = \frac{1}{N} \sum_{n=0}^{N-1} \exp(j\phi_m(n)) \exp\left(-j\frac{2\pi kn}{N}\right), \quad (3.7)$$

From (3.2) and (3.6) the system model can be written as:

$$Y_m(k) = X_m(k)H_m(k)I_m(0) + \varepsilon_m(k), \quad (3.8)$$

where the accumulated noise is defined as

$$\varepsilon_m(k) = ICI_m(k) + W_m(k) \quad (3.9)$$

The channel response in CO-OFDM systems can be obtained by periodically inserting training sequences. By assuming perfect channel estimation, synchronization [46], the recovered data after equalization can be expressed as

$$Z_m(k) = Y_m(k)/H_m(k) \quad (3.10)$$

As a result, we have

$$Z_m(k) = X_m(k)I_m(0) + \chi_m(k) \quad (3.11)$$

where the equalization-enhanced phase noise (EPPN) is defined as:

$$\chi_m(k) = \varepsilon_m(k)/H_m(k) \quad (3.12)$$

Due to the complicated interplay between laser phase noise, and fibre dispersion, most of ICI compensation techniques developed for OFDM systems in linear (radio or open space) channels [47, 48] cannot be effectively applied for CO-OFDM transmission systems. In addition, except the pulse shaping approach [49], ICI compensation techniques are usually highly complex and thus, cannot be applied effectively in high speed CO-OFDM transmission systems. A recent study [50] has shown that the EPPN term in the expression (3.12) can be simply treated as a zero mean Gaussian noise. In the expression (3.12),  $I_m(0)$  is usually referred to the common phase error as it corresponds to the time-average of the

laser phase noise over the  $m$ th OFDM symbol:

$$I_m(0) = \frac{1}{N} \sum_{n=0}^{N-1} \exp(j\phi_m(n)) \approx \exp(j\Phi(m)), \quad (3.13)$$

where  $\Phi(m)$  is the CPE of the  $m$ th OFDM symbol defined as:

$$\Phi(m) = \frac{1}{N} \sum_{n=0}^{N-1} \phi_m(n), \quad (3.14)$$

Finally, the system model can be simplified as

$$Z_m(k) = X_m(k) \exp(j\Phi(m)) + \chi_m(k) \quad (3.15)$$

In this case, the CO-OFDM system model with phase noise converges to the linear OFDM system model with constant phase offset [44]. As a result, even though the discussion is focused on CO-OFDM systems for fibre link, all the techniques and results presented in this chapter are fully applicable for traditional OFDM systems in radio frequency domain.

## 3.2 Quasi-pilot aided phase noise estimation for CO-OFDM

### 3.2.1 Introduction

The most widely used phase noise compensation (PNC) technique for CO-OFDM transmissions is pilot-aided (PA) technique due to its inherently low complexity. In fact, This technique is adopted from wireless communication [44]. However, the ultimate shortcoming of PA PNC is the required additional overhead. In this section a novel PNC scheme termed QPA phase noise compensation is discussed in details. The QPA method retains the use of pilot subcarrier (PS) at known frequencies to estimate the carrier phase; however, unlike the conventional PA scheme where pilot phases are predetermined, the pilot phases in QPA are data dependent. The major advantage of QPA estimation is that the number of PSs required for a similar performance to PA estimation can be reduced by a factor of 2, without significant additional complexity, power overhead and differential encoding.

It should be noticed that QPA is also a CPE-based scheme and thus, it is intended for application to non ICI-dominated channels. The effectiveness of the proposed method is demonstrated by comparing with common PNC methods, including PA, data-aided (DA) with M-th power law, RF-pilot and maximum-likelihood (ML) PNC methods.

### 3.2.2 QPA concept

In CO-OFDM system, the transmission channel response can be estimated by periodically transmitting training symbols for channel estimation, after which the phase drift is reset to 0. By transmitting a few PSs, the CPE can be estimated in PA method as [32, 44, 51]:

$$\bar{\Phi}_m = \arg \left( \frac{1}{N_p} \sum_{pilots} \frac{Z_m(k)X_m^*(k)}{|Z_m(k)X_m(k)|} \right) \quad (3.16)$$

where  $\arg(\cdot)$  is the phase angle of the information symbol,  $X_m(k)$  is the known transmitted information symbol and  $N_p$  is the number of PSs. It can be seen clearly in (3.16) that the accuracy of PA phase estimation technique is improved by increasing the number of PSs at the cost of proportionally increasing the overhead and so reducing the net data rate. To address this issue it is proposed that the effectiveness of PA phase estimation may be enhanced by modulating each pilot subcarrier with a data signal directly related to the signal on a data carrying subcarrier, rather than setting each pilot to a fixed predetermined state. As the pilots are no longer constant, this scheme is referred to as quasi-pilot aided estimation. Two specific examples of QPA based estimation are considered. In the first QPA scheme (QPA-1), all  $N_p$  pilot subcarriers are distributed equally in the first part of the OFDM band, taking the DC subcarrier as the symmetrical reference ( $k = 0$ ).  $N_p$  pilot subcarriers ( $X_m(k), k = k_1, k_2, k_{N_p}$ ) are chosen by the condition:

$$X_m(k) = X_m^*(-k) \quad (3.17)$$

where  $*$  stands for the complex conjugate operation. That is, each pilot subcarrier is the complex conjugate of the data carrying subcarrier equally spaced from the central reference. This proposal can be regarded as a novel method for realizing a transmission

scheme with semi-pilot (strongly encoded) symbols. Note that in general the positions of PSs and the correlated data carrying subcarriers can be chosen arbitrarily. Equation (3.17) provides an option of setting the pilots in QPA-1 scheme such that PSs and the correlated data carrying subcarriers are distributed equally among the OFDM band for achieving the best performance.

At the receiver, after performing channel estimation, each pilot subcarrier is coherently combined with its data carrying counterpart, eliminating the data modulation and enhancing signal to noise ratio (SNR). The overall CPE is then estimated by summing the resultant modulation free vectors and taking the argument, as shown in the following expression:

$$\bar{\Phi}_m = \arg \left( \sum_{\text{pilots}} Z_m(k)Z_m(-k) \right) \quad (3.18)$$

This simple approach allows the CPE to be estimated without any prior information on the phases of PSs. In addition to this, the CPE is calculated by taking into account  $2N_p$  subcarriers, which includes the complex conjugate data pilots in the first half and the actual data on the second half of the OFDM band. Thus, the accuracy of this estimation is similar to the PA phase estimation scheme whilst averaging the noise  $\chi_m(k)$  over  $2N_p$  pilot subcarriers. In order to show the SNR advantage of QPA-1 scheme, let us consider the case when only one pilot is used for simplicity, and the extension to many pilots is straightforward. By assuming that  $X_m(k) = X_m(-k) = 1$  and there is no ICI, we have:

$$Z_m(k)Z_m(-k) = \exp(2j\Phi_m) + \chi'_m(k) + \chi'_m(-k) + \chi_m(k)\chi_m(-k) \quad (3.19)$$

At intermediate-to-high SNR the product of the two noise terms can be neglected, leading to:

$$Z_m(k)Z_m(-k) = \exp(2j\Phi_m) + \chi'_m(k) + \chi'_m(-k) = \rho \exp(j(2\Phi_m + 2\theta)) \quad (3.20)$$

where  $\rho$  is the modulus,  $2\theta$  is the part of the complex noise that can be approximated to

white Gaussian noise with power  $NSR = SNR^{-1}$ . By applying QPA-1 we get:

$$\bar{\Phi}_m = \Phi_m + \theta, \text{ for } -\pi/2 < \Phi_m + \theta < \pi/2 \quad (3.21)$$

It is clear that the power of is  $NSR/4$ , while the power of the noise component tangential to complex exponential in the conventional method (equation (3.16)) is  $NSR/2$ . As a result, QPA-1 scheme gives 3 dB SNR gain over the conventional PA method.

In the second QPA scheme (QPA-2) instead of coding the pilots as direct conjugates of data subcarriers, the phases of  $N_p$  PSs are chosen such that their mean phase angle is opposite that of all the remaining data subcarriers, as specified by the condition:

$$\langle \arg(X_m(k)) \rangle_{pilots} + \langle \arg(X_m(k)) \rangle_{data} = 0, \quad (3.22)$$

where  $\langle \cdot \rangle$  stands for the averaging operation. So the phases of the pilot subcarriers can be chosen equal to meet the requirement of (3.22);  $\arg(X_m(k))_{pilots} = -\langle \arg(X_m(k)) \rangle_{data}$ . At the receiver, the CPE is estimated by summing the phases of all pilots and associated data subcarriers as follow:

$$\bar{\Phi}_m = \left( \langle \arg(Z_m(k)) \rangle_{pilots} + \langle \arg(Z_m(k)) \rangle_{data} \right) / 2, \quad (3.23)$$

Expression (3.23) also indicates that in QPA-2 the CPE is calculated without any prior knowledge of the phases of PSs. It is obvious that the accuracy of CPE estimation is improved significantly by taking all the subcarriers into consideration. The positions of PSs in QPA-2 scheme can be also chosen arbitrarily. However, for achieving the best performance, in QPA-2 scheme PSs should be equally distributed among the OFDM band. As the total phase of all symbols is constant, QPA-2 may be considered as a form of phase parity. Note that in QPA schemes PSs are not inserted into training symbols, thus there is no impact during the synchronization process.

The phase noise tolerance of PNC methods can be increased by using the information about the CPE of the previous symbol(s) with an iterative algorithm [52]. This approach is also applied here to QPA PNC. In the first stage of compensation; the laser phase noise

of the current symbol is compensated using the estimated CPE of the previous symbol. After that the difference between CPE estimations of the current and the previous symbols ( $\Delta \Phi_m = \Phi_m - \Phi_{m-1}$ ) is estimated using expression (3.18) or (3.22). This scheme is known as two-stage-iterative (TSI) QPA PNC and can be regarded as an iterative algorithm, which increases the laser phase noise tolerance (in term of cycle slip and click probability) of QPA schemes significantly.

### 3.2.3 Experimental results and discussions

To investigate the performance of QPA methods the same experimental setup was used as illustrated in Fig. 2.15 with 16QAM format. The two QPA PNC schemes are compared with RF and PA methods as a function of the OSNR, as shown in Fig. 3.2 for a combined laser linewidth of 200 kHz. The RF-pilot tone was added by detuning the IQ modulator to give a DC subcarrier (7 % power) separated from the 210 data subcarriers by a frequency guard band of 100 MHz. At the receiver, the DC subcarrier was filtered out for PNC using a low pass filter with an optimised bandwidth of 20 MHz. It can be seen in Fig. 3.3 that both QPA schemes outperform the PA PNC scheme and in particular 2 pilot QPA schemes offer similar performance to 4 pilot PA schemes confirming that the overhead can be effectively reduced by a factor of 2. Similarly, 2 pilot QPA outperforms the use of an RF-pilot tone. The RF-pilot tone method is strongly affected by the size of the frequency guard band surrounding the DC subcarrier; consequently with a small overhead (1 % in this experiment) the QPA method outperforms the RF method. In particular, 2 pilot QPA requires a 0.95 % overhead, which is almost equivalent to that of the RF-pilot tone. The impact of overhead on CPE estimation performance is illustrated in Fig. 3.3, showing BER at an experimentally measured OSNR of  $\sim 26$  dB. It can be seen that with the conventional PA method, 10 PSs are required for negligible penalty (less than 5 % degradation in BER). On the other hand, for both QPA schemes the required number of PSs is less than 6, a reduction of almost a factor of 2. Fig. 3.4 confirms that this advantage is maintained over a range of laser phase noises, with both 2 pilot QPA methods showing similar or enhanced performance compared to the PA method with 4 pilots for combined

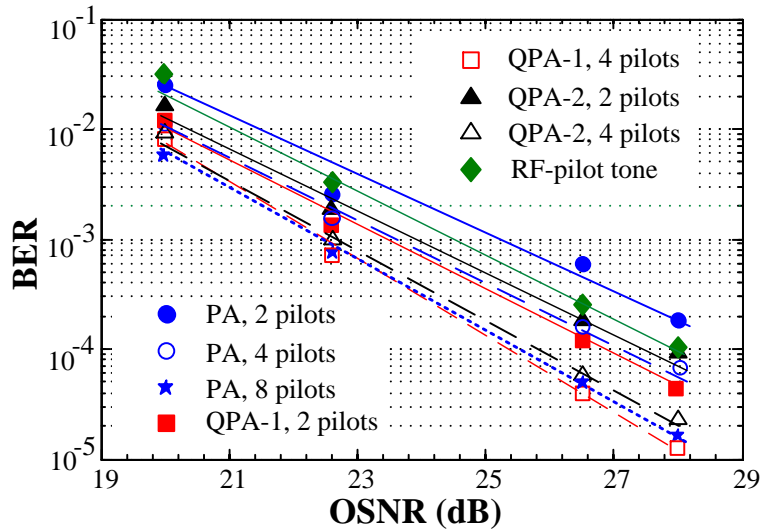


**Figure 3.2:** BER versus OSNR with 200 kHz combined linewidth in 40 Gb/s 16QAM OFDM transmission.

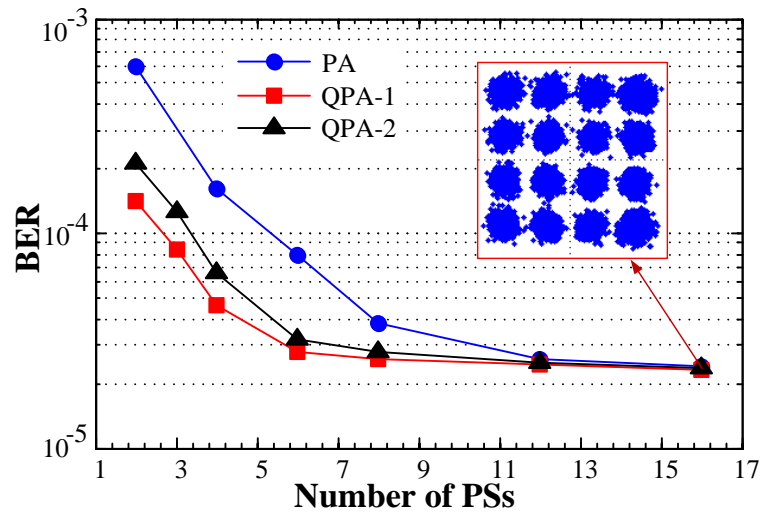


**Figure 3.3:** BER versus number of PSs at 26 dB OSNR in 40 Gb/s 16QAM OFDM transmission.

laser linewidths (artificially broadened) up to 800 kHz.

### 3.3 Blind phase noise estimation for CO-OFDM

As discussed in the previous section, quasi-pilot-aided techniques can effectively reduce the overhead due to pilot subcarriers by a factor of 2, without compromising the performance. In addition, a pre-emphasized pilot subcarrier technique was considered in [50], which significantly reduces the pilot subcarrier overhead at a cost of increasing the pilot subcarrier power overhead (up to 10 %). However, it is still desirable to remove completely

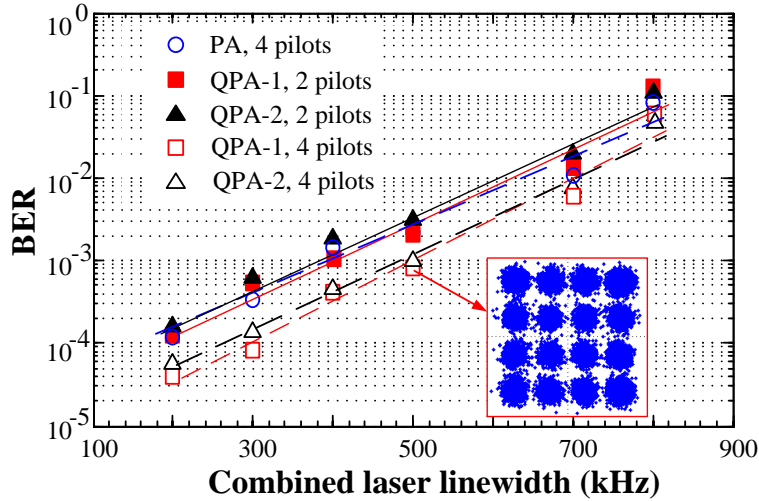


**Figure 3.4:** BER versus combined laser linewidth also at 26 dB OSNR in 40 Gb/s 16QAM OFDM transmission.

the overhead due to pilot subcarriers to maximize the systems SE and power consumption.

Blind phase noise estimation for CO-OFDM with a small number of subcarriers (up to 200) has attracted a lot of attention recently [53, 54]. In [53], a blind PNE method based on a decision directed (DD) algorithm has been considered for CO-OFDM. A major advantage of DD-based PNE scheme is that it is compatible with any modulation format. However, this technique suffers significantly from error propagation, and thus, it cannot be applied directly in the presence of a large laser phase noise. In [55] the concept of blind phase search (BPS) was proposed, which can be applied effectively without suffering from error propagation. However, the BPS technique also relies on DD (to estimate the mean-square-error) and a large number test phases (16 to 32) are required to achieve good performance and thus, being too complex for practical implementation.

To address the drawbacks of both BPS and DD-based PNE schemes, a novel DDF blind PNE technique has been proposed and experimentally demonstrated recently in [56, 57]. This DDF blind PNE scheme provides several advantages. Firstly, it offers a high performance without decision feedback, avoiding error propagation. Secondly, it requires only three test phases and thus significantly reduces the computational complexity in comparison to BPS. Finally, DDF blind scheme is also transparent to QAM formats.

In this section, a detailed analysis of DDF blind PNC technique is provided and its performance is investigated for high order modulation formats up to 64QAM. Two novel

cost functions are also discussed here to further reduce the complexity of DDF blind PNC scheme.

### 3.3.1 Blind phase noise tracking

In CO-OFDM systems, in general, blind PNE can be implemented without differential bit encoding. This is due to the fact that known training sequences are periodically inserted for channel estimation, after which the phase drift is reset to 0, providing the initial phase value. However, if square mQAM formats are considered, blind PNE algorithms can only estimate the phase wrapped in the interval  $[-\pi/4, \pi/4]$ . As a result, a phase tracking scheme is required for phase unwrapping to avoid the phase uncertainty issue. This can be done with a feedback loop (FL) or a digital phase tracking (DPT) algorithm implemented in a feed forward architecture.

**Feedback loop** In CO-OFDM systems, due to the relatively long symbol duration, one symbol-delay feedback loop can be effectively applied for phase tracking as shown in Fig. 3.5. In this case, the laser phase noise is compensated in a two-stage algorithm. In the first stage, the received  $m$ th OFDM symbol is first rotated using the estimated CPE from the previous symbol as

$$Z_m^1(k) = Z_m(k) \exp(-j\Phi_{m-1}) = X_m(k) \exp(-j\Delta\Phi_m) + \chi_m(k) \exp(-j\Phi_{m-1}) \quad (3.24)$$

where  $\Delta\Phi_m$  is the residual CPE after equalization. Note that this equalization stage does not change the noise statistics and variance as  $\chi_m(k)$  is Gaussian distributed. As a result, adding this equalization stage does not affect the performance of blind PNE algorithms. In the second stage of equalization, the residual CPE is estimated, compensated for and the phase is tracked as:

$$\Phi_m = \Phi_{m-1} + \Delta\Phi_m \quad (3.25)$$

Note that in this scheme, the phase can only be tracked if the residual CPE  $\Delta\Phi_m$  after equalization lies in the interval  $[-\pi/4, \pi/4]$ . Otherwise, phase cycle slip occurs, which

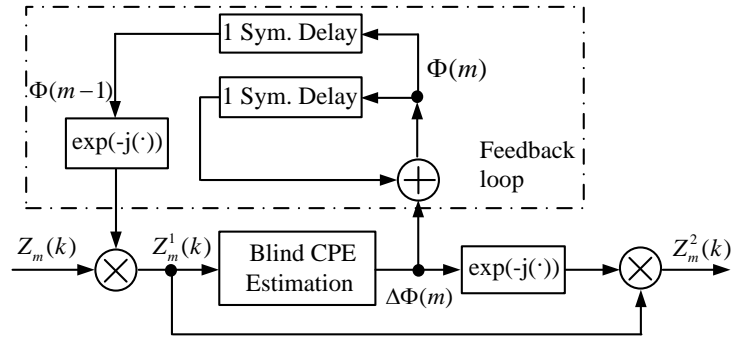


**Figure 3.5:** Block diagram of blind PNE with a feedback loop for phase tracking.

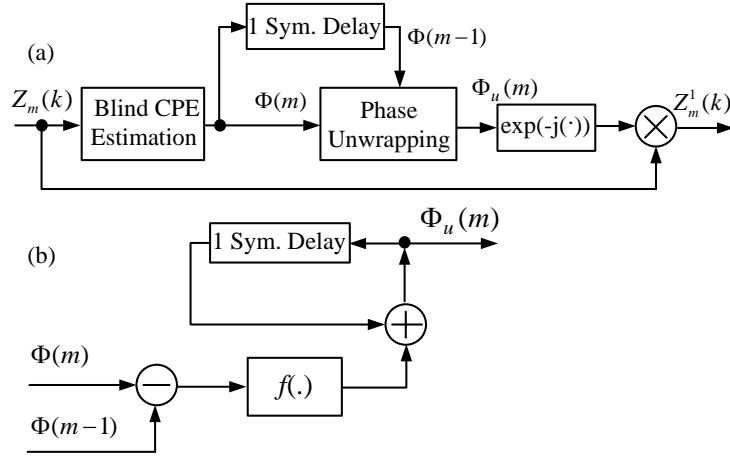


**Figure 3.6:** (a) block diagrams of (a) blind PNE schemes without feedback loop, (b) phase unwrapping block.

may lead to a catastrophic failure at the receiver.

**Digital phase tracking** The evolution of laser phase noise can also be tracked without a feedback loop using the following digital phase tracking algorithm

$$\Phi_m^u = \Phi_m + \sum_{k=1}^m f(\Phi_k - \Phi_{k-1}), \quad (3.26)$$

where the function  $f(x)$  keeps count of the phase cycles and is defined as:

$$f(x) = \begin{cases} \pi/2, & x < -\pi/4 \\ 0, & |x| \leq \pi/4 \\ -\pi/2, & x > \pi/4 \end{cases} \quad (3.27)$$

The general implementation block diagrams of blind PNE schemes without feedback loops and the phase unwrapping block are shown in the Fig. 3.6. This scheme employs only a single stage of compensation, and thus, can be much more computationally efficient in comparison to the previous scheme with FL. It can also be shown that the DPT algorithm (18) will fail if  $\Phi_m - \Phi_{m-1}$  lines outside in the interval  $[-\pi/4, \pi/4]$ .

**Cycle slip probability** For mQAM formats, it has been discussed above that phase tracking algorithm may fail if the difference between the CPEs of the two neighbouring OFDM symbols ( $\Phi_m - \Phi_{m-1}$ ) line outside the interval  $[-\pi/4, \pi/4]$ , leading to phase cycle-slip. As the laser phase noise  $\phi(t)$  is modelled as a Wiener process,  $\Phi_m - \Phi_{m-1}$  can be modeled as a random Gaussian distributed variable with zero mean and a variance  $\sigma^2 = 2\pi\nu T_s$ . As a result, the phase cycle-slip probability of blind PNE schemes can be calculated as

$$Ptr = 2Q\left(\frac{\pi}{4\sigma}\right) = 2Q\left(\frac{\pi}{4\sqrt{2\pi\nu T_s}}\right), \quad (3.28)$$

where  $Q$  is the Q-function,  $\nu$  is the combined laser linewidth,  $T_s$  is the total OFDM symbol duration including CP.

The cycle slip probability is shown in Fig. 3.7 as a function of the symbol duration linewidth product  $\nu T_s$ . In CO-OFDM systems, when cycle slip occurs it causes all bits to be in error until the end of the OFDM frame, where the phase drift is reset due to training sequence. For single carrier transmission, an acceptable cycle slip probability (without requiring differential logical detection) might be  $10^{-18}$  [58]. However, in CO-OFDM systems, because of training sequence, an acceptable cycle slip probability can be much higher. It has been shown in [50] that occurrence of cycle slip has little influence on the performance provided that is at least two order of magnitude less than the BER. As a result, for CO-OFDM system employing soft-decision FEC, it can be concluded that an acceptable cycle slip probability might be  $10^{-5}$ . As shown in Fig. 3.7, the cycle slip probability of  $10^{-5}$  occurs at  $\nu T_s = 5 \times 10^{-3}$ .

This particularly highlights the challenge for implementing blind PNE techniques in CO-OFDM systems with long symbol duration. As shown in Fig. 3.8, when the OFDM

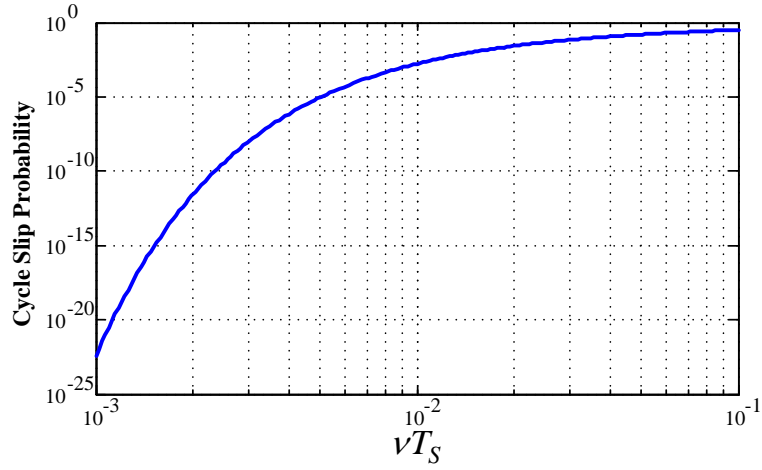


**Figure 3.7:** Phase cycle-slip probability as a function of symbol-duration-linewidth product in CO-OFDM systems with blind PNE.

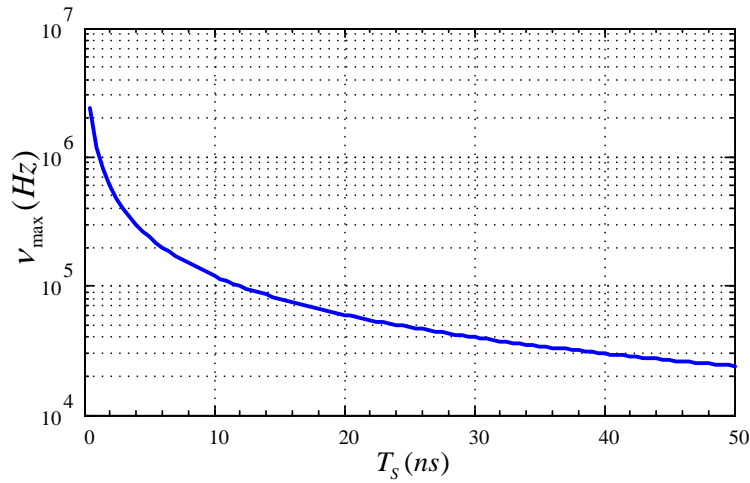


**Figure 3.8:** Maximum allowable laser linewidth as a function of symbol duration for implementing blind PNE in CO-OFDM systems.

symbol duration  $T_S=10$  ns, the laser linewidth  $\beta$  must be below 500 kHz in order to implement a fully blind PNE technique without differential bit encoding. However, for such systems, differential bit encoding and cycle slip can also be effectively avoided with quasi-blind PNE techniques where two bits are allocated in each OFDM symbol for phase tracking after blind PNE. This simple technique does not reduce the spectral efficiency and increase the complexity while significantly relaxing the requirements for transceivers lasers. The linewidth requirement of quasi-blind PNE technique is out of scope of this chapter and is open for future research.

### 3.3.2 Decision directed free PNC

In this section, a detailed theoretical analysis of the DDF blind PNE technique [56, 57] is provided. This technique uses the following cost function, which is the mean value of the squared product of the projections of real and imaginary parts after rotation by a phase angle  $\varphi$ :

$$J_1(\varphi) = E \left\{ \Re(Z_m(k) \exp(-j\varphi))^2 \Im(Z_m(k) \exp(-j\varphi))^2 \right\}_k \quad (3.29)$$

where  $E$  stands for the averaging operation over a portion or all of the subcarriers in the  $m$ th symbol. For squared QAM formats (e.g. QPSK, 16QAM, 32QAM) with identical probabilities of constellation points, the proposed cost function reaches its maximum value at  $\varphi = \Phi_m$ . This phenomenon can be explained by the fact that ideal squared QAMs provide a balance between the real and imaginary parts of constellation points, thus, maximizing the mean value of the squared product of the projections of real and imaginary parts [56, 57]. A similar cost function called dispersion minimization derotator, which is the dispersion of the projection of the constellation onto the real axis, was also considered in [59].

In a similar way with [59], the well-known stochastic gradient algorithm can be applied to maximize the cost function (3.29)

$$\begin{aligned} \varphi_{k+1} = & \varphi_k + \mu E \{ \Re(Z_m(k) \exp(-j\varphi)) \Im(Z_m(k) \exp(-j\varphi)) \} \\ & \times \left[ \Im(Z_m(k) \exp(-j\varphi))^2 - \Re(Z_m(k) \exp(-j\varphi))^2 \right] \end{aligned} \quad (3.30)$$

which exploits the fact that

$$\begin{aligned} (\partial/\partial\varphi) \Re(Z_m(k) \exp(-j\varphi)) &= \Im(Z_m(k) \exp(-j\varphi)) \\ (\partial/\partial\varphi) \Im(Z_m(k) \exp(-j\varphi)) &= -\Re(Z_m(k) \exp(-j\varphi)) \end{aligned} \quad (3.31)$$

However, stochastic gradient algorithm usually requires tens of iterative steps upon convergence. In this case, the complexity is still an issue, especially in high-speed RGI CO-OFDM systems. Therefore, it is desirable to calculate the CPE without iterative algorithms. It will be shown that this is possible using the cost function (3.29). Herein, the

analysis is focused on square QAM formats. If the probabilities of constellation points are identical, which usually the case for modern transmission systems, it is easily to show that the following assumptions are valid [59].

***Assumptions***

1. The second cross-moment is separable, i. e.,

$$E \left\{ \Re(X_m(k))^2 \Im(X_m(k))^2 \right\} = E \left\{ \Re(X_m(k))^2 \right\} E \left\{ \Im(X_m(k))^2 \right\} \quad (3.32)$$

2. Most cross-moments vanish

$$E \left\{ \Re(X_m(k))^h \Im(X_m(k))^s \right\} = 0 \quad (3.33)$$

if  $h \neq 2, s \neq 2$  and  $0 < h, s \leq 3$

3. The variances of the real and imaginary parts of the signal are the same

$$E \left\{ \Re(X_m(k))^2 \right\} = E \left\{ \Im(X_m(k))^2 \right\} \quad (3.34)$$

4.  $X_m(k)$  and  $\chi_m(k)$  are statistically independent

Under these assumptions, straightforward calculations show that

$$J_1(\varphi) = \frac{P_X^2}{8} \cos(4\varphi - 4\Phi_m) + \frac{P_X^2}{8} + \frac{1}{2} P_X \sigma_\chi^2 + \frac{1}{4} \sigma_\chi^2 \quad (3.35)$$

As a result, the cost function  $J_1(\varphi)$  can be written in this form

$$J_1(\varphi) = A \cos(4\varphi - 4\Phi_m) + B \quad (3.36)$$

where  $A, B, \Phi_m$  are three variables to be determined. Knowing the form of the cost function, the CPE ( $\Phi_m$ ) can be easily defined using just three test phases, for example,  $0, \pi/4$

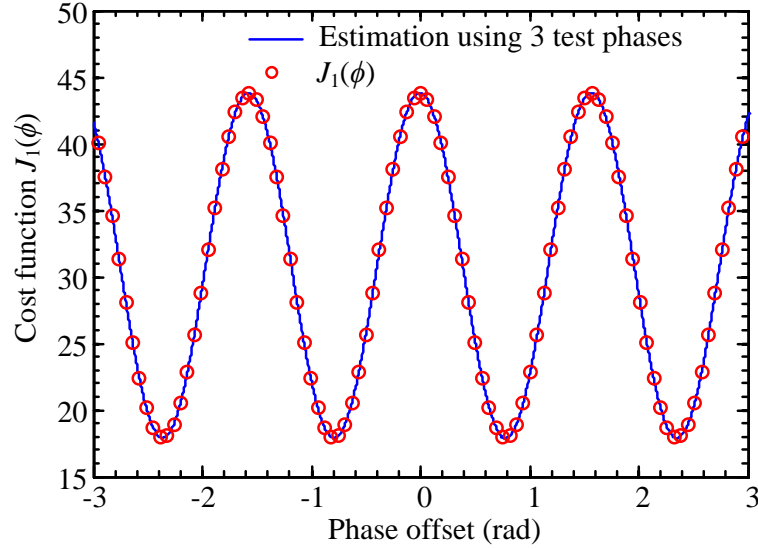


**Figure 3.9:** Calculated cost function  $J_1(\varphi - \Phi_m)$  and its estimations using three test phases as function of phase offsets for 16QAM with  $N = 200$  subcarriers and 6 dB.

and  $\pi/8$  as follows:

$$\begin{aligned}
 B &= (J_1(0) + J_1(\pi/4)) / 2 \\
 A &= \sqrt{(J_1(0) - B)^2 + (J_1(\pi/8) - B)^2} \\
 \Phi_m &= 0.25 \operatorname{sgn}(B - J_1(\pi/8)) \operatorname{acos}((J_1(0) - B) / A)
 \end{aligned} \tag{3.37}$$

where  $\operatorname{sgn}()$  is the sign function. The calculated cost function  $J_1(\varphi)$  and its estimation using 3 test phases for 16-QAM with a SNR of 6 dB and a typical value of subcarrier  $N = 200$  are compared in Fig. 3.9, showing no mismatch. Similar results (not shown here) were obtained for QPSK, 32QAM and 64QAM. This confirms that the cost function  $J_1(\varphi)$  can be very well approximated using three parameters  $A$ ,  $B$ ,  $\Phi_m$  as shown in Eq. 3.36. As a consequence, with DDF blind PNE technique, the CPE can be effectively calculated using only three test phases regardless of the modulation formats. This significantly reduces the implementation complexity in comparison with BPS, where 16-32 tests phases are required, depending on modulation formats. To calculate the cost function  $J_1(\varphi)$ , 3 real multiplications per symbol are required. To further reduce the implementation complexity, two novel cost functions with similar properties are proposed:

$$J_1(\varphi) = E \{ |\Re(Z_m(k) \exp(-j\varphi))| |\Im(Z_m(k) \exp(-j\varphi))| \}_k \tag{3.38}$$

$$J_1(\varphi) = E \{ |\Re(Z_m(k) \exp(-j\varphi))| + |\Im(Z_m(k) \exp(-j\varphi))| \}_k \quad (3.39)$$

Unfortunately, there are no simple close-form expressions for the two cost functions  $J_2(\varphi)$  and  $J_3(\varphi)$ . However, in a similar way to  $J_1(\varphi)$ , the cost functions  $J_2(\varphi)$  and  $J_3(\varphi)$  reach their maximum values at  $\varphi = \Phi_m$  for squared QAM formats. In addition, both cost functions  $J_2(\varphi)$  and  $J_3(\varphi)$  can be approximated well using the Eq. 3.36. As a result, the CPE can also be defined with the help of  $J_2(\varphi)$  and  $J_3(\varphi)$  using Eq. 3.37 with reduced complexities. To calculate the cost function  $J_2(\varphi)$  only one real multiplication/symbol is required thus, reduces the complexity by 3 times in comparison to  $J_1(\varphi)$ . Furthermore, in the case of  $J_3(\varphi)$ , no multiplications are required, offering very low complexity in implementation. However, the complexity reductions associated with the use of the cost functions  $J_2(\varphi)$  and  $J_3(\varphi)$  also come with a price. As shown in Fig. 3.10 the deviations of the calculated and approximated functions for  $J_2(\varphi)$  and  $J_3(\varphi)$  can be observed. This mismatch can degrade the performance of DDF PNE techniques employing  $J_2(\varphi)$  and  $J_3(\varphi)$ .

The root-mean-square-error (RMSE) of CPE as a function of SNR for DDF blind PNE techniques employing  $J_1(\varphi)$ ,  $J_2(\varphi)$  and  $J_3(\varphi)$  for 16QAM CO-OFDM transmission with 100 subcarriers are presented in Fig. 3.11. Herein, the RMSE is calculated using Monte-Carlo simulation with 10000 runs. In Fig. 3.11, the best performance is achieved with  $J_1(\varphi)$ , showing that a small RMSE of 0.1 rad can be achieved at SNRs  $> 5.3$  dB. This result clearly indicates the high tolerance of the DDF blind PNE technique to Gaussian noise. However, when  $J_2(\varphi)$  and  $J_3(\varphi)$  are employed the required SNRs for a RMSE of 0.1 rad are 5.8 dB (0.5 dB SNR penalty) and 6.8 dB (1.5 dB SNR penalty), respectively. However, the SNR penalties associated with the uses of  $J_2(\varphi)$  and  $J_3(\varphi)$  reduce if the number of subcarrier  $N$  is increased. As shown in Fig. 3.12, at a low value of  $N$  of 50, the SNR penalties of  $J_2(\varphi)$  and  $J_3(\varphi)$  are 1.1 dB and 2.4 dB, respectively. However, if  $N = 1000$ , SNR penalties of  $J_2(\varphi)$  and  $J_3(\varphi)$  are reduced to only 0.1 dB and 0.3 dB, respectively. This result indicates that if the number of OFDM subcarrier is large,  $J_2(\varphi)$  and  $J_3(\varphi)$  can be used efficiently instead of  $J_1(\varphi)$  to offer a very low complexity blind PNE.

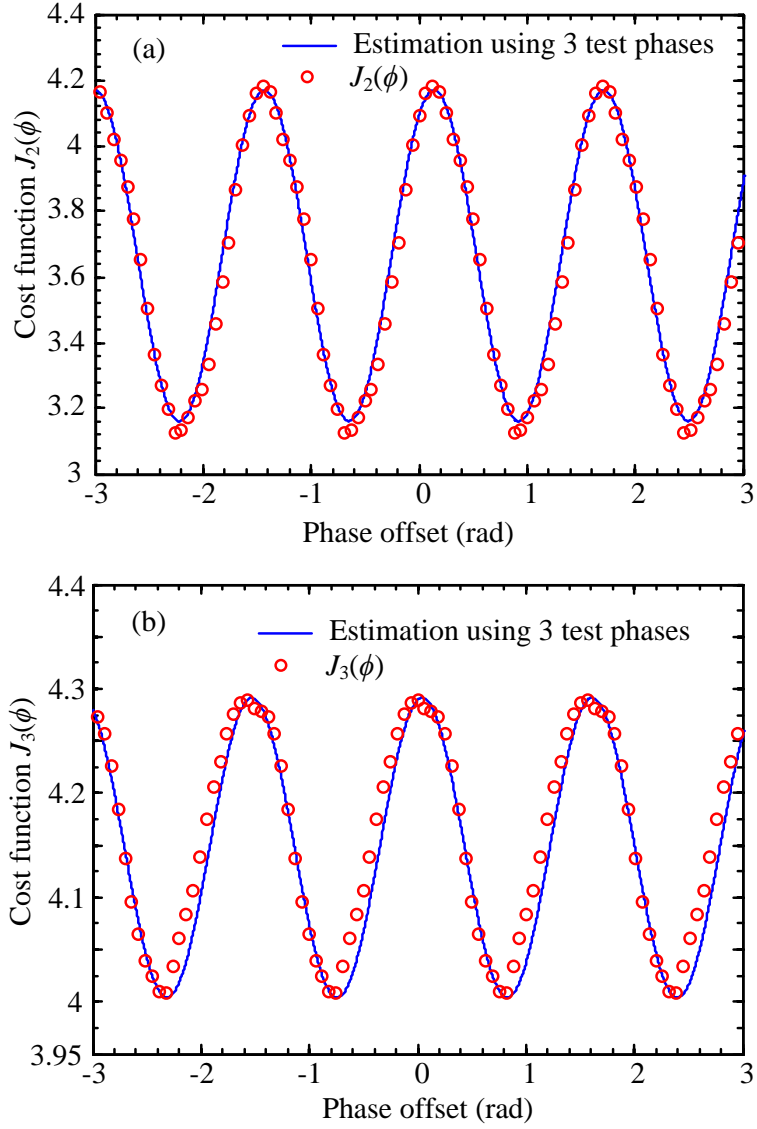


**Figure 3.10:** Calculated cost functions  $J_2(\varphi - \Phi_m)$ ,  $J_3(\varphi - \Phi_m)$  and its estimations using three test phases as function of phase offsets for 16QAM with  $N = 200$  subcarriers and  $SNR = 6$  dB.

### 3.3.3 Performance comparison

In this section, through numerical simulation, the performance of DDF blind PNE technique with different cost functions is compared with BPS and pilot-aided techniques. The discussion is focused on high order modulation formats, namely 16QAM and 64QAM. It has been shown experimentally in [56] that DD-based blind PNE technique performs poorly for such high modulation formats. As a result, DD blind PNE was not taken into account in the comparison. For investigation the performance of blind PNE techniques for CO-OFDM systems, there are two critical parameters, namely the number of OFDM subcarriers  $N$  and the symbol duration linewidth product  $\nu T_S$ . In this simulation,  $\nu T_S$  is

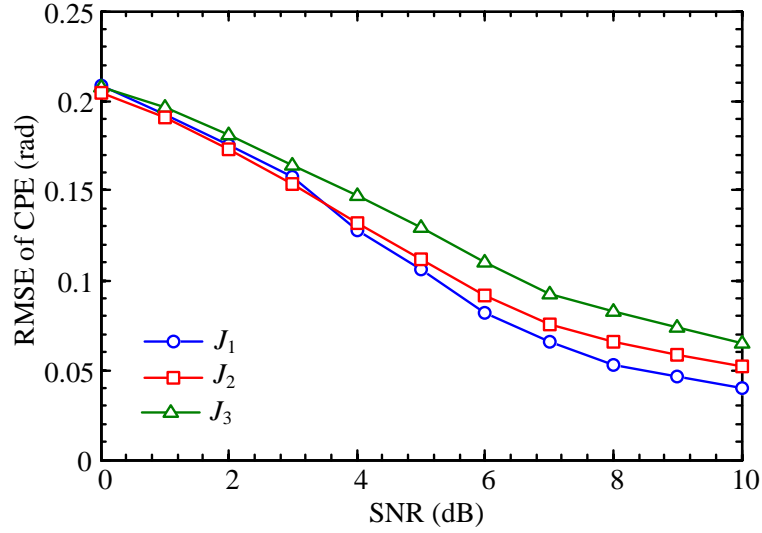


**Figure 3.11:** Root-mean-square-error (RMSE) of CPE as a function of SNR for DDF PNE techniques employing  $J_1(\varphi)$ ,  $J_2(\varphi)$  and  $J_3(\varphi)$  for 16QAM CO-OFDM transmission with  $N = 100$  subcarriers.

varied by varying the laser linewidth while the OFDM symbol duration is kept constant at 10 ns, which is equivalent to a subcarrier spacing of 100 MHz. The system BER is evaluated through direct error counting using Monte Carlo simulation with a total number of symbols of  $2 \times 10^5$  ( $8 \times 10^5$ ,  $1.2 \times 10^6$  bits for 16QAM and 64QAM, respectively). In the light of (3.15), only the back-to-back transmission regime is taken into account here for simplicity to study the tolerance of PNE techniques to AWGN and laser linewidth. The simulation results for 16QAM and 64QAM are presented in Fig. 3.13- Fig. 3.15.

In Fig. 3.13(a), the BER performances of PNE techniques, including PA-aided with 16 pilots, BPS with 16 test phases and DDF blind with FL, DPT and different cost functions are compared for  $\nu T_S = 5 \times 10^{-3}$  and  $N = 200$ . It can be seen that FL and DPT offer the same performance in all considered blind PNE techniques. Taking into account the fact that DPT is much more computationally efficient for practical implementations, only DPT is further considered. In Fig. 3.13(a), DDF blind with the cost function  $J_1(\varphi)$  shows the same performance in comparison to the complicated BPS with 16 test phases. This confirms the high performance of DDF blind PNE technique. Even though the complexity of DDF blind with  $J_1(\varphi)$  is relatively low in comparison to BPS, different cost functions, namely  $J_2(\varphi)$  and  $J_3(\varphi)$  can also be effectively applied to reduce further the complexity. In Fig. 3.13(a), DDF blind with  $J_2(\varphi)$  shows a similar performance in comparison to PA-

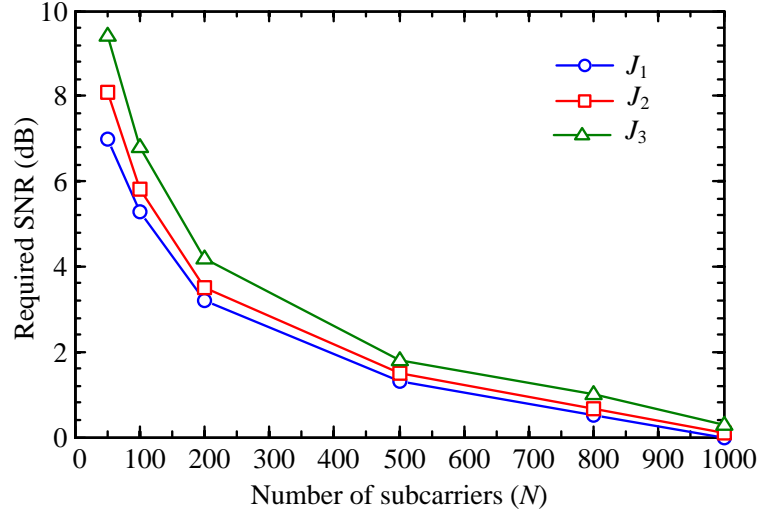


**Figure 3.12:** Required SNRs for a RMSE of 0.1 rad as a function of number of subcarriers ( $N$ ) for DDF PNE techniques employing  $J_1(\varphi)$ ,  $J_2(\varphi)$  and  $J_3(\varphi)$  for 16QAM CO-OFDM transmission.

aided with 16 pilots. On the other hand, the implementation of DDF blind with  $J_3(\varphi)$  leads to  $\sim 1$  dB SNR penalty at a BER level of  $10^{-3}$ .

Similar results for 64QAM for  $\nu T_S = 2 \times 10^{-3}$  is shown in Fig. 3.13(b). Here DDF with  $J_1(\varphi)$  also offers a similar performance in comparison to BPS. However, for 64QAM, the effectiveness of blind PNE technique is reduced as DDF blind with  $J_1(\varphi)$  and BPS does not offer significant performance advantage over PA-aided with 16 pilots. However, blind PNE techniques are still attractive here because of the high spectral efficiency offered. The constellation diagrams for 16QAM at  $SNR = 23$  dB before and after phase compensation with different PNE techniques are shown in Fig. 3.14.

The power penalties at a BER of  $10^{-3}$  as functions of  $\nu T_S$  for PA-aided, BPS and DDF blind PNE with different cost functions for 16QAM transmission with 200 subcarriers are shown in Fig. 3.15(a). At 1 dB SNR penalty, the linewidth tolerance of BPS and DDF blind with  $J_1(\varphi)$  is  $\nu T_S = 4 \times 10^{-3}$ . For DDF blind with  $J_2(\varphi)$  and  $J_3(\varphi)$  the linewidth tolerances are  $\nu T_S = 2 \times 10^{-3}$  and  $\nu T_S = 10^{-3}$ , respectively.

When the number of OFDM subcarrier is reduced to 100, DDF blind with  $J_1(\varphi)$  still shows excellent performance, with a similar linewidth tolerance to the case of 200 subcarriers. However, the performances of DDF blind with  $J_2(\varphi)$  and  $J_3(\varphi)$  degrade significantly. At 1 dB SNR penalty, the linewidth tolerance of DDF blind with  $J_2(\varphi)$  in this case is  $\nu T_S = 5 \times 10^{-4}$  while 1 dB SNR penalty even cannot be achieved with DDF blind with

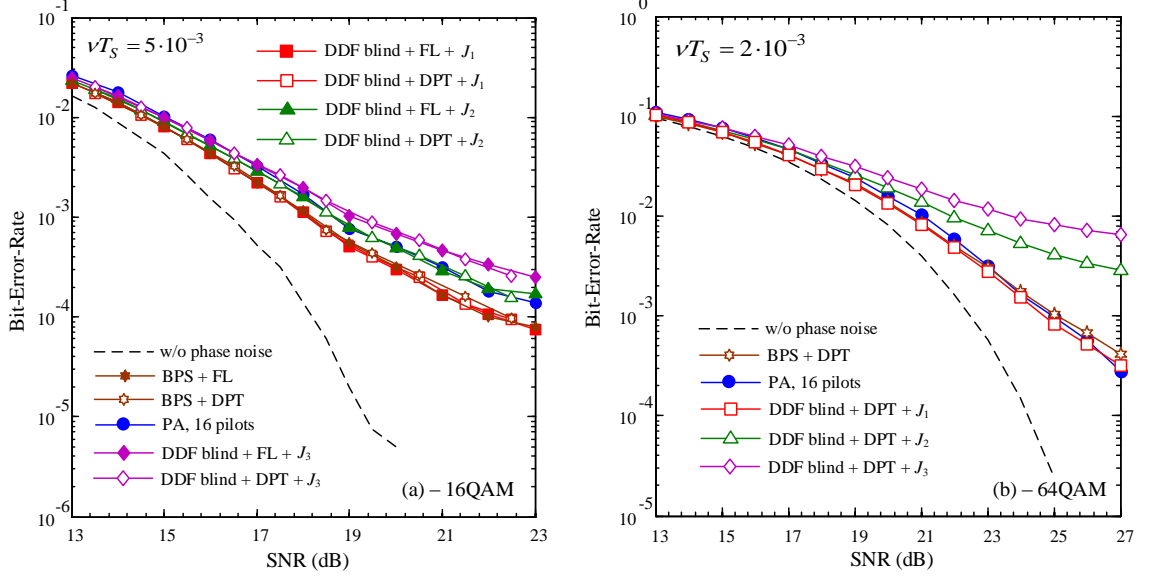


**Figure 3.13:** a) BER performances of PNE techniques, including PA-aided with 16 pilots (blue), BPS with 16 test phases (brown) and DDF blind PNE with different cost functions (red-  $J_1(\varphi)$ , green-  $J_2(\varphi)$ , pink-  $J_3(\varphi)$ ) with feedback loop (solid) and digital phase tracking (open) for 16QAM, the symbol duration linewidth product is  $5 \times 10^{-3}$ ; (b) BER performance of the same PNE (only showing digital phase tracking) for 64QAM, the symbol duration linewidth product is  $2 \times 10^{-3}$ .

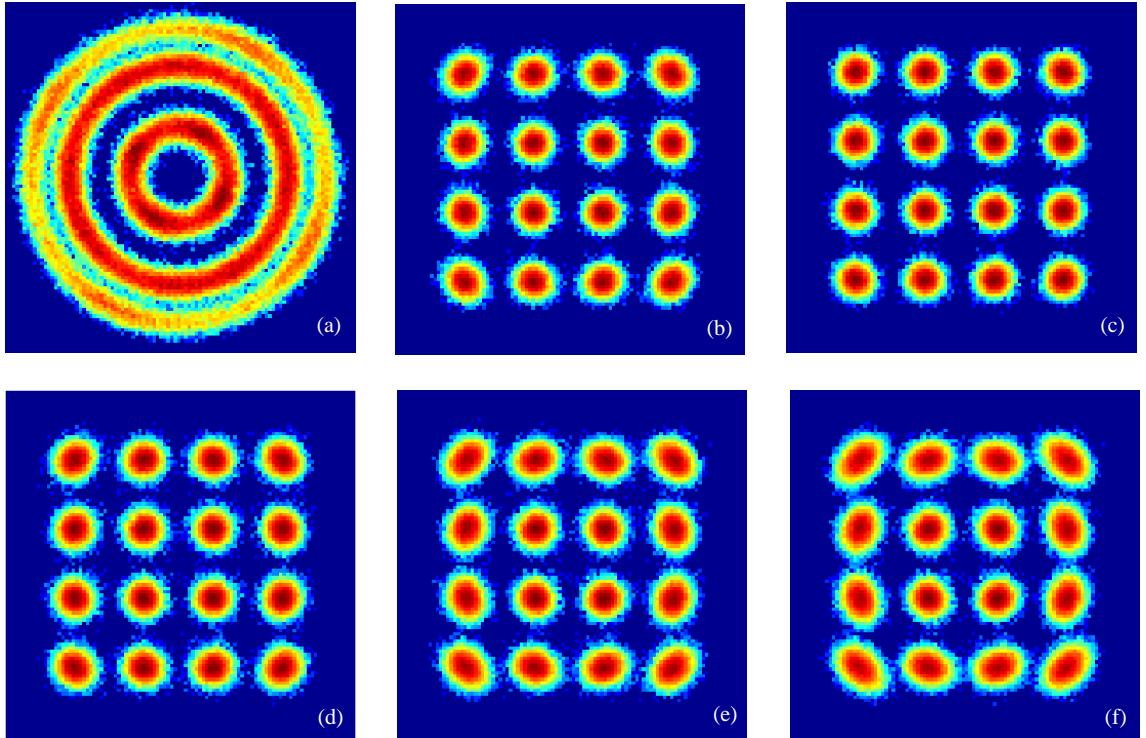


**Figure 3.14:** Constellation diagrams for 16QAM at a SNR of 23 dB, before PNE (a), after PNE using PA-aided technique with 16 pilots (b), after PNE with DDF blind PNE technique with digital phase tracking and  $J_1(\varphi)$  (c), after PNE using BPS with 16 test phases (d), after PNE DDF blind PNE technique with digital phase tracking and  $J_2(\varphi)$  and  $J_3(\varphi)$  (e, f).

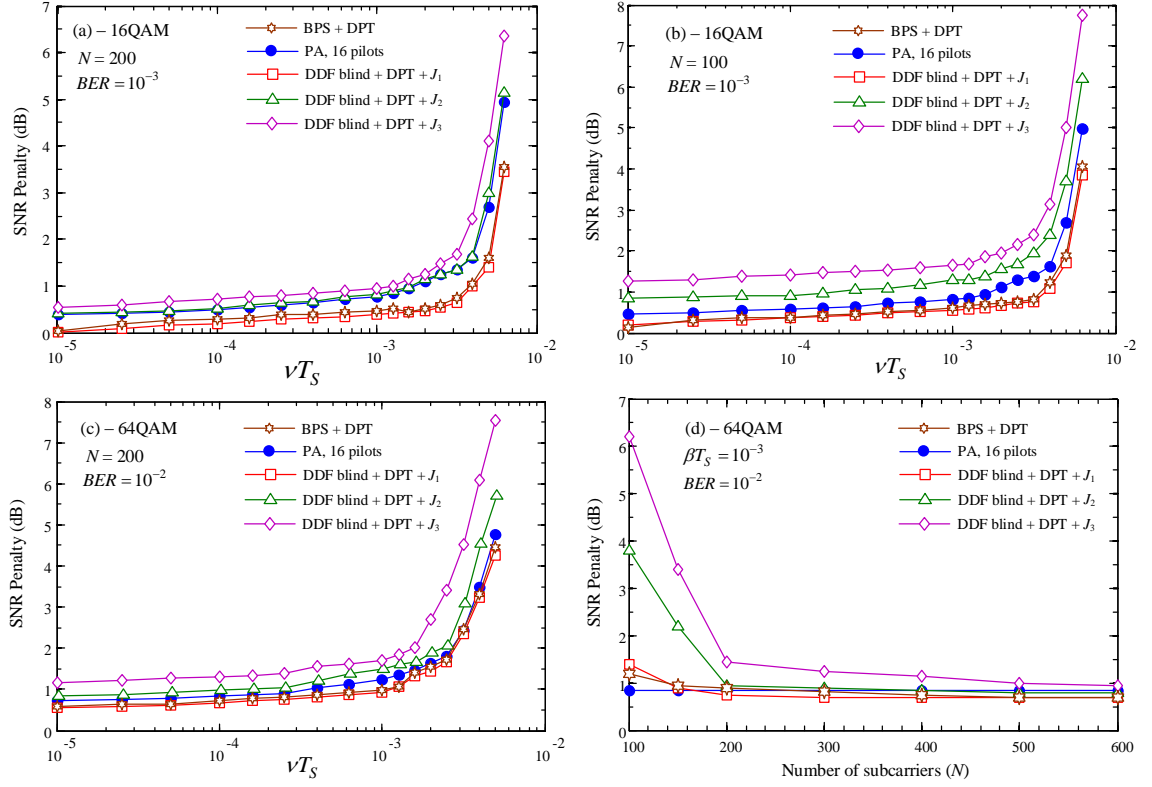


**Figure 3.15:** The SNR penalty at a BER of  $10^{-3}$  as a function of  $vT_S$  for PA-aided, BPS and DDF blind PNE with different cost functions for 16QAM transmission with 200 subcarriers; (b) similar result for 16QAM and 100 subcarriers; (c) similar result for 64QAM at a BER of  $10^{-2}$  and 200 subcarriers; (d) SNR penalty as a function of  $N$  at a BER of  $10^{-2}$  for 64QAM and  $T_S$  of  $10^{-3}$ .

$J_3(\varphi)$  for  $vT_S > 10^{-5}$ . This indicates that DDF blind with  $J_3(\varphi)$  is not suitable for a low value of  $N$ .

Similar results for 64QAM at a BER of  $10^{-2}$  and  $N = 200$  are shown in Fig. 3.15(c). At 1 dB SNR penalty, the linewidth tolerance of DDF blind with  $J_1(\varphi)$  in this case is  $vT_S > 10^{-3}$ . The SNR penalties as functions of  $N$  at a BER of  $10^{-2}$  for 64QAM and  $vT_S$  of  $10^{-3}$  are shown in Fig. 3.15(d). It should be noted, unlike other blind PNE techniques, the performance of PA-aided technique is independent of  $N$ . Blind phase search and DDF blind with  $J_1(\varphi)$  show excellent performance when  $N > 100$ . On the other hand, DDF blind with  $J_2(\varphi)$  and  $J_3(\varphi)$  should be considered only if  $N$  is equal or bigger than 200.

### 3.3.4 Complexity comparison

Herein, the complexities BPS and DDF blind PNE techniques are compared in term of the required number of real multipliers, adders, comparators and decisions. The root-square

| PNE                 | Multipliers | Adders     | Comparators | Decisions    |
|---------------------|-------------|------------|-------------|--------------|
| BPS                 | $4N_1M$     | $2N_1M$    | $M_1 + 1$   | $N_1M + N_1$ |
| DDF+ $J_1(\varphi)$ | $9N_1 + 4$  | $3N_1 + 4$ | 0           | 0            |
| DDF+ $J_2(\varphi)$ | $3N_1 + 4$  | $3N_1 + 4$ | 0           | 0            |
| DDF+ $J_3(\varphi)$ | 4           | $3N_1 + 4$ | 0           | 0            |

**Table 3.1:** Complexities of DDF and BPS Blind PNE Techniques

operation is counted as one multiplier. The result is shown in the Table I, where  $M$  is the number of test phases in BPS and  $N_1 \leq N$  is the number of subcarriers used for PNE. The required real multipliers for DDF blind PNE with  $J_1(\varphi)$  and  $J_2(\varphi)$  are around 7 and 21 times less than those of BPS with 16 test phases. The numbers of adders are also reduced by 10 times. In addition, DDF blind PNE does not require any comparators and decisions. This clearly indicates that DDF blind PNE is much more computational efficient than BPS.

### 3.4 Multiplier-free blind PNE for CO-OFDM

As discussed in the previous section, DDF blind is an effective blind PNE technique due to its high performance and relatively low complexity in comparison to BPS as only three test phases are required. However, in DDF blind technique multiplications are still required, which usually utilize a huge amount of hardware resources. As a result, a high performance, MF blind PNC technique is still desirable for realizing an efficient hardware implementation.

In this section, a novel MF blind PNC technique for QPSK and 16QAM CO-OFDM transmissions is demonstrated based on statistical properties of the received symbols phases, without requiring DD algorithm [60]. The proposed PNC technique also provides a comparable performance with DDF blind and BPS PNC techniques.

In order to realize a multiplier-free system, the polar coordinates instead of Cartesian is considered. It has been shown in [27] that, in the presence of fibre nonlinearity and laser phase noise, for each transmitted constellation point the received phase  $\varphi_m(k)$  is Gaussian distributed. As a result, the CPE can be estimated by calculating the mean value of the received phases for each constellation point. However, this approach requires a decision

directed algorithm, and thus suffers from error propagation for large phase noises. To avoid error propagation, we propose the removal of symbols with high error probabilities from the calculation. In other words, only symbols with lowest error probabilities (symbols in the interval with highest probability density or the most populated bin (MPB)) should be considered. In Bayesian statistics, the MPB is also referred as the credible interval.

In practical implementations, the MPB with a width of  $\alpha$  can be estimated using a simple scanning algorithm as shown in Fig. 3.16, where the scanning bin is moved from the left to the right (within a predefined range) with a small scanning step of  $\Delta\alpha$  ( $L_{k+1} = L_k + \Delta\alpha$ ). At each step, the number of symbols phases falling into the scanning bin is calculated ( $P_k$ ) and the MPB is then defined as the bin providing the largest number of samples ( $P_k$ ). This algorithm requires only comparator and counting operators, thus offering very low implementation complexity. The block diagram of the proposed MF blind PNC technique

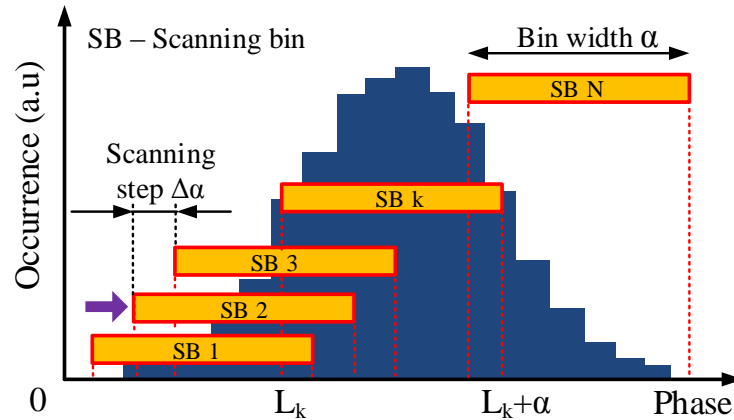


**Figure 3.16:** Estimating the MPB with a bin width of  $\alpha$  using the scanning algorithm with overlapping bins and small scanning step. The histogram with small bin width is also shown.

is shown in Fig. 3.17 for 16QAM. For QPSK signal the amplitude partitioning block can be removed. The proposed scheme can be described in 4 steps. In the first step, the received  $m$ th OFDM symbol is converted to polar coordinates using CORDIC algorithm [61], which uses only bit shifts and additions. The phases are used in all following steps while the amplitude is needed only for partitioning in the case of 16QAM, where all the information symbols from the middle ring are removed. Second, the symbols phases are rotated using the estimated CPE of the previous OFDM symbol. This step is necessary to avoid cycle slip as blind PNC algorithms can only deal with a CPE in a range of width

$\pi/2$ . Next, all symbols phases are wrapped into the interval  $[0, \pi/2]$  using the  $\text{mod}(:, \pi/2)$  function, which is performed only by comparator and addition operations. Finally, the MPB is estimated and the residual CPE is then calculated as the mean value of the symbols phases in the MPB as:

$$\Delta \Phi_m = \Phi_m - \Phi_{m-1} = E \{ \varphi_m(k) \}_{\varphi_m(k) \in \text{MPB}} \quad (3.40)$$

To achieve the best performance the bin width ( $\alpha$ ) and scanning step ( $\Delta\alpha < \alpha$ ) should be optimized. If the bin width is too small, the number of symbols phases falling in the MPB is also small and the impact of Gaussian noise can be significant. If the bin width is too big, the MPB may include symbols with high error probabilities leading to error propagation. Note that  $\alpha = \pi/2$  corresponds to the DD algorithm, performed in the phase domain. In addition, the scanning step should be small enough so the MPB can be accurately estimated, but no smaller than necessary to minimize complexity. Typical

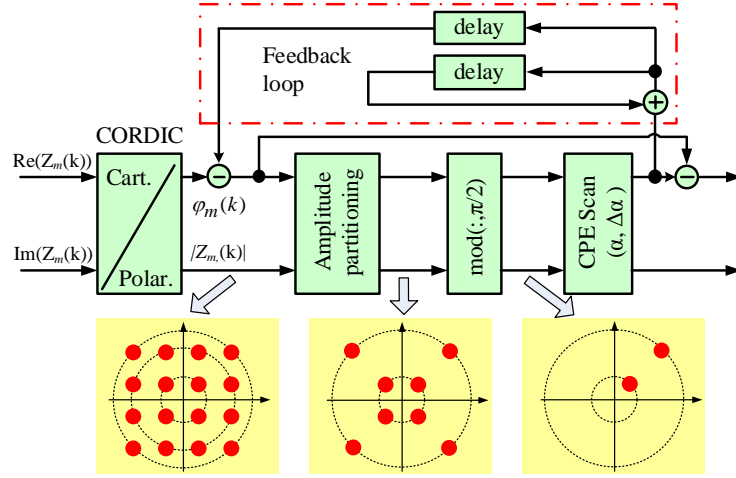


**Figure 3.17:** Block diagram of the proposed PNC technique for 16QAM CO-OFDM systems. For QPSK the amplitude partitioning block is not needed.

optimization results for  $(\alpha, \Delta\alpha)$  are shown in Fig. 3.18 for a 16QAM CO-OFDM system with 210 subcarriers and a symbol duration ( $T_s$ ) of 20.48 ns in the back-to-back case. The optimum value of bin width is found to be  $\sim \pi/8$  while  $\Delta\alpha$  can be as large as 0.15 for a value of  $\nu$  up to 600 kHz. At this optimum value of bin width, the proposed technique shows almost no penalty (less than 5% degradation in  $\log_{10}(\text{BER})$ ) in comparison to the case where the CPE is perfectly compensated by using all subcarriers as pilots (showed as

dash lines in Fig. 3.18) for all linewidths considered. This result clearly indicates the high performance of the proposed technique.

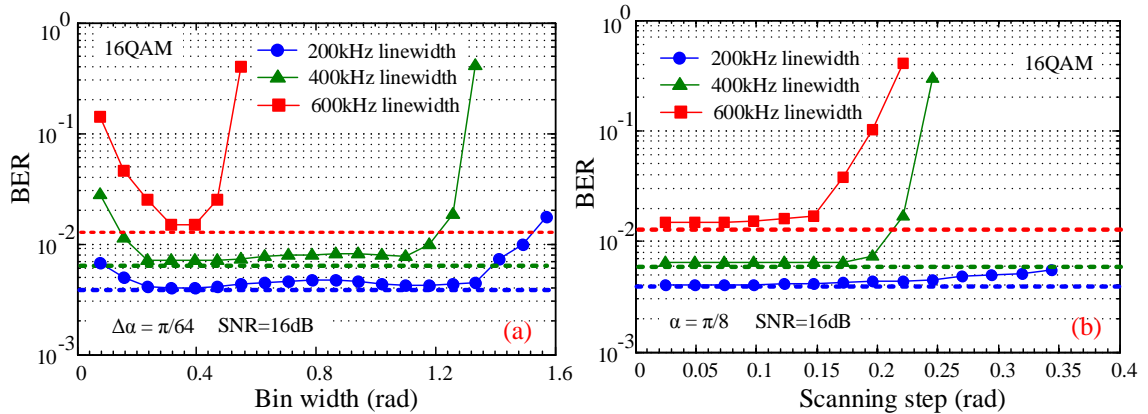


**Figure 3.18:** Impact of  $\alpha$  and  $\Delta\alpha$  on the performance of MF bind PNC technique in 16QAM CO-OFDM transmissions in back-to-back case. The dash lines show the BER performance when the CPE is perfectly compensated.

### 3.4.1 Experimental results and discussions

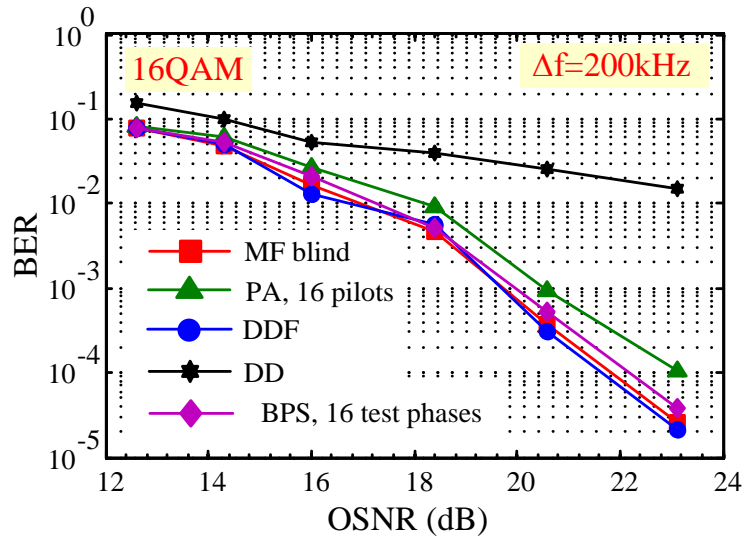


**Figure 3.19:** BER versus OSNR in back-to-back case for 40 Gb/s 16QAM CO-OFDM transmission.

To investigate the performance of QPA methods the same experimental setup was used as illustrated in Fig. 2.15 for QPSK and 16QAM formats. The proposed PNC scheme is compared with two-stage blind DD, DDF blind, BPS and pilot-aided (PA) methods in Fig. 3.19 and Fig. 3.20 for QPSK and 16QAM WDM CO-OFDM transmissions. In applying the proposed MF blind technique the optimisation parameters were chosen to be

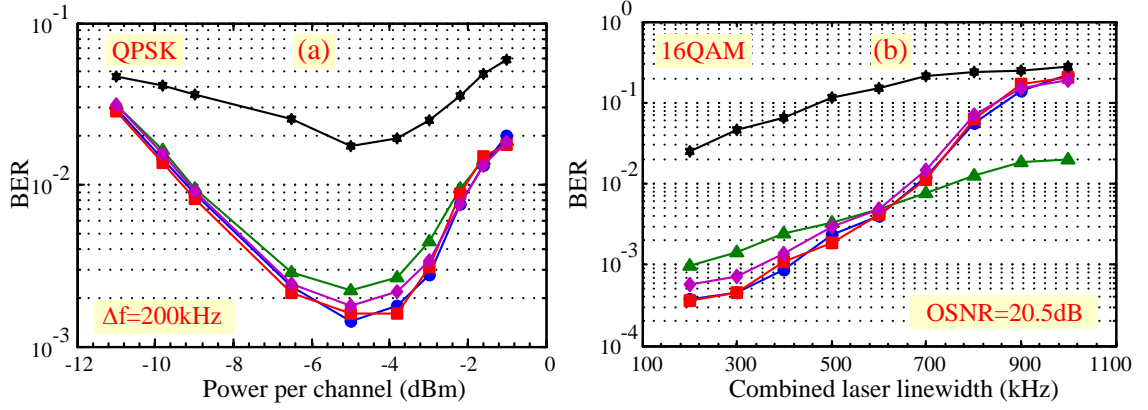


**Figure 3.20:** (a) BER versus power for 20 Gb/s QPSK transmission over 4000 km, (b) BER versus combined laser linewidth for 40 Gb/s 16QAM transmission in back-to-back case.

( $\alpha = \pi/8$ ,  $\Delta\alpha = \pi/64$ ). In this case, the MPB can be selected after 24 scanning steps. For comparison, alternative PNC techniques were considered and optimized according to [55, 62]. In Fig. 3.19 the proposed MF blind PNC technique outperforms PA with 16 pilots (7.6 % overhead) and shows a similar performance (less than 0.5 dB variation in the OSNR requirement at the BER of  $10^{-3}$ ) in comparison with highly complex BPS (16 test phases) and DDF blind. This clearly indicates that statistical digital signal processing techniques can be effectively applied for OFDM systems employing hundreds of subcarriers. In Fig. 3.20(b) all considered blind PNC techniques shows similar phase noise tolerance, degrading significantly if the residual CPE after the first equalization stage lies outside the range  $(\pi/4, \pi/4)$ . This indicates that the proposed MF blind PNC technique can be applied effectively, and without differential coding to systems with a combined laser linewidth up to 600 kHz ( $\nu T_s \sim 10^{-2}$ ).

### 3.5 Conclusion

Novel reduced complexity phase noise compensation techniques have been proposed for CO-OFDM transmission. By setting PSs in correlation with data subcarriers the overhead of pilot aided carrier phase estimation may be reduced by a factor of 2 for two different correlation techniques, namely conjugated pilots and phase parity pilots. In addition, in comparison with RF-pilot tone, the QPA methods can offer a similar performance at the same overhead while significantly reducing the complexity in implementation.

In addition, blind PNE can be effectively applied for CO-OFDM transmissions with BPS and DDF blind techniques. Using only three test phases, DDF blind PNE technique can offer a comparable performance in comparison with BPS with 16 tests phases, and thus, offering an effective solution for practical implementation. When the number of subcarriers is sufficient ( $N > 200$ ) the complexity of DDF blind can be further significantly reduced with two novel proposed cost functions.

Finally, based on the statistical properties of the received symbols phases an effective blind phase noise estimation technique for CO-OFDM systems can also be developed without any multiplications.

# Chapter 4

## Low-Complexity Fiber Nonlinearity

## Compensation Methods for CO-OFDM

**Son T. Le**, Mary E. McCarthy, Naoise Mac Suibhne, Andrew D. Ellis and Sergei K. Turitsyn, “Phase-conjugated Pilots for Fibre Nonlinearity Compensation in CO-OFDM Transmission,” *Journal of Lightwave Technology*, vol.33, no.5, pp.1-7, 2015 (**invited**).

**Son T. Le**, Mary E. McCarthy, Naoise Mac Suibhne, Mohammad A. Z. Al-Khateeb, Elias Giacomidis, Nick Doran, Andrew D. Ellis and Sergei K. Turitsyn, “Demonstration of Phase-conjugated Subcarrier Coding for Fiber Nonlinearity Compensation in CO-OFDM Transmission,” *Journal of Lightwave Technology*, vol.33, no.11, pp.2206-2212, 2015.

### 4.1 Introduction

Theoretically, the capacity of a fixed bandwidth Gaussian communication channel is logarithmically proportional to the signal-to-noise ratio [63]. As a result, the capacity of optical fibre communications channel should increase monotonically with the transmit signal power. However, the nonlinear distortion due to Kerr effect limits the maximum optical power that could be launched into an optical fibre (without degrading the system performance) [14, 64]. Fiber Kerr nonlinearity effect thus sets an upper bound on the achievable data rate in optical fibre communications using linear transmission techniques [14].

There have been extensive efforts in attempting to surpass the Kerr nonlinearity limit

through several nonlinearity compensation techniques and nonlinear transmission schemes [65–75]. digital back propagation (DBP) is an effective nonlinearity compensation method, which removes the nonlinear distortion by inverting the distorted signal at the receiver digitally, based on the fact that nonlinear impairment (signal-signal interaction, rather than signal-noise interaction is concerned) is a deterministic effect [68]. However, DBP has some serious challenges, limiting its success in practice so far. Firstly, accurate DBP requires a substantial increase in DSP complexity, proportional to the number of spans. Secondly, in WDM systems the effectiveness of DBP is significantly reduced as the neighbouring WDM channels are unknown to the compensator. In this case, only the impact of self-phase modulation, which only represents a minor part of the overall nonlinear impairment [14, 64], can be compensated. Finally, even though full band DBP could be achieved (with enormous complexity), it is still challenging to realize the full benefit of DBP because of PMD [76] and carrier frequency uncertainty problem [77] which leads to the incorrectness in optical field reconstruction. It has been shown in [77] that even a small carrier frequency deviation of 50 MHz can lead to a performance penalty of 2 dB. Talking into account the fact that commercial external cavity laser (ECL) can have a frequency deviation as much as several GHz, DBP seems to be unbeneficial for practical applications unless optical combs are employed at the transmitter [77].

Digital [78] and optical [67, 78, 79] optical phase conjugation (OPC) at the mid link or installed at the transmitter [80] are other well-known nonlinear compensation techniques that conjugate the signal phase after transmission in one segment of the link in order to achieve a net cancellation of the nonlinear phase shift using the nonlinearity generated in the second segment of the link. However, OPC modifies the transmission link by inserting a phase conjugator at the middle point of the link, and imposes significant symmetry conditions with respect to the phase conjugator, and thus, significantly reducing the flexibility in an optically routed network.

Recently, a breakthrough fibre nonlinearity compensation technique called phase conjugated twin wave (PCTW) has been proposed by X. Liu et al [81, 82]. PC-TW is a transponder-based technique that can be implemented with minimal additional optical hardware or DSP, providing a simple and effective solution in compensating optical fibre

nonlinearity. However, PCTW halves the SE, meaning that the maximum achievable SE in a PDM system with QPSK modulation format and PCTW scheme is only  $\sim 2$  bits/s/Hz, which is the same as those achieved in PDM BPSK transmission.

A modification of PCTW for coherent optical orthogonal frequency division multiplexing (CO-OFDM) exploring the Hermitian symmetry has also been proposed in [83], also at the cost of 50 % overhead. To address this drawback, a flexible nonlinear compensation scheme with the insertion of phase-conjugated pilots has been proposed for CO-OFDM in [84, 85]. This scheme allows the overhead to be adjusted (up to 50 %) according to the required performance gain, which is up to 4 dB. In this scheme, a portion of the OFDM subcarriers (up to 50 %) are transmitted as phase-conjugates of other subcarriers. The PCPs are used at the receiver to estimate the nonlinear distortion of their respective original subcarriers. The estimated distortion can also be used to compensate the nonlinear impairments in other subcarriers close to the PCP, thanks to the narrow OFDM subcarrier spacing (tens of MHz), which enhances the correlation between nonlinear phase shifts of neighbouring subcarriers. With this technique, the fibre nonlinearity impairments due to the Kerr effect in OFDM systems can be effectively compensated without the complexity of DBP or 50 % loss in capacity of PC-TW. The PCP technique can be effectively implemented in both single polarization and PMD systems, in both single channel and WDM systems. In other words, nonlinearity compensation using PCPs offers a simple, easy implementation applicable to any optical links where the level of nonlinear compensation may be readily tuned by selecting an appropriate number of PCPs.

In addition, a dual PCTW scheme combined with quadrature pulse shaping was also proposed for single carrier systems, yielding an improvement of  $\sim 1.2$  dB [86] without any overhead. Unfortunately, quadrature pulse shaping is required for dual PCTW, which cannot be applied effectively for multicarrier modulation formats such as CO-OFDM [87–89]. To address this issue, a PCSC scheme has been proposed in [90] by adopting the concept of dual PCTW to encoding and processing neighbouring OFDM subcarriers simultaneously. This proposed PCSC scheme can be effectively applied without any overhead and without suffering from the carrier frequency uncertainty problem, showing that performance gains of 1.5 dB and 0.8 dB for BPSK and QPSK transmissions, respectively.

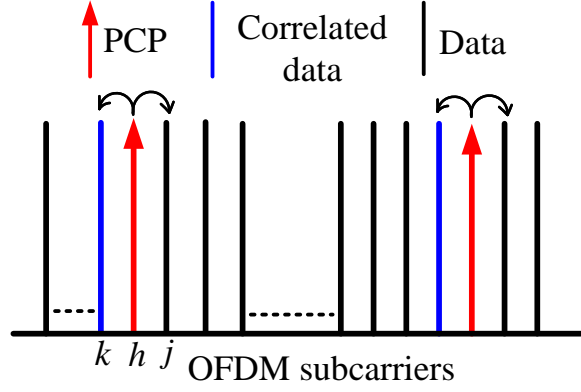


**Figure 4.1:** Inserting phase-conjugated pilots for fibre nonlinearity compensation.

In this chapter, the concepts of PCP and PCSC are discussed in details and effectiveness of PCP and PCSC techniques in WDM CO-OFDM transmissions with BPSK and QPSK modulation formats is experimentally demonstrated.

## 4.2 Phase conjugated pilots for fibre nonlinearity compensation in CO-OFDM transmission

### 4.2.1 Concept of PCP

Since the frequency spacing in an OFDM system is often small [91, 92] (tens of MHz) compared to the phase matching bandwidth of the link (few GHz [93]), at the end of the optical link, the nonlinear phase shifts on adjacent subcarriers will be strongly correlated. This implies that nonlinear distortion experienced in one spectral region may be used to estimate the distortion in other closely space regions, as observed in pilot tone compensation schemes [94]. Thus nonlinear compensation can be achieved by sparsely inserting PCPs across the OFDM band. The concept of inserting PCP is illustrated in the Fig. 4.1. Suppose the information symbol carried by the  $k$ th subcarrier is  $X(k) = A(k) \exp(j\varphi(k))$  where  $A(k)$  and  $\varphi(k)$  are the amplitude and the phase of this information symbol, then the phase conjugated symbol can be transmitted in the  $h$ th subcarrier,  $S(h) = S(k)^* = A(k) \exp(-j\varphi(k))$ , where  $()^*$  represents complex conjugation. To simplify the exposition, it is assumed here that during propagation nonlinear phase shifts, represented by  $\theta(k)$  and  $\theta(h)$ , are added

to these subcarriers. The received information symbols on the  $k$ th and  $h$ th subcarriers are  $Z(k) = A_r(k) \exp(j\varphi(k) + j\theta(k))$  and  $Z(h) = A_r(h) \exp(j\varphi(h) + j\theta(h))$ , respectively. If the frequency spacing between  $k$ th and  $h$ th subcarriers is small enough, the nonlinear phase shifts will be highly correlated,  $\theta(k) \approx \theta(h)$  providing the opportunity of cancelling the nonlinear phase shift on the  $k$ th subcarrier by averaging the received information symbol of a subcarrier and the subcarrier which carries its phase conjugate (after a second conjugation):

$$\bar{Z}(k) = (Z(k) + Z(h)^*) / 2 \approx A_r(k) \cos(j\theta(k)) \exp(j\varphi(k)) \quad (4.1)$$

This compensation technique is often referred in the literature as coherent superposition [95]. Note that the nonlinear phase shift on the original  $k$ th subcarrier can be estimated as [39]:

$$\theta(k) = \arg(Z(k)Z(h)) / 2 \quad (4.2)$$

Ideally, a data carrying subcarrier and its PCP should be closely spaced in frequency (adjacent) to maximize the level of correlation of the nonlinear phase shifts between these subcarriers. For those data carrying subcarriers which do not have PCPs, the nonlinear phase shift of the  $j$ th subcarrier can be estimated and compensated as:

$$\theta(j) = \arg \left( \sum_{k,h} \eta_{jkh} Z(k) Z(h) \right) / 2 \quad (4.3)$$

$$\bar{Z}(j) = Z(j) \exp(-j\theta(j))$$

where  $\eta_{jkh}$  is the FWM efficiency coefficient. In this thesis  $\eta_{jkh}$  is approximated either as 1 if  $j$  is the closest subcarrier to  $k$  or  $h$  and 0 otherwise.

By applying this fibre compensation technique, the fibre nonlinearity phase shifts on data subcarriers in an OFDM system can be compensated without conjugating all pairs of subcarriers. In this system configuration, several data carrying subcarriers are placed between conjugate pairs. The nonlinear phase shifts for all of these subcarriers are similar as long as the frequency spacing is small. These nonlinear distortions can be compensated using the estimated nonlinear distortion on the closest pair of subcarrier data and

phase conjugated pilot. As a result, one phase conjugated pilot can be used to compensate the nonlinear distortions on several subcarriers and the overhead due to phase conjugated pilots is relaxed and can be designed according to the requirement of a specific application.

Whilst the most accurate nonlinear compensation will be achieved by weighting and summing the nonlinear distortion estimated from all of the phase conjugate pairs, the nonlinear distortion on subcarriers which are not part of phase conjugate pairs can be estimated in various ways. The first approximation is to simply use the estimated nonlinear distortion from the nearest phase conjugate pair. The second approximation is to use a linear interpolation of the estimated nonlinear distortions from the two closest phase conjugate pairs (two points).

In common with PC-TW, the performance of a system based on PCP can be further improved with 50 % electrical dispersion pre-compensation (pre-EDC), which is applied to create a dispersion-symmetry along the transmission link. This dispersion map enhances the similarity between nonlinear distortions on subcarrier data and its phase conjugate, thus further improving the effectiveness of the proposed nonlinearity compensation scheme.

### **4.2.2 Simulation**

As a proof of concept, a simulation of the proposed PCP scheme for a single channel 112 Gb/s PDM QPSK CO-OFDM transmission was conducted. The simulation setup is shown in the Fig. 4.2. The data stream was first divided into x- and y-polarizations, each of which was then mapped onto 1400 subcarriers using QPSK modulation format and subsequently transferred to the time domain by an IFFT of size 2048 while zeros occupying the remainder. Our standard simulation was as follows, although some parameters were varied to illustrate the salient features of this nonlinearity compensation scheme. The OFDM useful duration was 50 ns (20 MHz subcarrier spacing), no cyclic prefix was added and the effect of polarization mode dispersion was ignored. The fibre link comprised 80 km spans of SSMF with a loss parameter of 0.2 dB/km, nonlinearity coefficient of 1.22 /W/km and dispersion of 16 ps/nm/km. The span loss was compensated by EDFAs with 16 dB of

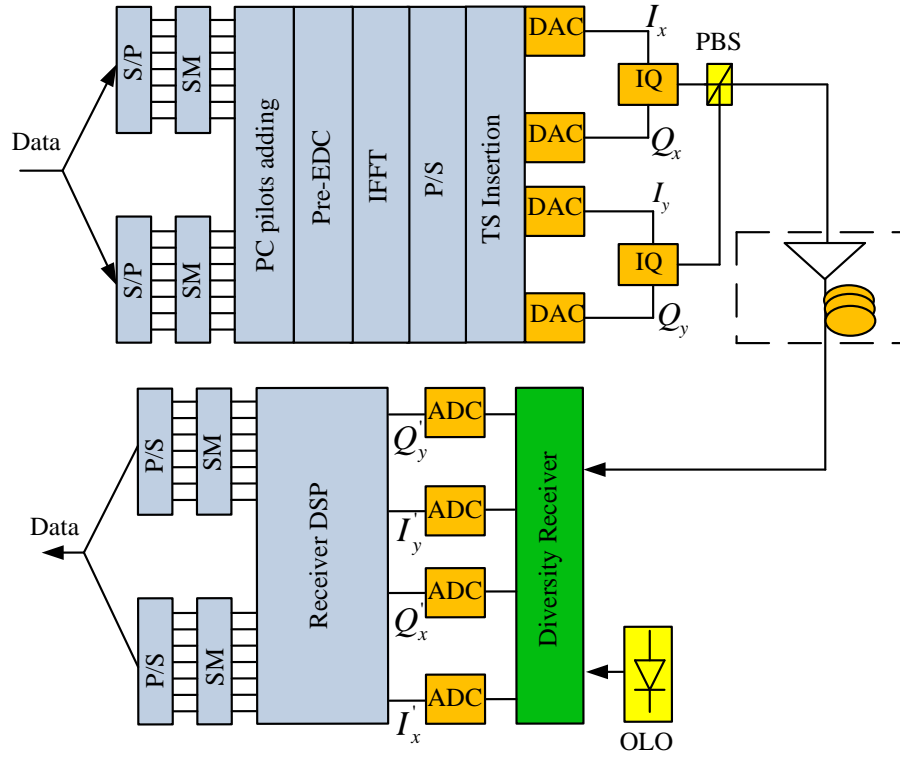


**Figure 4.2:** Block diagram of 112 Gb/s PDM CO-OFDM transmissions. S/P: serial/parallel conversion, P/S: parallel/serial conversion, SM: symbol mappings, TS: training symbol, DAC: digital-to-analog converter, ADC: analog-to-digital converter, I/Q: I/Q modulator, PBS: polarization beam splitter, OLO: optical local oscillator.

gain and 6 dB noise figure. The ASE noise is added inline to ensure that the interaction between signal and noise [96] is correctly captured. The transmitter and receiver lasers had the same linewidth of 100 kHz. The simulated time window contained 100 OFDM symbols (560,000 bits).

The received signal after coherent reception was first resampled and converted from serial to parallel for further processing, including chromatic dispersion compensation using a frequency domain equalizer (OFDE) employing the overlap-and-save method, channel estimation and equalization with the assistance of initial training sequence (2 training symbols every 100 symbols) using zero forcing estimation with MIMO processing [33], and nonlinear phase noise (NLPN) estimation and compensation. In order to compensate for NLPN using PCPs, it is necessary to compensate for the CPE introduced by the lasers phase noise and common phase shift due to the fibre nonlinearity first. To reduce the net overhead, this compensation is also achieved using all the PCPs as shown in [39], using a two-stage compensation scheme. After CPE compensation, the nonlinear distortions

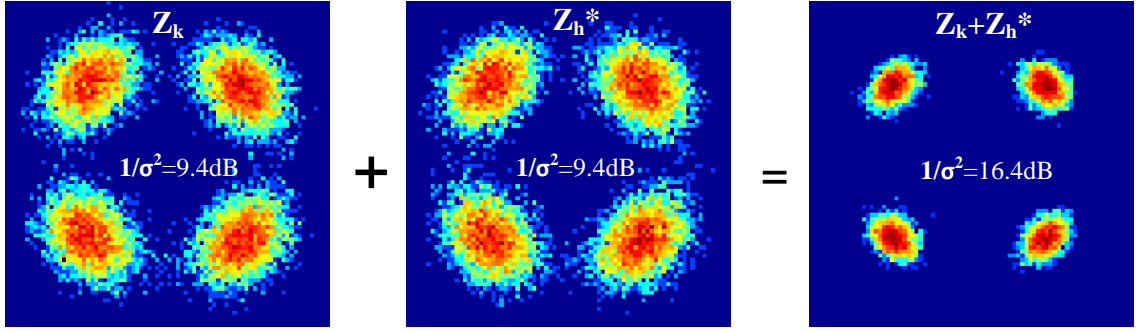


**Figure 4.3:** Nonlinear noise cancellation based on the coherent superposition of PCP pairs. The transmission distance is 1200 km, launch power is 5 dBm, ASE noise is not considered and 50 % pre-EDC is adopted.

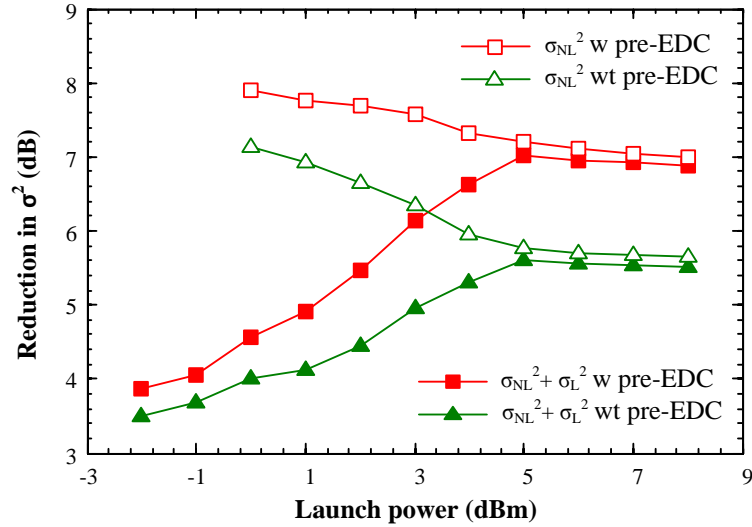


**Figure 4.4:** Measured reduction of signal variance from both nonlinear distortion ( $\sigma_{NL}^2$ ) and linear noise ( $\sigma_L^2$ ) as a function of the launch power, in systems with and without 50 % pre-EDC. The transmission distance is 1200 km, ASE noise is included.

tion of subcarriers data accompanied by PC pilots was compensated using Eq. 4.1 whilst the nonlinear distortions of other subcarriers were compensated using Eq. 4.3. In order to demonstrate effectiveness of the nonlinear noise cancellation scheme based on the coherent superposition of the PCP pairs, the ASE noise was firstly turned off. The simulation results are shown in the Fig. 4.3 for a 1200 km optical link with 5 dBm of the launch power. After coherent superposition, a dramatic reduction ( $\sim 7$  dB) of the nonlinear signal distortion variance ( $\sigma^2$ ) was observed, indicating that the nonlinear distortion on a data carrying subcarrier and those of its PC are highly anticorrelated, especially if the frequency spacing is small.

Figure 4.4 plots the reduction in the signal variance ( $\sigma^2$ ), which is equivalent to the

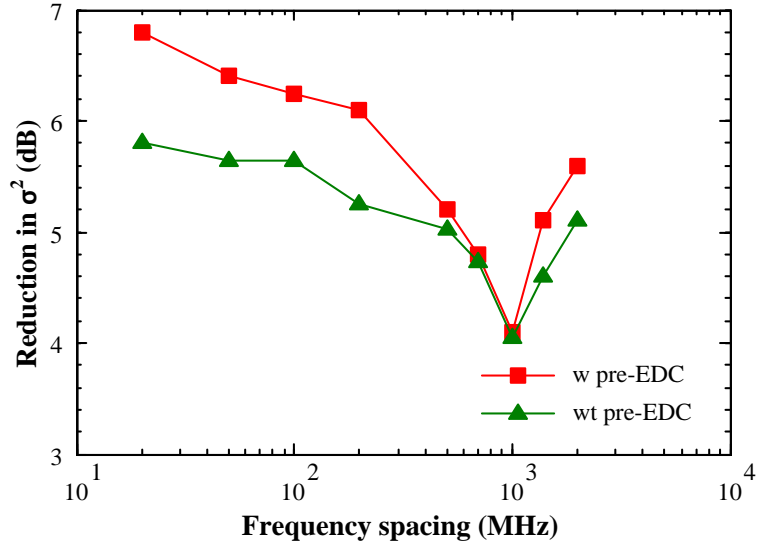


**Figure 4.5:** Measured reduction of signal variance as a function of the frequency spacing. The transmission distance is 1200 km, the launch power is 5 dB, ASE noise is included and the number of subcarriers is varied, keeping the same data rate (112 Gb/s).

SNR improvement, when coherent superposition is applied for PCP pairs in systems with and without 50 % pre-EDC (red and green respectively). The difference between the open and solid symbols illustrates the impact of ASE noise. When the launch power is small, the dominant limiting factor in the system is the ASE noise. As a result, the coherent superposition of the PCP pairs using 50 % pilots offers around  $\sim 3$  dB reduction of the signal variance, as expected from the linear effects of coherent superposition of two copies of the same signal. However, with increasing launch powers a larger reduction in  $\sigma^2$  eventually occurs, indicating the maximum effectiveness of the proposed nonlinear noise cancellation scheme. Note that in this regime, there is little impact from the addition of ASE noise suggesting that the system is limited by compensation accuracy rather than the fundamental parametric noise amplification process [96]. When 50 % pre-EDC is performed, the reduction of 2 is further enhanced, reaching around 7 dB at a high level of the launch power. When considering only the nonlinear noise distortion, an even higher reduction of  $\sim 8$  dB can be observed.

As mentioned before, the PCP compensation scheme relies on the correlation of nonlinear phase shifts of the data carrying subcarriers and PCPs; the effectiveness of this scheme depends strongly on the subcarrier frequency spacing. Figure 4.5 shows the reduction of signal variance  $\sigma^2$  as a function of the subcarrier frequency spacing (by varying

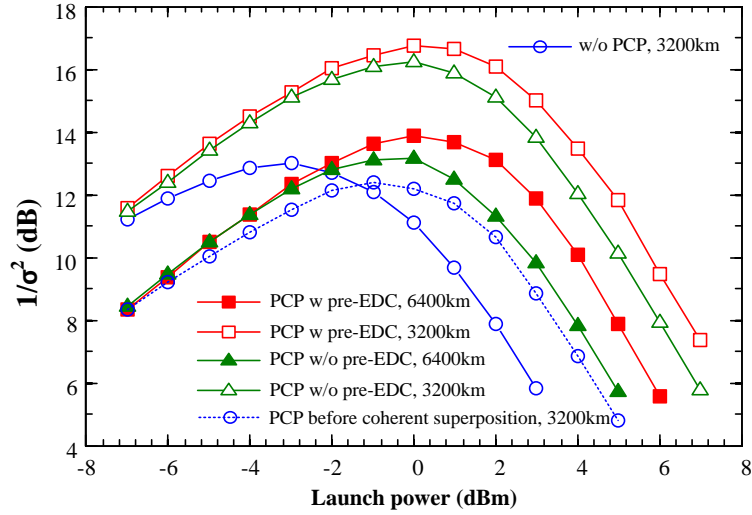


**Figure 4.6:** Nonlinear cancellation using coherent superposition of PCP pairs in long-haul 56 Gb/s (net data rate) CO-OFDM transmission. The transmission distances are 3200 km (open symbols) and 6400 km (closed symbols)

the number of the subcarriers). As expected, when the subcarrier frequency spacing increases, the benefit of coherent superposition scheme tends to decrease, from around 7 dB at a frequency spacing of 20 MHz to around 4 dB at a frequency spacing of 1 GHz (for the case of 50 % pre-EDC). The 3 dB nonlinear interaction bandwidth of the simulated system was around 1.1 GHz. However, the rapid dip in performance around 1 GHz is attributed (and 200 MHz without pre-dispersion) to a quasi-phase matching process [93,96,97] rather than a specific resonance with this bandwidth.

The effective SNR of 112 Gb/s OFDM systems with 50 % PCPs and without any PCPs are compared in Fig. 4.6. Note that, the spectral efficiency is reduced by a factor of 2 when 50 % of the subcarriers are transmitted as PCPs. In Fig. 6, by combining pre-EDC and PCP techniques, a reduction of around 4.5 dB in the signal variance can be achieved at a transmission distance of 3200 km at the cost of 50 % overhead. The nonlinear threshold is also increased by 9 dB with PCP compensation. This result clearly indicates that a substantial fraction of the nonlinear distortion can be mitigated by coherently adding the phase conjugated pilot and its correlated data subcarrier. As a result of this improvement, a longer transmission distance can be achieved. In Fig. 4.6 the effective SNR of system with 50 % PCP after 6400 km of transmission distance is also plotted for comparison purpose. As can be seen, this system still offers around 1.5 dB advantage in performance

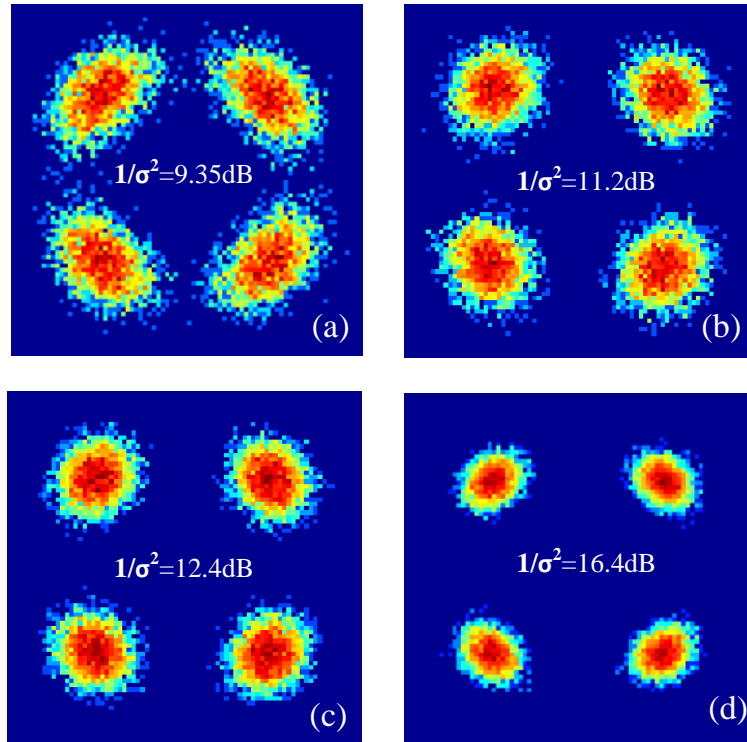


**Figure 4.7:** Received constellation diagrams in 112 Gb/s PDM CO-OFDM systems without (with the same bandwidth, before CS) (a) and with PCPs for fibre nonlinearity compensation (b - 12.5 %, c - 25 %, d - 50 % overhead). The Transmission distance is 1200 km, the launch power is 5 dBm.

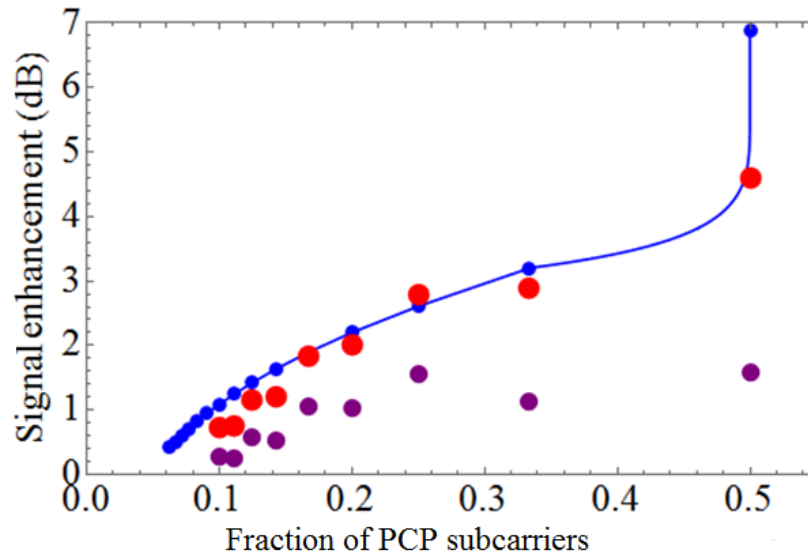


**Figure 4.8:** Signal enhancement of a 3200 km PDM NGI CO-OFDM system at the optimum launch power as a function of the fraction of subcarriers allocated as phase conjugate pilots, showing measured reduction in signal variance (red symbols), net gain after subtraction of overhead (purple) and predicted signal to noise ratio gain (blue symbols).

in comparison with OFDM system without PCP after 3200 km of transmission distance. This comparison indicates that the product of spectral efficiency and transmission distance can be significantly increased with PCP techniques, and is consistent with results obtained for PC-TW.

This implementation offers excellent performance but it requires 50 % overhead. The required overhead can be reduced by using the estimated nonlinear distortion on one pair of subcarrier data and its PCP to compensate the nonlinear distortions on other subcarriers. Specifically, one PCP can be used to compensate the nonlinear distortion of 2, 3, 4 or more data subcarriers at the cost of 33 %, 25 %, 20 % or smaller overhead respectively. In Fig. 4.7 the received constellation diagrams of systems with and without PCPs for fibre nonlinearity compensation are shown for different values of PCP overhead with the launch power deliberately set in the highly nonlinear region (+5 dBm). The trade-off between overhead due to PCPs and performance can be clearly observed. A better performance comes with the cost of larger overhead due to the transmission of additional PCPs.

The reduction in the signal variance (in dB) at the optimum launch power (difference of the minimum achievable  $\sigma^2$  in systems without and with PCPs) and the net benefit in dB (after extracting the spectral efficiency reduction due to the PCPs) as a function of the overhead due to PCPs are shown in the Fig. 4.8. With 50 %, 33 %, and 20 % overhead the achievable reduction in  $\sigma^2$  are 4.6 dB, 3.2 dB and 2.1 dB respectively, or approximately 0.1 dB per 1 % of overhead. It is believed that the reduction in  $\sigma^2$  enhancement as the overhead is reduced is initially due to lower coherent gain (a smaller number of subcarriers have the >3 dB benefit of coherent superposition), but eventually the subcarriers become spaced by more than the FWM efficiency bandwidth after which the nonlinear compensation starts to reduce. This is confirmed by a theoretical estimation (shown in blue). To obtain this estimation the normalized difference in nonlinear distortion from FWM [93] was computed for all possible subcarrier triplets whose nonlinear distortions fall on either the carrier or its conjugate. The sum of these nonlinearity compensation errors was used to estimate the level to which inter subcarrier nonlinearity is suppressed in the calculation of nonlinear noise. To give an upper bound on the compensation performance it is assumed that parametric noise amplification [96] is not compensated by the conjugates. The opti-

imum signal to noise ratio was used to calculate the BER for subcarriers with and without a phase conjugate assuming that coherent superposition enabled a 3dB enhancement in signal to noise ratio [81].

Finally the mean BER was used to calculate the required SNR to give the same performance without conjugate pilots. The curve fit between 33 % and 50 % conjugates assumes a linear interpolation of the nonlinear compensation error, but is dominated by the increasing effectiveness of the coherent superposition. An excellent fit is observed over a wide range of configurations with the exception of the case where 50 % of the subcarriers are phase conjugate pilots. It is believed that this error is due to a reduced benefit of coherent superposition when the noise fields are no longer statistically independent, due to their parametric amplification by the signal. In a practical system, a minimum overhead for CPE (4-10 %) would be required, and this overhead may be used to provide a certain level of nonlinear compensation without additional overhead.

### **4.2.3 Experimental setup and results**

The experimental set-up is shown in Fig. 4.9. It comprised a laser grid of five standard DFBs on 100 GHz grid which were substituted in turn by a 100 kHz linewidth laser. The DFBs are located between 193.5 to 193.9 THz. Additional loading channels (10 GHz of bandwidth) were generated using an ASE source which were spectrally shaped using a WSS [98]. The twenty loading channels were spread symmetrically around the test wavelengths so that the total bandwidth of the transmitted signal was 2.5 THz. A wideband filter was used to filter out of band ASE noise at the transmitter. The transmission path was an acousto-optic modulator (AOM) based re-circulating loop consisting of  $4 \times 100$  km spans of Sterlite OH-LITE (E) fibre, having 18.9 to 19.5 dB insertion loss. The loop switch was located in the mid-stage of the first EDFA and a gain flattening filter (GFF) was placed in the mid stage of the third EDFA. After propagation the signal was filtered using a 4.2 nm flat topped filter and coherently detected. The received electrical signals were then sampled by a real-time oscilloscope at 80 GS/s and processed offline in MATLAB.

The OFDM signal (400 symbols each of 20.48 ns length, 2 % cyclic prefix) encoded

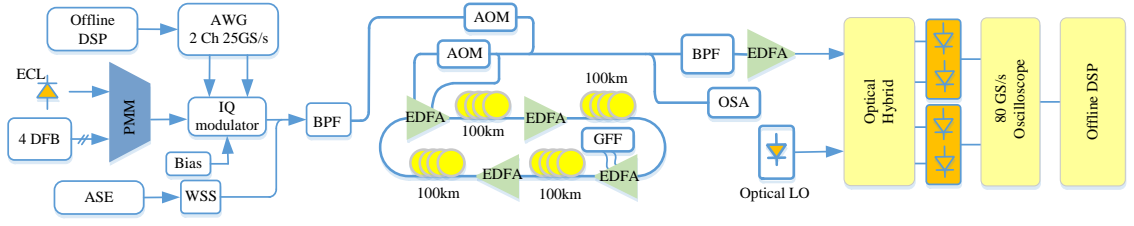


**Figure 4.9:** Schematic of experimental setup of WDM CO-OFDM transmission with PCPs for fibre nonlinearity compensation. ECL: external cavity laser, PMM: polarization maintaining multiplexer, WSS: Wavelength Selective Switch, DFB: distributed feedback laser, BPF: band-pass filter (optical), AOM: acousto-optic modulator, GFF: gain flatten filter, OSA: optical spectrum analyser, LO: local oscillator.

with QPSK modulation format was generated offline in MATLAB using an IFFT size of 512, where 210 subcarriers were filled with data and the remainder zeros giving a line rate of 20 Gb/s (18.2 Gb/s after cyclic prefix and FEC overhead are removed). When 25 %, 33.3 % and 50 % of OFDM subcarriers are transmitted with its PCPs the net data rates were 13.65 Gb/s, 12.12 Gb/s and 9.1 Gb/s respectively. In order to maximize the similarity between nonlinear phase noises on data subcarrier and PCP, data subcarrier and its PCP were placed next to each other. The DSP at the receiver included chromatic dispersion compensation using an overlapped frequency domain equalizer with overlap-and-save method, channel estimation and equalization with the assistance of initial training sequence (2 training symbols every 100 symbols), CPE compensation with the help of the PCPs [99] or 16 pilot subcarriers if PCPs were not transmitted, fibre nonlinearity compensation as described above, and symbol detection. The system performance was evaluated directly from the BER by processing 10 recorded traces ( $\sim 10^6$  bits). The measured BER is then converted to an equivalent Gaussian noise Q-factor in dB using the expression 2.1.

The effectiveness of the proposed PCP compensation scheme for fibre nonlinearity compensation in CO-OFDM is shown in Fig. 4.10, for the center channel. Before coherent superposition, the measured BER was  $\sim 1.2 \times 10^{-3}$ . However, after coherent superposition error free transmission was observed. This result clearly indicates that a substantial fraction of the nonlinear distortion, including both intra and inter-channel distortions, can be effectively compensated using coherent superposition of the data carrying subcarriers and the PCPs.

It can be seen in the Fig. 4.11, that by transmitting 50 % of OFDM subcarriers as PCPs

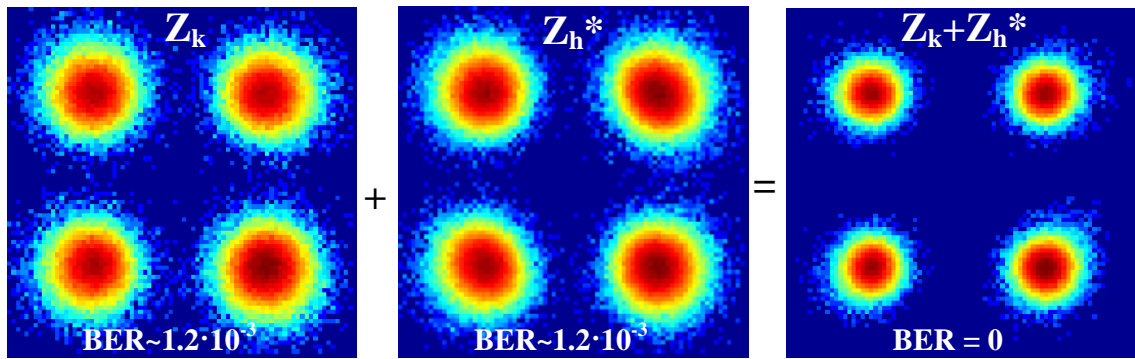


**Figure 4.10:** Cancellation of the nonlinear distortions by CS of subcarriers with its counterpart PCPs in WDM CO-OFDM transmission, 800 km of distance, the launch power (per/ch) was 0 dBm.

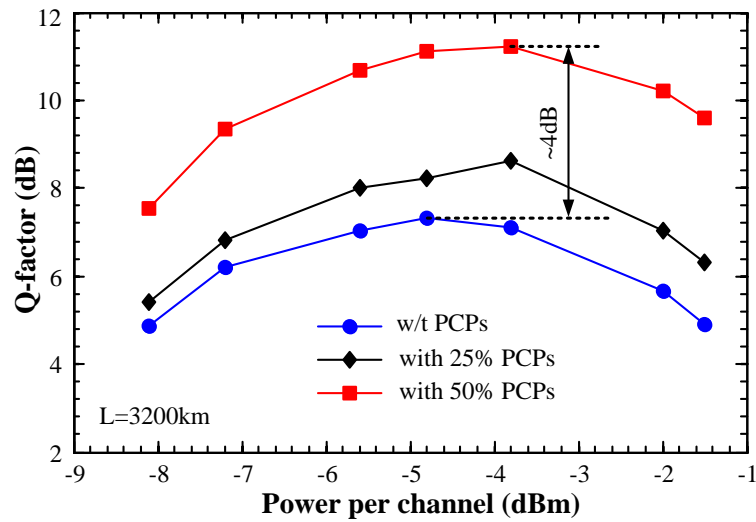


**Figure 4.11:** Q-factor of the center channel as a function of the launch power in system with and without PCPs for fibre nonlinearity compensation.

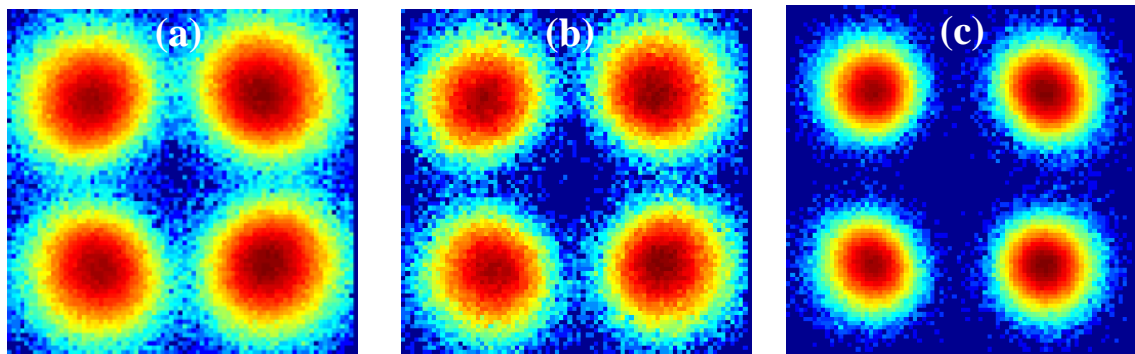


**Figure 4.12:** Constellation diagrams for the center channel at  $P_{in} = -1.5$  dBm for the cases of without PCPs (a) and with 25%, 50% of PCPs (b and c) respectively. The transmission distance is 3200 km

a dramatic ( $\sim 4$  dB) improvement in the systems Q-factor was achieved (after 3200 km of the transmission distance), which agrees well with the simulation result and is also comparable with results achieved with the conventional PC-TW technique [81]. The optimum launch power was increased by around 1 dB. The constellation diagrams for the center channel at  $P_{in} = -1.5$  dBm for the cases of with and without PCPs are shown in Fig. 4.12.

As mentioned before, the overhead can be reduced by using a smaller number of PCP. Specifically, one PCP can be used for 2, 3, 4 or more data subcarriers at the cost of 33 %, 25 %, 20 % or smaller overhead respectively. When the PCP overhead was reduced to 25 %, a performance improvement of around 1.5 dB was still achieved (Fig. 11(a)). This result confirms the possibility of using one PCP to compensate the nonlinear distortions of several data carrying subcarriers. Figure. 4.13 plots the Q-factor improvement as a function of the additional overhead due to the PCP, showing the trade-off between PCP overhead and performance gain. Since when PCPs were not transmitted, 8 % of OFDM subcarriers were allocated for phase noise estimation, the additional overhead for nonlinear compensations were 12 %, 17 %, 25 % and 42 % and the performance gains were 0.9, 1.2, 1.5 and 4 dB respectively. This result clearly shows the flexibility of the proposed PCP fibre nonlinearity compensation technique, allowing the number of PCP to be chosen to meet the performance requirement.

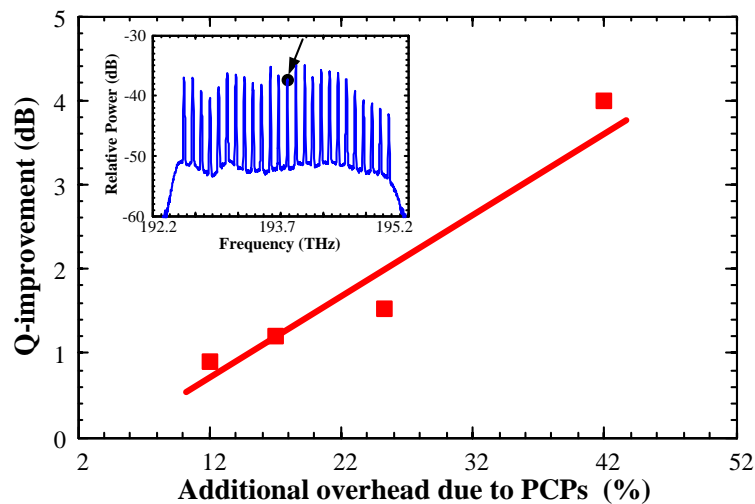


**Figure 4.13:** Performance gain as a function of the additional overhead due to PCPs for the center channel, after 3200 km of distance. Without PCPs, an overhead of  $\sim 8$  % was required for CPE compensation.

## 4.3 Phase conjugated subcarrier coding for fibre nonlinear mitigation in CO-OFDM Transmission

### 4.3.1 Concept of PCSC

In the PCSC scheme (Fig. 4.14) each pair of neighbouring OFDM subcarriers (with the indices of  $2k-1$  and  $2k$ , where  $k$  is an integer number) after symbol mapping are encoded before being fed into the IFFT block to generate the time-domain signal as [89, 100]:

$$\begin{cases} X_1(2k-1) = X(2k-1) + X(2k) \\ X_1(2k) = X^*(2k-1) - X^*(2k) \end{cases} \quad (4.4)$$

where  $(.)^*$  stands for the complex conjugation operation. At the receiver, before symbol demapping, the received information symbols in this subcarrier pair are decoded as:

$$\begin{cases} Z_1(2k-1) = Z(2k-1) + Z^*(2k) \\ Z_1(2k) = Z(2k-1) - Z^*(2k) \end{cases} \quad (4.5)$$

It should be noted that the PCSC can be considered as one-by-one mapping scheme which does not require any overhead. The only requirement of PCSC is that the number of OFDM subcarriers is even. The PCSC scheme modifies both the constellation set and probabilities of constellation points. As shown in the Fig. 4.14, if the input modulation format is BPSK with equal probability (0.5, 0.5) for each constellation point (-1, 1), the output constellation set will be a 3 ASK (-2, 0, 2) in which the symbol 0 occurs twice as often as the two other information symbols (-2, 2). This indicates that 50 % of BPSK OFDM subcarriers will be turned off after encoding. Similarly, if the input modulation format is QPSK, after encoding, the output constellation set will be a 9 QAM with unequal probabilities (Fig. 4.15), which can potentially reduce the nonlinear distortions on OFDM subcarriers due to the unequal power distribution across the OFDM band [91].

The sensitivities of OFDM systems with and without PCSC scheme in the Additive White Gaussian Noise channel are compared in Fig. 4.16, for different modulation for-

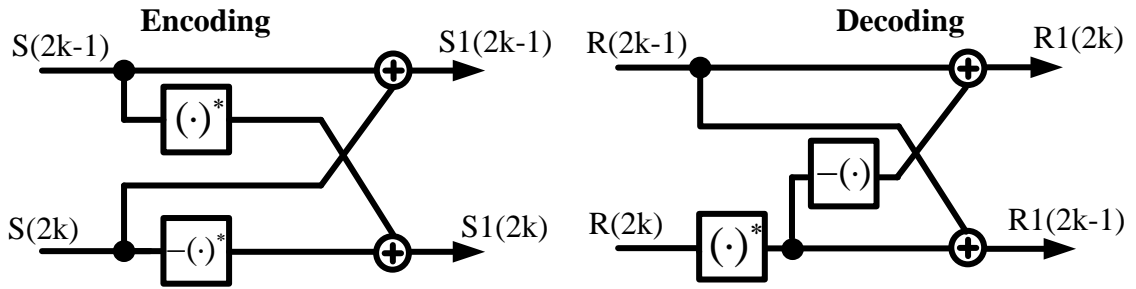


**Figure 4.14:** Phase-conjugated subcarrier coding scheme for CO-OFDM transmission.

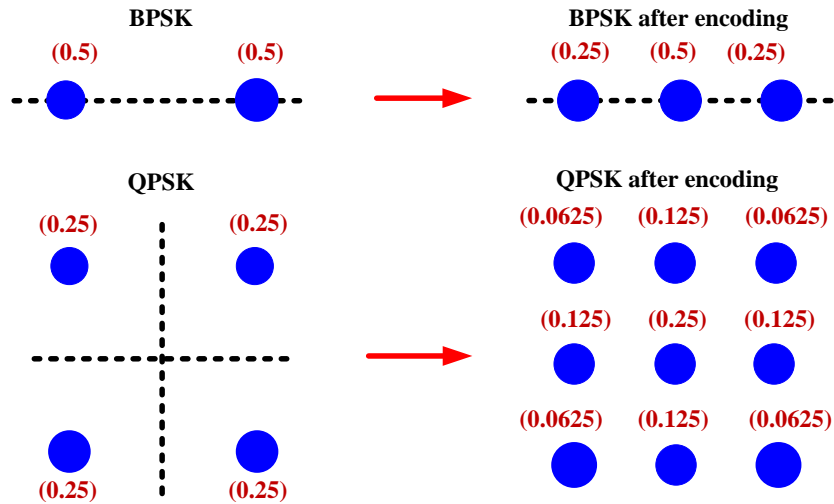


**Figure 4.15:** PCSC symbol mapping for BPSK and QPSK. the numbers (in red) are the probabilities of symbols in the constellation set.

mats, namely BPSK, QPSK, 8QAM. It can be seen that independently of the modulation format used, PCSC gives no performance gain or penalty (the same sensitivity) in linear transmission channels. This result indicates that PCSC is ineffective for CO-OFDM systems if the distortions on neighbouring subcarriers are Gaussian distributed and uncorrelated. However, if the OFDM subcarrier frequency spacing is small (tens of MHz) it can be expected that the nonlinear phase shifts on neighbouring subcarriers will be highly correlated. Thus, potential performance gain can be achieved by encoding and processing neighbouring subcarriers simultaneously at the transmitter and receiver. In order to enhance the similarity of nonlinear distortions on neighbouring OFDM subcarriers, pre-EDC is applied in this work to create a dispersion-symmetry along the transmission link as shown in Fig. 4.17.

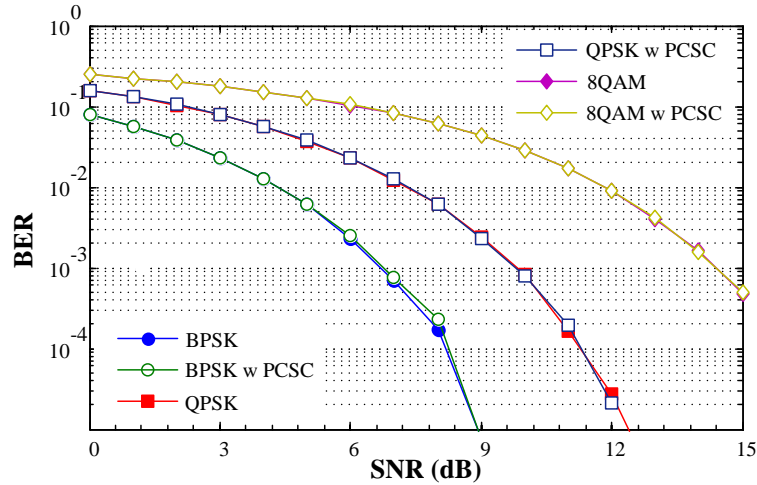


**Figure 4.16:** Sensitivities of OFDM systems with and without PCSC in the linear channel with white Gaussian noise.

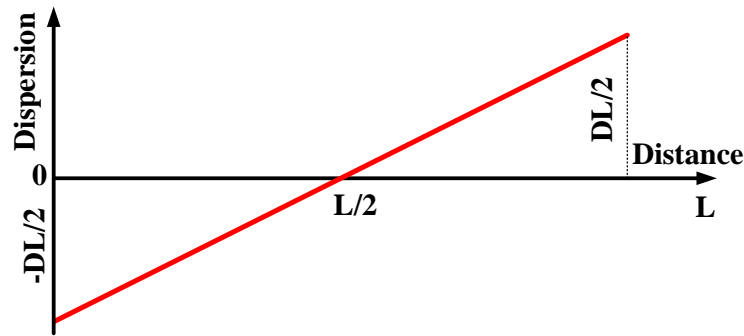


**Figure 4.17:** Dispersion map of an optical link with 50% pre-EDC.  $L$  is the link distance and  $D$  is the dispersion coefficient.

### 4.3.2 Simulation

As a proof of concept, a simulation of the PCSC scheme in a single channel 80 Gbaud PDM CO-OFDM transmission system with BPSK and QPSK modulation formats was conducted. It should be noted that the choice of signal bandwidth is not critical here. The simulation setup is shown in the Fig. 4.18. The data stream was first divided into x- and y-polarizations, each of which was then mapped onto 1000 subcarriers using BPSK and QPSK modulation formats and subsequently transferred to the time domain by an IFFT of size 2048 while zeros occupying the remainder. The OFDM useful symbol duration was 12 ns and a cyclic prefix of 0.4 ns was added for PMD compensation. The net bit-rate (after extracting 7% FEC) is 150 Gb/s and 300 Gb/s when BPSK and QPSK are adopted. The long-haul fibre link comprised 80-km spans of SSMF with a loss parameter of 0.2 dB/km,

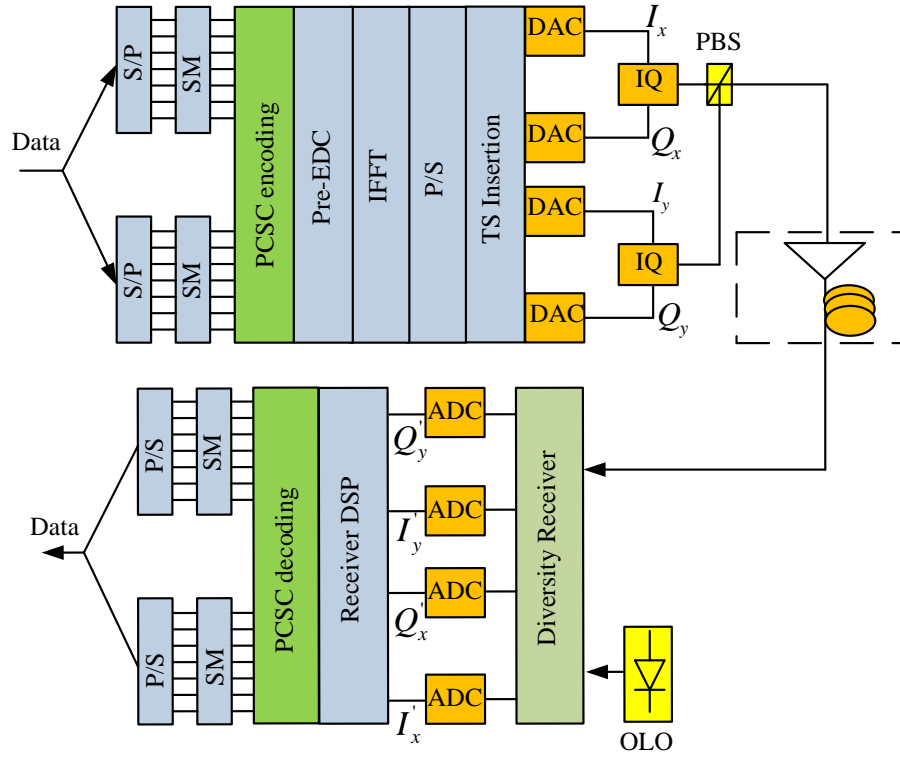


**Figure 4.18:** Block diagram of PDM CO-OFDM transmissions with PCSC. S/P: serial/parallel conversion, P/S: parallel/serial conversion, SM: symbol mappings, TS: training symbol, DAC: digital-to-analog converter, ADC: analog-to-digital converter, I/Q: I/Q modulator, PBS: polarization beam splitter, OLO: optical local oscillator.

nonlinearity coefficient of  $1.22 \text{ /W/km}$ , dispersion of  $16 \text{ ps/nm/km}$  and PMD coefficient of  $0.1 \text{ ps/km}^{0.5}$ . The span loss was compensated by Erbium-doped fibre amplifiers with  $16 \text{ dB}$  of gain and  $6 \text{ dB}$  noise figure. The amplified spontaneous emission noise is added inline to ensure that the interaction between signal and noise is correctly captured [96]. The transmitter and receiver lasers had the same linewidth of  $100 \text{ kHz}$ . The simulated time window contained 500 OFDM symbols ( $10^6$  bits for QPSK). The DSP at the receiver includes chromatic dispersion compensation using a frequency domain equalizer with overlap-and-save method, channel estimation and equalization with the assistance of initial training sequence (2 training symbols every 100 symbols) using zero forcing estimation with MIMO processing, common phase error compensation with the insertion of quasi-pilot subcarriers [39] (4 pilots every OFDM symbol) and symbol detection. The system performance is evaluated using the Q-factor derived directly from the BER.

Performances of the  $150 \text{ Gb/s}$  PDM CO-OFDM systems with and without the PCSC scheme (with and without pre-EDC) are compared in the Fig. 4.19. In this figure, the

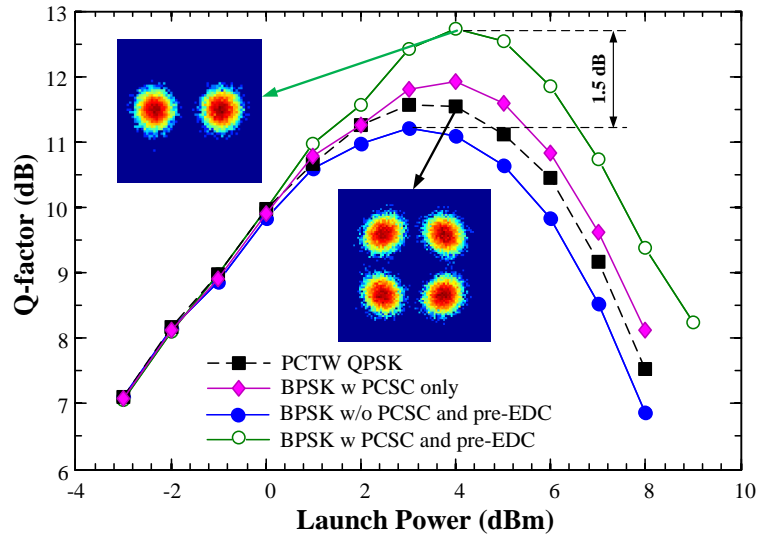


**Figure 4.19:** Q-factor as a function of the launch power in 150 Gb/s PDM CO-OFDM system with and without PCSC, the transmission distance is 8000 km.

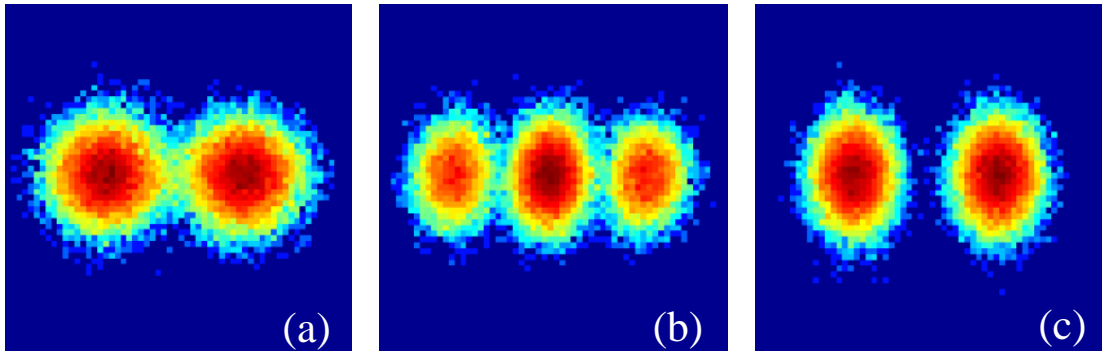


**Figure 4.20:** Constellation diagrams on x-polarization in 150 Gb/s PDM CO-OFDM system over 8000 km, 8 dBm of the launch power, a) without PCSC, b, c) with PCSC, before and after decoding.

performance of PCTW technique with QPSK modulation format providing the same SE ( $\sim 2$  bits/s/Hz) is also presented. As PCTW halves the SE, despite the effective nonlinear noise cancellation effect, PCTW with QPSK modulation format gives only around 0.5 dB advantage over the traditional BPSK PDM CO-OFDM transmission scheme. On the other hand, when the PCSC coding scheme combined with pre-EDC is applied, a performance improvement of 1.5 dB can be achieved without reducing the SE. When PCSC is applied without 50 % pre-EDC, a performance gain of  $\sim 0.7$  dB is observed. This result clearly indicates the benefit of pre-EDC in the proposed transmission scheme, which enhances the total gain to 1.5 dB. Interestingly, a nonlinear noise squeezing effect was observed (Fig. 4.20) in a similar manner as in single carrier system with real-valued signal and the

symmetrical dispersion map [101]. Without PCSC, the real and imaginary parts of each constellation point have the same distribution. However, with PCSC and the optimized pre-EDC, the PDF of the real part of each constellation point is significantly narrowed (Fig. 4.21). This nonlinear noise squeezing effect significantly reduces the BER in a transmission system using BPSK modulation format.

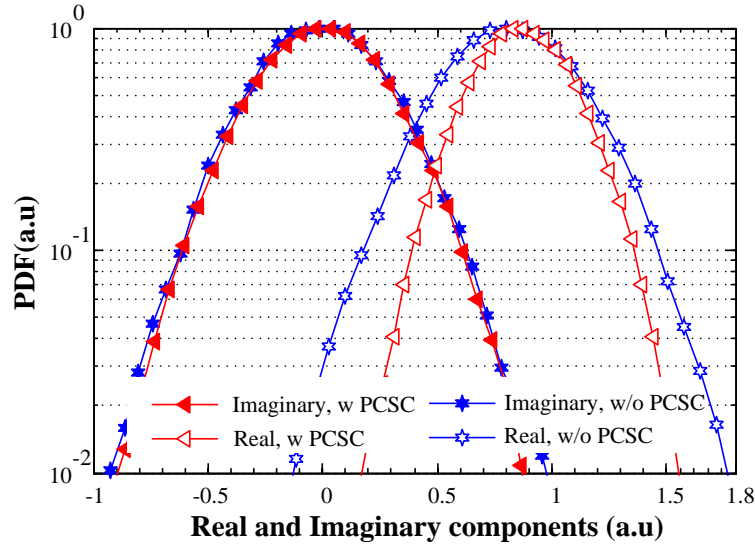


**Figure 4.21:** PDF of real and imaginary components for the 1 symbol in systems with and without the PCSC, the launch power was 7 dBm.

When the PCSC scheme combined with the optimized pre-EDC is applied for 300 Gb/s QPSK PDM CO-OFDM system, a performance improvement of around 0.7 dB is achieved, as shown in the Fig. 4.22. This result clearly indicates that the PCSC scheme also effectively mitigates the nonlinear distortions on OFDM subcarriers when QPSK modulation format is adopted. However, as QPSK cannot take the advantage of the nonlinear noise squeezing effect, the performance improvement in this case is only a half of those achieved with BPSK modulation format. In addition, without 50 % pre-EDC, PCSC does not provide a significant improvement in the systems performance. This result confirms the benefit of pre-EDC in applying the PCSC scheme (both for BPSK and QPSK modulation formats).

The performance gain offered by PCSC and pre-EDC as a function of frequency spacing is shown in Fig. 4.23 for BPSK and QPSK. Herein, the signal bandwidth is kept at 80 GHz, the number of OFDM subcarrier and the IFFT size are reduced accordingly to increase the OFDM subcarriers frequency spacing. For example, the number of OFDM

subcarrier and the IFFT size were set to 160 and 512 to increase the subcarriers spacing to 500 MHz. As expected, the performance gain decreases with the increasing of the frequency spacing. If the frequency spacing is comparable with the FWM bandwidth ( $\sim 1$  GHz), the performance gain in QPSK system becomes negligible ( $\sim 0.2$  dB). This result clearly indicates that the OFDM frequency spacing should be kept small in order to take the advantage of PCSC scheme.

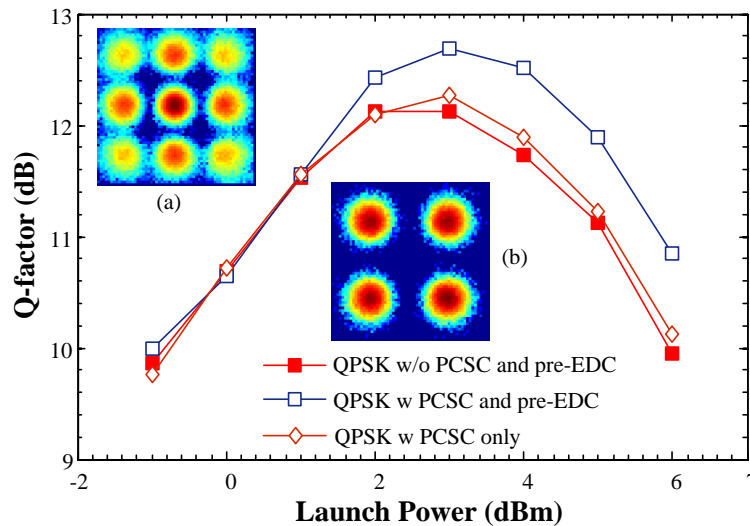


**Figure 4.22:** Q-factor as a function of the launch power in 300 Gb/s PDM CO-OFDM system with and without PCSC and constellation diagrams (before (a) and after (b) decoding) at 4 dBm, after 3200 km of transmission distance.

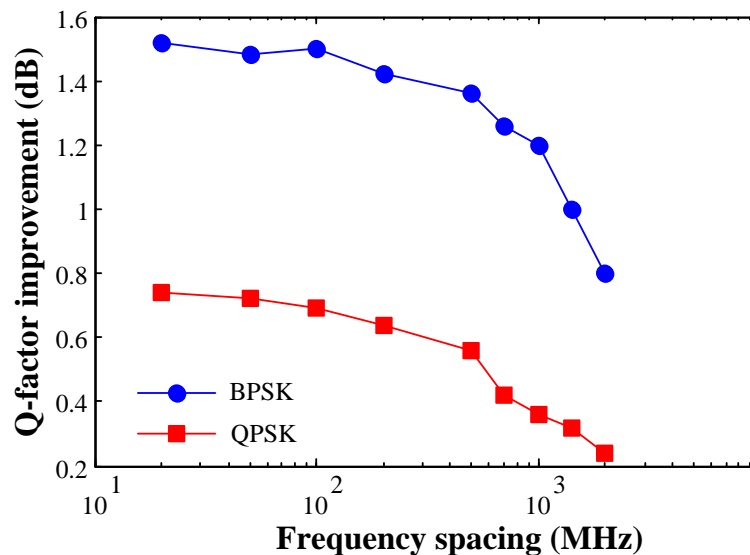


**Figure 4.23:** Performance gain in systems with PCSC as a function of the frequency spacing for different modulation formats.

### 4.3.3 Experimental setup and results

The experimental set-up is shown in Fig. 4.24. It comprised three standard DFBs on 25 GHz grid which were substituted in turn by a 100 kHz linewidth laser. Additional loading channels (10 GHz of bandwidth) were generated using an ASE source which were spectrally shaped using a wavelength selective switch (WSS). The twenty loading channels were spread symmetrically around the test wavelengths so that the total bandwidth of the transmitted signal was 0.575 THz. The transmission path was re-circulating loop consisting of a single span 100 km Sterlite OH-LITE (E) fibre, having around 19 dB insertion loss. A GFF was placed in the mid stage of the EDFA. After propagation the center channel was coherently detected. The received electrical signals were then sampled by a real-time oscilloscope at 80 GS/s and processed offline in MATLAB.

The OFDM signals (400 symbols each of 20.48 ns length, 2 % cyclic prefix) encoded with BPSK and QPSK modulation formats were generated offline in MATLAB using an IFFT size of 512, where 210 subcarriers were filled with data and the remainder zeros giving a line rate of 10 Gb/s and 20 Gb/s (9.1 Gb/s and 18.2 Gb/s after cyclic prefix and FEC overhead are removed) for BPSK and QPSK modulation formats respectively. The DSP at the receiver included synchronization, x- and y-polarizations combination using the maxima-ratio combining method [42], frequency offset compensation, chromatic dispersion compensation using an overlapped frequency domain equalizer with overlap-and-save method, channel estimation and equalization with the assistance of initial training sequence (2 training symbols every 100 symbols), phase noise compensation with the help 8 pilot subcarriers, and symbol detection. The system performance was evaluated directly from the BER by processing 10 recorded traces ( $\sim 10^6$  bits), the results also are expressed as a Q-factor.

The BER as a function of OSNR are compared in the back-to-back case for systems with and without PCSC in the Fig. 4.26. The optical spectra of BPSK signals after the transmitter and after 3200 km are shown in Fig. 4.27. In a good agreement with the simulation results presented in Fig. 4.16, the BER remains the same in systems with and without PCSC. This result clearly confirms that PCSC does not affect the system sensitivity in the

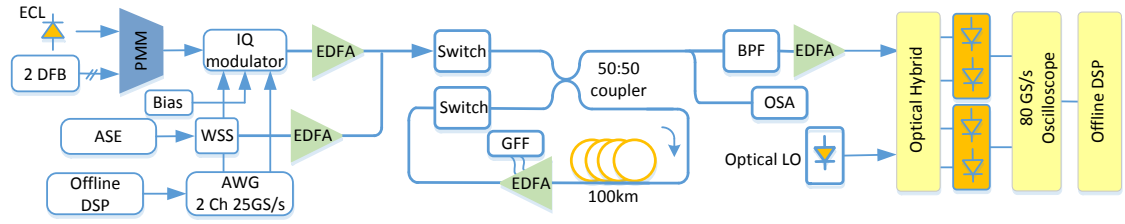


**Figure 4.24:** Schematic of experimental setup of WDM CO-OFDM transmission with PCPs for fibre nonlinearity compensation. ECL: external cavity laser, PMM: polarization maintaining multiplexer, WSS: Wavelength Selective Switch, DFB: distributed feedback laser, BPF: band-pass filter (optical), GFF: gain flatten filter, OSA: optical spectrum analyser, LO: local oscillator.

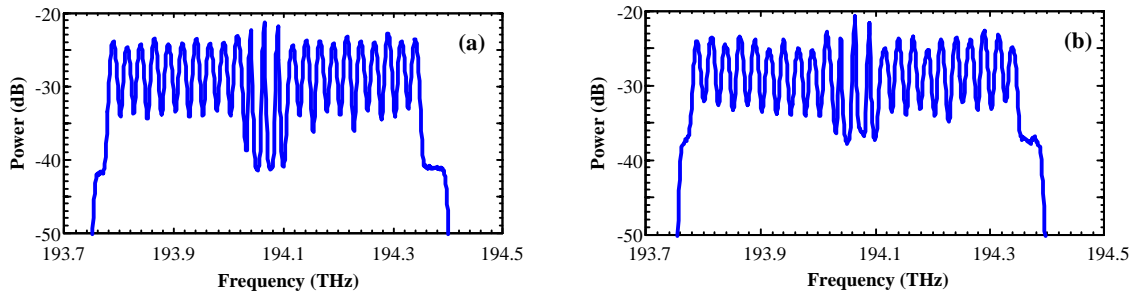


**Figure 4.25:** (a)-Optical spectrum after the transmitter. (b) optical spectrum after 2400 km of transmission distance.

back-to-back case. It should also be noted in Fig. 4.26 that the implementation penalty (at the BER level of  $10^{-3}$ ) is around 4 dB. The implementation penalty is due to the fact that no DAC equalization was implemented and the laser's drifting during the measurement and data recording process. The received constellation diagrams in BPSK transmission with and without PCSC (with pre-EDC) after 4000 km are shown in Fig. 4.27 for a launch power/channel of -3 dBm. It is clearly that the received signal quality is significantly increased when PCSC with 50 % pre-EDC is applied. This result confirms that the fibre nonlinearity impairment is effectively mitigated by encoding and processing neighbouring subcarriers by the PCSC scheme. Herein, the nonlinear noise squeezing effect can also be observed as the nonlinear distortion in the imaginary component of the received information symbol tends to be bigger than those of the real component. The Q-factor as a function of the launch power in BPSK transmissions with and without PCSC and pre-EDC is plotted in Fig. 4.28 for a transmission distance of 6000 km. The constellation diagrams at the optimum launch power for both cases are also included. In Fig. 4.28, a performance improvement of around 1.5 dB is observed, which is equivalent with the simulation result plotted in Fig. 4.19 for single channel transmission. This result indicates that PCSC with

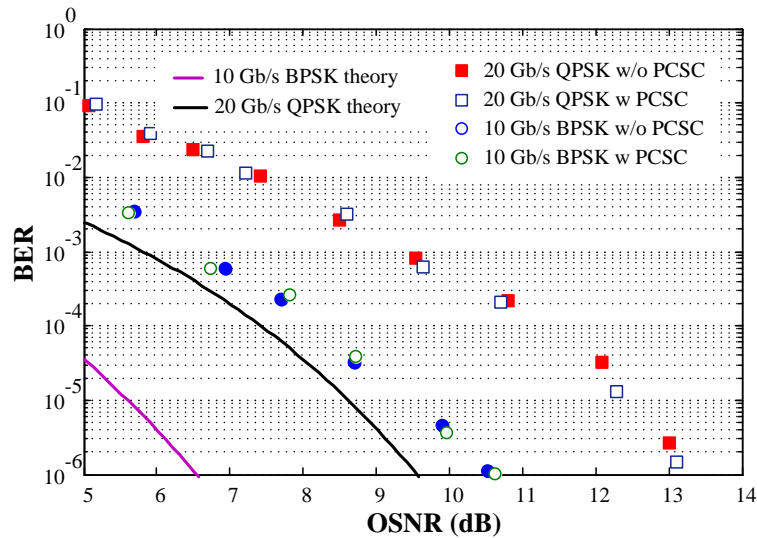


**Figure 4.26:** Back-to-back performance of OFDM systems with and without PCSC with BPSK and QPSK modulation formats.

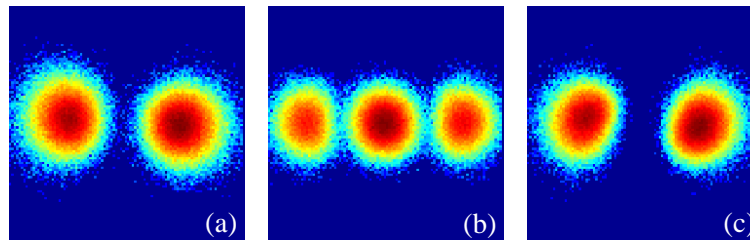


**Figure 4.27:** Received constellation diagrams of the center channel at 4000 km of transmission distance, the launch power/channel was -3 dBm, a) without PCSC, b, c) with PCSC, before and after decoding.

pre-EDC is also effective in compensating the nonlinear distortions due to cross phase modulation as long as the OFDM frequency spacing is small. This result confirms that PCSC is effective in both single and WDM transmission configurations.

It should be noted that without pre-EDC, PCSC only provides  $\sim 0.7$  dB performance gain. Moreover, pre-EDC without PCSC shows a slightly worse performance improvement ( $\sim 0.5$  dB). As a result, a combination of PCSC and pre-EDC is necessary to achieve the full benefit of the PCSC nonlinear mitigation scheme. The similar result for QPSK WDM CO-OFDM transmission is shown in Fig. 4.29, at a transmission distance of 4000 km. The performance enhancement observed is around 0.8 dB when PCSC combined with pre-EDC is applied, confirming that PCSC can also be effectively applied for a high SE modulation format such as QPSK. In Fig. 4.29, pre-EDC without PCSC does not improve the system performance. Similarly, without 50 % pre-EDC, PCSC does not provide a

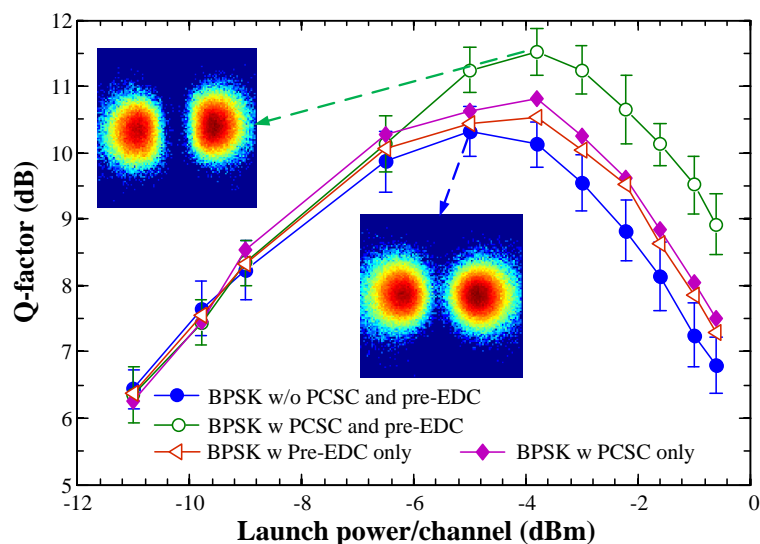


**Figure 4.28:** Q-factor as a function of the launch power/channel for the center channel in BPSK WDM CO-OFDM systems with and without PCSC, the transmission distance is 6000 km.

significant performance gain, which agrees well with the simulation result presented in Fig. 4.22. As a consequence, PCSC should be combined with pre-EDC to achieve the best performance for both BPSK and QPSK transmissions. As it was explained before, the nonlinear noise squeezing effect is not beneficial to a quadrature modulation format such as QPSK. As a result, the performance gain in QPSK transmission is smaller than those obtained in BPSK transmission.

## 4.4 Conclusion

The narrow frequency spacing in CO-OFDM leads to strong correlation of nonlinear distortions between neighbouring subcarriers. As a result, unlike the SC transmission scheme, the nonlinear distortions in CO-OFDM systems can be effectively mitigated in the frequency domain.

By transmitting a portion of OFDM subcarriers (up to 50 %) with its phase-conjugates, the fibre nonlinearity impairments can be mitigated in a flexible way. The PCPs can be used at the receiver to estimate the nonlinear distortions in the respective subcarriers and other subcarriers, which are not accompanied by PCPs. Simulation and experimental results show that, by varying the PCP overhead a performance improvement up to 4 dB can be achieved. In addition, the PCP technique can be effectively applied in both single po-

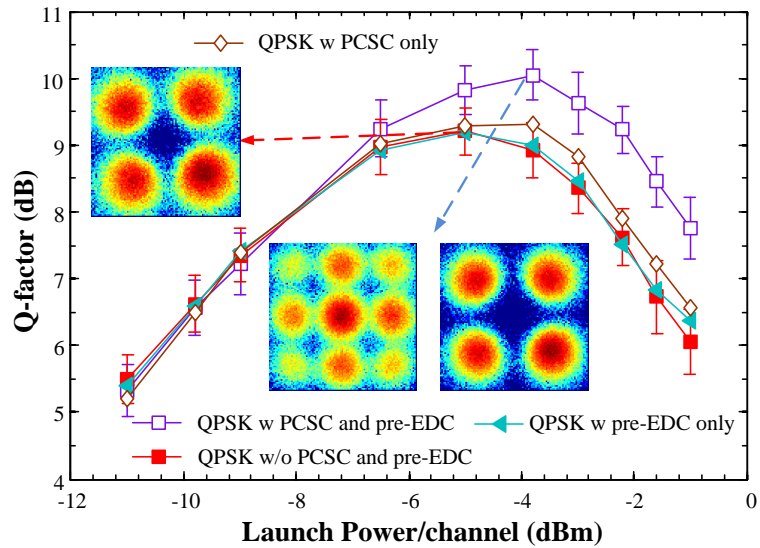


**Figure 4.29:** Q-factor as a function of the launch power/channel for the center channel in QPSK WDM CO-OFDM systems with and without PCSC, the transmission distance is 4000 km.

larization and polarization division multiplexed systems, in both single channel and wave length division multiplexing systems, thus, offering highest flexibility in implementations.

In addition, the fibre nonlinearity impairments in CO-OFDM transmission can also be effectively mitigated by processing neighboring subcarriers simultaneously using the PCSC scheme. This coding scheme is very simple and can be effectively combined with pre-EDC to achieve a performance improvement up to 1.5 dB. In similar maner to PCP technique, PCSC technique can also be effectively applied in both single polarization and PDM systems, in both single channel and WDM systems without suffering from carrier uncertainty problem.

## Chapter 5

# Nonlinear Fourier Transform Based Optical Communication Systems

**Son T. Le**, Jaroslaw E. Prilepsky, P. Rosa and Sergei K. Turitsyn, ‘ Nonlinear Inverse Synthesis for Optical Links with Distributed Raman Amplificatio,” Journal of Lightwave Technology, vol. 34, no. 5, pp. 1-9, Mar. 2016 (**invited**).

**Son T. Le**, Jaroslaw E. Prilepsky, and Sergei K. Turitsyn, “Nonlinear inverse synthesis technique for optical links with lumped amplification,” Opt. Express Vol. 23, Issue 7, pp. 8317-8328 (2015).

**Son T. Le**, J. E. Prilepsky, and S. K. Turitsyn, “Nonlinear inverse synthesis for high spectral efficiency transmission in optical fibres,” Opt. Express Vol. 22, Iss. 22, pp. 2672026741 (2014).

**Son T. Le**, Ian D. Philips, Jaroslaw E. Prilepsky, Paul Harper, Andrew D. Ellis and Sergei K. Turitsyn, “Demonstration of Nonlinear Inverse Synthesis Transmission over Transoceanic Distances,” Journal of Lightwave Technology, 2016.

### 5.1 Introduction

As discussed in the Chapter 1, the increasing demand from the growing number of bandwidth-hungry applications and on-line services (such as cloud computing, HD video streams,

on-line content sharing and many others) is pushing the required communication capacity of fibre optical systems close to the theoretical limit of a SSMF [14, 15], which is imposed by the inherent fibre nonlinearity [14]. In the last decade, extensive efforts have been made in attempting to suppress the impact of Kerr nonlinearity through various nonlinearity compensation techniques, including digital back-propagation [68], digital [78] and optical [79, 102] phase conjugations at the mid-link or installed at the transmitter [80], and phase-conjugated twin waves [81, 100]. However, there are still many limitations and challenges to overcome in applying the aforementioned nonlinear compensation methods in terms of flexibility and especially the implementation complexity. As a result, further research in novel methods to combat the impairments due to fibre nonlinearity is highly desirable.

In recent years, an alternative approach of designing fibre optical communication systems [66, 103–106], which takes into account the fibre nonlinearity as an essential element rather than a destructive effect has been actively discussed – the NFT-based approach. The main idea behind this approach is based on the fact that without perturbation the nonlinear Schrödinger equation (NLSE), which governs the propagation of optical signal in SSMF, is an integrable nonlinear system [107–110]. In particular, this means that the NLSE allows the existence of a special type of solutions: highly robust nonlinear waves, called solitons.

Solitons were proposed as the information carriers for the high-capacity fibre-optic communications [108, 110]. However, on-off keying transmission built on pure fundamental solitons (i.e., where the solitons have been used as individual information-bearing pulses) was affected by the soliton collision problems and ensuing limitations due to the inter-channel cross-talk in WDM lightwave transmission systems [108, 111] leading to the reduction in spectral efficiency; although some recent works demonstrated positive results with regard to coherent soliton-based transmission using multilevel modulation [112].

Another, less known in the optical communication community, consequence of the NLSEs integrability is that it allows one to present the field evolution within a special combination of nonlinear normal modes, including non-dispersive soliton modes and quasilinear dispersive radiation modes. The dynamics of individual nonlinear modes is essentially

linear, which means that the nonlinearity-induced cross-talk between these modes is effectively absent during the propagation [109, 113, 114] From an information and communication theory point of view, these nonlinear modes, which can be obtained by the NFT, can potentially be used to encode information that, in turn, can be recovered at the receiver without suffering from the nonlinear impairments [103, 109, 113, 114].

The prefiguration of this general idea was first introduced by Hasegawa and Nyu in [103], termed as eigenvalue communications. In the original version [103], this approach was focused on the invariance of the discrete eigenvalues (i.e., those attributed to the solitonic degrees of freedom) of the Lax operator associated with the NLSE, that were further used to encode and transmit information. In more general words, the class of digital processing approaches based on the integrability of the underlying dynamical system (at least in the leading approximation) opens fundamentally new possibilities for advanced modulation, coding, and transmission schemes, which are inherently resistant against the nonlinear fibre effects. The implementation of this research program leads to the foundation of a nonlinear communication theory.

Recently, two main directions in the NFT communications methodology have been proposed, which are categorized according to what part of the nonlinear spectrum (solitonic discrete part or continuous part) is used for the modulation and transmission. The approach of using discrete (solitonic) components of the nonlinear spectrum for data communications [115–120] is often referred to as nonlinear frequency division multiplexing (NFDM) and initial experimental demonstrations have been reported recently [115–117]. In [115] the transmission of a 4 Gb/s nonlinear frequency division multiplexing system in burst mode was demonstrated over 640 km. In this experiment, each burst, which carries 4 bits, contains two eigenvalues each modulated by QPSK constellations. In [117] 3-eigenvalue multi-soliton NFDM signals at 0.5 Gbaud was successfully transmitted over 1800 km. However, the nonlinear frequency division multiplexing method requires considerable optimization of the pulse shapes for the purpose of maximizing the resulting spectral efficiency [120]. The second approach based on the modulation of the continuous part of the nonlinear spectrum, was proposed in [104] and was assessed in detail numerically in [121–128] (for optical links with ideal Raman amplification, Erbium doped fibre

amplifiers (EDFAs), and non-ideal Raman amplification, respectively) and was termed there as the NIS method. Recently, both the continuous and discrete parts of the nonlinear spectrum have also been considered simultaneously [129].

In this chapter, firstly, the author discusses the NLSE model of optical fibre communication channel. Then an overview about NFT-based transmission method, NFT operations and basis system designs is given. Next, the implementation and performance analysis of NIS scheme, in which transmitted information is encoded directly onto the continuous part of the nonlinear signal spectrum, is considered in details. It is shown that OFDM is the preferable modulation format for NIS-based transmission schemes. Furthermore, the author proposed modified NIS schemes for optical links with EDFA and Raman-based amplifiers. Finally, the author presents the first experimental demonstration of NIS-based scheme over transoceanic distances.

## 5.2 NLSE model of optical fibre communication channel

The evolution of electrical field  $q(z, t)$  along a lossless single-mode optical fibre can be modelled using the NLSE [4, 107]:

$$i \frac{\partial q}{\partial z} - \frac{\beta_2}{2} \frac{\partial^2 q}{\partial t^2} + \gamma |q|^2 q = 0, \quad (5.1)$$

with  $z$  being a distance along the fibre,  $t$  is time in the frame co-moving with the velocity of the envelope. The parameter  $\beta_2$  is the characteristic of chromatic dispersion that can be negative for the anomalous dispersion (the most important practical case) or  $\beta_2 > 0$  for the normal dispersion  $\gamma$  is the nonlinear Kerr coefficient.

When dealing with the NFT it is convenient to work with the NLSE in the normalized form (the upper and lower signs correspond to the anomalous and normal dispersion cases):

$$i \frac{\partial q}{\partial z} \pm \frac{1}{2} \frac{\partial^2 q}{\partial t^2} + |q|^2 q = 0, \quad (5.2)$$

which can be obtained through the following rescaling of variables:

$$t/T_s \rightarrow t, \quad z/Z_s \rightarrow z, \quad q\sqrt{\gamma Z_s} \rightarrow q, \quad (5.3)$$

where  $T_s$  is a free parameter (e.g., a characteristic time scale of the input waveform) and the associated space scale is  $Z_s = T_s^2/|\beta_2|$ . Note that all the quantities in the normalized Eq. 5.2, namely,  $q$ ,  $t$ , and  $z$ , are now dimensionless.

## 5.3 Basic of NFT operations

In this section, the concepts of direct (forward) and inverse NFT (INFT) are reviewed. The basic functionality of NFT operation is to transform the signal  $q(z, t)$  at a fixed location  $z = z_0$  to the corresponding NFT spectrum. The INFT reverses this process, i.e., given a NFT spectrum it returns the corresponding signal  $q(z_0, t)$ .

### 5.3.1 Direct NFT

The direct NFT is computed from specific solutions  $v_{1,2}(t, \zeta) = v_{1,2}(t, \zeta; z_0)$  of the Zakharov–Shabat problem (ZSP)

$$\frac{dv_1}{dt} = q(z_0, t)v_2 - i\zeta v_1, \quad \frac{dv_2}{dt} = \mp \bar{q}(z_0, t)v_1 + i\zeta v_2, \quad (5.4)$$

for different values of the complex parameter  $\zeta = \xi + i\eta$ , which play the role of a nonlinear analog of frequency. The signal waveform  $q(z, t)$ , at a fixed location  $z = z_0$  in the ZSP, acts as a potential. The upper and lower signs correspond to the anomalous and normal dispersion according to Eq. (5.2). It is assumed here that  $q(z_0, t)$  decays at least exponentially for  $t \rightarrow \pm\infty$ , which is appropriate for practical applications. Specific solutions (the so-called Jost functions)  $\phi_{1,2}(t, \zeta)$  and  $\psi_{1,2}(t, \zeta)$  to the ZSP can be obtained from the

boundary conditions:

$$\phi_1(t, \zeta) = e^{-i\zeta t} + o(1), \quad \phi_2(t, \zeta) = o(1) \text{ for } t \rightarrow -\infty, \quad (5.5)$$

$$\psi_1(t, \zeta) = o(1), \quad \psi_2(t, \zeta) = e^{i\zeta t} + o(1) \text{ for } t \rightarrow +\infty, \quad (5.6)$$

In practical implementation, the pulse  $q(t)$  is truncated to have a finite duration (a symbol duration), and the initial conditions are set at the trailing or leading end of the finite-extent pulse. The little- $o$  notation used here indicates a difference that vanishes in the limit, e.g.,  $|\psi_1(t, \zeta) - e^{-i\zeta t}| \leq c/|t|$  for some unknown constant  $c > 0$ . It turns out that the pairs  $\tilde{\phi}_1 = -\bar{\phi}_2$  and  $\tilde{\phi}_2 = \bar{\phi}_1$  as well as  $\tilde{\psi}_1 = -\bar{\psi}_2$  and  $\tilde{\psi}_2 = \bar{\psi}_1$  solve the ZSP as well, and that all these different solutions are linearly dependent as follows:

$$\begin{pmatrix} \phi_1 \\ \phi_2 \end{pmatrix} = a(\zeta) \begin{pmatrix} \tilde{\psi}_1 \\ \tilde{\psi}_2 \end{pmatrix} + b(\zeta) \begin{pmatrix} \psi_1 \\ \psi_2 \end{pmatrix}, \quad (5.7)$$

$$\begin{pmatrix} \tilde{\phi}_1 \\ \tilde{\phi}_2 \end{pmatrix} = -\tilde{a}(\zeta) \begin{pmatrix} \psi_1 \\ \psi_2 \end{pmatrix} + \tilde{b}(\zeta) \begin{pmatrix} \tilde{\psi}_1 \\ \tilde{\psi}_2 \end{pmatrix}. \quad (5.8)$$

The functions  $a(\zeta)$  and  $b(\zeta)$  are usually referred to as *Jost scattering coefficients*. They serve as the basis on which the NFT spectrum is defined. Due to the boundary conditions, we have

$$a(\zeta) = \lim_{t \rightarrow \infty} \phi_1(t, \zeta) e^{i\zeta t}, \quad b(\zeta) = \lim_{t \rightarrow \infty} \phi_2(t, \zeta) e^{-i\zeta t}. \quad (5.9)$$

Another important property of the Jost scattering coefficients is that they satisfy  $|a(\xi)|^2 \pm |b(\xi)|^2 = 1$  for all real  $\xi$ , where the upper and lower signs refer to those in Eq. (5.2), (5.4). The NFT spectrum of the signal  $q(z_0, t)$  consists of two parts. The first part (continuous part) is given either by the left and or right reflection coefficient, respectively:

$$l(\xi) = \bar{b}(\xi)/a(\xi), \quad r(\xi) = b(\xi)/a(\xi), \quad \xi \in \mathbb{R}. \quad (5.10)$$

The second part of the NFT spectrum (discrete part) consists of the discrete eigenvalues  $\zeta_n = \xi_n + i\eta_n$ , which are the eigenvalues of the ZSP with a positive imaginary part  $\eta_n > 0$ ,

and their associated left or right norming constants, which are defined by the residue of  $l(\zeta)$  (or  $r(\zeta)$ ) at the point  $\zeta_n$ :

$$l_n = [b(\zeta_n) a'(\zeta_n)]^{-1}, \quad r_n = b(\zeta_n)/a'(\zeta_n), \quad (5.11)$$

where the prime designates the derivative with respect to  $\zeta$ . We therefore have four real parameters defining each solitary degree of freedom. The discrete eigenvalues can be characterized as the roots of the scattering coefficient  $a(\zeta)$  in the complex upper half-plane, i.e.,  $a(\zeta_n) = 0$  and  $\eta > 0$ . The complete (left or right) NFT spectrum of the signal  $q(z_0, t)$  is therefore given by

$$\Sigma_l = \left\{ l(\xi), [\zeta_n, l_n]_{n=1}^N \right\}, \quad \Sigma_r = \left\{ r(\xi), [\zeta_n, r_n]_{n=1}^N \right\}, \quad (5.12)$$

where  $N$  is the total number of solitons in the signal. The NFT spectrum characterizes the signal  $q(z_0, t)$  completely and can be used to recover it given that it vanishes sufficiently fast for  $|t| \rightarrow \pm\infty$ . Note that in the normal dispersion case, the signal cannot have solitonic components and either  $l(\xi)$  or  $r(\xi)$  are sufficient to uniquely recover the corresponding profile  $q(z_0, t)$ . The  $z$ -dependence of the NFT data,  $\Sigma_{l,r}(z)$ , is given by the following expressions:

$$\begin{aligned} \zeta_n(z) &= \zeta_n(z - z_0) \\ l(\xi, z) &= l(\xi, z_0) e^{-2i\xi^2(z-z_0)}, \quad l_n(z) = l_n(z_0) e^{-2i\zeta_n^2(z-z_0)}, \\ r(\xi, z) &= r(\xi, z_0) e^{2i\xi^2(z-z_0)}, \quad r_n(z) = r_n(z_0) e^{2i\zeta_n^2(z-z_0)}. \end{aligned} \quad (5.13)$$

It should be noted that the solitons disappear and the NFT reduces to conventional FT when the signal power becomes small. Any rescaled signal  $q_\varepsilon(t) = \varepsilon q(t)$  satisfies [105, 109]

$$\frac{\bar{r}(\xi, q_\varepsilon(t))}{\varepsilon}, \frac{l(\xi, q_\varepsilon(t))}{\varepsilon} \rightarrow -q(\omega)|_{\omega=-2\xi} \quad \text{when } \varepsilon \rightarrow 0, \quad (5.14)$$

where  $q(\omega) = \int_{-\infty}^{\infty} q(t) e^{-i\omega t} dt$ . Also note that, in optics, the Zakharov–Shabat system (5.4) also appears widely in the field of Bragg grating synthesis [130–132], where the

functions  $v_{1,2}$  play the role of slowly varying coupled mode amplitudes.

### 5.3.2 INFT operation (for the left set of scattering data)

The basic functionality of INFF is to map the scattering data  $\Sigma_{l,r}$  onto the field  $q(t)$ : This can be achieved via the Gelfand-Levitan-Marchenko equation for the unknown functions  $K_{1,2}(t, t')$  [107, 109, 133]. The Gelfand-Levitan-Marchenko equation written in terms of the left scattering data  $l(\xi)$  and  $l_n$ , read as

$$\begin{aligned} \bar{K}_1(\tau, \tau') + \int_{-\infty}^{\tau} dy L(\tau' + y) K_2(\tau, y) &= 0, \\ \mp \bar{K}_2(\tau, \tau') + L(\tau + \tau') + \int_{-\infty}^{\tau} dy L(\tau' + y) K_1(\tau, y) &= 0, \end{aligned} \quad (5.15)$$

for  $\tau > \tau'$ , where the upper and lower signs correspond to upper and lower ones in Eqs. (5.2), (5.4). In practical applications where the operations are performed on the finite interval of  $\tau$ , say  $0 < \tau < T$ , we have the finite region for the change of  $\tau'$ ,  $\tau' < |\tau|$ . For the anomalous dispersion [the sign “ $-$ ” in Eqs. (5.15)] the quantity  $L(\tau)$  can contain contributions from both solitonic (discrete) and radiation (continuous) spectrum parts,  $L(\tau) = L_{sol}(\tau) + L_{rad}(\tau)$ ,

$$L_{sol}(\tau) = -i \sum_n l_n e^{-i\xi_n \tau}, \quad L_{rad}(\tau) = \frac{1}{2\pi} \int_{-\infty}^{\infty} d\xi l(\xi) e^{-i\xi \tau}. \quad (5.16)$$

It is assumed here that all discrete eigenvalues have a unit multiplicity. The variable  $L_{rad}(\tau)$  is thus Fourier conjugated to the “nonlinear frequency”  $\xi$ , so that we can start not from the  $\xi$ -domain but immediately from the functions given by (5.16) in the  $\tau$ -domain. Having solved the Gelfand-Levitan-Marchenko equation (5.15) for  $K_{1,2}(\tau, \tau')$ , the solution in the space-time domain is recovered as  $q(t) = -2\bar{K}_2(t, t)$ . For the soliton-free case we have  $L_{sol}(\tau) = 0$ , and the only quantity participating in (5.15) is the FT of the left reflection coefficient  $l(\xi)$ :  $L(\tau) \equiv L_{rad}(\tau)$ . When one is interested in the solution  $q(Z, t)$  at distance  $z = Z$ , the quantity  $r(\xi)$  in (5.16) is replaced with  $l(Z, \xi)$ . So, the resulting solution of the Gelfand-Levitan-Marchenko equation (5.15) becomes the function of  $Z$ :  $K_{1,2}(Z; \tau, \tau')$ .

## 5.4 Basic designs of NFT-based communication systems

As the evolution of nonlinear spectrum is essentially linear in nonlinear lossless fibre channel (5.14), the nonlinear spectrum can be used for data modulation and transmission. The basic designs and concept of NFT-based transmission systems are presented in the Fig. 5.1. In general, NFT-based transmission systems can be divided into two major groups, which can be referred to as transmission in the nonlinear Fourier domain (NFD) and NFT-based DBP. In the first design (Fig. 5.1(b)), the transmitted information is encoded directly onto the nonlinear signal spectrum (discrete and/or continuous parts) via the INFT. So far, the modulations of continuous spectrum [104, 121], discrete spectrum [115–117] are often considered separately due to the numerical complexity of the full NFT-INFT cycle. The resulted transmission methods are usually termed as NIS and NFDM, respectively. In the second design (Fig. 5.1(c)), the NFTs are used to cancel the nonlinearity distortion in fibre optical communication systems. This can be effectively achieved in the nonlinear Fourier domain with single-tap phase-shift removal as the evolution of nonlinear spectrum is trivial.

In NFDM transmissions, if only one purely imaginary eigenvalue is modulated with on-off keying signal the resulted transmission scheme converges to the conventional soliton transmission scheme. In this case, the transmitted signal can be detected at the receiver without NFT operation (using the conventional time domain sampling receiver). In general, NFDM can be considered as multi-soliton transmission scheme, where one or more solitons, which are modulated in amplitude (imaginary part of eigenvalues), frequency (real part of eigenvalues) or initial position (discrete part,  $l_n(z)$ ), are transmitted simultaneously in one burst.

On the other hand, in comparison to NFDM, NIS is an orthogonal approach, where the vast amount of available degrees of freedom contained in the continuous part of the nonlinear spectrum is exploited for data transmission. As a result, various conventional modulation formats, such as QMAs, can be effectively combined with the NIS method, providing the flexibility in the systems design for achieving a high SE [104, 121, 134]. In addition, NIS is a fully DSP-based approach, and thus, it can be easily integrated with

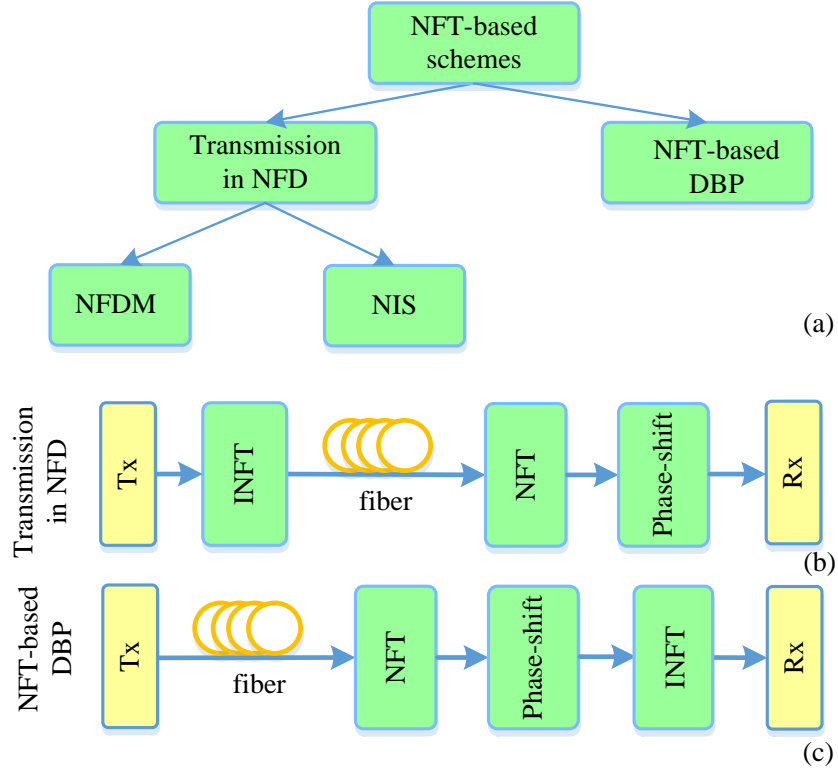


**Figure 5.1:** Basic designs of NFT-based transmission systems (a); transmission in the nonlinear Fourier domain (NFD) (b); nonlinear Fourier domain based BDP (NFD-DBP) (c).

the current coherent transmission technology. Finally, the numerical complexity of NIS, which is independent to the transmission distance, can be competitive and potentially even outperform that of the DBP based methods [121]. As a result, in this chapter the NIS transmission scheme is considered with a particular attention.

## 5.5 Numerical methods for NFT operations

In this section the numerical methods for forward and inverse NFT operations are discussed. Herein, the author focuses mainly on NIS systems and thus only numerical methods dealing with the continuous part of nonlinear signal spectrum will be discussed. In addition, for sake of computation convenience, only the left set of scattering coefficient  $(\Sigma_l = \{l(\xi), [\zeta_n, l_n]_{n=1}^N\})$  is considered.

### 5.5.1 Numerical methods for NFT

The continuous spectrum (i.e., Jost coefficients  $a(\xi)$  and  $a(\xi)$  and the corresponding left coefficient  $l(\xi)$ ), see Eq.(5.9)) can be computed by directly integrating the Zakharov–Shabat system (5.4) and then evaluating the limits for the corresponding Jost function components as:

$$a(\xi) = \lim_{t \rightarrow \infty} \phi_1(t, \xi) e^{i\xi t}, \quad b(\xi) = \lim_{t \rightarrow \infty} \phi_2(t, \xi) e^{-i\xi t}. \quad (5.17)$$

Several discretization and integration methods have been proposed to solve the ZSP (5.4), including the forward and center discretizations with first-order Euler method [135], the fourth-order Runge-Kutta method [136], and the piecewise-constant approximation (PCA) method [137]. From an implementation point of view, the PCA method offers an attractive solution because it can be implemented effectively in parallel to reduce the computational time [137]. In addition, despite the fact that the Runge-Kutta method is of a higher order, the extra accuracy can be lost because of the additional dependence of its numerical error on the eigenvalue [137]. This phenomenon limits the usefulness of the Runge-Kutta algorithm to a region inside the unit circle around the origin in the complex plane of the eigenvalues. Therefore, only the PCA method will be considered in this thesis. The other numerical methods for computing the FNFT are discussed in [133] and in the references therein.

Although the ZSP is defined on the infinite time line, we must truncate the potential outside a sufficiently large interval in order to make the numerical solution possible. As a result, we reduce the infinite-line spectral problem to a problem with a finite width potential and to the corresponding boundary conditions for the truncated potential.

Now, we recall the basic elements of the PCA, which is conceptually a variant of a layer peeling algorithm applied for the solution of the ZSP [137]. The potential  $q(t)$  is truncated outside a sufficiently large interval  $(T_0; T_0)$ . Inside this interval,  $q(t)$  is chosen to be constant,  $q_n = q(t_n)$ , on each elementary subinterval (or numerical time-step)  $(t_n - \Delta t/2; t_n + \Delta t/2)$ , where  $t_n = T_0 + n\Delta t$ ,  $\Delta t = T_0/M$  is the time step, and  $2M + 1$  is the total number of discretization points inside the considered truncation interval. The idea

of the PCA method is based on the fact that Eq. (5.4) can be solved exactly inside each elementary subinterval for an arbitrary value of the spectral parameter  $\xi$  as:

$$\Phi(t_n + \Delta t/2, \xi) = T(q_n, \xi) \Phi(t_n - \Delta t/2, \xi), \quad (5.18)$$

where  $\Phi = (\phi_1 \quad \phi_2)^T$  and the transfer matrix  $T(q_n, \xi)$  is given by:

$$\begin{aligned} T(q_n, \xi) &= \exp \left[ \Delta t \begin{pmatrix} -j\xi & q_n \\ -q_n^* & j\xi \end{pmatrix} \right] \\ &= \begin{pmatrix} \cosh(k\Delta t) - j\xi k^{-1} \sinh(k\Delta t) & q_n k^{-1} \sinh(k\Delta t) \\ -\xi^* k^{-1} \sinh(k\Delta t) & \cosh(k\Delta t) + j\xi k^{-1} \sinh(k\Delta t) \end{pmatrix}, \end{aligned} \quad (5.19)$$

here  $k = j\sqrt{q_n^2 + \xi^2}$  is a constant parameter in each interval  $\Delta t$ .

The scattering problem can be solved by propagating the solution iteratively, starting from  $T_0$  towards the right truncation border  $T_0$ , using the set of transfer matrices  $T(q_n, \xi)$  given by Eq. (5.19). The final result can be expressed as:

$$\begin{aligned} \Phi(T_0 - \Delta t/2, \xi) &= \Pi(\xi) \Phi(-T_0 + \Delta t/2, \xi), \\ \Pi(\xi) &= \prod_{n=1}^{2M} T(q_n, \xi) \end{aligned} \quad (5.20)$$

The initial condition (5.5) defined at the right truncation end can be written as:

$$\Phi(-T_0 - \Delta t/2, \xi) = \begin{pmatrix} 1 \\ 0 \end{pmatrix} \exp(-j\xi(-T_0 - \Delta t/2)), \quad (5.21)$$

Then, at the left end of the full interval we have:

$$\begin{aligned}\Phi(T_0 - \Delta t/2, \xi) &= \begin{pmatrix} a(\xi)e^{-j\xi(T_0 - \Delta t/2)} \\ b(\xi)e^{j\xi(T_0 - \Delta t/2)} \end{pmatrix} = \begin{pmatrix} \Pi_{11}(\xi) & \Pi_{12}(\xi) \\ \Pi_{21}(\xi) & \Pi_{22}(\xi) \end{pmatrix} \Phi(-T_0 - \Delta t/2, \xi) \\ &= \begin{pmatrix} \Pi_{11}(\xi) & \Pi_{12}(\xi) \\ \Pi_{21}(\xi) & \Pi_{22}(\xi) \end{pmatrix} \begin{pmatrix} e^{-j\xi(-T_0 - \Delta t/2)} \\ 0 \end{pmatrix},\end{aligned}\tag{5.22}$$

and, therefore, the Jost coefficients are given by:

$$a(\xi) = \Pi_{11}(\xi)e^{2j\xi T_0}, \quad b(\xi) = \Pi_{21}(\xi)e^{-j\xi \Delta t}\tag{5.23}$$

In general, when the potential  $q(t)$  is truncated outside the interval  $(T_{min}, T_{max})$  with arbitrary borders, the expression (5.23) can be modified as:

$$a(\xi) = \Pi_{11}(\xi)e^{j\xi(T_{max} - T_{min})}, \quad b(\xi) = \Pi_{21}(\xi)e^{-j\xi(T_{max} + T_{min} - \Delta t)}\tag{5.24}$$

One can notice that the PCA method has some interesting similarities to the transmission line theory, in which the potential  $q(t)$  can be considered as the distributed parameter of the line [138]. From (5.19), one can see that the transfer matrixes  $T(q_n, \xi)$  can be calculated independently of each other. As a result, the PCA algorithm can be easily implemented in parallel to reduce the computational time for high-speed NIS-based systems.

To demonstrate the performance of the PCA method, a rectangular pulse as an example (see, e.g., [105]) is considered:

$$q(t) = \begin{cases} A, & t \in [T_1, T_2] \\ 0, & \text{otherwise} \end{cases}\tag{5.25}$$

The continuous spectrum of this rectangular pulse is given by:

$$l(\xi) = \frac{\bar{A}}{j\xi} \left( 1 - \frac{\sqrt{\xi^2 + |A|^2}}{j\xi} \cot \left( \sqrt{\xi^2 + |A|^2} (T_2 - T_1) \right) \right)\tag{5.26}$$

In Fig. 5.2 the continuous spectra of the rectangular pulse with different amplitudes are

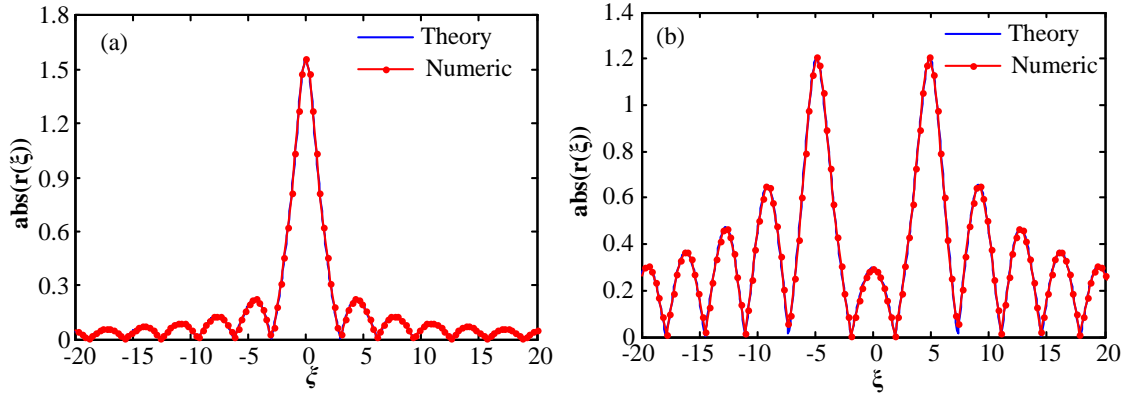


**Figure 5.2:** (a) Continuous spectrum of rectangular pulse for  $A = 1, T_2 - T_1 = 1$  (b) Continuous spectrum of rectangular pulse for  $A = 6, T_2 - T_1 = 1$ .

compared, which are calculated using the analytical formula (5.26) and the numerical PCA method. The normalized root mean squared error (RMSE) of the PCA is defined as follows:

$$MSE = \frac{1}{A} \sqrt{\frac{1}{N} \sum_{k=1}^N |l_{exact}(\xi_k) - l_{numeric}(\xi_k)|^2} \quad (5.27)$$

The dependence of the normalized RMSE on the time resolution  $dt$  is shown in Fig. 5.3.

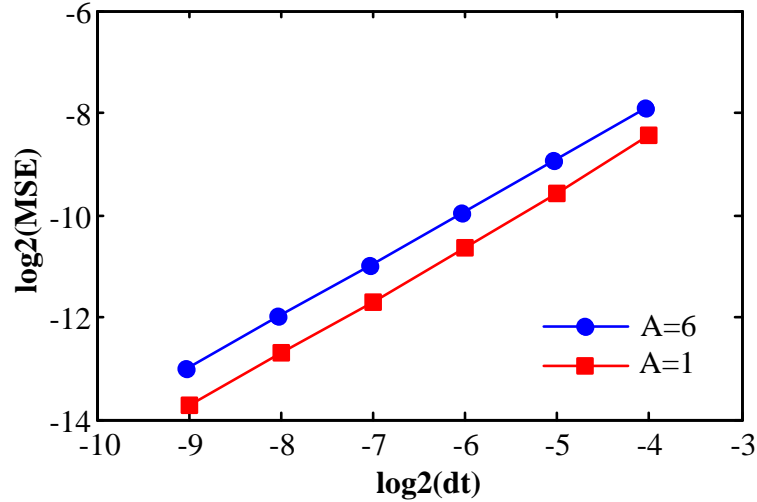


**Figure 5.3:** Mean square error as a function of the simulation time resolution ( $dt$ )

One can note that the RMSE of the PCA method depends on the pulse amplitude or, in general, on the total signal energy. This is a fundamental challenge of PCA and other numerical methods for calculating the forward NFT.

## 5.5.2 Numerical methods for INFT

In this section, only the case of anomalous dispersion, which is of practical interest, is considered. In addition, as mentioned before, the case when discrete part is absent, is focused. On the other words, the INFT considered here is for NIS transmission scheme. As mentioned before, in optics the methods for numerical INFT computation were largely studied with respect to the Bragg gratings synthesis and characterization. Most of the approaches are based on the numerical solution of Gelfand-Levitan-Marchenko equation (5.15).

The Gelfand-Levitan-Marchenko equations (5.15) can be written in this form:

$$\begin{aligned}\bar{K}_1(\tau, \tau') + \int_{-\infty}^{\tau} dy L(\tau' + y) K_2(\tau, y) &= 0, \\ \bar{K}_2(\tau, \tau') - \int_{-\infty}^{\tau} dy L(\tau' + y) K_1(\tau, y) &= L(\tau + \tau'),\end{aligned}\tag{5.28}$$

where  $L(\tau)$  is the linear inverse FT of  $l(\xi)$  and given by:

$$L(\tau) = \frac{1}{2\pi} \int_{-\infty}^{\infty} d\xi l(\xi) e^{-i\xi\tau}.\tag{5.29}$$

To solve Eq. 5.28 numerically, the following change of the variables is used [139, 140]:

$$u(\tau, s) = K_1(\tau, \tau - s), \quad v(\tau, t) = \bar{K}_2(\tau, t - \tau),\tag{5.30}$$

and then the Gelfand-Levitan-Marchenko equation in the form (5.28) can be rewritten as:

$$\begin{aligned}u(\tau, s) + \int_s^{2\tau} \bar{L}(t - s) v(\tau, t) dt &= 0, \\ v(\tau, t) - \int_0^t L(t - s) u(\tau, s) ds &= L(t),\end{aligned}\tag{5.31}$$

Functions  $u(\tau, t)$  and  $v(\tau, t)$  are defined inside the interval  $0 \leq t \leq 2\tau \leq 2T_0$ . The INFT is

then given by:

$$q(t) = 2v(t, 2t - 0) \quad (5.32)$$

Following the discretization procedure provided in [139, 140], the interval  $0 \leq t \leq 2T_0$ , where the function  $L(t)$  is known, is divided into segments of length  $h = 2T_0/N$ . The discrete variables  $t_n$ ,  $s_k$ , and  $\tau_m$  are defined as:

$$\begin{aligned} s_k &= h(k - 1/2), \quad k = 1, 2, \dots, m \\ t_n &= h(n - 1/2), \quad n = 1, 2, \dots, m \\ \tau_m &= mh/2, \quad m = 1, 2, \dots, N \end{aligned} \quad (5.33)$$

The grid functions are also defined as:

$$u_n^{(m)} = u(\tau_m, t_n), \quad v_n^{(m)} = v(\tau_m, t_n), \quad L_n = L(nh) \quad (5.34)$$

Using the rectangular quadrature scheme to approximate the integrals in Eq. (5.31), one obtains the following discrete form of the Gelfand-Levitan-Marchenko equation:

$$\begin{aligned} u_k^{(m)} + h \sum_{n=k}^m \bar{L}_{n-k} v_n^{(m)} &= 0 \\ v_n^{(m)} - h \sum_{k=1}^m L_{n-k} u_k^{(m)} &= L_n \end{aligned} \quad (5.35)$$

The  $m$ th mesh element of the INFT (in the time domain) is then given by:

$$q^{(m)} = 2v_m^{(m)} \quad (5.36)$$

Equations (5.35) can now be written in a matrix form as:

$$\mathbf{G}^{(m)} \begin{pmatrix} \mathbf{u}^{(m)} \\ \mathbf{v}^{(m)} \end{pmatrix} = \mathbf{b}^{(m)} \quad (5.37)$$

where  $\mathbf{b}^{(m)}$  is formed from the zero vector of dimension  $m$  and the vector of dimension  $m$  with components  $L_n$ ;  $\mathbf{G}^{(m)}$  in (5.37) is a square matrix of dimensions  $2m \times 2m$ , which has

the following form:

$$\mathbf{G}^{(m)} = \begin{pmatrix} \mathbf{E}^{(m)} & h\mathbf{L}^{\dagger(m)} \\ -h\mathbf{L}^{(m)} & \mathbf{E}^{(m)} \end{pmatrix} \quad (5.38)$$

Here,  $E^{(m)}$  is the identity (unity)  $m \times m$  matrix,  $\mathbf{L}$  is the lower triangular Toeplitz  $m \times m$  matrix of the form:

$$\mathbf{L}^{(m)} = \begin{pmatrix} L_0 & 0 & 0 & \cdots & 0 \\ L_1 & L_0 & 0 & \cdots & 0 \\ L_2 & L_1 & L_0 & \cdots & 0 \\ \vdots & \vdots & \vdots & \ddots & \vdots \\ L_{m-1} & L_{m-2} & L_{m-3} & \cdots & L_0 \end{pmatrix}, \quad (5.39)$$

and  $\mathbf{L}^{\dagger(m)}$  is the Hermitian conjugate of the matrix  $\mathbf{L}^{(m)}$ .

One can see that  $\mathbf{L}^{(m)}$  is a Toeplitz  $m \times m$  matrix and, as a result,  $\mathbf{G}^{(m)}$  is also a Toeplitz matrix, which is however non-Hermitian (in contrast to that considered in [140]). In order to solve Eq. (5.37), it is necessary to determine the inverse of the matrix  $\mathbf{G}^{(m)}$ . Owing to the special structure of a Toeplitz matrix, its inversion can be obtained using fast algorithms, such as the fast algorithm proposed in [141]. After obtaining the inverse of  $\mathbf{G}^{(m)}$ , the  $m$ th element of the INFT can be calculated as  $q^{(m)} = 2v_m^{(m)}$ .

However, the direct utilization of the approach from [140] for the inversion of a Hermitian Toeplitz matrix implies that at each step one has to update the matrix  $\mathbf{L}^{(m)}$  with one row and one column; i.e., one has a rank 1 update for  $\mathbf{L}^{(m)}$  for each consecutive iteration,  $m = 1, 2, \dots, N$ . In turn, this means that the rank of the whole matrix  $\mathbf{G}^{(m)}$  increases by 2 when one proceeds to the next iteration step,  $m + 1$ . Thus, one cannot apply directly the iteration scheme for the inversion of the non-Hermitian Toeplitz matrix from Zohars method [141], as it assumes the rank 1 matrix update at each iterative step. Therefore, for the non-Hermitian case considered in this study, the approach from [140] is generalized: at every step, say number  $m$ , of the proposed algorithm (which can be named the outer broadening scheme, in contrast to the inner broadening suggested in [140]) the modified matrix  $\tilde{\mathbf{G}}^{(m)}$  with the rank  $N + m$  is used:

$$\tilde{\mathbf{G}}^{(m)} = \begin{pmatrix} \mathbf{E}^{(N)} & h\mathbf{L}^{\dagger(m)} \\ -h\mathbf{L}^{(m)} & \mathbf{E}^{(m)} \end{pmatrix} \quad (5.40)$$

where, as before,  $\mathbf{E}^{(m)}$  is the identity matrix of the corresponding rank. One can see that this modified matrix (5.40) is obtained by taking the first  $N + m$  rows and columns of the general rank  $2N$  matrix  $\mathbf{G}^{(N)}$  from Eqs. (5.37), (5.38). Then, at the  $m$ -th step the modified right hand side vector (cf. Eq. (5.37)) is redefined:

$$\tilde{\mathbf{b}}^{(m)} = [0, 0, \dots, 0, L_0, L_1, \dots, L_{m-1}]^T \quad (5.41)$$

The dimension of  $\tilde{\mathbf{b}}^{(m)}$  is obviously  $N + m$ . The inverse matrix  $\tilde{\mathbf{G}}^{(m)-1}$  at each step is now obtained by the straightforward application of the iterations used in Zohar's method. Finally, one can convolve the modified inverse matrix with the modified right-hand-side vector,  $\tilde{\mathbf{G}}^{(m)-1}\tilde{\mathbf{b}}^{(m)}$ , and takes the last element of the resulting vector to get  $\tilde{v}_m^{(m)}$ ; note that its value is exactly the same as it would be for  $v_m^{(m)}$  if one applies the inner broadening and rank 2 updating from work [140]. The desired distribution in the time domain,  $q(m)$ , is again obtained by using Eq. (5.36) with  $\tilde{v}_m^{(m)}$  inserted. At the next  $(m + 1)$ -th step one takes  $N + m + 1$  rows and columns from the full matrix  $\mathbf{G}^{(N)}$ , Eq. (5.38), to obtain the next  $\tilde{\mathbf{G}}^{(m+1)}$  Toeplitz matrix, so that the rank of the iterative update for this method is just 1, which allows us to perform the next Zohars iteration [141]. Subsequently, one composes the consecutive right hand-side vector  $\tilde{\mathbf{b}}^{(m+1)}$ , convolves it with the inverse matrix  $\tilde{\mathbf{G}}^{(m+1)-1}$  to get  $\tilde{v}_{m+1}^{(m+1)}$ , and then recovers the next value in the time domain  $q^{(m+1)}$ . Repeating these operations for  $m = 1, 2, \dots, N$  gives us the complete recovery of the profile  $q(t)$  for the desired time-domain interval. Note that although here a non-Hermitian case corresponding to the anomalous dispersion NLSE is considered, the same idea with the rank 1 matrix updating can be applied to the inversion of the Hermitian matrix, which in the case of the Gelfand-Levitan-Marchenko equation corresponds to the normal dispersion NLSE [134] or in a number of problems referring to the Bragg grating synthesis [142].

In order to confirm the validity of this numerical approach, the following time-domain

signal, whose exact INFT is known [143], is taken into account:

$$L(t) = v\alpha e^{-\alpha t}, \quad (5.42)$$

where  $\alpha > 0$  and  $-1 \leq v \leq 1$ . The exact solution for the INFT with  $L(t)$  given by Eq. (5.42) is:

$$q(t) = -\frac{4\alpha v\sigma(\sigma-1)}{(\sigma-1)^2 e^{-2\sigma\alpha t} + v^2 e^{2\sigma\alpha t}}, \quad (5.43)$$

where  $\sigma = \sqrt{1+v^2}$ . The numerical and analytical results for the INFT of  $L(t)$  are

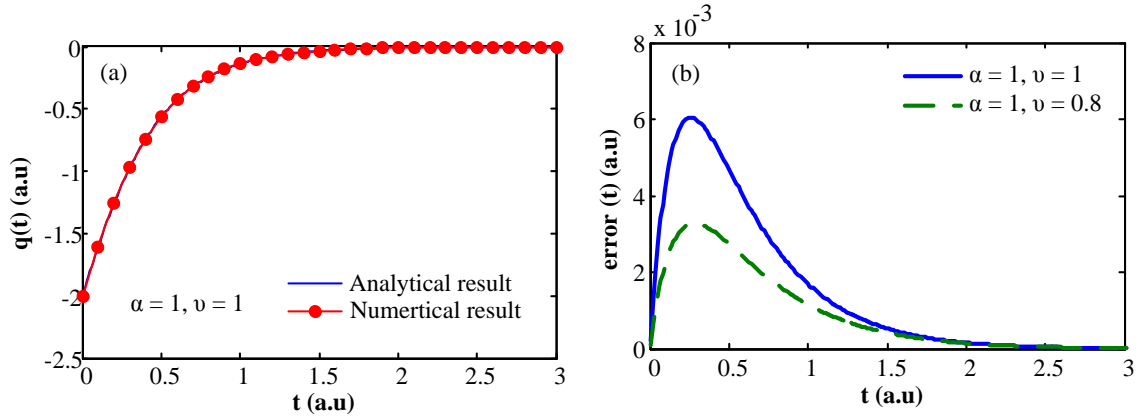


**Figure 5.4:** Comparison between the numerical and analytical results. (a) numerical and analytical solution for  $q(t)$ ,  $dt = 0.01$ . (b) error of numerical method as a function of  $t$

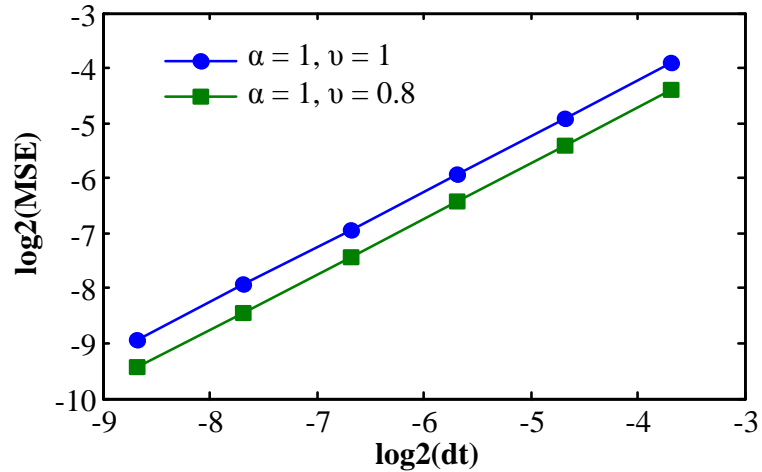


**Figure 5.5:** RMSE as a function of the time resolution  $dt$

compared in Fig. 5.4. The RMSE of this numerical BNFT method, normalized by the peak value of  $L(t)$ , is shown in Fig. 5.5 as a function of the time resolution  $dt$ . A similar behavior with the NFT data behavior has been observed before (see Fig. 5.3), where the

RMSE value also increases with the growth of the input signal power. This increase of the numerical error imposes limitations to the signal launch power in the NIS-based systems.

## 5.6 NIS transmission methods for lossless fibre links

Nonlinear inverse synthesis has been actively discussed recently as an effective technique to combat the fibre nonlinear impairments [104, 121]. In this section, the basic block functions of an NIS-based coherent optical communication system and performances of NIS-based transmission systems with OFDM and Nuqyist pulse shaping formats are presented. For simplicity, only the single channel NIS-based transmission is considered here. The impact of inter-channel nonlinear interference on NIS-based transmission is left for future research.

### 5.6.1 Basis of NIS-based transmissions

The basic block functions of NIS-based optical communication systems are depicted in Fig. 5.6. At the transmitter, the transmitted binary data sequence is first digitally encoded

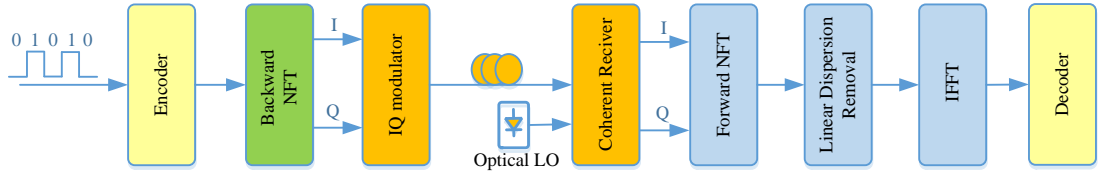


**Figure 5.6:** Block diagram of NIS-based optical communication systems

onto a complex waveform ( $s(t)$ ) using an arbitrary modulation format and coding technique. After the encoder, the linear Fourier spectrum of the encoded complex waveform,  $S(\omega)$ , is mapped onto the continuous part of the nonlinear spectrum of a complex signal  $q(t)$  using the INFT (i.e., by solving the Gelfand-Levitan-Marchenko equation). Let  $l(\xi)$  denote the continuous part of the nonlinear spectrum of  $q(t)$  (the left coefficient). Then, the mapping operation of the IBNFT block can be expressed as:

$$l(\xi)|_{\xi=-\omega/2} = -S(\omega) \quad (5.44)$$

The complex signal,  $q(t)$ , is then fed into the IQ modulator for direct up-converting into the optical domain and launched into the fibre. It is noted that the only additional DSP block required in the transmitter of a NIS-based system is the INFT block, which maps the encoded information onto the continuous part of the nonlinear spectrum of the complex signal ( $q(t)$ ). The complex transmitted signal ( $q(t)$ ) in this case is soliton-free, meaning that the nonlinear spectrum contains no discrete part. At the receiver, the real and imaginary parts of the transmitted signal are detected with a coherent receiver. The nonlinear spectrum of the received signal is obtained by using the forward NFT. After the propagation over a lossless optical fibre channel the interplay between nonlinearity and dispersion can be removed in the nonlinear Fourier domain using a single tap phase shift removal as:

$$\bar{S}(\omega) = -l(L, -\omega/2)e^{j\omega^2 L/2}, \quad (5.45)$$

where  $L$  is the transmission distance.

Then, having performed the phase-shift removal, the complex waveform  $s(t)$  can be recovered using the IFFT operation and, finally, it can be fed into the standard decoder for data detection. As described above, the DSP at the receiver of an NIS-based system involves solving the ZSP and a single linear compensation step to remove the nonlinear impairments without reverse propagation. This clearly demonstrates the advantage of the NIS method over the other nonlinear compensation techniques as the complexity of NIS method is distance independent.

## 5.6.2 Computational complexities of NIS method

An important quantity to consider with regard to the NIS (and generally NFT-based) transmission methods is the numerical complexity (the number of floating point operations) of the NFT-based processing. This can be compared to, e.g., the popular DBP technique for the removal of nonlinear signal distortions [68]. For the latter, one reads the transmitted waveform at the receiver, inserts it as an input for the noiseless NLSE, swaps the sign of  $z$ , and then solves the NLSE in a backward direction down to the initial point  $z = 0$ . The numerical solution of the NSLE is usually performed by using different modifications of a

split-Step Fourier method (SSFM) [4], which typically requires  $M_z N \log(N)$  floating point operations. Here, the value of the numerical factor depends on the order (and type) of the SSFM and it is usually of the order of 10 or more, where  $N$  is the number of discretization points in the time domain, and  $M_z$  the number of steps in  $z$  (the distance along the fibre).  $M_z$  is linearly proportional to the overall transmission length and can also depend on the pulse power when the latter is high enough and the elementary dispersion step in  $z$  becomes comparable to or larger than a nonlinear step; see [4] for more details and direct references with regard to the SSFMs performance and accuracy. In realistic problems, for long-haul transmission lines one typically has  $M_z \gg 1$ . In turn, the NIS method involves just two separate nonlinear transforms, INFT at the transmitter and NFT at the receiver. Each of the NFTs requires  $N^2$  floating-point operations with the use of well-developed traditional methods; see [135,137] for the estimations and comparison of the PCA method, and [140] and references therein for the Hermitian BNFT based on the Toeplitz matrix inversion applied to the Bragg gratings synthesis. Even with this estimation in mind, the numerical complexity of the NIS can already be comparable with that of DBP for sufficiently long transmission lines [104]. However, the recent advancements in numerical NFT indicate that the complexity of NIS can be potentially reduced even further than  $N^2$  operations.

Herein, for the solution of the Gelfand-Levitan-Marchenko equation (INFT) the method based on the Toeplitz matrix inversions [140] is utilized. A number of works propose stable superfast algorithms for the Toeplitz matrix inversion [144, 145], where the reported number of the floating point operations is only  $N \log^2(N)$  or  $N \log^3(N)$ , so that it is generally comparable with the numerical complexity of a single FFT operation (the recent advancements in superfast Toeplitz matrix inversion methods are summarized in [145].) This means that it is already approximately of the same order as required for a single step of the SSFM used in the DBP method.

Another direction in the development of the NIS approach is the increase of the precision of the INFT, which actually limits the performance of the NIS; see Fig. 5.5. In particular, in [146] the authors suggested the usage of higher-order integration schemes when proceeding to the matrix equations, to gain a higher accuracy for the Hermitian

Gelfand-Levitan-Marchenko equation solution while keeping the same order of the numerical complexity. Potentially, there are many different variants for the INFT methods [140, 141, 143, 147, 148] applicable to the Hermitian version of the Gelfand-Levitan-Marchenko equation, most of which can be generalized to the case of the non-Hermitian Gelfand-Levitan-Marchenko equation (without solitons), opening the possibility for a versatile design of the NFT-based processing schemes. For the ZSP (INFT), very recent studies [149, 150] suggest that the recovery of the continuous part of the nonlinear spectrum, utilized further in this study, can be achieved in only  $N \log^2(N)$  operations; actually, this fact demonstrates the advantage of the NIS method based exactly on the continuous part of the nonlinear spectrum, since for the solitonic part the complexity of the FNFT and BNFT can be sufficiently higher. Therefore, this complexity is again comparable with that of just a single SSPM step.

Because of the estimations given above, the author believes that the NIS-based transmission methods can be highly competitive and even eventually outperform DBP in terms of numerical complexity for the digital signal processing, especially when long-haul transmission is addressed. With the application of the methods having higher accuracy, the performance characteristics of NIS can also be potentially enhanced further, and the availability of different solutions for the numerical NFT operations makes the particular design of the NIS-based transmission lines fairly flexible.

### 5.6.3 Simulation results and discussions

In this subsection, a study of the performance of high-bit-rate, high-SE NIS-based systems in comparison with systems employing DBP and having the same parameters is presented. As the NFTs are performed here with the signal decaying to zero at the far ends, the

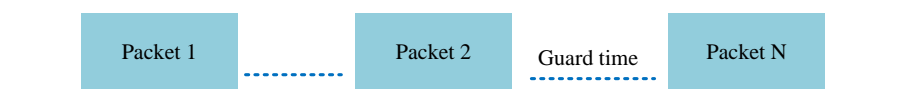


**Figure 5.7:** Illustration of a burst mode transmission, in which neighbouring packets are separated by a guard time

proposed NIS approach is appropriate for the burst mode transmission (Fig. 5.7) of a multi-access network, in which neighbouring packets are separated by a guard time. The guard

time duration is chosen 20 % longer than the channel memory, which, in this case, is the fibre chromatic dispersion induced memory (14 ns). Different packet data can be sent from the same or different transmitters. Herein, for simplicity it is assumed that all packet data are from the same transmitter.

The author takes into account the high-SE transmission modulation schemes, namely, the OFDM and single-carrier system with Nyquist pulse shaping (Nyquist-shaped). 56-Gbaud OFDM and Nyquist-shaped NIS-based transmission systems are designed (in burst mode) with high SE-modulation formats; namely, QPSK, 16QAM, and 64QAM. The net data rates (within the useful burst duration or excluding the guard interval) of these systems, after removing 7 % overhead due to the FEC, were 100 Gb/s, 200 Gb/s, and 300 Gb/s, respectively. The guard time duration is chosen as 20 % longer than the fibre chromatic dispersion induced memory for a 2000 km-link (14 ns). For the OFDM NIS-based system, the IFFT size was 128, where 112 subcarriers were filled with data (with Gray-coding) while the remaining subcarriers were set to zero. The useful OFDM symbol duration was 2 ns and no cyclic prefix was used for the linear dispersion removal. After the IFFT, the time domain OFDM signal was fed into the BNFT block. For simplicity it is assumed that each packet data contains only one OFDM symbol. In the case of Nyquist-shaped system, each packet data contains 128 symbols. An oversampling factor of 40 was used for both OFDM and Nyquist-shaped system, resulting in a total simulation bandwidth of around 2 THz. The oversampling factor of 40 was adopted to diminish the numerical errors associated with the BNFT and FNFT for achieving an accurate estimate of the performance for the NIS approach. In this work, all the DSPs are performed for the same value of the oversampling factor (i.e. 40).

The transmission link was assumed to be lossless (with ideal Raman amplification), for which the ASE noise density is expressed through the fibre link parameters as:

$$N_{ASE} = \alpha L h f_s K_T, \quad (5.46)$$

where  $\alpha$  is the fibre loss,  $L$  is the transmission distance,  $h f_s$  is the photon energy,  $f_s$  is the optical frequency of the Raman pump providing the distributed gain, and  $K_T$  is the

photon occupancy factor, which is taken to be equal to 1.13 for the Raman amplification of the fibre-optic communication systems at room temperature [14]. In simulation, it was assumed that the long-haul fibre link consisted of 80-km spans of SSMF with a loss parameter of 0.2 dB/km, nonlinearity coefficient of 1.22/W/km, and dispersion of 16 ps/nm/km. To demonstrate a more realistic transmission condition a photon occupancy factor of 4 is used in simulation, and the ASE noise was added after each fibre span. At the receiver, after coherent detection, the FNFT was performed by employing the PCA method to obtain the nonlinear spectrum (left reflection coefficient). The single-tap phase-shift removal was then performed to recover the nonlinear spectrum of the transmitted signal, which was followed by the IFFT operation and then the feeding of the outcome into the standard decoder. In this simulation, it is assumed to have a perfect timing synchronization, the transmitter laser and the local oscillator are noiseless and no frequency offset is considered. For simplicity, only the transmission of a single packet is considered. Monte-Carlo simulation is then performed to estimate the system performance using the error vector magnitude (EVM) and direct error counting method. For convenience, the estimated system BER is then converted into Q-factor.

**NIS performance without the ASE noise** Firstly, the case of without ASE noise is considered. In this case, fibre nonlinearity is the only impairment. The linear spectra of OFDM signals before and after the BNFT are shown in the Fig. 5.8. It can be seen that after the INFT, the linear spectrum of the OFDM signal does not broaden significantly, indicating that the NIS method combined with the OFDM can be potentially applied for a WDM transmission or even multiplexed into superchannels. However, the performance of the NIS scheme for the WDM transmission is beyond of the scope of this thesis, and only single channel transmission is considered here. In addition, the impact of linear filtering is not considered also. The linear and nonlinear inter-channel crosstalks in NIS-based systems are important subjects for future research.

Figure 5.9 compares the performance of the 100 Gb/s OFDM and Nyquist systems with and without the NIS method for fibre nonlinearity compensation. Herein, the fibre nonlinearity is the only channel's impairment. The QPSK modulation format was used.

The performance indicator is the Q-factor, which is calculated through the EVM [22]. In Fig. 5.9, almost no mismatch is observed between the back-to-back performance (without ASE noise) and the performance after 2000 km of SSFM for NIS-based systems. It can be noted that the back-to-back performance in the investigated NIS-based system is limited by around 45 dB even in the noiseless case. This is due to numerical errors associated with the finite sampling frequency and guard interval duration. The limitation due to the finite sampling frequency is technological which can be suppressed using more efficient NFT algorithms. However, the performance limitation due to the finite guard interval duration is fundamental which can be suppressed only by increasing the guard interval duration. However, increasing the guard interval duration reduces the system spectral efficiency.

The result presented in Fig. 5.9 confirms that the NIS-based approach can perfectly compensate for the deterministic impairment due to the fibre nonlinearity, using just a single-tap linear dispersion removal for the nonlinear spectrum at the receiver. This result demonstrates the potential of the NIS method as a novel alternative approach for compensating the fibre nonlinearity impairments in optical communication. However, one can note that the back-to-back performance of NIS-based systems deteriorates when the input signal power increases. In particular, if the launch power is above 0 dBm, NIS-based system actually offers a worse performance in comparison to the traditional transmission system (Fig. 5.9 (b)). Fortunately, such a high power regime is out of interest for the system under investigation.

The performance degradation in NIS-based systems when the input power is increased can be explained by the fact that the numerical error of NFTs grows with the increase of input signal power, as shown in Fig. 5.3 and Fig. 5.5. Consequently, the accuracy of the NFT operations imposes a technological limit on the NIS-based transmission systems. This limitation is not fundamental as the accuracy of NFT operations can be increased with novel algorithms or computational efforts. In particular, the reduction of the relative error of the NFTs is achieved by increasing the sampling rate. However, this approach cannot be ultimately effective because of the limitation of the time sampling resolution in the current ADC/DAC technology. A more practical but challenging approach would be to develop more accurate and efficient algorithms for performing the backward and forward

NFTs. As a result, a lot of efforts have yet to be applied in this direction to make the NIS methods performance more efficient, keeping in mind the constraints in the time sampling resolution.

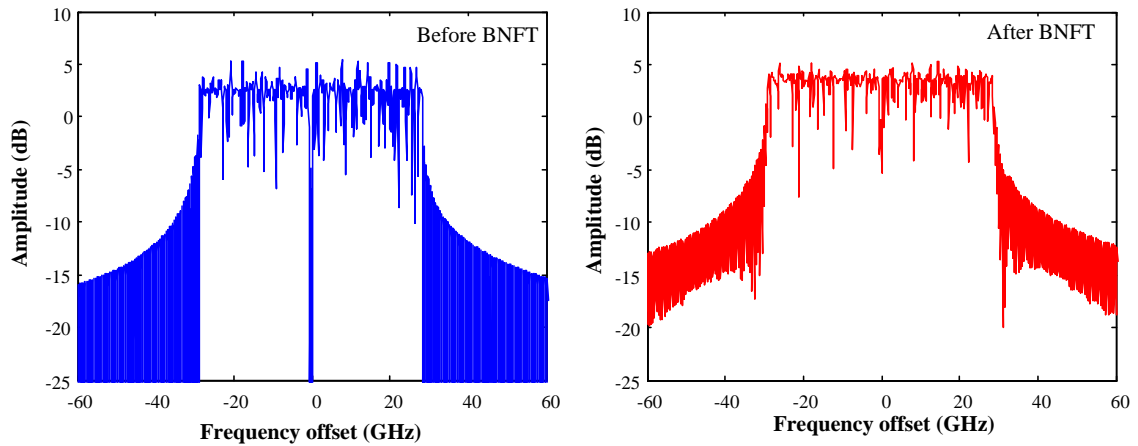


**Figure 5.8:** Linear spectra of OFDM signals before and after BNFT, the launch power is 0 dBm.

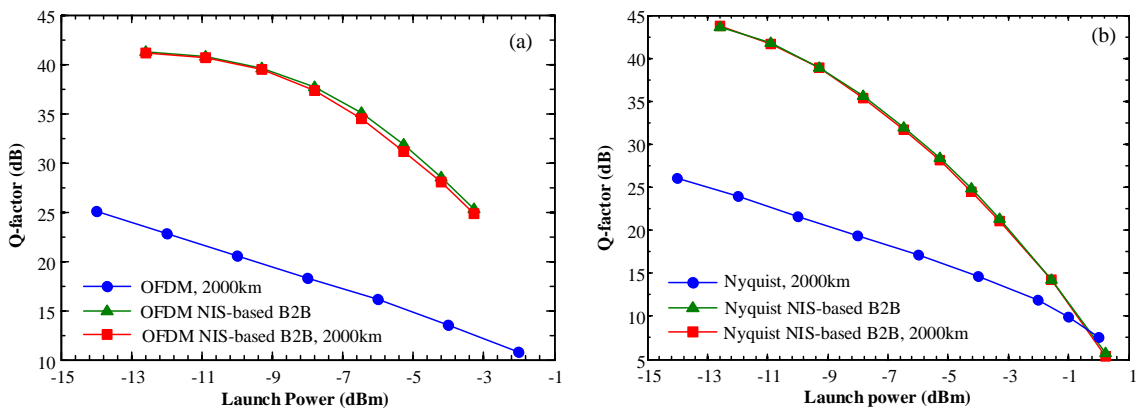


**Figure 5.9:** Q-factor as a function of the launch power for the (a) OFDM and (b) Nyquist-shaped NIS-based systems without the ASE noise.

**Performance comparison of NIS versus DBP** In this paragraph, the performances of the OFDM and Nyquist-shaped systems with the use of the NIS and DBP methods for fibre nonlinearity compensation are compared. For the implementation of DBP, the received signal is first filtered with an 8th order low-pass filter having a bandwidth of 40 GHz. Subsequently, the optical field is reconstructed and the signal is back-propagated with a different number of steps per single span, indicating the numerical complexity of the corresponding DBP realization.

In Fig. 5.10, the Q-factors of OFDM systems with NIS and DBP are compared. One

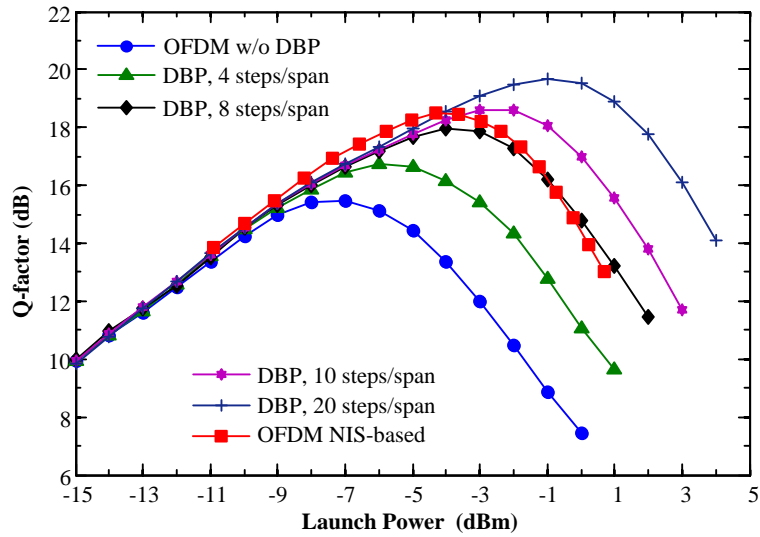


**Figure 5.10:** Performance comparison of the 100 Gb/s QPSK OFDM systems with the NIS vs. the DBP methods for fibre nonlinearity compensation. The receiver filter bandwidth used was 40 GHz, the distance is 2000 km.

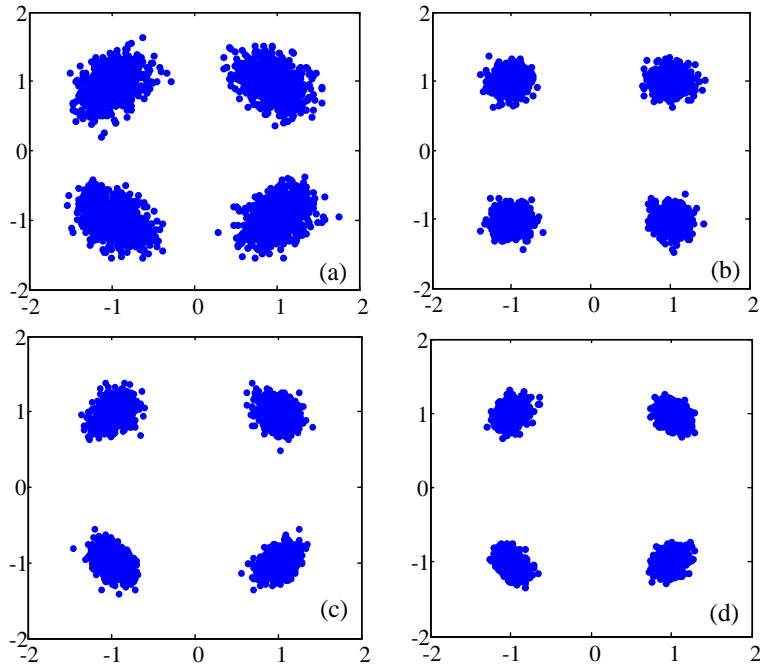


**Figure 5.11:** Constellation diagrams at the optimum launch powers of the 100 Gb/s QPSK OFDM systems with and without the NIS and DBP methods for fibre compensation; (a) without NIS and DBP, (b) with the NIS method, (c) DBP with 10 steps/span, (d) DBP with 20 steps/span.

can see that the OFDM NIS-based system offers over 3.5 dB advantage over the traditional OFDM system (for the single channel transmission case), confirming the effectiveness of the proposed approach for fibre nonlinearity compensation. This performance improvement is comparable with that of DBP with 10 steps per span. The launch power in the NIS-based system is limited to -4 dBm (the optimum launch power), which the author

believes is mainly due to the numerical errors of the backward and forward NFT at the transmitter and receiver, respectively. This argument is also supported by the fact that the Q-factor of the OFDM NIS-based system decreases faster than that of the DBP for the high-input powers. The constellation diagrams of the OFDM systems with NIS and DBP recorded at the corresponding optimum launch powers are shown in Fig. 5.11. It should be noted that the received constellation diagram in system with 10 steps per span DBP clearly indicates the presence of residual nonlinear phase noise. On the other hand, the constellation diagram in system with NIS approach looks “rounded”, indicating that nonlinear phase noise has been fully compensated. The main residual impairment here is the numerical error of the NFTs.

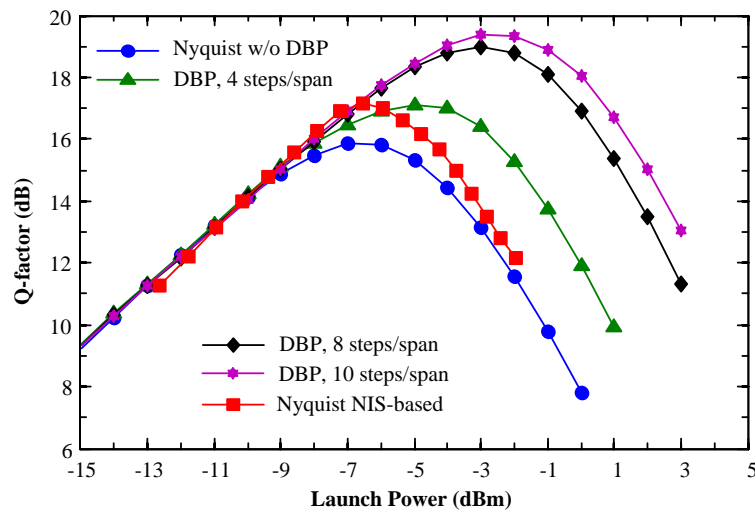


**Figure 5.12:** Performance comparison of the 100 Gb/s QPSK Nyquist-shaped systems with the NIS and DBP methods for fibre nonlinearity compensation. The receiver filter bandwidth is 40 GHz, the distance is 2000 km.

In Fig. 5.12, the performance of the 100 Gb/s (excluding the guard interval) Nyquist-shaped systems with and without the NIS and DBP techniques is compared. It is evident that for the NIS method a performance improvement of about 1.5 dB can be achieved. This improvement is comparable with what can be realized with the DBP approach using 4 steps per span. In this simulations, it is observed that the OFDM and Nyquist-shaped systems have similar performance, which agrees well with some current numerical and experimental comparisons of the OFDM and Nyquist-shaped systems [151, 152]. However, when combining it with the NIS method, OFDM displays a much better performance. In the considered system configuration, the optimum Q-factor of the OFDM NIS-based

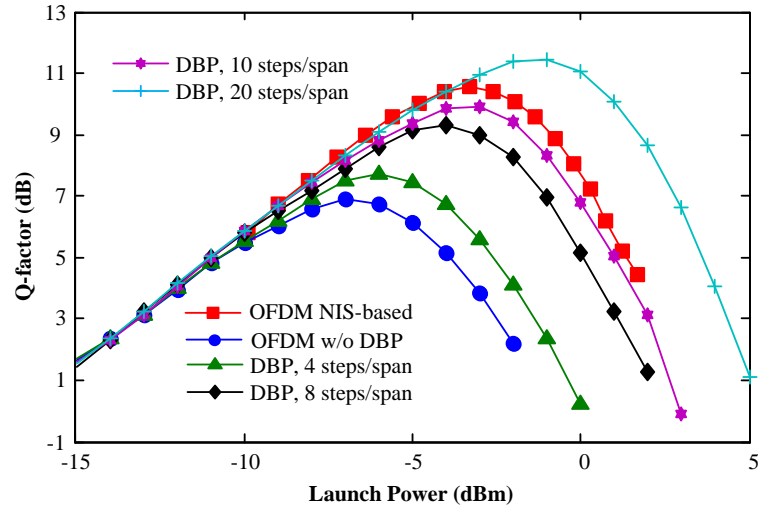


**Figure 5.13:** Constellation diagrams at the optimum launch powers of the 100 Gb/s QPSK OFDM systems with and without the NIS and DBP methods for fibre compensation; (a) without NIS and DBP, (b) with the NIS method, (c) DBP with 10 steps/span, (d) DBP with 20 steps/span.

system is around 19 dB, while for the Nyquist-shaped NIS-based system the optimum Q-factor is approximately 17.5 dB. It is also noted that the OFDM NIS-based system has a better performance than the Nyquist-shaped NIS-based one in the back-to-back regime. This indicates that the numerical error associated with the NFT transformations for the same power is smaller for the OFDM than for the Nyquist-shaped signal. This is due to the fact that the OFDM signal has a smaller L1-norm in comparison with that of the Nyquist-shaped signal having the same power.

Another advantage of the OFDM over the Nyquist-shaped signal for the NIS-based system is that after the dispersion unrolling, the IFFT block is not required for OFDM NIS-based systems because in the OFDM signal the information is encoded in the frequency domain, and hence the conversion to the time domain is not necessary. As a result, the OFDM modulation is a more suitable modulation format for NIS-based systems in comparison to the Nyquist-shaped signal. Consequently, for higher order modulation formats, such as 16QAM or 64QAM, only the OFDM modulation of the nonlinear spectrum is further employed in combination with the NIS method.

When combining with a higher modulation format, such as 16QAM, the OFDM NIS-based approach offers nearly 4 dB advantage over the traditional OFDM scheme in single channel transmission scheme (Fig. 5.13). The transmission bit rate in this case was increased to 200 Gb/s. It can be seen that for the 16QAM modulation format, the OFDM

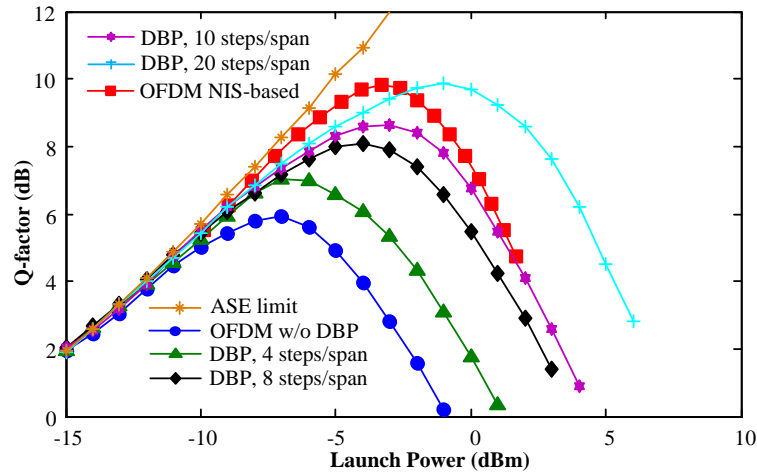


**Figure 5.14:** Performance comparison of the 300 Gb/s 64QAM OFDM systems with the NIS and DBP methods for fibre nonlinearity compensation. The receiver filter bandwidth was 40 GHz, the distance is 800 km.

NIS-based system outperforms the DBP with 10 steps per span. The simulation results for the 300 Gb/s 64QAM OFDM NIS-based system are compared in Fig. 5.14 with the conventional OFDM and OFDM with DBP. In these simulations, the performance indicator Q-factor was calculated through direct error counting. It can be seen that for such high-order modulation format, the OFDM NIS-based system displays almost the same performance as that of the DBP with 20 steps per span. The performance improvement in comparison with the conventional OFDM system is about 4.5 dB, which is larger than the values achieved for the QPSK and 16QAM modulation formats. This result indicates that a greater performance advantage of the OFDM NIS-based system over the traditional approaches can be reached for higher-order modulation formats, and shows the considerable benefit of the NIS method for fibre nonlinearity compensation for high-SE transmission systems.

Figure 5.14 also presents the curve indicating the ASE transmission limit: For calculating it, the nonlinearity is completely removed. It can be seen that the curve for the NIS-based transmission generally goes above those for the DBP in the noise-dominated region. However, it does not intersect the limiting line. This behavior reveals that the NIS-based transmission is less sensitive to the noise-induced corruption than the DBP, and the refinements of the NFT processing techniques can improve the NIS performance even further. However, it is also expected that the noise-signal nonlinear interaction is the ul-

time limitation in NIS-based transmission systems. This limitation is fundamental and cannot be overcome with more efficient NFT algorithms and system designs.

## 5.7 NIS for optical links with lumped amplification

It has been shown in the previous section that the NIS method is a promising digital signal processing technique for combating fibre nonlinearity impairments. However, because the NIS method is based on the integrability property of the lossless NLSE, the original approach can only be applied directly to optical links with ideal distributed Raman amplification. A modified NIS scheme for optical link with lumped amplification has been proposed recently in [122] by taking into account the average effect of the loss to obtain an integrable model (lossless path-averaged (LPA) model), to which the NIS is still applicable. In this section, the performance of modified NIS scheme for standard optical links with lumped amplifiers such as EDFAs is discussed in details. The author numerically demonstrates the feasibility of the modified NIS scheme in a burst mode with OFDM transmission scheme with advanced modulation formats (e.g., QPSK, 16QAM, and 64QAM), showing a performance improvement up to 3.5 dB; these results are comparable to those achievable with multi-step per span digital back-propagation.

### 5.7.1 LPA model for optical links with EDFAs

In this section, the derivation of the LPA NLSE for modeling the propagation of signal in optical links with EDFA-based lumped amplification [153, 154] reminded. One can start with the standard NLSE governing the propagation of a complex slow-varying optical-field envelope  $q(z, t)$  along a single-mode optical fibre [153, 154] (that is, in-between two consecutive amplifiers):

$$jq_z - \frac{\beta_2}{2}q_{tt} + \gamma q|q|^2 = -j\frac{\alpha}{2}q \quad (5.47)$$

where  $z$  stands for the propagation distance and  $t$  is the retarded time in the frame moving with the group velocity of the envelope. Here, the case of anomalous dispersion (that is, the constant chromatic dispersion coefficient is  $\beta_2 < 0$  in Eq. (5.47)) is focused

(focusing type of NLSE [104, 107]). The higher-order dispersion terms are not considered here; By introducing the standard [153, 154] change of variable:  $q = \exp\left(-\frac{\alpha}{2}z\right)A$  we have:

$$jA_z - \frac{\beta_2}{2}A_{tt} + \gamma \exp(-\alpha z)A|A|^2 = 0 \quad (5.48)$$

Assuming (following [153, 154]) that the dynamic of the envelope  $A(z, t)$  does not change significantly after each fibre span having the length  $L_s$ , the distance-dependent nonlinear coefficient in Eq. 5.48 can be replaced by its average value over each fibre span:

$$\gamma_1 = \frac{1}{L_s} \int_0^{L_s} \gamma \exp(-\alpha z) dz = \gamma \frac{G-1}{G \ln(G)}, \quad (5.49)$$

where  $G$  is total loss over the fibre span,  $G = \exp(\alpha L_s)$ . In other words, this is a well-known replacement of space-varying nonlinear phase shift by the average nonlinear phase shift (an effective nonlinear length). The obtained LPA NLSE can be written as:

$$jA_z - \frac{\beta_2}{2}A_{tt} + \gamma_1 A|A|^2 = 0 \quad (5.50)$$

Given the input field  $q(z, t)$ , the normalized mean square error (NMSE) produced by replacing the exact model (5.47) with the LPA NLSE (5.50), is introduced as:

$$NMSE = \frac{\langle |q_2(Z, t) - q_1(Z, t)|^2 \rangle}{\langle |q_1(Z, t)|^2 \rangle} \quad (5.51)$$

where  $\langle \rangle$  stands for the averaging over the whole considered time interval,  $q_1(Z, t)$  and  $q_2(Z, t)$  are the two output fields obtained using the standard NLSE (5.47) and the LPA NLSE model (5.50). The NMSE can be considered as the effective inverse signal-to-noise ratio, indicating the relative noise power introduced by the inaccuracy of the LPA NLSE model. As a result, it can be expected that a DSP technique based on the usage of the model (5.50) would contribute some additional effective noise to the processed signal. The power of this additional noise can be estimated using the NMSE calculated by (5.51). Taking into account the fact that the current optical communication systems employing FEC are designed to deal with a received SNR of less than 20 dB, we can predict that a NMSE of

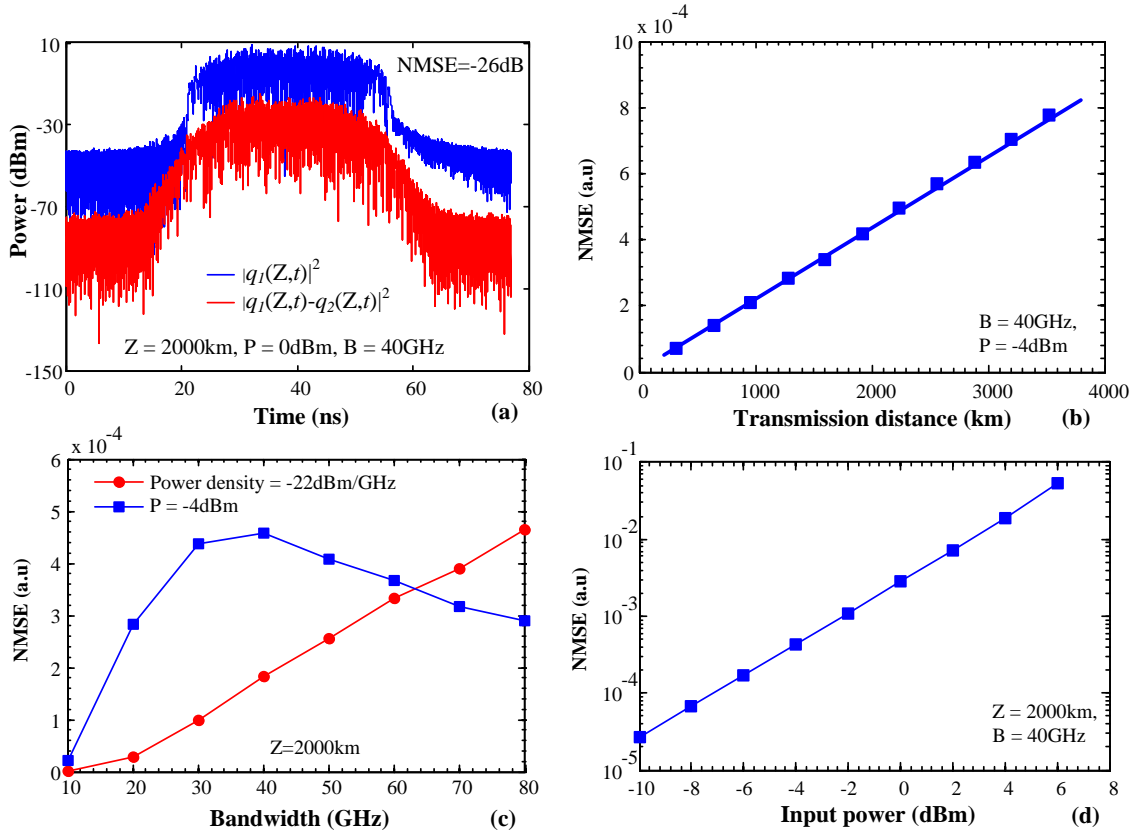


**Figure 5.15:** A comparison of output fields obtained by using the standard NLSE and the LPA NLSE, the amplifier spacing is 80 km. (b) NMSE as a function of the transmission distance. (c) NMSE as a function of the signals bandwidth for a given input power and a given input power density. (d) NMSE as a function of the input power.

less than -20 dB ( $< 0.01$ ) would not have a significant impact on the effectiveness of the DSP based on the model (5.50). As a result, it is believed that the model (5.50) can be used if the resulted NMSE is less than -20 dB.

Herein, the validity of the model (5.50) is numerically studied for the optical links with the EDFA-based amplification by considering the NMSE and its dependence on critical parameters as such the signals bandwidth, input power and the link distance. As an example, QPSK Nyquist-shaped system is taken into account. The modulation format of choice is not critical here. The input field consists of 210 QPSK symbols with sinc pulse-shape. The optical links consist of 80 km spans of SSMF with a loss parameter of 0.2 dB/km, nonlinearity coefficient of 1.22 /W/km, and dispersion coefficient 16 ps/nm/km. In Fig. 5.15(a) the mismatch between the output fields obtained by the standard NLSE and the LPA NLSE is plotted. The corresponding NMSE is 0.0024 ( $\sim -26$  dB), which indicates that the LPA NLSE can be used effectively to model the propagation of signal

in optical links with lumped amplification. However, as the LPA NLSE is an approximate approach, its accuracy depends on the system and signal parameters. Fig. 5.15(b) shows that the NMSE increases linearly with the transmission distance. In addition, as can be seen in Fig. 5.15(c), the NMSE also increases almost linearly with the signal bandwidth when the power spectral density is fixed. If the input power is fixed, the NMSE increases with the signals bandwidth only when the bandwidth is small. With bandwidth larger than approximately 40 GHz, the NMSE decreases with the increase of the signals bandwidth. This phenomenon can be understood if we recall that when the bandwidth is increased while the signal power is fixed, the power spectral density decreases effectively reducing the impact of fibre nonlinearity. This, in turn, reduces the impact of the distance-dependent nonlinear coefficient in (5.50). Fig. 5.15(d) shows that the NMSE increases linearly in the log-scale with the input power (increase with  $P^k$ , where  $k \sim 2$ ), showing that the input power is the most critical parameter in applying the LPA NLSE to model the propagation of signal in optical links with EDFA-based amplification.

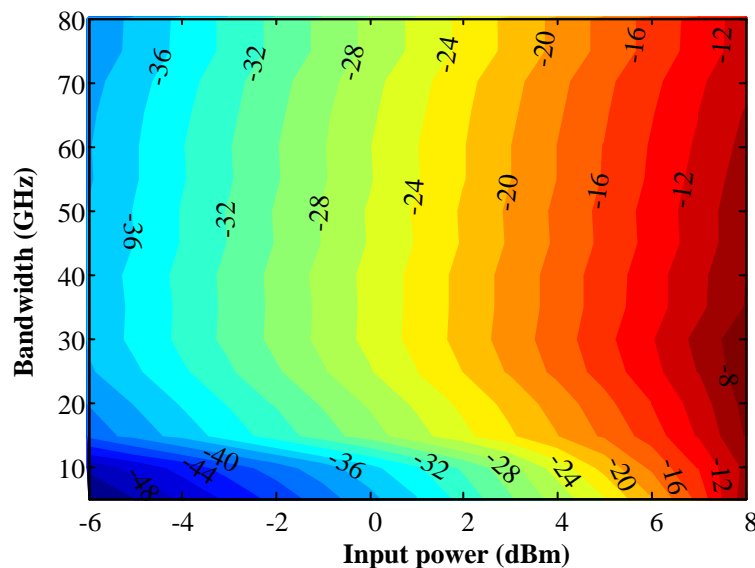


**Figure 5.16:** Level curves of NMSE (in dB) indicating the error of using LPA NLSE (5.50), plotted as a function of the signals bandwidth (in GHz) and the input power (in dBm) for the propagation distance 2000 km.

Figure 5.16 shows the NMSE as a function of the signals bandwidth (in GHz) and the input power (in dBm) for a 2000 km link. Taking a value of NMSE of -20 dB as the threshold, Figure 5.16 reveals that the LPA NLSE can be used to model the propagation of signal in optical links with EDFA-based amplification if the launch power is less than 3 dBm, al-

most independently of the signal bandwidth. In addition, the launch power threshold can be increased by increasing the signal bandwidth. This leads to an important result that an appropriate NIS scheme based on the model (5.50) can be used effectively to combat the fibre nonlinearity impairments in optical links with the EDFA-based amplification.

## 5.7.2 Simulation results and discussions

By using the LPA model 5.50 a modified NIS scheme for optical links with lumped amplification can be effectively developed. In general, the only difference between the NIS scheme for the lossless optical links and the links with EDFA-based amplification is related to the normalization procedure, as the Gelfand-Levitan-Marchenko equation and ZSP are appropriate only for the NLSE in the normalized form. Before solving the Gelfand-Levitan-Marchenko equation, the input optical field  $s(t)$  is normalized using the LPA NLSE (5.50) as follows:

$$\frac{t}{T_s} \rightarrow t, \quad \frac{z}{Z_s} \rightarrow z, \quad s\sqrt{\gamma_1 Z_s} \rightarrow s \quad (5.52)$$

where  $T_s$  is a free time normalization parameter (e.g., a characteristic time scale of the input waveform) and the associated space scale is  $Z_s = T_s^2 / |\beta_2|$ ;  $\gamma_1$  is the path-averaged nonlinear coefficient defined by Eq. (5.49). Herein, 56-Gbaud OFDM NIS-based transmission systems (in burst mode) with high SE-modulation formats; namely, QPSK, 16QAM, and 64QAM, are considered. The simulation setup is similar to those described in subsection (5.6.3).

**NIS performance without ASE noise** It has been shown in the previous section that when the ASE noise is ignored (fibre nonlinearity is the only systems impairment) the NIS method can perfectly compensate the deterministic impairment due to the fibre nonlinearity, using just a single-tap linear dispersion removal for the nonlinear spectrum at the receiver. In other words, the fibre nonlinearity has no impact on the system performance, which is now limited by the transceivers impairments. On the other hand, as the NIS method for optical links with the EDFA-based amplification is developed from the

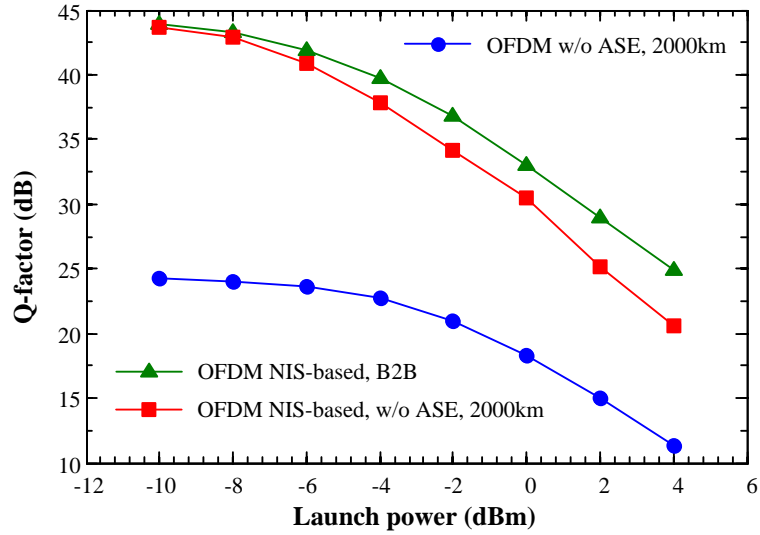


**Figure 5.17:** Q-factor as a function of the launch power for 100 Gb/s QPSK OFDM NIS-based system in the back-to-back case and in a 2000 km optical link, the ASE is ignored

approximate LPA NLSE, the perfect nonlinearity compensation cannot be achieved even in the absence of the ASE noise. This is a fundamental limitation due to the approximation of the model 5.50.

A comparison of back-to-back performance and the transmission performance when ignoring the ASE noise would indicate the performance penalty associated with the use of PLA NLSE in the NIS scheme for links with EDFA-based amplification. Such comparison is shown in Fig. 5.17 for 112 Gb/s QPSK OFDM NIS-based system in a 2000 km optical link. The Q-penalty associated with the use of PLA NLSE increases with the launch power. At a launch power of 4 dBm, the PLA NLSE would give a Q-penalty of 5 dB. This phenomenon can be explained by the fact that the inaccuracy (measured with the NMSE) of the PLA NLSE increases with the input power (Fig. 5.15(d)). As a result, any DSP technique based on the PLA NLSE would potentially provide a performance penalty, which also increases with the input power. In addition, it was shown in the previous section that the accuracy of the numerical algorithms employed here for solving the Gelfand-Levitan-Marchenko equation and ZSP problems also decreases when signals power is increased. As a result, the performances of NIS-based systems are limited at high power by the numerical errors.

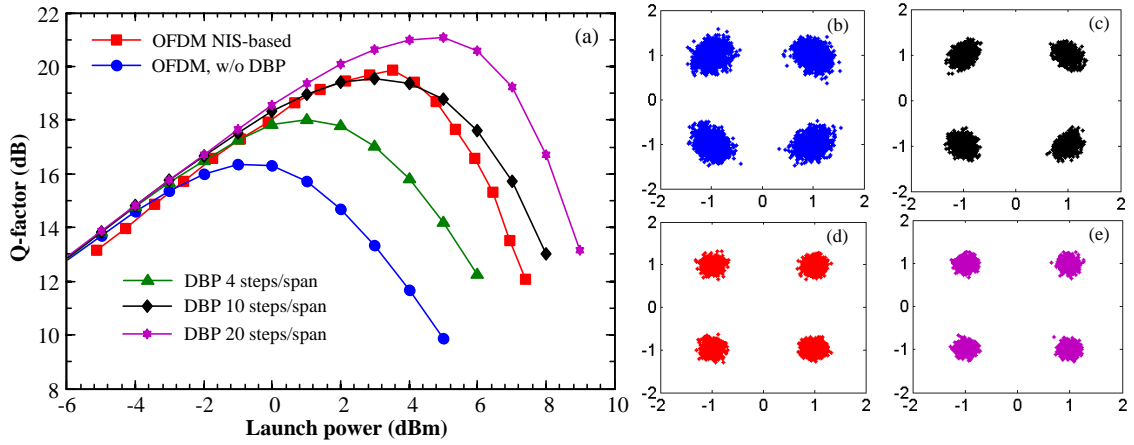


**Figure 5.18:** Performance comparison of the 100 Gb/s QPSK OFDM systems with the NIS vs. the DBP methods for fibre nonlinearity compensation, and constellation diagrams at the optimum launch powers for the cases: (b) without NIS and DBP, (c) DBP with 10 steps/span (d) with the NIS method, (e) DBP with 20 steps/span. The propagation distance is 2000 km.

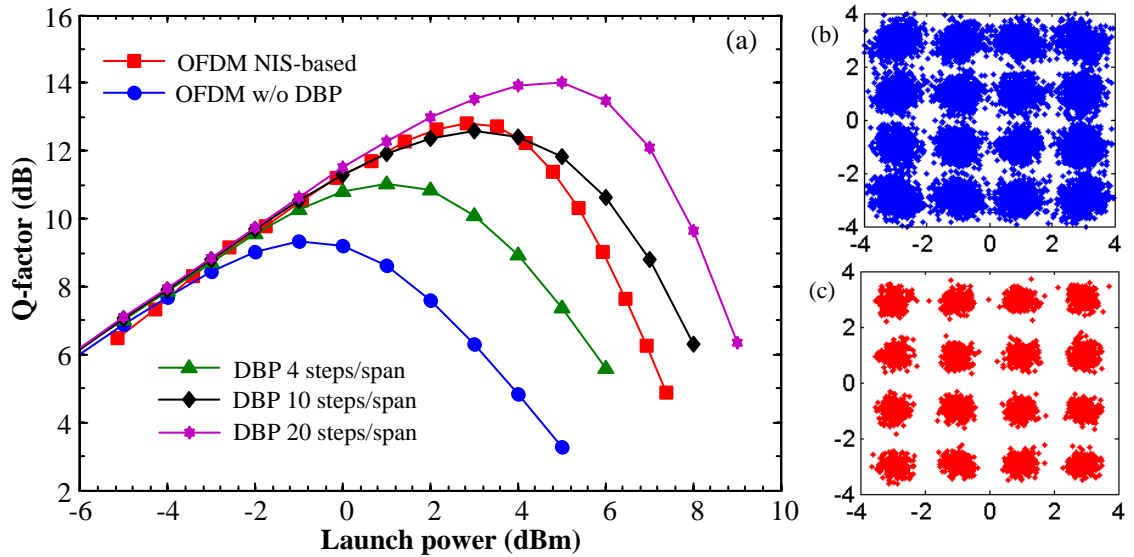


**Figure 5.19:** Performance comparison of the 200 Gb/s 16QAM OFDM systems with the NIS vs. the DBP methods for fibre nonlinearity compensation and constellation diagrams at the optimum launch powers for (b) Without NIS and DBP, (b) with the NIS method. The transmission distance is 2000 km.

**Performance comparison of NIS versus DBP in the presence of ASE noise** In this paragraph, in order to demonstrate the feasibility of the proposed NIS method for practical optical links with EDFA-based amplification, the performance of the NIS with DBP in high-SE OFDM transmission systems is compared. For the implementation of DBP, the received signal is first filtered with an 8th-order low-pass filter with a bandwidth of 40 GHz. Subsequently, the optical field is reconstructed and the signal is back-propagated with a different number of steps per single span. The performances for QPSK and 16QAM sys-

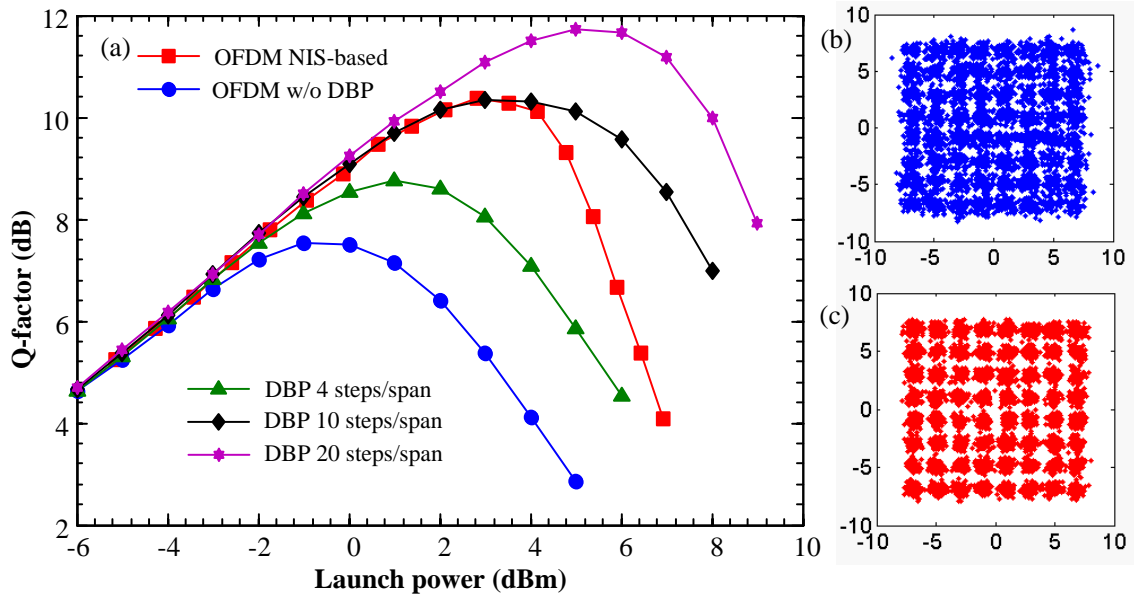


**Figure 5.20:** Performance comparison of the 300 Gb/s 64QAM OFDM systems with the NIS vs. the DBP methods for fibre nonlinearity compensation and constellation diagrams at the optimum launch powers for (b) Without NIS and DBP, (b) with the NIS method. The transmission distance is 640 km.

tems were evaluated using the well-known error vector magnitude (EVM), while direct error counting was adopted for 64QAM. The measured BER for the discussion convenience is then converted to an equivalent Gaussian noise Q-factor in dB for the convenience in discussion.

The comparison of NIS and DBP for OFDM systems with QPSK, 16QAM and 64QAM modulation formats are shown in Fig. 5.18, Fig. 5.19, and Fig. 5.20 respectively. It can be seen that, almost independently of modulation formats, the proposed NIS method offers a performance gain of approximately 3.5 dB over the OFDM system without DBP. This performance gain is comparable with those achieved with a highly complex DBP with 10 steps per span. The results obtained here agree well with prior results presented in [155] for low signal region, where the modulation of the continuous part can be directly achieved as the discrete part of the nonlinear spectrum does not exist. However, beside the serious limitation in the signal power, the approach proposed in [155] requires highly complex maximum likelihood detection scheme, which is not suitable for practical applications.

It should be mentioned that the NIS method for optical links with EDFA-based amplification proposed here provides the same complexity as the NIS method proposed for lossless optical links. It is believed that the overall complexity of the NIS method could be

significantly reduced further by taking into account recent advancement in fast algorithms for performing the INFT [147] and NFT [149, 156] and thus can be even lower than DBP employing more efficient algorithms.

## 5.8 Modified NIS for optical links with distributed raman amplification

Recently, a modified NIS scheme for optical link with distributed Raman amplification has also proposed in [123] based on the LPA model for such links. In this section, the impact of the non-ideal Raman gain profile on the performance of NIS-based transmission systems is discussed in details. A LPA NIS scheme which offers 3 dB performance gain regardless of the particular Raman profile is presented. To demonstrate the effectiveness of the LPA NIS scheme, without loss of generality, the author considers here open-cavity random distributed feedback (DFB) laser Raman amplification, as this scheme provides the best performance among various other Raman amplification schemes.

### 5.8.1 Random DFB raman amplification

In this subsection an open-cavity random DFB laser Raman amplification scheme is taken into account. This scheme can provide various gain profiles by controlling the forward pump power (FPP) [157].



**Figure 5.21:** Schematic of the random DFB laser Raman amplifier.

The schematic design of the random DFB laser Raman amplifier that allows achieving 2nd order pumping with a single wavelength pump is shown in Fig. 5.21. In this scheme, a high reflectivity (99 %) fiber Bragg grating (FBG) centered at 1455 nm with 200 GHz bandwidth is deployed at the end of the transmission span to reflect back-scattered Rayleigh Stokes-shifted light from the backward pump (at 1366 nm) and stimu-

late random DFB lasing at 1455 nm (wavelength of the FBG). This random DFB laser acts as the first order pump, together with 2nd order pump, to amplify the signal at 1550 nm. The lack of an FBG on the side of the forward pump significantly reduces the relative-intensity-noise transfer from the forward pump to the Stokes-shifted light at 1455 nm [158–161], which can seriously hinder coherent transmission [162].

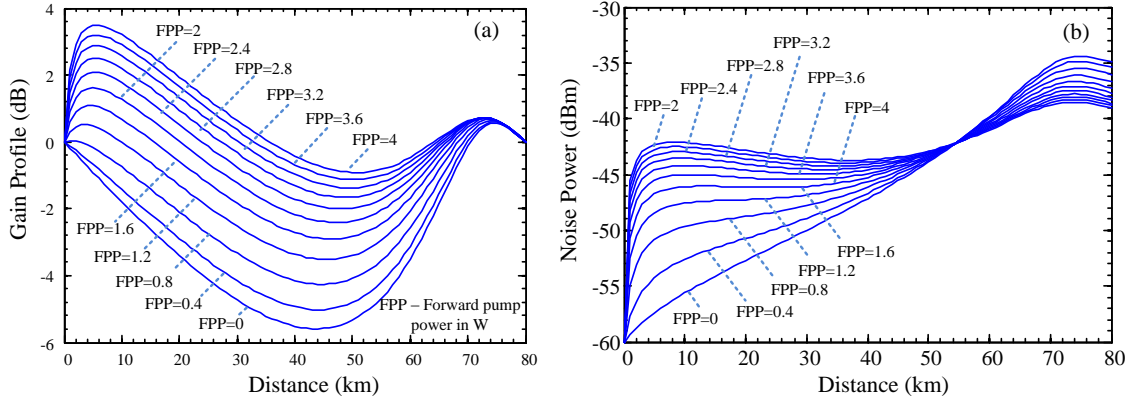


**Figure 5.22:** Raman gain (a) and noise (b) profiles along 80 km SMF span for different value of the forward pump power (FPP).

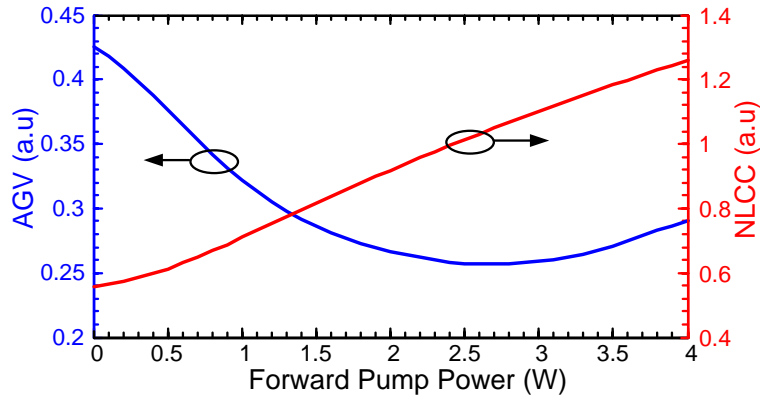


**Figure 5.23:** AGV and NLCC as a function of the forward pump power; the span length was 80 km.

The signal and noise power excursion is simulated for different pump power ratios in Raman amplifiers using the experimentally verified model [163] with an appropriate boundary conditions and fully depolarized Raman pumps. The backward pump powers were chosen accordingly to provide a net gain of 0 dB. The simulated gain and noise profiles along 80 km length SMF span are shown in Fig. 5.22 for different FPPs (up to 4 W due to practical interest). It can be seen in Fig. 5.22 that, when the FPP is increased, the Raman gain increases while the noise power decreases, leading to a better signal-to-

noise ratio.

To characterize the non-flatness of the Raman gain profile, the average gain variation (AGV) of the Raman gain profile is defined as:

$$AGV = \int_{z=0}^L |G(z) - k| dz, \quad k = \frac{1}{L_s} \int_{z=0}^L G(z) dz \quad (5.53)$$

where  $G(z)$  is the Raman gain normalized to 1 at the beginning of the span,  $L_s$  is the span length, and  $k$  is termed as the nonlinear correction coefficient (NLCC). The AGV is shown in Fig. 5.23 as a function of the FPP. The FPP = 0 case corresponds to the backward-pumping-only scheme. From Fig. 5.23 we can see that the AGV can be effectively reduced by increasing the FPP (up to its optimum value) at the cost of increasing the system power consumption. The optimum value of FPP was found to be  $\sim 2.7$  W, giving the AGV  $\approx 0.255$ . By varying the FPP to vary the AGV we can effectively investigate the impact of Raman gain flatness on the NIS-based transmission systems.

## 5.8.2 NIS for non-ideal distributed Raman amplification

As discussed in the previous subsection, for practical Raman amplification schemes, the non-flatness level characterized by the AGV, can be as high as 0.43 (for backward-pumping-only scheme). This high level of non-flatness may deprive all the nonlinearity cancellation benefit of NIS and of other NFT-based transmission schemes. As a result, the LPA model for Raman-based optical links should be developed in a similar manner to EDFA-based optical links Eq. (5.50) in order to apply NIS and, potentially, other NFT-based transmission schemes.

The general model of the NLSE for optical links with Raman amplifiers can be written as:

$$jq_z - \frac{\beta_2}{2} q_{tt} + \gamma_1 q|q|^2 = jg(z)q, \quad (5.54)$$

where  $g(z)$  is the distributed distance-dependent Raman gain coefficient.

Herein, it is assumed that the same pumping scheme is applied to all fibre spans. In this case,  $g(z)$  is a periodic function with a period equal to the span length. By introducing

the standard change of variables [164]:

$$q(z, t) = \exp\left(\int_0^z g(y)dy\right)A(z, t), \quad (5.55)$$

Eq. (5.54) can be rewritten as:

$$jA_z - \frac{\beta_2}{2}A_{tt} + \gamma G(z)A|A|^2 = 0, \quad (5.56)$$

which is the lossless NLSE with a distance-dependent nonlinear coefficient; here  $G(z)$  is the instantaneous gain

$$G(z) = \exp\left(2\int_0^z g(y)dy\right) \quad (5.57)$$

It can be assumed here that the dynamic of the envelope  $A(z, t)$  does not change significantly after each fibre span. In this case, the distance-dependent nonlinear coefficient in (5.56) can be replaced by its averaged value over each fibre span, giving the effective LPA NLSE [164]:

$$jA_z - \frac{\beta_2}{2}A_{tt} + \gamma\left(\int_0^{L_s} G(z)dz/L_s\right)A|A|^2 = 0, \quad (5.58)$$

From an engineering point of view, the LPA NLSE model can be obtained from the general NLSE model by removing the loss term and updating the nonlinear coefficient in such way that the nonlinear phase-shift acquired by the signal during propagation over one span is unchanged. Of course, the LPA NLSE is an approximated model so its accuracy depends strongly on the signal and system parameters such as bandwidth, pulse shape, power and transmission distance. However, the approximation 5.55 leads to a fundamental limitation of NI-based systems in fibre link with Raman amplification.

Given the input field  $q(z, t)$ , the NMSE produced by replacing the exact model (5.54) with the LPA NLSE (5.58), can be evaluated using Eq. 5.51. The NMSE can be considered as the inverse SNR, indicating the relative noise power introduced by the inaccuracy of the LPA NLSE model. It can be expected that a DSP technique based on the usage of the model (5.58) would add additional effective noise to the processed signal. The power of this additional noise can be estimated using the NMSE calculated by Eq. 5.51. Herein,

the validity of the model (5.58) is numerically studied by considering the NMSE and its dependence on critical signals parameters. As an example, a 56 Gbaud ( $112 \times 0.5$  Gbaud) OFDM signal with 16QAM modulation format is taken into account, noting that the modulation format of choice is not critical here.

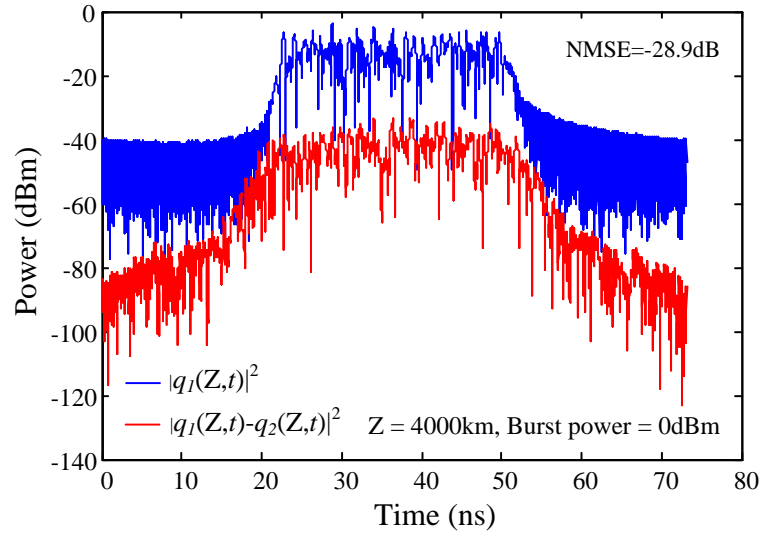


**Figure 5.24:** A comparison of output fields obtained by using the standard NLSE and the LPA NLSE for 50 Raman spans (4000 km) and a burst power of 0 dBm.

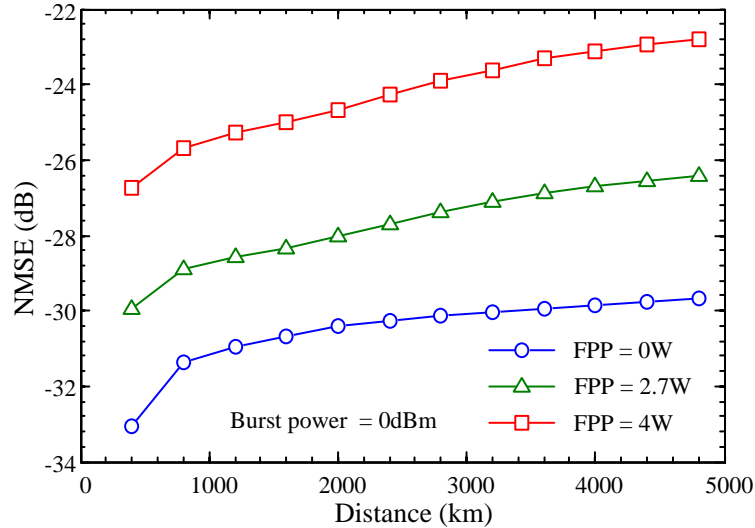


**Figure 5.25:** NMSEs as functions of the transmission distance for different values of the FPP. The burst power is fixed at 0 dBm.

In Fig. 5.24 the mismatch between the output fields obtained by the standard NLSE and the LPA NLSE is plotted for a transmission distance of 4000 km and burst power of 0 dBm. The corresponding NMSE is around -29 dB, which indicates that the LPA NLSE can be used effectively to model the propagation of signal in optical links with

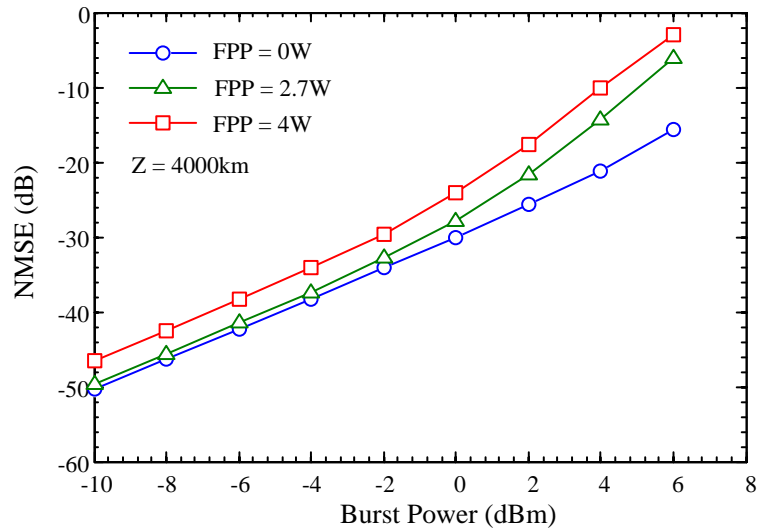


**Figure 5.26:** NMSEs as functions of the burst power for different values of the FPP. The transmission distance is fixed at 4000 km.

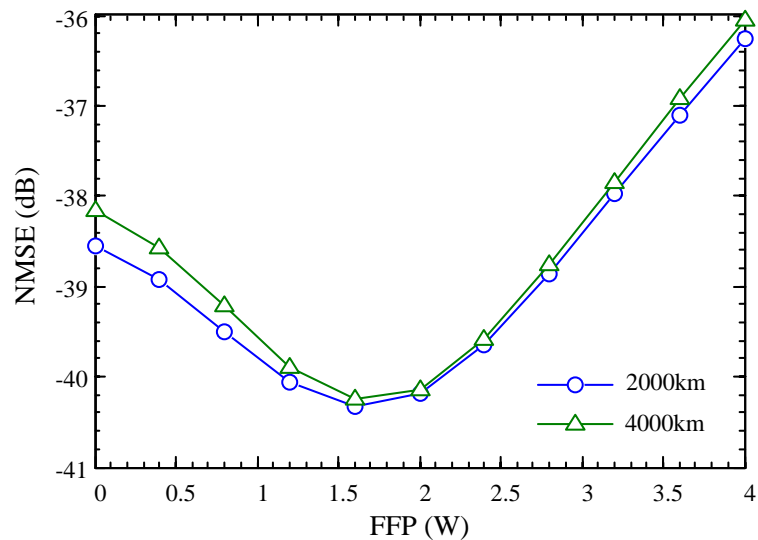


**Figure 5.27:** NMSEs as functions of the FPP for different values of the transmission distances. The normalized power is fixed at -4 dBm..

distributed Raman amplification. The dependences of NMSE to transmission distances and burst power are depicted in Fig. 5.25, Fig. 5.26. Taking a value of NMSE of -20 dB as the threshold, Fig. 5.25, Fig. 5.26 reveal that the LPA NLSE can be used effectively if the burst power is below 0 dBm for distances up to 5000 km.

It can be noted in Fig. 5.25, Fig. 5.26 that the NMSE increases with the FPP, showing that the accuracy of model (5.58) decreases with the increasing of the FPP if the burst power is fixed. However, in practice, using a higher FPP leads to a lower optimum input signal power. As a result, the accuracy of model (5.58) subjected to the variation of FPP

should be evaluated when fixing the normalized burst power which is defined as:

$$P_{norm} = P \left( \int_0^{L_s} G(z) dz / L_z \right) \quad (5.59)$$

The dependence of NMSE normalized burst power is depicted in Fig. 5.27, showing that the highest accuracy of model (5.58) is achieved at FPP  $\sim 1.5$  W. This is interesting that this value is different to the value of FPP which minimizes the AGV ( $\sim 2.7$  W). This result suggests that the shape of the Raman profile is also important, in addition to the AGV.

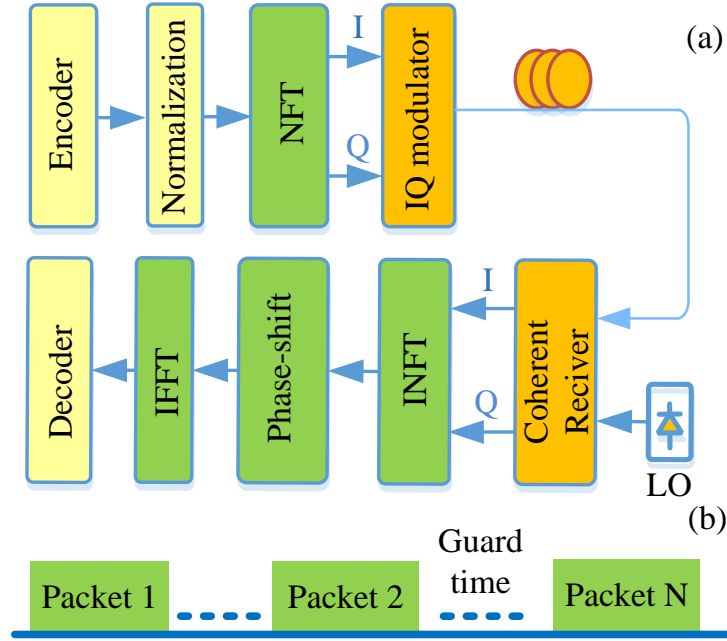


**Figure 5.28:** (a) Block diagram of NIS-based transmission systems, (b) Illustration of a burst mode transmission.

Based on the obtained LPA NLSE model, an appropriate modified NIS scheme accounting for the non-ideal Raman gain profile can be developed as shown in Fig. 5.28(a). Firstly, the normalization is performed on the initial signal  $q(t)$  (modulated with arbitrary pulse shape and modulation format) to bring the LPA NLSE model to the standard normalized form:

$$\frac{t}{T_s} \rightarrow t, \quad \frac{z}{Z_s} \rightarrow z, \quad q\sqrt{\gamma k Z_s} \rightarrow q, \quad (5.60)$$

where the time normalization  $T_s$  is a free parameter (e.g., a characteristic time scale or a reciprocal bandwidth) and the associated space scale is  $Z_s = T_s^2 / |\beta_2|$ ;  $k$  is NLCC defined

as in Eq. (5.53). The dependence of the NLCC on FPP is shown in Fig. 5.23 (red curve).

After the normalization, the linear Fourier spectrum of the encoded input waveform is mapped onto the continuous part of the nonlinear spectrum of another signal ( $q(t)$ ) to be transmitted using the INFT, according to Eq. 5.44. The generated complex signal,  $q(t)$ , is then fed into the IQ modulator for direct up-converting into the optical domain and launched into the fibre. At the receiver, the real and imaginary parts of the transmitted signal are detected with a coherent receiver. The nonlinear spectrum of the received signal is then obtained by using the NFT. As the evolution of the signal nonlinear spectrum is linear and trivial within the LPA NLSE model, the linear Fourier spectrum of the initial encoded complex signal can be recovered by applying a single step linear phase-shift removal using Eq. 5.45. Then, having unrolled the dispersion-induced phase shift, the initial encoded waveform  $s(t)$  can be recovered using the IFFT operation and, finally, it can be fed into the standard decoder for data detection. In general, the DSP at the receiver of an NIS-based system involves a single NFT operation and a single linear compensation step to remove the nonlinear impairments without reverse propagation, independently of the transmission distance. This is a significant advantage of the NIS method over the other nonlinear compensation techniques.

### 5.8.3 Simulation results and discussions

As discussed in section 5.6.3, the NIS transmission method can be combined with any modulation formats and transmission schemes. A comparison of OFDM and single carrier transmission with Nyquist pulse shaping for NIS-based systems was provided in section 5.6.3, revealing that the OFDM is a more suitable modulation format because it provides a smaller L1-norm because of the high signal dynamic range. As a result, in this section only the OFDM scheme is considered.

Herein, a 16QAM 56-Gbaud OFDM NIS-based systems is designed in the burst mode regime (Fig. 5.28(b)), as the NFT operations have to be performed on return-to-zero signals. In this scheme, the neighbouring packets are separated by a guard time, which is 20% longer than the dispersion induced memory.

For simplicity, it is assumed that each packet data contains only one OFDM symbol. To generate the OFDM signals, the IFFT size of 1024 was used, where 112 subcarriers were filled with data (with Gray-coding) while the remaining subcarriers were set to zero for oversampling purpose. The useful OFDM symbol duration is 2 ns. No cyclic prefix was added to the signal. The net data rate, after removing 7% overhead due to the FEC, was 200 Gb/s (considering only the bursts bit-rate). Herein, it is aimed to show that DSP techniques based on model (5.58) can be applied effectively even in the long-haul optical communication systems with as large a bandwidth as 56 GHz. The propagation of signal in fibre link was simulated using the split-step Fourier method with a step size of 1 km, using the gain profile shown in Fig. 5.22. The Raman noise was modelled as a Gaussian noise, which was added to the signal after each step (1 km), following the simulated noise profiles shown in Fig. 5.22(b). The system performance was evaluated through the EVM and the estimated BER was then converted to the Q-factor.

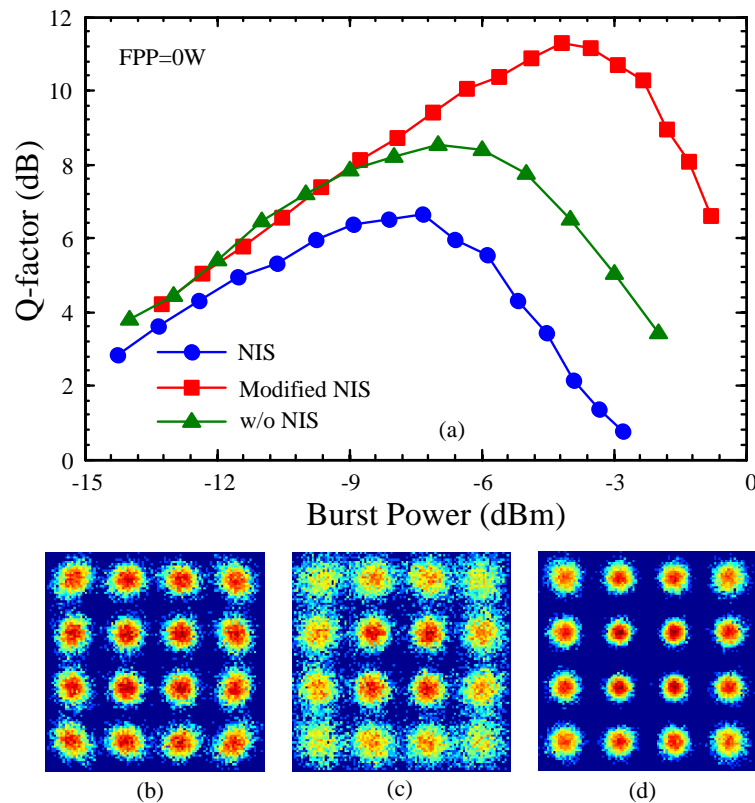


**Figure 5.29:** (a)-Performance comparison of OFDM systems with and without NIS, and the modified NIS scheme for  $FPP = 0$  W (backward pumping only case), (b)-(d) constellations at the optimum launch powers for system without NIS (b), with NIS (c) and with the modified NIS (d) schemes at  $FPP = 0$  W, respectively.

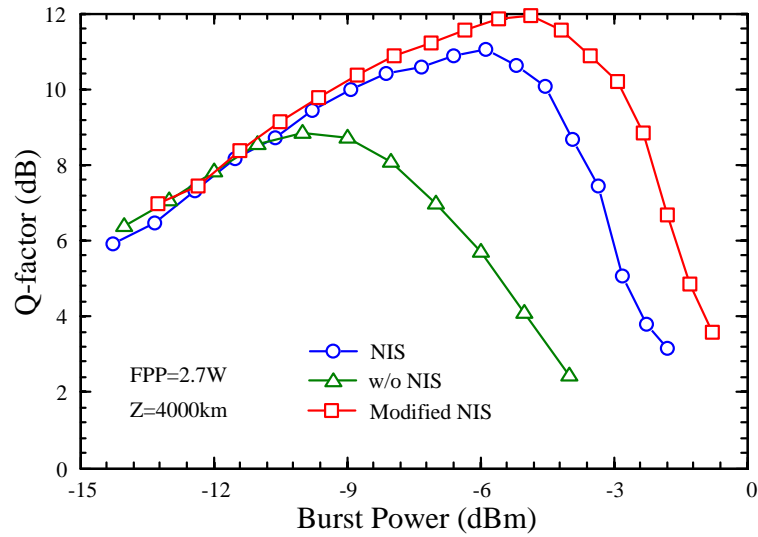


**Figure 5.30:** Performance comparison of OFDM systems with and without NIS, and the modified NIS scheme for FPP = 2.7 W. The transmission distance is 4000 km.

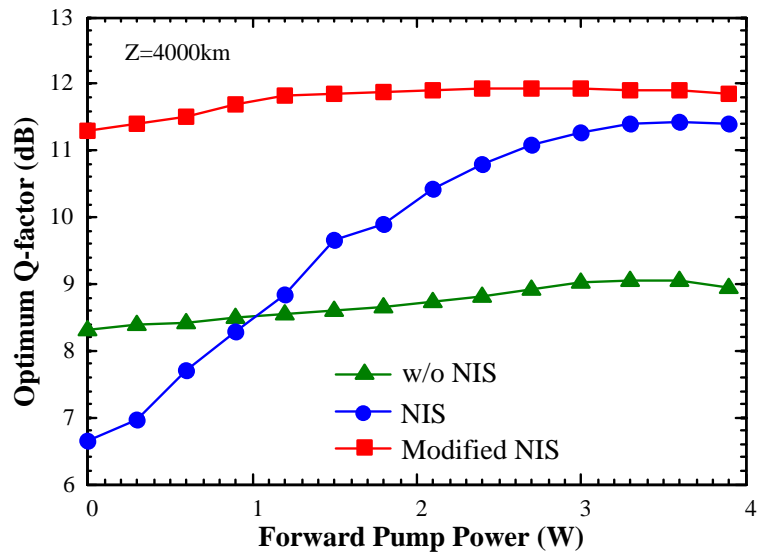


**Figure 5.31:** Optimum Q-factor as a function of FPP for OFDM systems with and without NIS, and the modified NIS scheme. The transmission distance was 4000 km.

The performance of OFDM systems with and without NIS, and with the proposed modified NIS scheme is compared in Fig. 5.29(a) for the backward pumping only scheme (FPP = 0 W). For OFDM system without NIS, only the compensation of chromatic dispersion was applied. For the case of backward pumping scheme (FPP = 0 W), because of the high non-flatness level of the Raman gain profile ( $AGV \sim 0.43$ ), applying directly the NIS method worsens the system performance by  $\sim 2$  dB. This result clearly indicates that the non-ideal Raman gain profile has a significant impact on the NIS-based systems: When the AGV is high ( $AGV \sim 0.43$  if FPP = 0 W), the NIS method cannot produce any advantage

due to the wrong power estimate. However, if the modified NIS scheme is employed, a Q-factor improvement of  $\sim 3$  dB is observed. This effectively means that the performance of the NIS scheme is enhanced by 5 dB by simply employing the NLCC that takes into account the non-ideal gain profile along the span. The received constellations at optimum launch powers for three systems under investigation are shown in Fig. 5.29(b)-(d).

A similar performance comparison result is plotted in the Fig. 5.30 when  $FPP = 2.7$  W, which provides the smallest level of non-flatness of the Raman gain profile. It should be noted here that by increasing the FPP, the Raman noise figure is reduced, which can be referred from the performance at the low power level. It can be seen in Fig. 5.30 that the NIS method gives around 2 dB performance gain if  $FPP = 2.7$  W. In this case, the AGV is relatively small (0.255), and the NIS scheme still offers a meaningful performance gain. However, if one uses the modified NIS method based on Eq. (5.58), an extra  $\sim 1$  dB gain is achieved, giving a total performance gain of  $\sim 3$  dB.

The optimum Q-factors in systems with and without NIS and with the modified NIS schemes are presented in Fig. 5.31 as functions of the FPP. As expected, when the FPP is increased from 0 W to 2.7 W, the achievable performance of NIS-based system increases dramatically as a result of the decrease in the AGV. However, increasing further the FPP, which increases the AGV accordingly (if  $FPP > 2.7$  W), does not decrease the performance of NIS-based system. This phenomenon is attributed to the reduction of the amplifier noise figure when the FPP is increased. On the other hand, the modified NIS scheme offers around 3 dB gain in Q-factor, independently of the FPP (the gain variation is below 0.5 dB). This indicates that if the modified NIS method is applied, the forward pump is not necessary, which offers a significant reduction in the cost and power consumption when designing the NIS-based systems with Raman amplifications.

## 5.9 Experimental demonstration of NIS transmission over transoceanic distances

In this section, the generation, detection and transmission performance over transoceanic distances of 10 Gbaud NIS-based signal, in which the transmitted information is encoded directly onto the continuous part of the signal nonlinear spectrum, are experimentally demonstrated. By applying effective digital signal processing techniques, a reach of 7344 km was achieved with a bit-error-rate ( $2.1 \times 10^{-2}$ ) below the 20 % FEC threshold. This represents an improvement by a factor of  $\sim 12$  in data throughput-distance product compared with other previously demonstrated NFT-based systems [117, 165], showing a significant advance in the active research area of NFT-based communication systems.

### 5.9.1 Experimental setup of 10 Gbaud NIS-based OFDM transmission

To demonstrate the possibility of encoding and detecting information using the signals nonlinear spectrum, a 10 Gbaud NIS-based system in burst mode is designed and its transmission performance over transoceanic distances is experimentally evaluated.

**Tx DSP and setup** The schematic of the experimental setup, together with the Tx, Rx DSP are shown in the Fig. 5.32(a-c), where the green blocks indicate the required additional DSP blocks for NIS-based transmission. For each burst and each predefined launch power, a 10 Gbaud OFDM waveform (one OFDM symbol, 6 ns of duration, no cyclic prefix) was generated offline using an IFFT (size of 128), where 60 subcarriers were filled with QPSK data and the remaining subcarriers were set to 0 for oversampling purposes. Guard bands of 12 ns were added to both the beginning and the end of the OFDM symbol to avoid inter-burst interference effects, giving a total burst period of 30 ns (the bit-rate is 4 Gb/s). The generated signal was then normalized using the lossless path average NLSE model for optical links with lumped amplification. The resulting signal was upsampled (by a factor of 10 times) before being fed into the INFT block. Herein, the INFT maps the

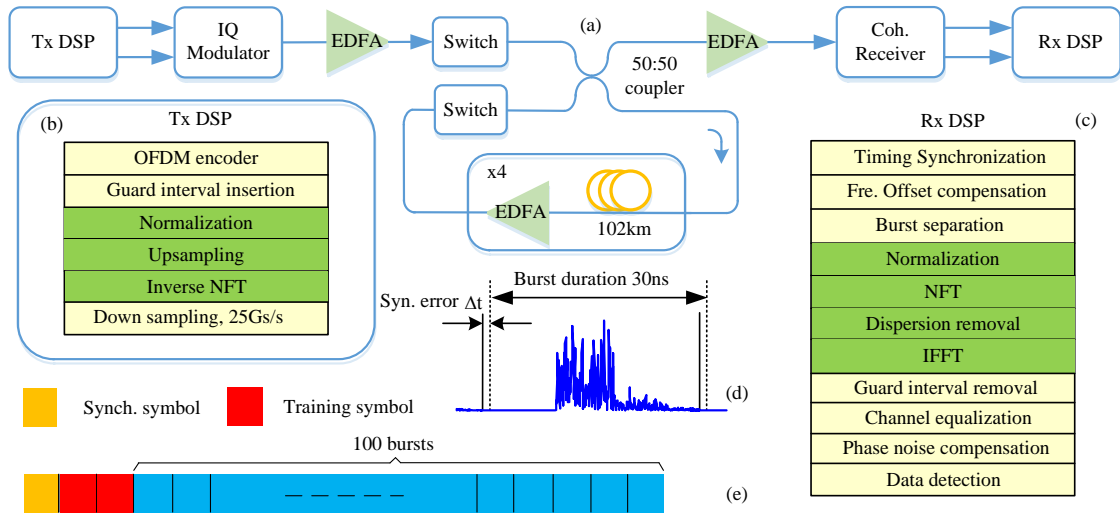


**Figure 5.32:** (a): Schematic of the experimental setup of 10 Gbaud NIS-based transmission in fibre link with EDFA-only amplification; (b) block diagram of the Tx DSP; (c) block diagram of the Rx DSP; (d) illustration of a transmitted burst with a duration of 30 ns carrying 120 bits (60 QPSK symbols) and illustration of synchronization error, (e) - structure of the transmitted signal, including one synchronization symbol, two training symbols for channel estimation and 100 OFDM NIS-based bursts.

linear spectrum of the input signal to the continuous part of the nonlinear spectrum of the output signal. Since the OFDM waveform was used as the input signal of the INFT block, the continuous part of the nonlinear spectrum of the output signal was directly modulated by QPSK data. Upsampling is necessary here to reduce the error associated with the INFT. Finally, the generated signal after INFT was downsampled to 25 Gs/s before being loaded into the arbitrary waveform generator with a DAC providing around 5.6 bits of effective resolution (over a bandwidth of 12.5 GHz) and fed through a linear amplifier to drive an IQ modulator.

**Recirculating loop** The transmission experiment used a re-circulating loop consisting of a  $4 \times 102$  km span Sterlite OH-LITE (E) fibre ( $\sim 19$  dB insertion loss per span) and a gain flattening filter (leveller). In addition to the channel under test, 10 loading channels with  $\sim 5$  nm guard band in each side were used. The signals were amplified in EDFAs with a noise figure of 6 dB. At the receiver, the channel under test was filtered and amplified (using a low-gain EDFA) before being coherently detected using a real-time 80 Gs/s sampling oscilloscope. Both the transmitter laser and local oscillator were external cavity lasers each with a linewidth of  $\sim 100$  kHz.

**Rx DSP** The Rx DSP (Fig. 5.32(c)) firstly used a training symbol to perform both timing synchronization and frequency offset compensation. The signal was then separated into a number of discrete 30 ns bursts before being normalised according to the lossless path averaged model 5.50. The normalized power was adjusted to be slightly different from the actual launch power to account for the power variation during each re-circulation resulting from wavelength dependent gain-loss imperfections. After normalization, the NFT was performed to recover the continuous part of signals nonlinear spectrum and single-tap dispersion compensation was performed to remove the effects of both the chromatic dispersion and fibre nonlinearity, according to Eq. 5.45. Next, the IFFT was performed to recover the transmitted time domain signal and then the guard bands were removed and the resulting signal was fed into the traditional OFDM receiver. For the NIS-based systems, synchronization error ( $t$ ) will result in a frequency dependent phase shift in the nonlinear Fourier domain:

$$l(q(t - \Delta t), \xi) = l(q(t), \xi) e^{-2j\xi\Delta t}, \quad (5.61)$$

where  $l(q(t), \xi)$  is the continuous part of the nonlinear spectrum of the signal  $q(t)$ . Since the synchronization error is constant for all bursts in one frame, the resulting frequency dependent phase shift can be readily corrected through a single-tap channel estimation and equalization using training sequences. Herein, the first two bursts were used for channel estimation (Fig. 5.32(e)). The impact of laser phase noise was compensated after channel estimation using 4 pilot subcarriers in each OFDM burst. The common phase error, the impact of which on the NIS-based systems is similar to those of the conventional linear transmission schemes, is corrected. Finally, the system performance was evaluated directly from the BER by processing 10 recorded traces (each with 100 bursts), and the results are expressed as a Q factor.

## 5.9.2 Simulation results

In general, NIS-based transmission scheme can be understood as a nonlinear pre-distortion technique. At the transmitter, the linear spectrum of an encoded signal is mapped to the

continuous part of the nonlinear spectrum of another signal to be transmitted over the fibre link. As this mapping operation is nonlinear, the generated signal via the INFT block strongly depends on the inputs signal power. In Fig. 5.33, different output signals of the INFT block given the same input OFDM waveform with different power levels are compared. It can be seen that, as the input signal power is increased, the amount of signals energy contained in the decaying tail generated after INFT also increases. This long decaying tail tightens the DAC resolution requirement in NIS-based transmission systems. Herein, we assume that the signals energy contained in the tail generated after INFT is small enough and can be eliminated when defining the effective burst power in following discussions. The effective burst power is defined as the ratio of the total signal energy within a burst to the initial signal duration (before INFT, 6 ns).

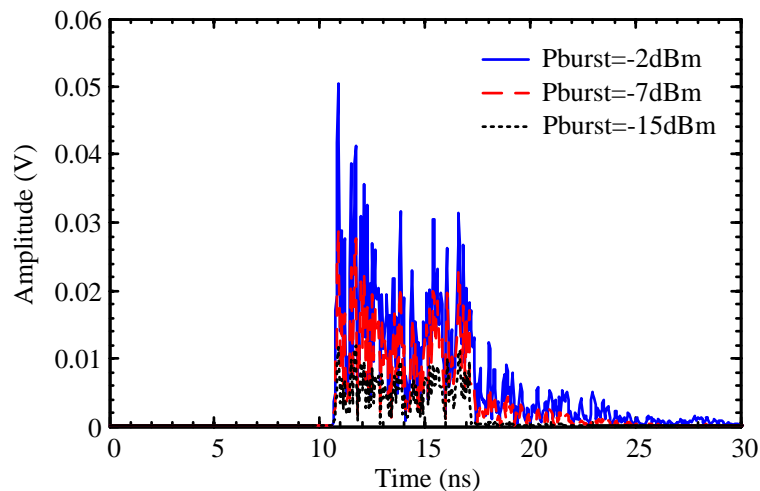


**Figure 5.33:** Comparison of output signals of the INFT block given the same input 10 Gbaud OFDM waveform with different power levels.

One important property of the nonlinear spectrum is that the discrete part is absent and the continuous part converges to the ordinary Fourier transform at low power values [66,105]. As a result, at low signal power values, the traditional receiver (without NFT and IFFT blocks, Fig. 5.32(c)) can also be used in NIS-based transmissions. However, as the signal power is increased the continuous part of the signals nonlinear spectrum diverges to its linear counterpart leading to performance penalty if the conventional receiver (without NFT) is employed.

Extensive simulations were performed to understand the performance penalty associ-

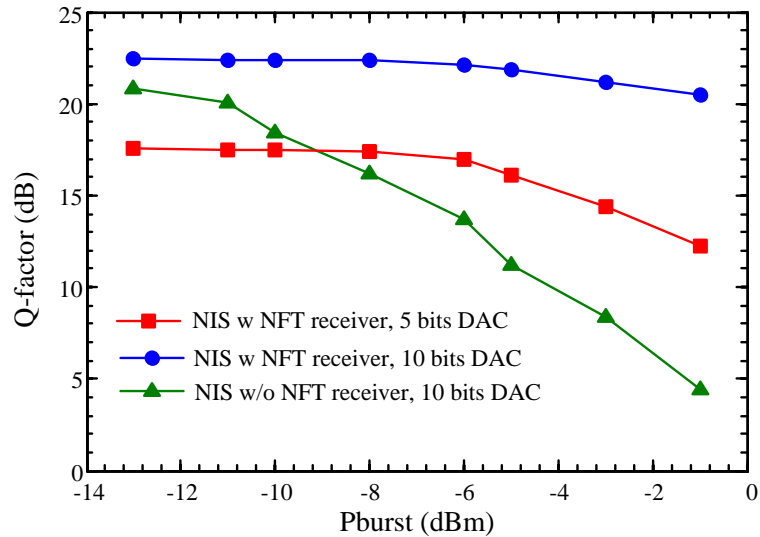


**Figure 5.34:** Simulated back-to-back performance of NIS-based 10 Gbaud OFDM system at 25 Gs/s with and without NFT receiver. The DAC resolutions are 5 and 10 bits, no noise was added.

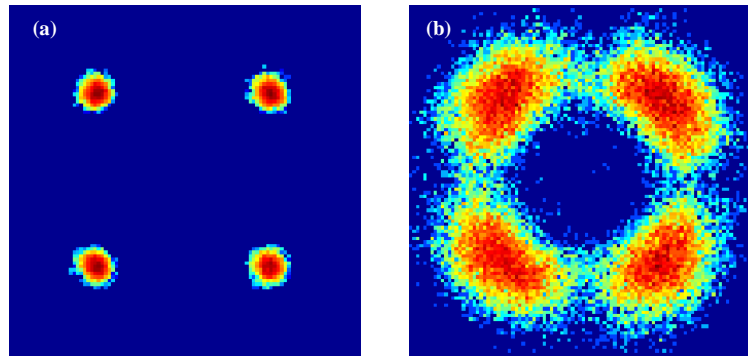


**Figure 5.35:** Received constellations of NIS-based 10 Gbaud OFDM system at 25 Gs/s with and without NFT receiver, Pburst = -3dBm.

ated with a conventional OFDM receiver and the finite DAC resolution. In simulation, the system performance was evaluated through error vector magnitude and then was converted to Q-factor for comparison purposes. In Fig. 5.34 the back-to-back performances of NIS-based 10 Gbaud OFDM systems sampled at 25 Gs/s with and without NFT receivers are compared. To eliminate the impact of DAC resolution, we first considered a high DAC resolution of 10 bits. In Fig. 5.34, if the NFT receiver is employed (blue curve with circle marker), only slight performance degradation ( $\sim 2$  dB) is observed if the burst power is increased from -13 dBm up to -1 dBm. The performance degradation is due the fact that increasing the signal power leads to a longer decaying tail, a part of which falls outside the burst duration of 30 ns and is truncated. When the conventional receiver (without NFT)

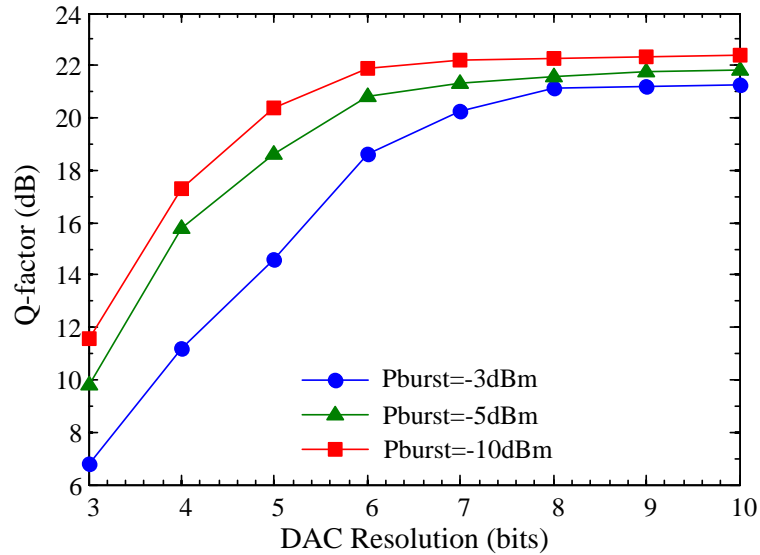


**Figure 5.36:** Simulated back-to-back performance of NIS-based 10 Gbaud OFDM system sampling at 25 Gs/s with different values of the burst power the Tx DAC resolutions.

is employed, the performance penalty significantly increases with the increasing of the burst power. This clearly indicates that the NFT receiver is mandatory for the NIS-based systems operating with medium-to-high signal power. The received constellations of NIS-based 10 Gbaud OFDM systems with and without NFT receiver are compared in Fig. 5.35, for a burst power of -3 dBm.

If the DAC resolution is reduced to a practical value of 5 bits, a significant performance penalty can be observed, ranging from  $\sim 5$  dB for -13 dBm burst to  $\sim 8$  dB for a -1 dBm burst. This result clearly indicates that the performance penalty due to a low DAC resolution increases with the growth of the burst power. It is believed that this is due to the fact that a higher DAC resolution is required to preserve the longer decaying tail when the burst power is increased. However, it is clearly that this performance penalty is technological which can be mitigated by increasing the DAC resolution and using more efficient NFT algorithms.

The performances of NIS-based 10 Gbaud OFDM systems as functions of the DAC resolution for different burst power values are plotted in Fig. 5.36. In this figure the required DAC resolutions for negligible performance penalty are 6 bits, 7 bits and 8 bits for  $P_{burst} = -10$  dBm, -5 dBm and -3 dBm, respectively.

### 5.9.3 Experimental results and discussions

**Back-to-back performance** The performances of OFDM systems with and without NIS as functions of OSNR for different burst power values are given in Fig. 5.37, where closed symbols and solid lines with open symbols depict the experimental and simulation results, respectively. At a low burst power value the OSNR penalty compared with the conventional OFDM system (with the same parameters) is as small as 1 dB. However, the OSNR penalty of the NIS-based system increases quickly with the rise of the burst power. It should be noted that, unlike the conventional transmission systems, the back-to-back performance of NIS-based systems depend on both the OSNR and the signal power.

At a high burst power value of -2 dBm, a BER level of  $10^{-3}$  ( $Q \sim 9.8$  dB) could not be achieved. As discussed above, we attribute this phenomenon to the fact that a higher burst power requires a higher DAC resolution due to the longer decaying tail. As a result, with a fixed DAC resolution ( $\sim 5.6$  bits) and a fixed guard interval duration, the OSNR penalty increases with the rise of the burst power.

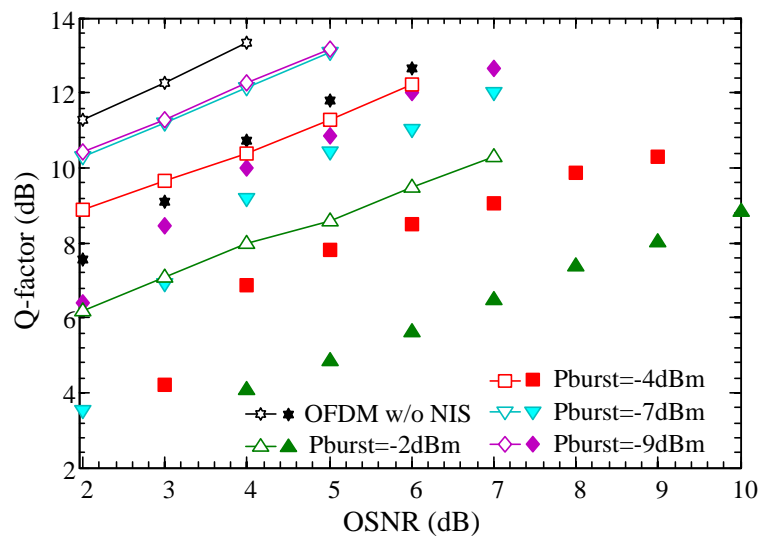


**Figure 5.37:** Back-to-back performances of 10 Gbaud OFDM and NIS-based OFDM systems for different burst power values. Closed symbols are experimental data. The solid lines with open symbols are simulation results, the DAC resolution was set to 5 bits.

This phenomenon can also be confirmed by simulation results presented in Fig. 5.37, where the OSNR penalty increases significantly with the rise of the burst power (the effective DAC resolution was fixed at 5 bits). In comparison to simulation results obtained with ideal Rx and Tx with a limited DAC resolution as the only impairment, the implementa-

tion penalty also increases with the rise of the burst power. This result clearly suggests that NIS-based systems are also very sensitive to other transceiver imperfections such as Rx ADC resolution, DAC, ADC transfer functions and laser phase noises. As a result, novel and effective transceivers equalization techniques are desirable to minimize the back-to-back implementation penalty. This is an important topic for future research.

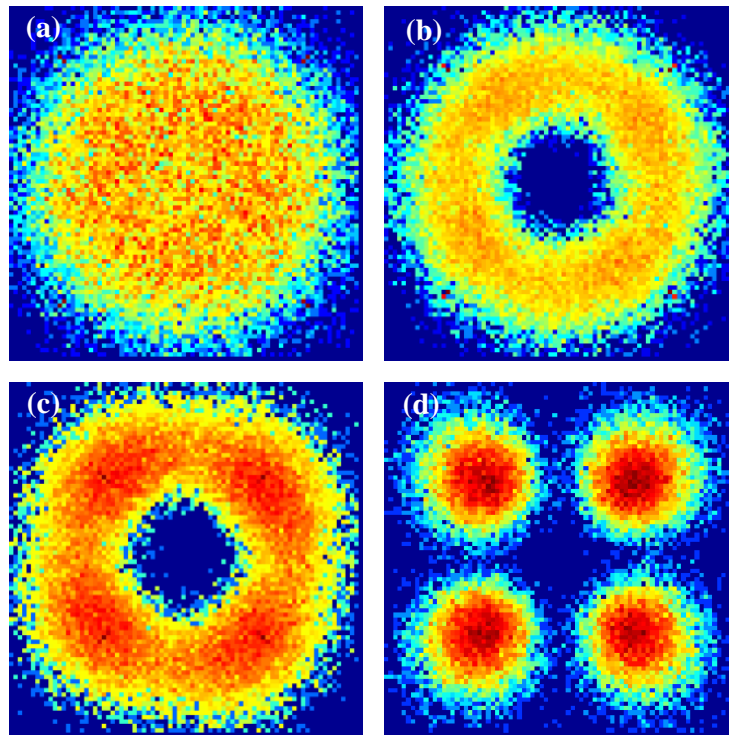


**Figure 5.38:** Constellation diagrams at the burst power of -5 dBm after 4080 km of transmission distance, (a) before dispersion removal, (b) before channel estimation, (c) before phase noise compensation, (d) final constellation after phase noise compensations.

**Experimental transmission performance** Typical constellation diagrams after several receiver DSP blocks, including single-tap dispersion removal, channel estimation, and phase noise estimation, are presented in Fig. 5.38 for the burst power of -5 dBm after a distance of 4080 km. At each step, the constellation was achieved by feeding the obtained signal directly into the conventional OFDM receiver. After the single tap dispersion removal, a clear open eye can be observed (Fig. 5.38((b)). Next, channel estimation was performed to remove the frequency dependent phase-shift due to synchronization error. The obtained constellation, Fig. 5.38(c), clearly shows that the synchronization error induced phase-shift was effectively removed. The final constellation diagram, Fig. 5.38(d),

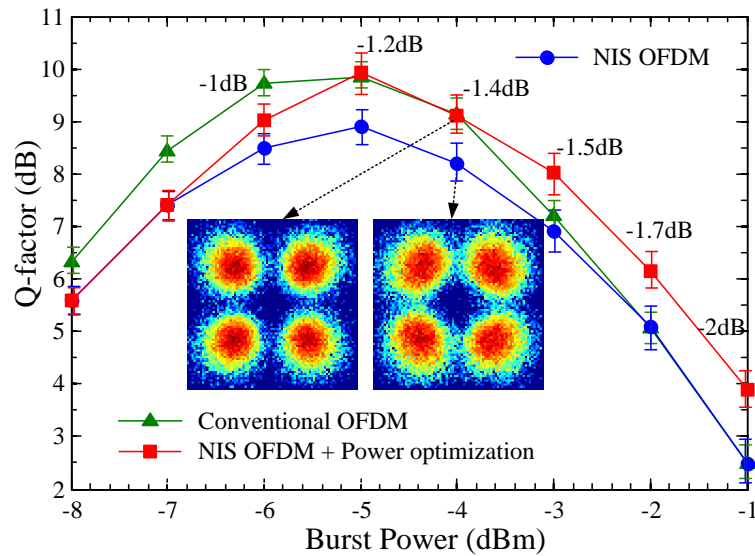


**Figure 5.39:** Q-factor as a function of the burst power after 4080 km. The numbers are power correction values for each burst power value.

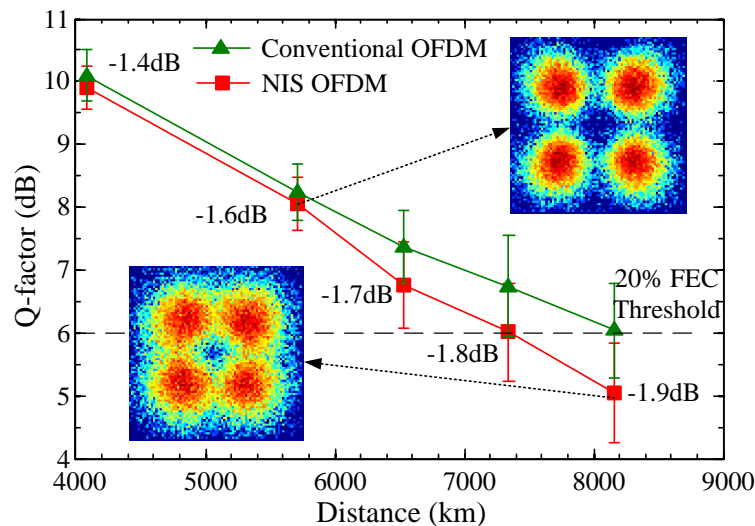


**Figure 5.40:** Optimum Q-factor as functions of the transmission distance. The numbers are power correction values for each distance value at the optimum burst power.

indicates that the transmitted QPSK data was successfully recovered.

The performance of the conventional OFDM system (without NFTs at both Tx and Rx) and the NIS-based OFDM system are compared in Fig. 5.39 for the 4080 km distance. If the receiver normalized power was set to be equal to the launch power, the optimum Q-factor was found to be  $\sim 9$  dB (blue curve), which is  $\sim 0.9$  dB worse than the conventional OFDM system. However, by adjusting the normalized power an additional 1 dB gain in Q-factor can be achieved (red curve), which is comparable to the conventional OFDM system. At the launch power of  $-5$  dBm, the optimum receiver normalised power was

-6.2 dBm. The power correction value in this case was - 1.2 dB. This phenomenon is attributed to the gain-loss imperfection of the loop, which leads to the power variation after each re-circulating loop, degrading the accuracy of the nonlinear pre-distortion technique. In the highly nonlinear regime, by optimizing the normalized power the NIS-based OFDM system shows up to 2 dB performance advantage over the conventional OFDM system, and 1 dB increase in the nonlinear threshold. It is believed that the low DAC resolution hinders the observation of further performance benefit of NIS-based system, although parametric noise amplification [74] and the finite guard interval may also contribute to performance degradation.

The optimum Q-factors as functions of transmission distance is depicted in Fig. 5.40, for NIS-based and the conventional OFDM systems. Equal performance over both systems to  $\sim 5700$  km can be observed, where the conventional system starts to outperform the NIS-based system. Again this is thought to be due to the reasons outlined above. After propagation over 18 loops (7344 km) the BER obtained ( $2.1 \times 10^{-2}$ ) was below 20% FEC threshold. This result indicates the record distance reach of any NFT-based systems up date. Taking into account the expected uncertainty in measured Q factor from the finite sample size, it is believed that these results are close to those observed for conventional OFDM.

## 5.10 Conclusion

Nonlinear Fourier transform is a promising technique to combat the nonlinearity impairments in fibre-optic communication systems. In this chapter, the author has presented several important developments of NFT-based communication systems with particular focus on NIS transmission scheme. Firstly, a comprehensive guidance for designing NFT-based communication systems is presented. It is then showed that the NIS method can be successfully combined with high-SE transmission techniques (e.g., OFDM, Nyquist-shaped) and advanced modulation formats, such as QPSK, 16QAM, and 64QAM, offering a performance gain up to 4.5 dB, which is comparable with the DBP compensation method employing multi-steps per span. Next, an extension of the NIS scheme and of the entire

nonlinear Fourier transform approach based on the usage of path-averaged NLSE is proposed which can be effectively applied in optical links with EDFA-based and non-ideal Raman amplifications. Finally, the record distance reach (7344 km at BER= $2.1 \times 10^{-2}$ ) of any NFT-based systems by encoding and detecting information on/from the continuous part of the nonlinear signal spectrum using the NIS-based transmission ideology is experimentally demonstrated . In comparison with the conventional system, the NIS-based system shows up to 2 dB performance gain in the highly nonlinear regime. However, the overall system performance benefit is hindered by the transceivers imperfections, the low DAC resolution and other system designs constrains, leaving good potential for further system performance improvement using NFT technique.

# Chapter 6

## Conclusion

### 6.1 General conclusion

In this thesis, it has been shown that DSP is the enabling technology for future OFDM-based superchannel transponders. This thesis has developed various high performance, flexible and low complexity DSP techniques for laser phase noise and fibre nonlinearity compensation in CO-OFDM transmissions.

For laser phase noise compensation, three novel DSP techniques, namely QPA, DDF blind and MF blind PNC techniques have been proposed. QPA technique effectively reduces the overhead of the traditional PA method by a factor of 2 without increasing the complexity. As a result, this technique is suitable for systems where low complexity is the priority. DDF blind is a low-complexity blind PNC technique, where only 3 test phases are required for effective PNC. This technique is suitable for RGI CO-OFDM systems with up to 200 subcarriers for maximizing the SE as the overhead due to pilot subcarriers can be significant here. MF blind PNC technique offers another option for phase noise compensation with ultra-low computational effort as no multipliers are required. With the development of DDF blind and MF blind techniques, the impact of laser phase noise in CO-OFDM systems can be effectively removed with low computational complexity, offering a practical option for maximizing the SE of multi-band CO-OFDM superchannel transponders. This also closes the gap between overheads of OFDM-based and Nyquist-based superchannels.

For fibre nonlinearity compensation, two novel high performance and low-complexity techniques, namely PCP and PCSC, have been proposed. PCP offers a simple trade-off between performance gain and overhead, which is not possible for the conventional PCTW technique for single carrier transmission systems. The development of PCP technique offers a huge advantage for CO-OFDM systems over single carrier systems in term of the possibility to trade the overhead to distance reach. As mentioned in the introduction, flexibility is an important feature of the next generation optical transmission systems. On the other hand, PCSC technique offers an excellent performance without any overhead for BPSK transmissions. As a result, this technique is very suitable for long-haul transmissions. Both PCP and PCSC techniques are very simple and minimum efforts are needed when switching from one technique to another.

In addition, in this thesis, important developments for NFT-based transmission systems have been also presented. Various important systems NFT-based designs have been discussed. The NIS transmission scheme has been investigated in details. Modified NIS schemes, which are appropriate for fibre links with EDFA-based and non-ideal Raman amplifications, have been also proposed. The obtained results clearly show the high potential of NFT technique for combating the nonlinear effects in fibre-optic communication systems. Even though NFT technology is still in its infancy, the obtained results in this thesis clearly demonstrate that this is a promising technique for designing nonlinear-free optical communication network.

## **6.2 Future research**

Future superchannel transponders should be adaptive and highly flexible in term of trading off the bit-rate to transmission distance. As a result, rate adaptive FEC, hybrid modulation formats or constellation probabilistic shaping would be highly desirable. However, rate adaptive FEC, hybrid modulation formats and constellation probabilistic shaping modify the signal statistical properties, which may have significant impacts on blind DSP techniques. As a consequence, these following topics will be highly important for future research:

1. Optimum hybrid QAM for rate-adaptive superchannel transponders.
2. Optimum rate-adaptive FEC for superchannel transponders and its transmission performance and complexity comparison to hybrid QAM.
3. Blind PNC techniques for transmission systems with hybrid QAM.
4. Blind PNC techniques for transmission systems with probabilistic constellation shaping.
5. Flexible fibre nonlinear compensation techniques for transmission systems with hybrid QAM and probabilistic constellation shaping.

In addition, as mentioned earlier, NFT-based method is still in its early development. As a result, significant further research efforts are required to transform this concept to practical applications. In particular, these following research topics will be highly important.

1. NFTs for dual-polarization systems. This is highly important to maximize the achievable SE in NFT-based systems.
2. NFT-based nonlinear multiplexers and demultiplexers for NFT-based WDM transmissions.
3. Low complexity NFT operations.
4. Effective DSP techniques for mitigations of transceivers' imperfections in NFT-based transmission systems.
5. Optimum modulation formats and FEC schemes for NFT-based transmission systems
6. Understanding the signal $\times$ noise interaction in the nonlinear Fourier domain and the ultimate system performance limitation of NFT-based transmission systems.

# Bibliography

- [1] K. Kao and G. Hockham, “Dielectric-fibre surface waveguides for optical frequencies,” *Proceedings of the Institution of Electrical Engineers*, vol. 113, no. 7, p. 1151, 1966.
- [2] I. Hayashi, M. B. Panish, P. W. Foy, and S. Sumski, “Junction lasers which operate continuously at room temperature,” *Applied Physics Letters*, vol. 17, no. 3, pp. 109–111, 1970.
- [3] R. J. Sanferrare, “Terrestrial Lightwave Systems,” *AT&T Technical Journal*, vol. 66, no. 1, pp. 95–107, 1987.
- [4] G. P. Agrawal, *Fiber-Optic Communication Systems*. Wiley, 4th ed., 2010.
- [5] R. Mears, L. Reekie, I. Jauncey, and D. Payne, “Low-noise erbium-doped fibre amplifier operating at 1.54 $\mu\text{m}$ ,” *Electronics Letters*, vol. 23, no. 19, pp. 1026–1028, 1987.
- [6] P. J. Winzer, “High-spectral-efficiency optical modulation formats,” *Journal of Lightwave Technology*, vol. 30, no. 24, pp. 3824–3835, 2012.
- [7] Cisco, “Cisco Visual Networking Index: Forecast and Methodology, 2014-2019. Available online at [http://www.cisco.com/c/en/us/solutions/collateral/service-provider/ip-ngn-ip-next-generation-network/white\\_paper\\_c11-481360.pdf](http://www.cisco.com/c/en/us/solutions/collateral/service-provider/ip-ngn-ip-next-generation-network/white_paper_c11-481360.pdf),” 2015.
- [8] X. Liu, S. Chandrasekhar, and P. J. Winzer, “Digital Signal Processing Techniques Enabling Multi-Tb/s Superchannel Transmission: An overview of recent advances

- in DSP-enabled superchannels,” *Signal Processing Magazine, IEEE*, vol. 31, no. 2, pp. 16–24, 2014.
- [9] D. Qian, M.-F. Huang, E. Ip, Y.-K. Huang, Y. Shao, J. Hu, and T. Wang, “101.7-Tb/s (370294-Gb/s) PDM-128QAM-OFDM Transmission over 355-km SSMF using Pilot-based Phase Noise Mitigation,” in *2011 Optical Fiber Communication Conference and Exposition and the National Fiber Optic Engineers Conference*, pp. 1–3, 2011.
- [10] S. Sano, Akihide, Kobayashi, Takayuki, Yamanaka, H. Matsuura, AkihikoKawakami, and H. Miyamoto, Yutaka Ishihara, Koichi Masuda, “102.3-Tb/s (224 x 548-Gb/s) C- and extended L-band All-Raman transmission over 240 km using PDM-64QAM single carrier FDM with digital pilot tone,” in *Optical Fiber Communication Conference*, p. PDP5C.3, 2012.
- [11] P. J. Winzer, “Making spatial multiplexing a reality,” *Nature Photonics*, vol. 8, no. 5, pp. 345–348, 2014.
- [12] D. Soma, K. Igarashi, Y. Wakayama, K. Takeshima, Y. Kawaguchi, N. Yoshikane, T. Tsuritani, I. Morita, and M. Suzuki, “2.05 Peta-bit/s Super-Nyquist-WDM SDM Transmission Using 9.8-km 6-mode 19-core Fiber in Full C band,” in *ECOC*, (Valencia, Spain), 2015.
- [13] B. J. Puttnam, R. S. Luís, W. Klaus, J. Sakaguchi, J.-M. D. Mendinueta, Y. Awaji, N. Wada, Y. Tamura, T. Hayashi, M. Hirano, and J. Marciante, “2.15 Pb/s Transmission Using a 22 Core Homogeneous Single-Mode Multi-Core Fiber and Wideband Optical Comb,” in *ECOC*, (Valencia, Spain), 2015.
- [14] R.-j. Essiambre, S. Member, G. Kramer, P. J. Winzer, G. J. Foschini, B. Goebel, and S. Member, “Capacity Limits of Optical Fiber Networks,” vol. 28, no. 4, pp. 662–701, 2010.
- [15] A.D. Ellis and D. Cotter, “Approaching the Non-Linear Shannon Limit,” *Journal of Lightwave Technology*, vol. 28, pp. 423–433, feb 2010.

- [16] S. Chandrasekhar, X. L. X. Liu, B. Zhu, and D. W. Peckham, "Transmission of a 1.2-Tb/s 24-carrier no-guard-interval coherent OFDM superchannel over 7200-km of ultra-large-area fiber," in *European Conference on Optical Communication*, vol. 2009-Suppl, pp. 7–8, 2009.
- [17] X. Liu, S. Chandrasekhar, P. J. Winzer, T. Lotz, J. Carlson, J. Yang, and G. Cheren, "1.5-Tb/s Guard-Banded Superchannel Transmission over 56 16QAM Signals with 5.75-b/s/Hz Net Spectral Efficiency," in *ECOC*, 2012.
- [18] G. Raybon, S. Randel, a. Adamiecki, P. J. Winzer, L. Salamanca, R. Urbanke, S. Chandrasekhar, a. Konczykowska, F. Jorge, J. Y. Dupuy, L. L. Buhl, S. Draving, M. Grove, and K. Rush, "1-Tb/s dual-carrier 80-GBaud PDM-16QAM WDM transmission at 5.2 b/s/Hz over 3200 km," *2012 IEEE Photonics Conference, IPC 2012*, pp. 6–7, 2012.
- [19] S. T. Le, M. E. McCarthy, and S. K. Turitsyn, "Optimized Hybrid QPSK/8QAM for CO-OFDM Transmissions," in *International Symposium on communications systems Networks and Digital Signal Processing*, 2014.
- [20] S. Haykin, *Communication Systems*. John Wiley & Sons, Inc, 2001.
- [21] R. Schmogrow, B. Nebendahl, M. Winter, A. Josten, D. Hillerkuss, S. Koenig, J. Meyer, M. Dreschmann, M. Huebner, C. Koos, J. Becker, W. Freude, and J. Leuthold, "Error Vector Magnitude as a Performance Measure for Advanced Modulation Formats," *IEEE Photonics Technology Letters*, vol. 24, pp. 61–63, jan 2012.
- [22] R. A. Shafik, S. Rahman, and R. Islam, "On the Extended Relationships Among EVM, BER and SNR as Performance Metrics," in *Electrical and Computer Engineering, 2006. ICECE '06. International Conference on*, pp. 408–411, 2006.
- [23] H. Bao and W. Shieh, "Transmission simulation of coherent optical OFDM signals in WDM systems," *Optics Express*, vol. 15, no. 8, pp. 4410–4418, 2007.

- [24] Z. Fan, L. Yazhi, W. Yandan, L. Li, Z. Lixin, C. Zhangyuan, and W. Chengbin, "Experimental Comparison of Different BER Estimation Methods for Coherent Optical QPSK Transmission Systems," *Photonics Technology Letters, IEEE*, vol. 23, no. 18, pp. 1343–1345, 2011.
- [25] G. Goldfarb and G. Li, "BER estimation of QPSK homodyne detection with carrier phase estimation using digital signal processing," *Optics Express*, vol. 14, no. 18, p. 8043, 2006.
- [26] S. T. Le, K. J. Blow, V. K. Menzentsev, and S. K. Turitsyn, "Comparison of numerical bit error rate estimation methods in 112Gbs QPSK CO-OFDM transmission," in *Optical Communication (ECOC 2013), 39th European Conference and Exhibition on*, pp. 1–3, 2013.
- [27] S. T. Le, K. J. Blow, V. K. Mezentsev, and S. K. Turitsyn, "Bit Error Rate Estimation Methods for QPSK CO-OFDM Transmission," *Lightwave Technology, Journal of*, vol. 32, no. 17, pp. 2951–2959, 2014.
- [28] S. T. Le, M. E. McCarthy, N. Mac Suibhne, E. Giacomidis, N. J. Doran, A. D. Ellis, and K. J. Blow, "Comparison of Bit Error Rate Estimation Methods for QPSK CO-OFDM Transmission," *IEEE Photonics Technology Letters*, vol. 26, pp. 2244–2247, nov 2014.
- [29] A. Carena, G. Bosco, V. Curri, P. Poggiolini, M. T. Taiba, and F. Forghieri, "Statistical characterization of PM-QPSK signals after propagation in uncompensated fiber links," in *Optical Communication (ECOC), 2010 36th European Conference and Exhibition on*, pp. 1–3, 2010.
- [30] J. C. Cartledge, J. Downie, J. E. Hurley, X. Zhu, and I. Roudas, "Bit Error Ratio Performance of 112 Gb/s PM-QPSK Transmission Systems," *Journal of Lightwave Technology*, vol. 30, pp. 1475–1479, may 2012.

- [31] H. L. Fan, J. F. Sun, P. Yang, and D. S. Li, "A robust timing and frequency synchronization algorithm for HF MIMO OFDM systems," *2010 Global Mobile Congress, GMC'2010*, vol. 2, no. 4, pp. 822–839, 2010.
- [32] S. Randel, S. Adhikari, and S. L. Jansen, "Analysis of RF-pilot-based phase noise compensation for coherent optical OFDM systems," *IEEE Photonics Technology Letters*, vol. 22, no. 17, pp. 1288–1290, 2010.
- [33] S. L. Jansen, I. Morita, T. C. W. Schenk, and H. Tanaka, "121.9-Gb/s PDM-OFDM Transmission With 2-b/s/Hz Spectral Efficiency Over 1000 km of SSMF," *Lightwave Technology, Journal of*, vol. 27, no. 3, pp. 177–188, 2009.
- [34] L. Xiang, S. Chandrasekhar, Z. Benyuan, P. J. Winzer, A. H. Gnauck, and D. W. Peckham, "448-Gb/s Reduced-Guard-Interval CO-OFDM Transmission Over 2000 km of Ultra-Large-Area Fiber and Five 80-GHz-Grid ROADMs," *Lightwave Technology, Journal of*, vol. 29, no. 4, pp. 483–490, 2011.
- [35] R. Kudo, T. Kobayashi, K. Ishihara, Y. Takatori, A. Sano, and Y. Miyamoto, "Coherent Optical Single Carrier Transmission Using Overlap Frequency Domain Equalization for Long-Haul Optical Systems," *Lightwave Technology, Journal of*, vol. 27, no. 16, pp. 3721–3728, 2009.
- [36] S. J. Savory, "Digital filters for coherent optical receivers," *Optics Express*, vol. 16, no. 2, p. 804, 2008.
- [37] Z. Wang, Y. Qiao, Y. Xu, and Y. Ji, "Statistical characterization of the nonlinear noise in 2.8 Tbit/s PDM-16QAM CO-OFDM system," *Optics Express*, vol. 21, no. 15, pp. 18034–18042, 2013.
- [38] X. Chen and W. Shieh, "Closed-form expressions for nonlinear transmission performance of densely spaced coherent optical OFDM systems.," *Optics express*, vol. 18, pp. 19039–54, aug 2010.

- [39] S. T. Le, T. Kanesan, E. Giacomidis, N. Doran, and A. Ellis, "Quasi-pilot Aided Phase Noise Estimation for Coherent Optical OFDM Systems," *Photonics Technology Letters, IEEE*, vol. 26, no. 5, pp. 504–507, 2014.
- [40] Q. Zhuge, C. Chen, and D. V. Plant, "Dispersion-enhanced phase noise effects on reduced-guard-interval CO-OFDM transmission.," *Optics express*, vol. 19, no. 5, pp. 4472–4484, 2011.
- [41] T. M. Schmidl and D. C. Cox, "Robust frequency and timing synchronization for OFDM," *IEEE Transactions on Communications*, vol. 45, no. 12, pp. 1613–1621, 1997.
- [42] K. Kikuchi and S. Tsukamoto, "Evaluation of Sensitivity of the Digital Coherent Receiver," *Journal of Lightwave Technology*, vol. 26, no. 13, pp. 1817–1822, 2008.
- [43] E. Giacomidis, M. A. Jarajreh, S. Sygletos, S. T. Le, F. Farjady, A. Tsokanos, A. Hamié, E. Pincemin, Y. Jaouën, A. D. Ellis, and N. J. Doran, "Dual-polarization multi-band optical OFDM transmission and transceiver limitations for up to 500 Gb/s uncompensated long-haul links," *Optics Express*, vol. 22, no. 9, pp. 10975–10986, 2014.
- [44] S. Wu and Y. Bar-Ness, "OFDM Systems in the Presence of Phase Noise: Consequences and Solutions," *Communications, IEEE Transactions on*, vol. 52, no. 5, p. 855, 2004.
- [45] L. Tomba, "On the effect of Wiener phase noise in OFDM systems," *Communications, IEEE Transactions on*, vol. 46, no. 5, pp. 580–583, 1998.
- [46] S. T. Le, M. E. McCarthy, E. Giacomidis, and N. J. Doran, "Adaptive Time Synchronization and Frequency Offset Estimation for CO-OFDM," in *International Symposium on communications systems Networks and Digital Signal Processing*, 2014.

- [47] Y. Mostofi, D. C. Cox, and A. Bahai, "ICI mitigation for mobile OFDM receivers," in *Communications, 2003. ICC '03. IEEE International Conference on*, vol. 5, pp. 3351–3355 vol.5, 2003.
- [48] A. F. Molisch, M. Toeltsch, and S. Vermani, "Iterative Methods for Cancellation of Intercarrier Interference in OFDM Systems," *Vehicular Technology, IEEE Transactions on*, vol. 56, no. 4, pp. 2158–2167, 2007.
- [49] T. Kanesan, S. T. Le, D. Roque, and A. D. Ellis, "Non-rectangular perfect reconstruction pulse shaping based ICI reduction in CO-OFDM," *Optics Express*, vol. 22, no. 2, pp. 1749–1759, 2014.
- [50] Q. Zhuge, M. H. Morsy-Osman, and D. V. Plant, "Low overhead intra-symbol carrier phase recovery for reduced-guard-interval CO-OFDM," *Journal of Lightwave Technology*, vol. 31, no. 8, pp. 1158–1169, 2013.
- [51] W. Shieh, "Maximum-Likelihood Phase and Channel Estimation for Coherent Optical OFDM," *Photonics Technology Letters, IEEE*, vol. 20, no. 8, pp. 605–607, 2008.
- [52] C. Shengjiao, K. Pooi Yuen, and Y. Changyuan, "Decision-Aided, Pilot-Aided, Decision-Feedback Phase Estimation for Coherent Optical OFDM Systems," *Photonics Technology Letters, IEEE*, vol. 24, no. 22, pp. 2067–2069, 2012.
- [53] M. E. Mousa-Pasandi and D. V. Plant, "Zero-overhead phase noise compensation via decision-directed phase equalizer for coherent optical OFDM.," *Optics express*, vol. 18, no. 20, pp. 20651–20660, 2010.
- [54] H. Youngsun and C. Wonzoo, "Non-Data-Aided Phase Noise Suppression Scheme for CO-OFDM Systems," *Photonics Technology Letters, IEEE*, vol. 25, no. 17, pp. 1703–1706, 2013.
- [55] T. Pfau, S. Hoffmann, and R. Noé, "Hardware-efficient coherent digital receiver concept with feedforward carrier recovery for M-QAM constellations," *Journal of Lightwave Technology*, vol. 27, no. 8, pp. 989–999, 2009.

- [56] S. T. Le, M. E. McCarthy, N. M. Suibhne, P. A. Haigh, E. Giacomidis, N. J. Doran, A. D. Ellis, and S. K. Turitsyn, "Decision-Directed-Free Blind Phase Noise Estimation for CO-OFDM," 2015.
- [57] S. Le, P. Haigh, A. Ellis, and S. Turitsyn, "Blind Phase Noise Estimation for CO-OFDM Transmissions," *Journal of Lightwave Technology*, vol. PP, no. 99, pp. 1–1, 2015.
- [58] M. G. Taylor, "Phase Estimation Methods for Optical Coherent Detection Using Digital Signal Processing," *Lightwave Technology, Journal of*, vol. 27, no. 7, pp. 901–914, 2009.
- [59] C. Wonzoo, W. A. Sethares, and C. R. Johnson, "Performance analysis of blind adaptive phase offset correction based on dispersion minimization," *Signal Processing, IEEE Transactions on*, vol. 52, no. 6, pp. 1750–1759, 2004.
- [60] S. T. Le, N. M. Suibhne, M. E. McCarthy, A. D. Ellis, and S. K. Turitsyn, "Multiplier-free Blind Phase Noise Estimation for CO-OFDM Transmission," in *ECOC*, (Valencia, Spain, paper Mo.4.3.6), 2015.
- [61] J. E. Volder, "The CORDIC Trigonometric Computing Technique," *Electronic Computers, IRE Transactions on*, vol. EC-8, no. 3, pp. 330–334, 1959.
- [62] M. E. Mousa-Pasandi and D. V. Plant, "Zero-overhead phase noise compensation via decision-directed phase equalizer for coherent optical OFDM," *Optics Express*, vol. 18, no. 20, pp. 20651–20660, 2010.
- [63] C. E. Shannon, "A Mathematical Theory of Communication," *The Bell System Technical Journal*, vol. 27, pp. 379–432, 1948.
- [64] P. P. Mitra and J. B. Stark, "Nonlinear limits to the information capacity of optical bre communications," pp. 1027–1030, 2001.
- [65] D. Rafique, J. Zhao, and A. D. Ellis, "Digital back-propagation for spectrally efficient WDM 112 Gbit/s PM m-ary QAM transmission," *Optics Express*, vol. 19, no. 6, pp. 5219–5224, 2011.

- [66] J. E. Prilepsky, S. A. Derevyanko, and S. K. Turitsyn, "Nonlinear spectral management: Linearization of the lossless fiber channel," *Optics Express*, vol. 21, no. 20, pp. 24344–24367, 2013.
- [67] I. Phillips, M. Tan, M. F. Stephens, M. McCarthy, E. Giacomidis, S. Sygletos, P. Rosa, S. Fabbri, S. T. Le, T. Kanesan, S. K. Turitsyn, N. J. Doran, P. Harper, and A. D. Ellis, "Exceeding the Nonlinear-Shannon Limit using Raman Laser Based Amplification and Optical Phase Conjugation," in *Optical Fiber Communication Conference*, (San Francisco, California), p. M3C.1, Optical Society of America, 2014.
- [68] E. Ip and J. M. Kahn, "Compensation of Dispersion and Nonlinear Impairments Using Digital Backpropagation," *Journal of Lightwave Technology*, vol. 26, pp. 3416–3425, oct 2008.
- [69] E. Giacomidis, S. T. Le, M. Ghanbarisabagh, M. McCarthy, I. Aldaya, S. Mhatli, M. A. Jarajreh, P. A. Haigh, N. J. Doran, A. D. Ellis, and B. J. Eggleton, "Fiber nonlinearity-induced penalty reduction in CO-OFDM by ANN-based nonlinear equalization.," *Optics letters*, vol. 40, pp. 5113–6, nov 2015.
- [70] E. Giacomidis, S. T. Le, I. Aldaya, J. Wei, M. McCarthy, N. Doran, and B. Eggleton, "Experimental Comparison of Artificial Neural Network and Volterra based Nonlinear Equalization for CO-OFDM," in *Optical Fiber Communication Conference*, p. W3A.4, OSA, mar 2016.
- [71] E. Giacomidis, S. Mhatli, T. Nguyen, S. T. Le, I. Aldaya, M. McCarthy, and B. Eggleton, "Kerr-Induced Nonlinearity Reduction in Coherent Optical OFDM by Low Complexity Support Vector Machine Regression-based Equalization," in *Optical Fiber Communication Conference*, p. Th2A.49, OSA, mar 2016.
- [72] E. Giacomidis, I. Aldaya, M. A. Jarajreh, A. Tsokanos, S. Le, F. Farjady, Y. Jaouen, A. D. Ellis, and N. J. Doran, "Volterra-based reconfigurable nonlinear equalizer for coherent OFDM," *IEEE Photonics Technology Letters*, vol. 26, no. 14, pp. 1383–1386, 2014.

- [73] S. T. Le, M. McCarthy, S. K. Turitsyn, I. Phillips, D. Lavery, T. Xu, P. Bayvel, and A. Ellis, "Optical and Digital Phase Conjugation Techniques for Fiber Nonlinearity Compensation," in *OECC*, 2015.
- [74] A. Ellis, S. T. Le, M. Al-Khateeb, S. Turitsyn, G. Liga, D. Lavery, T. Xu, and P. Bayvel, "The impact of phase conjugation on the nonlinear-Shannon limit," in *IEEE Summer Topical*, 2015.
- [75] M. Jarajreh, E. Giacomidis, I. Aldaya, S. T. Le, A. Tsokanos, Z. Ghassemlooy, and N. J. Doran, "Artificial Neural Network Nonlinear Equalizer for Coherent Optical OFDM," *Photonics Technology Letters*, vol. 27, no. 4, 2015.
- [76] G. Liga, T. Xu, A. Alvarado, R. I. Killey, and P. Bayvel, "On the performance of multichannel digital backpropagation in high-capacity long-haul optical transmission," *Optics Express*, vol. 22, no. 24, pp. 30053–30062, 2014.
- [77] N. Alic, E. Myslivets, E. Temprana, B. P. P. Kuo, and S. Radic, "Nonlinearity Cancellation in Fiber Optic Links Based on Frequency Referenced Carriers," *Lightwave Technology, Journal of*, vol. 32, no. 15, pp. 2690–2698, 2014.
- [78] C. Xi, L. Xiang, S. Chandrasekhar, B. Zhu, and R. W. Tkach, "Experimental demonstration of fiber nonlinearity mitigation using digital phase conjugation," in *Optical Fiber Communication Conference and Exposition (OFC/NFOEC), 2012 and the National Fiber Optic Engineers Conference*, pp. 1–3, 2012.
- [79] S. L. Jansen, D. Van den Borne, B. Spinnler, S. Calabro, H. Suche, P. M. Krummrich, W. Sohler, G. D. Khoe, and H. de Waardt, "Optical phase conjugation for ultra long-haul phase-shift-keyed transmission," *Lightwave Technology, Journal of*, vol. 24, no. 1, pp. 54–64, 2006.
- [80] S. Watanabe, S. Kaneko, and T. Chikama, "Long-Haul Fiber Transmission Using Optical Phase Conjugation," *Optical Fiber Technology*, vol. 2, no. 2, pp. 169–178, 1996.

- [81] X. Liu, a. R. Chraplyvy, P. J. Winzer, R. W. Tkach, and S. Chandrasekhar, "Phase-conjugated twin waves for communication beyond the Kerr nonlinearity limit," *Nature Photonics*, vol. 7, pp. 560–568, may 2013.
- [82] X. Liu, "Twin-Wave Based Optical Transmission with Enhanced Linear and Non-linear Performances," *Journal of Lightwave Technology*, vol. PP, no. 99, p. 1, 2014.
- [83] X. Yi, X. Chen, C. Li, M. Luo, Q. Yang, Z. Li, and K. Qiu, "Experimental Demonstration of Digital Coherent Superposition of Optical OFDM Subcarrier Pairs for Mitigation of Linear and Nonlinear Phase Noise," *Optical Fiber Communication Conference*, vol. 1, no. 3, p. Tu3G.6, 2014.
- [84] S. T. Le, M. E. McCarthy, N. M. Suibhne, A. D. Ellis, and S. K. Turitsyn, "Phase-conjugated Pilots for Fibre Nonlinearity Compensation in CO-OFDM Transmission," 2014.
- [85] S. T. Le, M. E. McCarthy, N. MacSuibhne, A. D. Ellis, and S. K. Turitsyn, "Phase-conjugated Pilots for Fibre Nonlinearity Compensation in CO-OFDM Transmission," *Lightwave Technology, Journal of*, vol. PP, no. 99, p. 1, 2015.
- [86] T. Yoshida, T. Sugihara, K. Ishida, and T. Mizuochi, "Spectrally-efficient Dual Phase-Conjugate Twin Waves with Orthogonally Multiplexed Quadrature Pulse-shaped Signals," *Optical Fiber Communication Conference*, p. M3C.6, 2014.
- [87] W. Shieh, X. Yi, Y. Ma, and Q. Yang, "Coherent optical OFDM: has its time come? [Invited]," *Journal of Optical Networking*, vol. 7, no. 3, pp. 234–255, 2008.
- [88] J. Zhao and A. D. Ellis, "A Novel Optical Fast OFDM with Reduced Channel Spacing Equal to Half of the Symbol Rate per Carrier," in *Optical Fiber Communication Conference*, (San Diego, California), p. OMR1, Optical Society of America, 2010.
- [89] S. T. Le, M. E. McCarthy, N. M. Suibhne, M. A. Z. Al-Khateeb, E. Giacomidis, N. Doran, A. D. Ellis, and S. K. Turitsyn, "Demonstration of Phase-Conjugated Subcarrier Coding for Fiber Nonlinearity Compensation in CO-OFDM Transmission," *Journal of Lightwave Technology*, vol. 33, no. 11, pp. 2206–2212, 2015.

- [90] S. T. Le, E. Giacomidis, N. Doran, A. D. Ellis, and S. K. Turitsyn, "Phase-conjugated Subcarrier Coding for Fibre Nonlinearity Mitigation in CO-OFDM Transmission," in *ECOC*, (Cannes, France, paper We.3.3.2), 2014.
- [91] S. T. Le, K. Blow, and S. Turitsyn, "Power pre-emphasis for suppression of FWM in coherent optical OFDM transmission," *Optics Express*, vol. 22, no. 6, pp. 7238–7248, 2014.
- [92] F. Buchali, R. Dischler, and X. Liu, "Optical OFDM: A promising high-speed optical transport technology," *Bell Labs Technical Journal*, vol. 14, no. 1, pp. 125–146, 2009.
- [93] D. A. Cleland, A. D. Ellis, and C. H. F. Sturrock, "Precise modelling of four wave mixing products over 400 km of step-index fibre," *Electronics Letters*, vol. 28, no. 12, pp. 1171–1173, 1992.
- [94] B. Inan, S. Randel, S. L. Jansen, A. Lobato, S. Adhikari, and N. Hanik, "Pilot-tone-based nonlinearity compensation for optical OFDM systems," in *Optical Communication (ECOC), 2010 36th European Conference and Exhibition on*, pp. 1–3, 2010.
- [95] X. Liu, S. Chandrasekhar, P. J. Winzer, a. R. Chraplyvy, R. W. Tkach, B. Zhu, T. F. Taunay, M. Fishteyn, and D. J. DiGiovanni, "Scrambled coherent superposition for enhanced optical fiber communication in the nonlinear transmission regime.," *Optics express*, vol. 20, pp. 19088–95, aug 2012.
- [96] D. Rafique and A. D. Ellis, "Impact of signal-ASE four-wave mixing on the effectiveness of digital back-propagation in 112 Gb/s PM-QPSK systems.," *Optics express*, vol. 19, pp. 3449–54, feb 2011.
- [97] A. D. Ellis and W. A. Stallard, "Four wave mixing in ultra long transmission systems incorporating linear amplifiers," in *Non-Linear Effects in Fibre Communications, IEE Colloquium on*, pp. 6/1–6/4, 1990.
- [98] N. M. S. M. E. McCarthy S. T. Le, P. Harper, and A. D. Ellis, "High Spectral Efficiency Transmission Emulation for Non-Linear Transmission Performance Estima-

tion for High Order Modulation Formats,” in *ECO*, (Cannes, France, paper P.5.7), 2014.

- [99] S. T. Le, T. Kanesan, M. McCarthy, E. Giacomidis, I. Phillips, M. F. Stephens, M. Tan, N. J. Doran, A. D. Ellis, and S. K. Turitsyn, “Experimental Demonstration of Data-dependent Pilot-aided Phase Noise Estimation for CO-OFDM,” in *Optical Fiber Communication Conference*, (San Francisco, California), p. Tu3G.4, Optical Society of America, 2014.
- [100] S. T. Le and S. Turitsyn, “Techniques for Noise and Nonlinear Impairments Compensation in CO-OFDM Transmission,” in *ICTON*, 2015.
- [101] X. Liu, S. Chandrasekhar, P. J. Winzer, R. W. Tkach, and A. R. Chraplyvy, “406 . 6-Gb / s PDM-BPSK Superchannel Transmission over 12 , 800-km TWRS Fiber via Nonlinear Noise Squeezing,” pp. 13–15, 2013.
- [102] D. M. Pepper and A. Yariv, “Compensation for phase distortions in nonlinear media by phase conjugation,” *Optics Letters*, vol. 5, no. 2, pp. 59–60, 1980.
- [103] a. Hasegawa and T. Nyu, “Eigenvalue communication,” *Journal of Lightwave Technology*, vol. 11, pp. 395–399, mar 1993.
- [104] J. E. Prilepsky, S. a. Derevyanko, K. J. Blow, I. Gabitov, and S. K. Turitsyn, “Non-linear Inverse Synthesis and Eigenvalue Division Multiplexing in Optical Fiber Channels,” *Physical Review Letters*, vol. 113, p. 013901, jul 2014.
- [105] M. I. Yousefi and F. R. Kschischang, “Information Transmission using the Nonlinear Fourier Transform, Part I: Mathematical Tools,” pp. 1–17, feb 2012.
- [106] A. Maruta, “Eigenvalue Modulated Optical Transmission System,” in *OECC*, (Shanghai, China), 2015.
- [107] V. E. Zakharov and a. B. Shabat, “Exact theory of two-dimensional self-focusing and one-dimensional self-modulation waves in nonlinear media,” *Soviet Physics JETP*, vol. 34, no. 1, pp. 62–69, 1972.

- [108] A. Hasegawa, *Optical solitons in fibers*, vol. 2. 2003.
- [109] M. J. Ablowitz, D. J. Kaup, A. C. Newell, and H. Segur, “The inverse scattering transform-fourier analysis for nonlinear problems,” *Studies in Applied Mathematics*, vol. 53, pp. 249–315, 1974.
- [110] Y. S. Kivshar and G. P. Agrawal, *Optical Solitons: From Fibers to Photonic Crystals*, vol. 1. 2003.
- [111] M. Chertkov, A. Peleg, and I. Gabitov, “Inelastic interchannel collisions of pulses in optical fibers in the presence of third-order dispersion,” 2004.
- [112] J. E. Prilepsky, S. A. Derevyanko, and S. K. Turitsyn, “Temporal Solitonic Crystals and Non-Hermitian Informational Lattices,” *Phys. Rev. Lett.*, vol. 108, no. 183902, 2012.
- [113] Osborne A. R., “The inverse scattering transform: tools for the nonlinear Fourier analysis and filtering of ocean surface waves,” *Chaos, Solitons & Fractals*, vol. 5, pp. 2623–2637, 1995.
- [114] A. S. Fokas and I. M. Gelfand, “Integrability of linear and nonlinear evolution equations and the associated nonlinear Fourier transform,” *Letters in Mathematical Physics*, vol. 32, pp. 189–210, 1994.
- [115] V. Aref, H. Bülow, K. Schuh, and W. Idler, “Experimental Demonstration of Nonlinear Frequency Division Multiplexed Transmission,” in *ECOC*, (Valencia, Spain), 2015.
- [116] H. Buelow, “Experimental Assessment of Nonlinear Fourier Transformation Based Detection under Fiber Nonlinearity,” 2014.
- [117] D. Zhenhua, S. Hari, G. Tao, Z. Kangping, M. I. Yousefi, L. Chao, P. K. A. Wai, F. R. Kschischang, and A. P. T. Lau, “Nonlinear Frequency Division Multiplexed Transmissions Based on NFT,” *Photonics Technology Letters, IEEE*, vol. 27, no. 15, pp. 1621–1623, 2015.

- [118] H. Terauchi and A. Maruta, "Eigenvalue modulated optical transmission system based on digital coherent technology," in *OptoElectronics and Communications Conference held jointly with 2013 International Conference on Photonics in Switching (OECC/PS), 2013 18th*, pp. 1–2, 2013.
- [119] H. Terauchi, Y. Matsuda, A. Toyota, and A. Maruta, "Noise Tolerance of Eigenvalue Modulated Optical Transmission System Based on Digital Coherent Technology," vol. 0, no. July, pp. 778–780, 2014.
- [120] S. Hari, F. Kschischang, and M. Yousefi, "Multi-eigenvalue communication via the nonlinear Fourier transform," in *Communications (QBSC), 2014 27th Biennial Symposium on*, pp. 92–95, 2014.
- [121] S. T. Le, J. E. Prilepsky, and S. K. Turitsyn, "Nonlinear inverse synthesis for high spectral efficiency transmission in optical fibers.," *Optics express*, vol. 22, no. 22, pp. 26720–41, 2014.
- [122] S. T. Le, J. E. Prilepsky, and S. K. Turitsyn, "Nonlinear inverse synthesis technique for optical links with lumped amplification," *Optics Express*, vol. 23, no. 7, p. 8317, 2015.
- [123] S. T. Le, J. E. Prilepsky, M. Kamalian, P. Rosa, M. Tan, J. D. Ania-Castañón, P. Harper, and S. K. Turitsyn, "Modified Nonlinear Inverse Synthesis for Optical Links with Distributed Raman Amplification," 2015.
- [124] S. T. Le, I. Philips, Y. Prilepsky, P. Harper, N. Doran, A. D. Ellis, and S. Turitsyn, "First Experimental Demonstration of Nonlinear Inverse Synthesis Transmission over Transoceanic Distances," in *OFC*, 2016.
- [125] S. T. Le, I. D. Philips, J. E. Prilepsky, P. Harper, A. D. Ellis, and S. K. Turitsyn, "Demonstration of Nonlinear Inverse Synthesis Transmission over Transoceanic Distances," *Journal of Lightwave Technology*, vol. PP, 2016.

- [126] S. T. Le, J. E. Prilepsky, P. Rosa, J. D. Ania-Castanon, and S. K. Turitsyn, “Non-linear Inverse Synthesis for Optical Links with Distributed Raman Amplification,” *Journal of Lightwave Technology*, vol. 34, no. 5, 2016.
- [127] S. T. Le, S. Wahl, D. Lavery, J. E. Prilepsky, and S. K. Turitsyn, “Reduced Complexity Nonlinear Inverse Synthesis for Nonlinearity Compensation in Optical Fiber,” in *CLEO*, 2015.
- [128] S. Wahls, S. T. Le, J. E. Prilepsky, H. V. Poor, and S. K. Turitsyn, “Digital Back-propagation in the Nonlinear Fourier Domain,” 2015.
- [129] I. Safari and M. Tavakkolnia, “Signalling over nonlinear fibre-optic channels by utilizing both solitonic and radiative spectra,” in *Networks and Communications (EuCNC)*, 2015.
- [130] R. Feced, M. N. Zervas, M. A. Muriel, M. Durkin, M. Ibsen, and M. N. Zervas, “An efficient inverse scattering algorithm for the design of nonuniform fiber Bragg gratings,” *IEEE Journal of Quantum Electronics*, vol. 35, no. 8, pp. 1105–1115, 1999.
- [131] J. Skaar, L. Wang, and T. Erdogan, “On the synthesis of fiber Bragg gratings by layer peeling,” *IEEE Journal of Quantum Electronics*, vol. 37, no. 2, pp. 165–173, 2001.
- [132] L. Poladian, “Iterative and Noniterative Design Algorithms for Bragg Gratings,” *Optical Fiber Technology*, vol. 5, no. 2, pp. 215–222, 1999.
- [133] M. I. Yousefi and F. R. Kschischang, “Information Transmission using the Nonlinear Fourier Transform, Part II: Numerical Methods,” pp. 1–17, apr 2012.
- [134] E. G. Turitsyna and S. K. Turitsyn, “Digital signal processing based on inverse scattering transform,” *Optics Letters*, vol. 38, pp. 4186–4188, 2013.
- [135] J. S. Bulirsch and R., *Introduction to Numerical Analysis, 2nd ed.* Springer-Verlag, 1993.

- [136] S. Burtsev, R. Camassa, and I. Timofeyev, “Numerical algorithms for the direct spectral transform with applications to nonlinear Schrodinger type systems,” *Journal of Computational Physics*, vol. 147, no. 1, pp. 166–186, 1998.
- [137] G. Boffetta and A. R. Osborne, “Computation of the direct scattering transform for the nonlinear Schroedinger equation,” *Journal of Computational Physics*, vol. 102, 1992.
- [138] T. Kuusela, J. Hietarinta, K. Kokko, and R. Laiho, “Soliton experiments in a nonlinear electrical transmission line,” *European Journal of Physics*, vol. 8, pp. 27–33, 1987.
- [139] O. V. Belai, E. V. Podivilov, O. Y. Schwarz, D. A. Shapiro, and L. L. Frumin, “Finite Bragg grating synthesis by numerical solution of Hermitian Gel’fand-Levitan-Marchenko equations,” *Journal of the Optical Society of America B*, vol. 23, no. 10, pp. 2040–2045, 2006.
- [140] O. V. Belai, L. L. Frumin, E. V. Podivilov, and D. A. Shapiro, “Efficient numerical method of the fiber Bragg grating synthesis,” *Journal of the Optical Society of America B*, vol. 24, no. 7, pp. 1451–1457, 2007.
- [141] S. ZOHAR, “Toeplitz Matrix Inversion: The Algorithm of W. F. Trench ,” *Journal of the Association for Computing Machinery*, vol. 16, no. 4, pp. 561–592, 1969.
- [142] J. Bland-Hawthorn and V. Steblina, “Comparison of Inverse Scattering Algorithms for Designing Ultrabroadband Fibre Bragg Gratings,” *Optics Express*, vol. 17, pp. 1995–2004, 2009.
- [143] G. Xiao and K. Yashiro, “An efficient algorithm for solving Zakharov-Shabat inverse scattering problem,” *IEEE Transactions on Antennas and Propagation*, vol. 50, pp. 807–811, jun 2002.
- [144] M. V. Barel, G. Heinig, and P. Kravanja, “A Stabilized Superfast Solver for Non-symmetric Toeplitz Systems,” *SIAM J. Matrix Anal. Appl.*, vol. 23, pp. 494–510, 2001.

- [145] M. Stewart, *Fast algorithms for structured matrix computations*, vol. in Handbo. Chapman & Hall, 2013.
- [146] L. L. Frumin, O. V. Belai, E. V. Podivilov, and D. A. Shapiro, “Efficient numerical method for solving the direct Zakharov-Shabat scattering problem,” *Journal of the Optical Society of America B*, vol. 32, no. 2, pp. 290–296, 2015.
- [147] S. Wahls and H. V. Poor, “Inverse Nonlinear Fourier Transforms Via Interpolation : The Ablowitz-Ladik Case,” pp. 1848–1855, 2014.
- [148] S. Wahls and H. V. Poor, “Fast inverse nonlinear Fourier transform for generating multisolitons in optical fiber,” 2015.
- [149] S. Wahls and H. V. Poor, “Introducing the fast nonlinear Fourier transform,” *2013 IEEE International Conference on Acoustics, Speech and Signal Processing*, pp. 5780–5784, may 2013.
- [150] S. Wahls and H. V. Poor, “Introducing the fast nonlinear Fourier transform,” in *Proceedings of International Conference on Acoustics, Speech, and Signal Processing (ICASSP 2013)*, IEEE, pp. 5780–5784, 2013.
- [151] S. Kilmurray, T. Fehenberger, P. Bayvel, and R. I. Killey, “Comparison of the non-linear transmission performance of quasi-Nyquist WDM and reduced guard interval OFDM,” *Optics Express*, vol. 20, no. 4, pp. 4198–4205, 2012.
- [152] Y. Lu, Y. Fang, B. Wu, K. Wang, W. Wan, F. Yu, L. Li, X. Shi, and Q. Xiong, “Experimental comparison of 32-Gbaud Electrical-OFDM and Nyquist-WDM transmission with 64GSa/s DAC,” in *ECOC*, (London, UK), 3013.
- [153] A. H. Kodama and Y, *Solitons in Optical Communications* . Oxford University Press, 1996.
- [154] S. K. Turitsyn, T. Schäfer, K. H. Spatschek, and V. K. Mezentsev, “Path-averaged chirped optical soliton in dispersion-managed fiber communication lines,” *Optics Communications*, vol. 163, no. 13, pp. 122–158, 1999.

- [155] M. I. Yousefi and F. R. Kschischang, “Information Transmission using the Nonlinear Fourier Transform, Part III: Spectrum Modulation,” pp. 1–19, feb 2013.
- [156] S. Wahls and H. V. Poor, “Fast Numerical Nonlinear Fourier Transforms,” p. 17, feb 2014.
- [157] M. Tan, P. Rosa, I. D. Phillips, and P. Harper, “Long-haul Transmission Performance Evaluation of Ultra-long Raman Fibre Laser Based Amplification Influenced by Second Order Co-pumping,” in *Asia Communications and Photonics Conference 2014*, (Shanghai), p. Ath1E.4, Optical Society of America, 2014.
- [158] M. Tan, P. Rosa, M. Iqbal, I. D. Phillips, and J. D. A.-C. J. Nuño, “RIN Mitigation in Second-Order Pumped Raman Fibre Laser Based Amplification,” 2015.
- [159] P. Rosa, S. T. Le, G. Rizzelli, M. Tan, and J. D. Ania-Castañón, “Signal power asymmetry optimisation for optical phase conjugation using Raman amplification.,” *Optics express*, vol. 23, pp. 31772–8, dec 2015.
- [160] M. Tan, P. Rosa, S. T. Le, M. A. Iqbal, I. D. Phillips, and P. Harper, “Transmission performance improvement using random DFB laser based Raman amplification and bidirectional second-order pumping.,” *Optics express*, vol. 24, pp. 2215–21, feb 2016.
- [161] P. Rosa, M. Tan, I. D. Phillips, S. Le Thai, J. D. Ania-Castanon, S. Sygletos, and P. Harper, “Unrepeated DP-QPSK transmission over 350 km standard fibre using URFL based amplification,” in *Asia Communications and Photonics Conference 2014*, p. Ath4E.5, OSA, nov 2014.
- [162] M. Tan, P. Rosa, S. T. Le, I. D. Phillips, and P. Harper, “Evaluation of 100G DP-QPSK long-haul transmission performance using second order co-pumped Raman laser based amplification,” *Optics Express*, vol. 23, no. 17, pp. 22181–22189, 2015.
- [163] J. Ania-Castañón, “Quasi-lossless transmission using second-order Raman amplification and fibre Bragg gratings,” *Optics Express*, vol. 12, no. 19, pp. 4372–4377, 2004.

- [164] S. K. Turitsyn, B. G. Bale, and M. P. Fedoruk, “Dispersion-managed solitons in fibre systems and lasers,” *Physics Reports*, vol. 521, no. 4, pp. 135–203, 2012.
- [165] V. Aref, H. Bülow, K. Schuh, and W. Idler, “Experimental Demonstration of Non-linear Frequency Division Multiplexed Transmission,” 2015.